Suspensions of particles interacting with porous matrices : transport, deposition and accumulation.

Gaétan Gerber

Suspensions of particles interacting with porous matrices: a fertile ground for transport, deposition and accumulation.

Thesis presented by

Gaétan Gerber

In fulfillment of the title of

Doctor of Philosophy in Physics

from

Université Paris-Est, France

Thesis defended on October 25th, 2019
In front of

Prof.	Patrice Bacchin	Université Paul Sabatier - LGC	Reviewer, President
Prof.	Rajandrea Sethi	Politecnico di Torino - DIATI	Reviewer
Prof.	Emilie Dressaire	University of California, Santa Barbara	Examiner
Dr.	Laurent Lassabatère	ENTPE - LEHNA	Examiner
Prof.	Philippe Coussot	IFSTTAR	Director
Prof.	David A. Weitz	Harvard University - SEAS	Co-director

Abstract (english version)

From the separation of products on industrial filters to the propagation of pollutants in soils or the transmission of micro-organisms in biological tissues, the transport of particles through porous matrices is ubiquitous. Particle-matrix interactions involve crucial deposition mechanisms, often studied by numerical simulations, global measurements or reduced (1D or 2D) systems. By making adapted 3D porous media (transparent random packings of spheres), and taking advantage of original internal observations (MRI, confocal microscopy), we have been able to directly visualize and analyze the whole range of transport and deposition dynamics at the global and local scales. Varying in turns the particles size (tens of nanometers to tens of microns), long-range interactions (electrostatic or magnetic) and shape (from unique spheres to clusters), all deposition regimes are finally mapped according to three key parameters: particle confinement (particle/pore size ratio), particle-surface affinity, and inter-particle aggregation ability.

Two examples highlight the diversity of these regimes. First, we show that non-colloidal particles of sufficient size tend to clog pores by accumulating in pore size clusters, which ultimately constitute regions avoided by the flow. A critical cluster concentration (percolation) corresponds to a system saturation, i.e. caking. Further insights on the impact of the particle shape on the clogging dynamics are also proposed. On another side, for non-clogging colloidal particles, we show that particle accumulation is a self-limited mechanism, towards a deposited fraction associated with a balance between the colloidal cohesive energy and the local flow (drag energy varying with evolving porosity). In the end, the classification of the main deposition regimes combined with simple predictive models allows an application of these results to a broad range of systems.

Abstract (version française)

La séparation de produits industriels par filtration, la propagation de polluants dans les sols ou la transmission de micro-organismes au sein de tissus biologiques ont en commun le transport de particules au travers de matériaux poreux (matrices). Les interactions particule-matrice engendrent des phénomènes de dépôts de particules, le plus souvent étudiés par simulations numériques, mesures globales ou via des systèmes modèles réduits (1D ou 2D). Grâce à des milieux poreux adaptés (empilements transparents et aléatoires de sphères) et à des méthodes originales d'observation interne (IRM, microscopie confocale), une visualisation directe des dynamiques de transport et de dépôt est rendue possible à l'échelle locale. En variant successivement la taille des particules (de la dizaine de nanomètres à la dizaine de microns), leurs propriétés d'interaction (électrostatique ou magnétique) et leur forme (de sphères uniques à agrégats), tous les régimes de dépôts sont in fine classifiés selon trois paramètres clés : le confinement des particules (rapport de tailles particule/pore), leur affinité avec la matrice et leur potentiel d'agrégation.

Deux exemples illustrent en particulier la diversité des régimes étudiés ; chacun étant associé à un modèle prédictif simple permettant une application directe à un large panel de systèmes. D'une part, le coincement stérique de particules non-colloïdales conduit à la formation d'amas de taille comparable aux pores, déviant l'écoulement. Une concentration critique de ces bouchons correspond à une saturation de la matrice et divergence des dépôts (blocage complet du système). D'autre part, l'adsorption de particules colloïdales aux parois de la matrice est étudiée selon leur mode de transport et potentiel d'agrégation. Leur accumulation est associée à un mécanisme atypique d'autorégulation équilibrant la cohésion entre particules et les forces visqueuses évoluant avec la porosité ; allant jusqu'à empêcher un blocage du système.

Acknowledgements/Remerciements

Les travaux présentés dans ce manuscrit résultent de discussions et de rencontres qui m'ont fait évoluer scientifiquement et personnellement au cours de mes trois années de thèse. De Champs-sur-Marne à Boston, de nombreuses personnes méritent pour cela ma sincère reconnaissance.

Du côté français, je souhaite remercier...

Philippe, pour avoir été un *très grand* directeur de thèse et m'avoir appris à raisonner par moi-même et à valoriser efficacement mes travaux ; par son écoute de toute heure (et tout fuseau horaire), sa confiance, sa pédagogie et sa rigueur,
Stéphane, pour m'avoir initié avec passion aux subtilités de la RMN,
Jules, pour m'avoir en 2015 proposé le stage qui a permis toute la suite ; et m'avoir ensuite poussé à me dépasser,

Mes parents et ma famille, pour leur soutien inconditionnel dans tous mes projets,
Lise, pour son soutien de tous les jours et sa patience face à la distance,

Thibault, pour m'avoir empêché d'être trop sérieux par sa bonté communicative,
Francesco, pour m'avoir éclairé scientifiquement et humainement,
Nidal, pour son naturel réconfortant, au travail et en dehors,
Asmaa, pour sa gentillesse et son aide pour maîtriser les bubulles,
Les plus vieux (Marie, Meng, Aymeric, Blandine, François, Xiao, Alizée, Oumar, Michel, Jennifer, ...) pour leur conseils,
Mention spéciale pour Alizée dont la thèse a inspiré le début de ces travaux,
Les successeurs (Florian (Le Pilier), Leila, Elie, Elisa) qui assurent une belle relève au labo,
Mes étudiants français - Meriem, Elisa et Jordy - pour m'avoir suivi avec tant de motivation dans nos projets,

Les chercheurs de Képler (Julie, Laurent, Olivier, Florence, Dennis, François, Xavier, Jean-Noël, Abdoulaye, Yacine, ...) ; avec une pensée pour la Running Team,
Plus particulièrement Olivier, pour son aide dans mon projet d'hydrogels moussés,
L'équipe technique (David, Christophe, Cédric, Pascal) pour avoir

Contents

General introduction

Introduction

On which simple principle rely key processes like air and water conditioning, or waste treatment? The answer is filtration, which benefits from important innovations to efficiently isolate unwanted products. Now, what mechanism enables nutrients to travel from the soil under our feet to the roots of plants and up to their leaves? The infiltration, through the ground, of water loaded with needed minerals and resources. Finally, what innovation is on the verge of revolutionizing targeted drug delivery? The creation of specialized drugs, transported specifically through the bloodstream to organs in need. Despite their differences, all three answers have one trait in common: *the controlled transport of particles by a fluid, through a complex environment*.

The transport of particles from one point of space to another by a fluid can have real positive impacts, like the ones we listed, but can also have disastrous consequences. Pollutants from industrial or urban sources can for instance join groundwaters and end up with nutrients in the plants we consume. The same duality appears in the example of the bloodstream: the same flow beneficial to drug delivery is a vector for the propagation of tumor cells, leading to metastasis. The point highlighted here is that understanding the specificities of particles and of particles transport is critical to predict their outcome when transported.

Another crucial point appeared through our examples: the fate of particles is fully linked to the medium they flow through. Depending on the composition, geometry and properties of the surrounding system, flowing particles can interact with it in a variety of ways. They can be passively transported, physically stopped, or transformed or degraded by chemical reactions. Before the complexity and the extent of these considerations, a simple statement prevails: for a concept as old and simple as filtration, a few examples are far from enough to build a complete understanding of the interactions between flowing particles and their environment. Encompassing this diversity of situations is the challenge we set for the present work.

Contents description

This work aims at exploring the most useful of the many possible interactions between suspensions of particles and water-saturated porous media. Various kinds of particles and different porous media are used along the studies, with one common goal: extract new fundamental understanding of each situation.

In the first chapter, we will review the current state of the art on the physics behind filtration, and on the current way particle transport is explained. The standard modern methods used to study transport and deposition in porous media will also be tackled. In the light of this overview, the approach chosen for the present work will be detailed and motivated.

This approach will lead to the choice of several general methods, like imaging by Nuclear Magnetic Resonance or confocal microscopy. Hand in hand with the methods, follow the materials used along our experimental studies, in particular the chosen suspensions of particles and porous systems. All these concepts shape the contents of the second chapter.

Finally, the main results of this work will be introduced in four chapters. Different but complementary cases will be introduced. From the straightforward case of passive particles flowing through simple pore networks, the question of the impact of particle size will be raised (chapter 3). Then, the case of particles interacting between themselves will be tackled (chapter 4), before focusing on particles mainly interacting with the porous system surrounding them (chapter 5). Finally, the challenge of coupled particle-particle-medium interactions will be faced (chapter 6).

Chapter 1

State of the art

In this chapter, the scope of our study will be set through the eyes of the current literature. From a general description of porous media and flow in porous media, the question of the flow of suspensions of particles will be derived. Then, a review of the understanding of various interactions between suspended particles and the structure of porous systems will be drawn, in the light of the science of filtration. Finally, standard approaches for the study of particle transport will be presented, as well as common experimental techniques.

1.1 Particle flow in saturated porous media

1.1.1 Describing porous media

1.1.1.1 Generic definition

The present work aims at better describing the behavior of suspensions of particles in generic porous media. To understand this behavior, it is important to clarify before hand some important characteristics of porous structures.

Commonly, a porous medium is a material containing a solid phase and a void phase. When the solid phase is predominant or equivalent in volume fraction to the voids, the structure is referred to as a *matrix* filled with *pores*. Common examples range from food products (bread, cheeses like gruyère) to industrial products (sponges, filters; see Fig.1.1.a) or building materials (wood, concrete; see Fig.1.1.b). When the solid phase is limited to a few volume percents of the structure, it is referred to as a *skeleton* surrounding a large void phase. Examples include foamed materials or aero/hydro-gels [Sehaqui et al. 2011] [Phalippou 2002] (see Fig.1.1.c). These are examples at a scale we are used to interact with, but basically any system can be considered as a porous medium depending at a small or large enough scale considered.

A porous medium can be characterized by its *absolute porosity* ϵ defined as the total pore volume over the total volume of material. It is a single value estimation of the free

Figure 1.1: Examples of common porous media. (a) Industrial products: washing sponge and fuel filters. (b) Building materials: wood logs and concrete wall. (c) Engineered materials: low-density ceramic foam and aerogel.

space in a specific system. For example, large holes in a French baguette makes it porous at 70 to 80% [Shehzad et al. 2010] while the porosity of common rocks like limestone or marble ranges from 1 to 10% [Manger 1963]. It is a good indicator but does not answer the question of interest here: can another phase flow through the void phase? Indeed, a system can have a large absolute porosity but with all its pores unconnected. An example is ceramic or metal foams with a porosity approaching 60% but made of isolated bubbles. Since the matrices do not allow any gas or liquid to flow through them, the porosity is unaccessible by standard means. The question of *connectivity* is addressed by the notion of *effective porosity* ϵ_e, defined as the ratio between the interconnected pore volume and the total volume. Note that porosity can also be defined for 2D systems like a grid. The absolute and effective porosities are then equal and defined as the surface of holes normalized by the total surface of the sheet.

Furthermore, the concept of *interconnection* depends once again on the scale considered: two holes in a sponge can seem separated by a wall and isolated, but are connected if one considers the micro-porosity of the wall itself. The impact of the scale of the study of porous media has been a study in itself, notably by [Whitaker 1969] and [Greenkorn 1981].

From porosity at the scale of a material, it is tempting to scale down and characterize individual void entities: pores. By definition, any cavity or element participating to the porosity is a pore, which makes their description quite arbitrary. Similarly, a pore throat is defined as a narrow area connecting pores, without clear criteria to distinguish the two species.

[Nimmo 2004] confirms that the very notions of pore and pore size are questionable when applied to 3D systems with a complex internal geometry, like soils. As illustrated in Fig.1.2 (left), the majority of the void phase in a soil sample usually is a single tortuous

pathway extended over large distances (all across the section in this picture). Therefore, it can be seen as a single narrow pore (or pore throat), or as a series of numerous small pores (of characteristic dimension the width of the pathway) strongly connected.
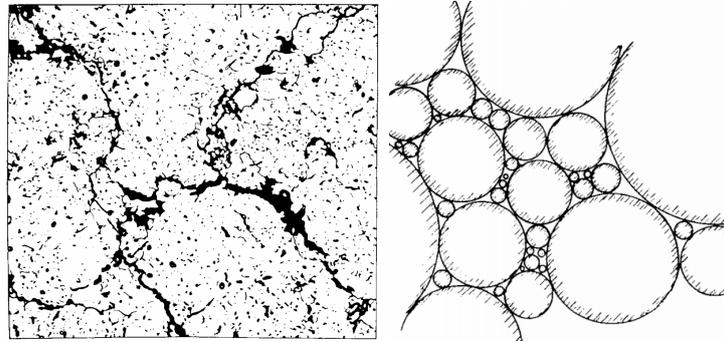
Figure 1.2: (left) Cross section (40×40 mm^2) of a typical soil sample with pore space in black. Only pores bigger than 0.1 mm appear. Some pores appear connected (long lines), some isolated (dots). Adapted by J.R. Nimmo from Lafeber, 1965, Aust. J. Soil Res., v. 3, p. 143. (right) Packing of polydisperse spheres, as a model for soils. From Hillel, 1980, Fundamentals of soil Physics, Academic Press, p.97.

In the end, the conceptual vocabulary that was introduced here shows how challenging a generic precise description of porous media remains. Some reference works like [Dullien 1979] offer qualitative definitions of pore structure with the help of 3D reconstructions and fractal, statistic or stochastic theories, but a proper description is only possible on a case-by-case basis.

Many other fundamental properties of porous media have critical impact in some situations, like the anisotropy of the system [Rice et al. 1970], it heterogeneity [Alabi 2011], its permeability [Katsube and Hume 1987], its surface state and surface area [Paykov and Hawley 2013].

1.1.1.2   Model media: bead packings

Given the diversity and complexity of porous media, fundamental research on this topic focused early on model systems. Henry Darcy likely initiated such practices when he performed column experiments on packed sand grains in 1856, to discover what is now know as Darcy's law [Brown 2002]. Ever since, packed grains kept being studied as model systems for many reasons. Packing spheres or grains in a column is experimentally easy and offers infinite variations of size, roughness, or shape. Paradoxically, simple spheres offer very complex yet controlled pore space structures when packed. [Hillel 1980] for instance confirmed the interest of packs of polydisperse spheres as models for the pore structure of soils (Fig.1.2 (right)).
Extensive studies described the many ways spheres or spheroids can organize themselves

when packed together. For spheres of equal dimension, Gauss postulated two centuries ago (it has been proved since) that the greatest possible solid fraction was 0.74. This density can be described by two regular lattices: the cubic close pack (*fcc*, face-centered cubic) and the hexagonal close-pack (*hcp*) illustrated in Fig.1.3 [Krishna and Pandey 1981]. Even in this ideal arrangement with a known porosity ($\epsilon = 1 - 0.74 = 0.26$), the pore space appears complex to describe due to the curvature of each sphere (see red domain on Fig.1.3, right).
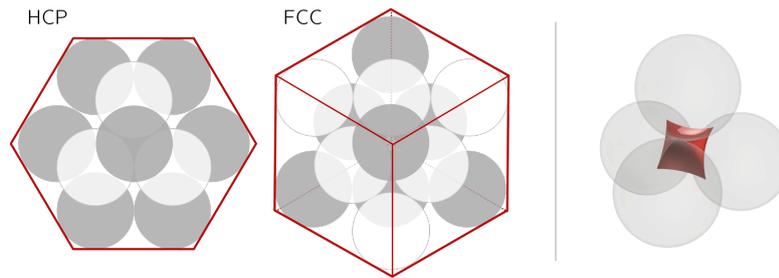
Figure 1.3: Close packs of equal spheres. (left) Hexagonal and face-centered cubic lattices. (right) 3D view of four spheres forming a tetrahedron, and of the pore space between them.

The community has also been widely studying random packs of spheres of equal size, i.e. spheres stacked in a non-optimal way. Due to defects in the arrangement of the spheres, the porosity in this case ranges from 0.35 (random close pack, or RCP) to 0.48 (very loose pack), depending on the production method. Since RCP are created and used in the present work, they are further characterized in the Materials section based in particular on the works of [Dullien 1979], [Nolan and Kavanagh 1994] and [Torquato et al. 2000].

They are more interesting to study than FCCs in the sense that the defects in the pack create a broader pore size distribution and more configurations between beads (various orientations, number of contact between beads, etc.), while retaining well characterized average properties.

1.1.2   Flow in water-saturated porous media

1.1.2.1   Saturation conditions

As above mentioned, the connected porosity of a system allow other phases to fill the space. In many cases this phase is gaseous, like air at ambient conditions, CO_2 for sequestration purposes [Jiang et al. 2017], or natural gas (mostly methane) in rock reservoirs [Yousif et al. 1991]. In other cases, the filling phase is liquid, for instance water in soils, oil in rock reservoirs or electrolytes in porous electrodes for batteries [Qu 2014].

At this day, porous media with a void phase saturated with water remain the most

extensively studied, because of their abundance in nature and as reference cases for the massive water treatment and oil & gas industries. We then refer to *saturated* conditions. Reference works on that matter include [Bear 1972] and [Carman 1997], who present the fundamentals of flow dynamics in porous media for homogeneous and immiscible fluids. Even-though more complex situations are of great interest (foam, air-water or oil-water two phases flow [Whitaker 1986]), the present work will focus on saturated conditions for all the challenges they still offer.

1.1.2.2 Hydrodynamics

Reynolds number
Knowing the type of flow taking place in the fluid domain is key to the understanding of fluid dynamics. The Reynolds number Re compares the inertial forces to the viscous forces for a fluid of velocity v and kinematic viscosity $\nu = \mu/\rho$, over the characteristic scale l:

$$Re = \frac{vl}{\nu}$$

At low Reynolds ($Re \ll 1$), the viscous forces dominate and the fluid motion is smooth and constant. This regime is called *laminar*. At high Reynolds ($Re \gg 1$), predominant inertial forces tend to induce flow instabilities. It is the *turbulent* regime. Note that all flows considered in this work will be laminar.

Navier-Stokes equations
In saturated conditions, a pressure difference across the system triggers a flow of the liquid phase through the medium. This motion is generally described by the Navier-Stokes equation. For an incompressible fluid (like water), neglecting the effect of gravity, the equation is:

$$\frac{\partial \vec{v}}{\partial t} + (\vec{v}.\vec{\nabla})\vec{v} - \nu\vec{\nabla}^2\vec{v} = -\frac{\vec{\nabla}p}{\rho} \tag{1.1}$$

With p the pressure, ρ the uniform (incompressible) fluid density, ν the kinematic viscosity, $\vec{v}$ the velocity field and $\vec{\nabla}$ the divergence operator ($\partial/\partial x$, $\partial/\partial y$, $\partial/\partial z$; in cartesian coordinates). The term in $(\vec{v}.\vec{\nabla})\vec{v}$ describes the convective motion of the fluid, while $\vec{\nabla}^2\vec{v}$ describes the diffusive or dispersive motion. This form of the Navier-Stokes equations is therefore also called advection-diffusion equation.

Darcy derivation
A useful equation for fluid flow in a porous system is Darcy's law, derived from the Navier-Stokes equation. It states that the flow-rate Q is proportional to the cross-section of the flow A, the pressure drop between the outlet and the inlet of the medium $\Delta p = p_{out} - p_{in}$, and inversely proportional to the dynamic viscosity of the fluid μ and

the length of the system. The proportionality coefficient defines the permeability of the medium, k $[m^2]$.

$$Q = -\frac{kA\Delta p}{\mu L}$$

As expected, it predicts that fluid flows from high to low pressures: $p_{out} < p_{in}$ implies $\Delta_p < 0$, hence a positive discharge Q (in the direction of the system, from inlet to outlet).

A related common variable is Darcy's velocity $q = Q/A$ $[m.s^{-1}]$. From this value of flux, the average fluid velocity in the system can be deduced by considering that only a fraction of the volume (the porosity ϵ) is available to the flow. The fluid velocity (also called *seepage* velocity or *pore* velocity) writes:

$$v = q/\epsilon \tag{1.2}$$

From these standard average considerations, important studies managed to characterize the local velocity and pressure fields in any geometry of porous system. Given the complexity of the problem and boundary conditions, a large mathematical and computational effort is needed, like in the works from [Vazquez 2006] or [Zarghami et al. 2014] among others.

Hagen-Poiseuille flow

To avoid a complete modelling of the velocity field, a standard way to simplify the system is to see the porous medium as a continuity of cylindrical tubes in which the flow is uniaxial. For example, let us consider a pressure gradient along the x direction (depth) and solve, in the transverse direction r, the velocity profile $v_r = v$. We assume in addition an incompressible newtonian fluid and a stationary ($\partial\vec{v}/\partial t = 0$) and laminar flow. From the mass continuity equation, the incompressibility assumption implies $\partial\rho/\partial t = -\vec{\nabla}.(\rho\vec{v}) = 0$. Then (1.1) becomes

$$\mu\frac{d^2v}{dr^2} = \frac{dp}{dx}$$

In a pore of radius R, with the origin of r taken at the center of the pore, no-slip conditions impose $v(-R) = 0$ and $v(R) = 0$. Integrating twice over r and applying these boundary conditions lead to (1.3).

$$v(r) = \frac{1}{2\mu}\frac{dp}{dx}\left(r^2 - R^2\right) \tag{1.3}$$

The profile (known as Poiseuille profile) is quadratic. As before, the pressure gradient dp/dx is further expressed as the difference in pressure (highest minus lowest) over the length of the system $\Delta p/L$. Moreover, the maximum velocity occurs at the center of the pore, hence $v_{max} = v(r = 0) = \Delta pR^2/4\mu L$.

v_{max} can be expressed as a function of the average pore velocity $\bar{v}$, that is usually easier to estimate (see (1.2)). Indeed, the velocity averaged over the cross-section πR^2 of the pore (cylindrical coordinates) shows that the average velocity is half the maximum velocity:

$$\bar{v} = \frac{1}{\pi R^2} \int_0^R \int_0^{2\pi} v(r) r \, dr \, d\theta$$

$$\bar{v} = \frac{v_{max}}{2}$$

As a final note, the velocity profile (1.3) can be rewritten as a function of the pore radius and the average velocity only:

$$v(r) = v_{max}\left(1 - \frac{r^2}{R^2}\right) = 2\bar{v}\left(1 - \frac{r^2}{R^2}\right)$$

1.1.3 From fluid to suspension

1.1.3.1 Defining a suspension

It has been shown in introduction that many cases of flow in porous media not only include pure single-phase fluids, but also fluids in which particles are suspended. Since this work focuses on such fluids, called *suspensions*, they need to be better defined.

A common way of describing a suspension is to consider insoluble solid bodies dispersed in a liquid medium, of size ranging from nanometers to micrometers. A suspension is defined by its kinetic stability, that is the ability for particles to remain uniformly distributed (constant mean inter-particle distance over time). In terms of mechanisms, it means that particles do not aggregate or sediment. In real systems, the effects of gravity are difficult to eradicate since the slightest difference of density between the fluid and the suspended particles leads to sedimentation (or creaming). Therefore, the definition of a suspension also sometimes includes that particles are easy to re-suspend if settling occurs. In addition to their kinetic stability, most suspensions are thermodynamically stable, which means that they are at chemical and thermal equilibrium.

Let us clarify the forces at play when considering stability questions. Three main forces stand out: gravity, viscous forces and thermal agitation; possibly with magnetic or electrostatic contributions (see DLVO and extended DLVO theories, section 1.3.1). Each of them is now detailed:

- The gravity force (weight) $\vec{P} = m\vec{g}$ always applies (on Earth) to a particle of mass m and brings it downwards. In a fluid, $\vec{P}$ is balanced by the buoyancy force (based on Archimedes' principle), opposed to the weight and equal in amplitude to the weight of the volume of fluid displaced by the presence of the particle.

This quantity writes $m_{fluid}g = \rho_{fluid}V_{particle}g$. The net force resulting from this competition is:

$$\vec{F_g} = m\vec{g} - \rho_{fluid}V_p\vec{g} = (\rho_{part} - \rho_{fluid})V_p\vec{g}$$

$$\vec{F_g} = \frac{1}{6}\Delta\rho\pi d_p^3\vec{g} \tag{1.4}$$

In particular, particles with a higher/lower density than the fluid tend to sink/float respectively. Particles iso-dense with the fluid are not impacted by gravity.

- The drag force is the resistance of the fluid against the motion of an object, here a particle. It is equivalently a friction force in the referential of a fixed particle passed by fluid, and a drag force in the referential of fluid dragging a particle.

  The drag force (with ρ_f the fluid density, A the cross-sectional area of the particle, v the relative velocity of the particle to the fluid and C_D the drag coefficient) writes

$$F_D = \frac{1}{2}\rho_f A C_D v^2$$

The drag coefficient C_D highly depends on the flow conditions. At low Reynolds number (like in this work) is it inversely proportional to the Reynolds number itself $Re = vd_p/\nu$ (taking the characteristic of Re as the particle size, where the drag applies). Hence

$$F_D = \frac{1}{2}\rho_f\pi\left(\frac{d_p}{2}\right)^2\frac{3}{8}\frac{\nu}{vd_p}v^2$$

$$F_D = 3\pi\mu d_p v \tag{1.5}$$

Therefore, the drag is in low Reynolds laminar conditions proportional to the velocity (and the particle size).

From the actions of gravity and drag, it is interesting to deduce the velocity of a particle sinking (or creaming) in a fluid and subject to viscous friction. Due to (1.4), a non-isodense particle moves upwards or downwards, which induces friction in the opposite direction according to (1.5). At balance, the terminal velocity v_t of the moving particle is (1.6).

$$F_g - F_D = 0$$

$$v_t = \frac{1}{18}\frac{\Delta\rho g d_p^2}{\mu} \tag{1.6}$$

Let us consider a model pore of size w. In this pore, a particle of higher density than the fluid will settle in a time $t_{settle} = w/v_t$. It gives a criterion for the suspension's stability: $t_{settle} \ll t_{experiment}$. In other words, that no settling (or equivalently creaming) occurs during the time of the experiment.

- Then, a common element keeping particles in movement against settling is the Brownian motion. To describe it, the particles composing the fluid have to be considered (water molecules for example). A suspended particle significantly larger than these molecules (for example a nanoparticle) is assumed to follow two behaviors: a straight trajectory at constant velocity, turning into an instantaneous accelerated trajectory when bumping into a smaller particle or a wall. The motion resulting from that is a stochastic process commonly described through the diffusion coefficient D, proportional to the thermal energy and to the *mobility m* of the particle:

$$D = mk_bT$$

The mobility is defined as the ratio of the velocity of the particle v to the drag force (viscosity force) F_d applied on the particle. These variables are linked by the Stokes' law (valid at low Reynolds) $F_d = 6\pi\mu d_p/2v$. Hence the law know as the Stokes-Einstein or Stokes-Einstein-Sutherland relation (1.7) [Einstein 1905] [Sutherland 1904]. From this formula, the diffusion coefficient in a system is usually easy to estimate.

$$D = \frac{2k_bT}{6\pi d_p\mu} \tag{1.7}$$

Back to the stochastic process mentioned above, a particle has the same chances to move in any direction following the bumps. Its average displacement over time $< x(t) >$ is zero. Its average quadratic displacement however is shown proportional to D and the elapsed time t: $< x^2(t) >= 2Dt$. The latter relation gives a estimation of how far a particle can on average diffuse during a given time t: $\sqrt{2Dt}$; and for example compare this distance with the particles displacement due to drag or settling.

The extent of the diffusion transport of particles is also usually evaluated by an estimation of the Peclet number Pe. It compares the convective and diffusive transfers to assess which one predominates at the scale l considered:

$$Pe = \frac{lv}{D}$$

Based of these forces, qualitative ways to assess stability exist, like the comparison proposed by [Larson 1999] between gravitational work and thermal agitation: $(d_p/2)^4\Delta\rho g/k_BT$.

Numerical applications applied to the present work are provided in Table 2.4, section 2.1.

Many methods have been tested (and proved) to increase the stability of suspensions. Most are based on reducing inter-particle interactions by increase in the continuous phase viscosity, addition of sterically efficient additives or specific treatment of the surface of the particles.

1.1.3.2 Hydrodynamics & solid-solid interactions

The laws of fluid dynamics established for pure fluid globally hold for dilute suspensions. Still, some variations can apply due to a coupling between the particles and the flow. In particular, particles of finite size are subject to a fine effect called *migration* [Yuan et al. 2018]. In a Poiseuille flow, velocity gradients exist transversally to the flow. In such gradients, the two sides of a finite-size particle are subject to slightly different velocities. This difference creates shear which tends to displace the particles towards the center of the pore where gradients are lower; they *migrate*.

The motion of particles within a porous medium is also strongly impacted by their interactions with the medium itself; more precisely its surfaces. This point is key to the present work, as it presents the basis phenomena driving all future observations.

In a model laminar flow in iso-dense conditions, far from any boundary, a particle is expected to be dragged and reach the same velocity as the fluid. It follows the streamlines imposed by the flow. From this ideal case, several forces (the same that helped us define the stability of a suspension) can complicate the particle's motion.

- If the condition of particle-fluid iso-density is not verified, the particle will settle (equivalently float) while flowing. This additional force will make the particle change streamline over time and eventually intercept the bottom surface of the geometry. There, it may stop or be dragged depending on the local geometry, roughness, friction conditions, etc.

  As a side note, the center of a settled particle is still located at one particle radius from the surface. This geometrical limit implies that particles are on average located closer to the center of the pore. In consequence, the average particle velocity is higher than the average fluid velocity, because they are sterically constrain to locations of higher average velocity.

- The finite size of the particles is also at the origin of *interception* events independent of gravity. To explain this, we consider a particle following a streamline passing at some instant at a distance from the surface shorter than the particle's radius. Naturally, the particle will hit the surface. Then, again, depending on the local conditions it can bounce back to a streamline further from the surface, roll on the surface or even stop.

- It is also interesting to assess when the motion of a particle in a pore can be driven by diffusive transport. We consider the Peclet number at the length scale of the particle $Pe = v(r)d_p/D$, with v the velocity at the location r of the particle in the pore (from center to pore radius R). By definition, $Pe = 1$ ascribes a transition between diffusive and advective transports. This condition can be valid in a pore at a location where $v = D/d_p$. We define this location as at a distance δ from the pore wall ($R - \delta$ from the pore center). Assuming a model Poiseuille flow, (1.8) is verified and leads to (1.9).

$$\frac{D}{2d_p\bar{v}_0} = 1 - \left(\frac{R-\delta}{R}\right)^2 \tag{1.8}$$

$$\delta = R\left(1 - \sqrt{1 - \frac{D}{2d_p\bar{v}_0}}\right) \tag{1.9}$$

Following this framework, the transport in a layer δ from the pore wall (*diffusive layer*) is driven by thermal agitation. Some situations in this work will highlight how important this effect can become on the particle deposition mechanisms.

- Some other more specific effects affecting the motion of particles can be cited, like the convective flows expected in dead-ends (large areas at low velocity) or particle-particle collision events at high enough concentration.

Incidentally, the question of concentration has not been raised so far because only dilute conditions (i.e. independent particles in suspension) are considered in this work. Sill, is it an important point that has to be kept in mind.

1.1.4 Towards numerous applications

It is clear now that the mechanisms making a particle enter in contact with an element of surface are numerous and diverse. They strongly depend on the properties (density, mobility) of the particles and on the velocity field in the pores; in particular at the boundaries of the porous matrices.

So far, we mostly described how a particle flows in a porous geometry and what forces eventually lead to a particle-medium encounter. The question is now to assess the consequences of such situations, i.e. the fate of the particles. Several outcomes can be imagined: the particle may stop, attach to the medium, react with it, etc. Interestingly, critical applications rely on these effects as driving forces (the outcome makes a process more efficient) or limit (the outcome constrains the process).

A first important application relying on particle-medium interactions is *filtration*. Indeed, stoppage, attachment or reaction outcomes all result in the separation of a particle

from the fluid phase, which is by definition the role of a filter. The extent of this topic is massive. It began as early as four thousand years ago where sand and gravel packs were used by ancient Greeks to reduce the turbidity of drinking water. Since that time, the science of filtration has greatly progressed, mainly because of its wide application in tools of the daily-life or industrial processes. Again, the key vision here is that stoppage events can help separate, purify or clean systems with high efficiencies.

That being said, the notion of filtration is associated with efficient particle stoppage. Some other applications also rely on particle-medium interactions but focus preferably on understanding how particles propagate and eventually modify the medium. It is the case for instance for the study in porous media like biological tissues/bodies or soils. This change in paradigm makes us leave the field of filtration to tackle the topic of *particle transport and deposition*. The vision is indeed different: the particle stoppage mechanisms have to be understood to prevent, control or predict the accumulation of particles and make the most of medical or remediation solutions.

These two visions define two sides on a same topic, each one constituted of its own literature and concepts. They will therefore by treated separately in the two following sections.

1.2 Physical separation: the basis of filtration

Efficient solid-liquid separation (or filtration) is a recurrent question in many large industries. It gave rise to a rich literature and reference frameworks like [Tien and Ramarao 1989], [Cheremisinoff 1998] or more recently [Sparks 2012]. Key applications like membrane filtration couple several complex deposition phenomena [Zularisam et al. 2006] [Bacchin et al. 1995], but filtration systems historically rely on one main way to separate particles from the fluid, that we will now detail: their physical stoppage driven by the filter's geometry.

1.2.1 Single pore clogging

1.2.1.1 Size-exclusion

Let us consider a particle flowing towards a constriction (pore). If the particle is bigger than the pore, it is stopped. If the particle is smaller, it passes through. Since it is purely geometric, this condition is known as *size exclusion*. It is completed by a second natural phenomenon known as *bridging*: a few particles arriving simultaneously in front of a hole smaller than their cumulated sizes will clog if they form a stable bridge above the hole.

These mechanisms can easily be extended to a 2D problem, with a suspension of particles flowing through a grid (matrix of identical pores) or a mesh (intricate fibers, membranes), which corresponds to *surface filtration*. It also embraces the *sieving* method, commonly used in the making of batches of particle with a controlled size distribution [Wills et al. 2006], in cooking (flour sifting for example) [Ruhlman 2010], or in industrial waste (notably plastic) separation [Kosvintsev et al. 2003] [Crawford and Quinn 2017].

Even-though surface filtration has been an industrial problem for decades, mostly treated empirically, some studies provide a fundamental approach of the question. [Ramachandran and Fogler 1999] made the first direct observation of clogging events, coupled with pressure drop measurements. [Roussel et al. 2007] later showed that spherical particles arriving against 2D meshes are subject to stoppage events (bridging) driven by the probability of presence of particles in front of the holes, based on the particle to hole size ratio and the solid fraction of the suspension. Complementary experimental validations came from [To et al. 2001] or [Jenkins et al. 2011].

A general framework for clogging (more generally for discrete bodies passing through a bottleneck) was formulated by [Zuriguel et al. 2015]. From systems of very different scales and natures, they propose a clogging phase diagram making a qualitative link between a characteristic clogging length and forces acting for/against the creation of bridges of elements. In addition, the occurrence of bridging events are known to depend on many conditions, like the concentration of the suspensions [Sharp and Adrian 2005], [Goldsztein 2005] or the presence of an obstacle on top of the constriction [Lozano et al. 2012] (actually reducing clogging probability by changing the local pressure conditions).
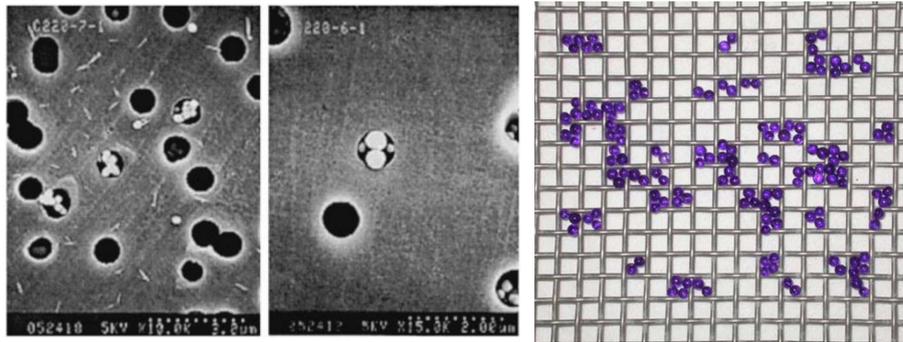
Figure 1.4: (left) Adapted from [Ramachandran and Fogler 1999]. SEM pictures of $\approx$ 200 nm latex particles bridging holes of etched polycarbonate membranes.
(right) Adapted from [Roussel et al. 2007]. Bridges formed by 3 mm grains over 5 mm square sieve. Authors report an average number of particles involved per bridge $n = 2.34$.

Recent studies tend to describe more locally the mechanisms, like [Koivisto and Durian 2017] who investigated the micro-states preceding the clogging of a single circular pore. They linked the micro-states to the pore to particle size ratio and wetting conditions, to show that bridging is driven more by specific particle positions in the hole region than by their momenta and trajectories.

1.2.1.2 Caking effect

Some studies highlight the direct consequence of surface filtration: the accumulation of particles on top of the filter once it is clogged (*cake*). Reference books like [Cheremisinoff 1998] on industrial liquid filtration show how this caking effect can be used as a feature and not a bug, by recalling that a stack of accumulated particles is in most cases easier to remove than particles clogged in the intricate depth of a porous system, which simplifies industrial cleaning.

Following the question of the evolution of a cake and its removal, experimental studies like [Eker et al. 2016] focused on the evolution of the caking phenomenon via pressure drop and flow-rate monitoring, for *prognostics* purposes (i.e. prediction of the failure/replacement time of a filter). With a similar purpose but on the simulation side, [Dong et al. 2009] directly modeled the settling of spherical particles subject to contact forces, buoyancy and drag over a fixed membrane permeable to the carrying fluid only.

1.2.1.3 Additional parameters

More specific studies on particle sizes also led to interesting cases. A good example is the study of polydispersity, for instance by [Redner and Datta 2000] and [Mustin and Stoeber 2010]. They both used - respectively by simulation and experiments - large

distributions of particle sizes and of pores sizes to identify two regimes: (i) an average pore larger than the average particle size results in slow clogging initiation, while (ii) an average pore of comparable size or smaller than the average particle results in instant clogging. Overall, the time needed to block a system relates to the concentration of particles larger than the holes. Note that it implies that the knowledge of the mean particle diameter is not sufficient to describe channel clogging of polydisperse suspensions, but that the complete distribution has to be considered.

Beyond particle size, single pore clogging depends on other critical parameters like particle rigidity/deformability, local density or multiplication potential (growth). A good overview on these parameters and related clogging and bridging probabilities comes from [Dressaire and Sauret 2017].

1.2.2 Physical separation in depth

1.2.2.1 Beyond single-layer filters

A set of experiments carried by [Ghidaglia 1996] well embodies the transition happening between surface considerations and particles transported deeper in a porous medium. They show the importance of the particle size even when it is on average smaller than the pores. From (large) particles subject to instant surface clogging, the authors decrease the particle size to allow them to pass the surface of a 3D pack of beads. While small enough particles completely pass through, a transition regime appears for intermediate size particles (see Fig.1.5). This shows that despite their passage of the surface layer, particles get stuck deeper in the system. The difficulty to directly observe clogging (and later caking) mechanisms make this interesting transition state still poorly understood.
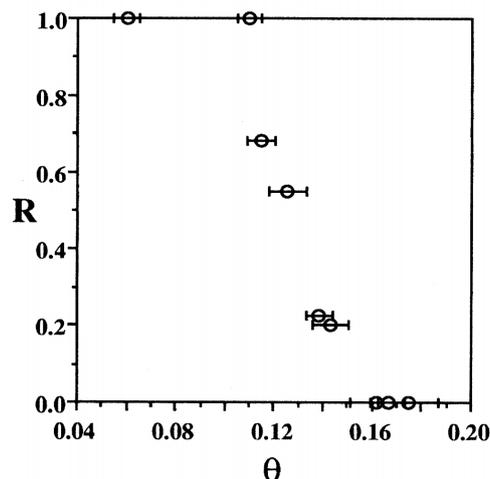
Figure 1.5: From [Ghidaglia 1996]. Ratio R of particles exiting to those entering a column of packed beads, versus the ratio θ of the diameters of mobile particles to fixed spheres forming the pack.

The latter observations are related to the *straining* mechanism. When particles flow through multi-layer media, they do not encounter single pore sizes anymore but a succession of pores and pore throats of variable size. Depending on the local geometry, they can be geometrically stopped in small pore throats but do not significantly affect the porosity or flow conditions. Such events are equivalent to clogging but can occur over large depths of system and do not dramatically affect the passage of other particles in the pore space. The influence of pore size distribution on the straining of colloids was revealed by [Sakthivadivel 1966] [Sakthivadivel 1969] or [Herzig et al. 1970].

1.2.2.2 Deep-bed filtration

As we have seen, the size of suspended particles can lead them to penetrate porous systems and clog in the pore space deeper than the surface layer. *Depth filtration* extends *surface filtration* to these cases. A framework has been set by [Ives 1970] and [Tien and Ramarao 1989] for deep-bed granular filters, as well as by [Arbabi and Sahimi 1990] and [Ryan and Elimelech 1996] for subsurface particle transport.

The studies on this topic remain at this day mostly empirical, because tightly linked to questions of filter efficiency and performance. For example, experimental studies focused on the overall distribution of particles clogging in multi-layer filters and showed that particles tend to clog closer to the top surface. Their distribution over depth (x) follows an exponential decay ($exp(-x/\lambda)$), whith λ the characteristic penetration distance called the *filter coefficient* [Iwasaki et al. 1937] [McDowell-Boyer et al. 1986]. This result is major for the estimation of filters dimensions or lifetimes, and paves the way to more specific studies of the propagation and deposition of particles in depth.

1.3 Physico-chemical separation: ruling depth deposition

The physical separation considered so far is less relevant when questions of particle transport and deposition over large distances are raised. For example, while it is a pillar of physical filtration since the 60s, straining has been shown important in soil transport only more recently by [Bradford, Yates, et al. 2002] [Bradford, Simunek, et al. 2003]. Despite efforts to better understand the internal mechanisms of straining through observations [Xu et al. 2006] or 2D models [Auset and Keller 2006], the impact of straining on the overall dynamics of depth deposition could still benefit from further research.

Nevertheless, it is important to point out that for questions of depth deposition, straining only comes as a secondary order mechanisms of particle stoppage. Indeed, depth studies rely on particles of negligible size before the porosity, which means straining and clogging are expected to be rare. If any, additional particle-matrix interactions get the upper hand, leading to predominant physico-chemical bounding events between particles and surfaces.

1.3.1 Attachment mechanisms

Among all particle-surface attachment events, the most common rely on electrostatic interactions described by the DVLO theory.

1.3.1.1 Electrostatic interactions

An electrostatic force is an attractive or repulsive force between two stationary electrically charged particles. Its general form is known as Coulomb's law (1785), function of the distance r from the considered particle surface towards to other particle: $F(r) = k_e q_1 q_2 / r^2$, with k_e Coulomb's constant, and q_i the magnitude of the charge at the surface of particle i. Two natural consequences arise: (i) F is attractive for particles of opposite charge ($q_1 q_2 < 0$) and repulsive otherwise. (ii) F is greater when the particles are closer and quickly decays with the distance.

The fact that particles get charged usually results from them being in suspension. In common solvents and depending on their nature, the chemical groups at the surface of the particles can dissociate/ionize. A telling example, relevant to this work, in the dissociation of the $Si - OH$ groups at the surface of silica beads in surface groups $Si - O^-$ and protons H^+ in suspension. This effect creates a layer of counter-ions (i.e. ions of opposite charge that the surface) near the surfaces, while maintaining the overall neutral charge of the system.

This ionic region is called the electrical double layer (EDL), commonly subdivided in two regions: (i) the Stern layer close to the surface where ions are strongly bounded to

the surface and immobilized, and (ii) the diffuse layer (also called Gouy-Chapman layer) where mobile ions are loosely bounded to the surface charges. The thickness of the diffuse layer is not exactly driven by the surface dissociation, but more by a competition between two opposite forces. On the one hand coulombian forces pushing them against the surface; on the other hand the repulsive osmotic pressure driving them away from the surface.

When the surfaces of two particles get at a distance of the order of the thickness of the EDL, their ionic environment overlap. The resulting electrostatic interaction is commonly assessed by introducing the electrostatic potential Φ^{EL}. It is introduced with respect to the bulk, i.e. $\Phi \to 0$ far from the considered surface/particle.

Several models quantify this potential, based on the description of the EDL and in particular on the description of the ionic concentration between the surfaces and the surface charge densities. Reference models have been developed by [Helmholtz 1853] and Gouy and Chapman, later refined by Stern and Grahame [Grahame 1947]. In the Gouy-Chapman model, under the Debye-Hückel approximation, the potential reads:

$$\Phi^{EL}(r) = \Phi_d exp(-\kappa(r-d)) \approx \Phi_d exp(-\kappa r)$$

Where Φ_d is the value of the potential at a distance d from the surface, defined as the outer Helmholtz plane. Specifically, it is the closest distance the surface of the two particles can approach each-other (of the order of 0.5 nm, often negligible before the inter-surfaces distance). κ is the Debye-Hückel parameter, directly linked to the ionic concentration in the inter-surfaces gap. This notion is further detailed in Chapter 2 and Chapter 6 on concrete use cases.

Generally speaking, electrostatic interactions are widely recognized as one of the most influential parameter in the studies on the transport and deposition of charged particles. They rule both:

- the affinity of particles between themselves. Since particles of identical charge (in sign and amplitude) electro-statically repel each-other, it helps maintaining particles at a distance, i.e. prevents agglomeration.

- the affinity between the particles and the surface of the porous matrix. In the case of particle/surface opposite charges (attractive forces), they drive the adsorption of particles to the surface.

In addition from the expression here-above, different formulations of Φ^{EL} have been developed by [Hogg et al. 1966], [Wiese and Healy 1970] or [Gregory 1975]. These models differ in particular by considering constant surface potential or constant surface charge, hence slightly modified expressions reflecting the same general trends. The latter

case is for instance expressed by (1.10).

$$\Phi^{EL} = 32\pi d_p \epsilon \left(\frac{ze}{k_b T}\right)^2 \gamma(\Phi_1)\gamma(\Phi_2) exp(-\kappa d) \tag{1.10}$$

With $\gamma(\Phi) = \tanh(ze\Phi/4kT)$, Φ the surface potential, z the valence of the ions in solution and e the elementary charge. The indexes 1 and 2 refer to the two interacting materials. The pre-factor 32 is valid for a sphere-plate approach, while 16 is usually used for a sphere-sphere interaction. (1.10) is valid when the interacting surfaces are a distance small before the particle size ($d/d_p < 1$) and a Debye length fulfilling $\lambda < 0.2d_p$.

1.3.1.2 The DLVO theory

The second type of forces playing an important role in inter-particular interactions are the Van der Waals forces. They represent the atomic or molecular interactions, induced by their polarization. Due to fluctuations in the atomic electronic density, a dipole is created and can interact attractively with other surrounding dipoles. Because no electronic bound is created, the Van der Waals forces are considered weak and vanish a short distances from the interacting surfaces (a few nanometers). They are usually considered as the most influential (short-range) attractive interactions between particles.

The balance between electrostatic and Van der Waals forces is classicaly explained through the DLVO theory, developed by [Derjaguin and Landau 1941] and [Overbeek and Verway 1947]. It states that the total interaction energy is the sum of the Van der Waals and electrostatic contributions:

$$\Phi^{tot} = \Phi^{VdW} + \Phi^{EL}$$

With Φ^{EL} the electrostatic potential that we just characterized. A formulation of Φ^{VdW} comes for example from [Gregory 1981]. For two approaching spheres (at a distance d) its expression is (1.11). For a sphere approaching a surface an multiplication factor $1/2$ is introduced.

$$\Phi^{VdW} = -\frac{Hd_p}{12d(1 + 14d/\lambda)} \approx -\frac{Hd_p}{12d} \tag{1.11}$$

Here, λ is the wavelength of the interaction, commonly assumed large before the inter-surface distance d, hence the presented approximation. H is the Hamaker constant of the system, usually estimated from the Hamaker constants of each material composing the system. For two interacting materials (indexes 1 and 2) separated by a fluid (index 3), an estimation of of the global constant is $H_{132} \approx (\sqrt{H_{11}} - \sqrt{H_{33}})(\sqrt{H_{22}} - \sqrt{H_{33}})$. The specific constants H_{ii} are tabulated for the most common materials.

It is worth noting that Φ^{VdW} increases with the particle size and is considered to have an significant impact only at short inter-bodies distances ($\Phi^{VdW} \propto d^{-1}$).

A large number of studies proved the validity of the DLVO theory, like [Li et al. 2008] or [Chen and Elimelech 2008]. Given that attractive/repulsive interactions largely depend on the ionic conditions, the modulation of these conditions has also been an important object of interest to control and tune particle attachment properties [Ryan and Gschwend 1994], [Hahn et al. 2004], [Grolimund and Borkovec 1999].

The original DLVO theory has also been extended to take in account additional forces like steric interactions (for stabilizers in suspension for instance), osmotic forces [Vincent et al. 1986], or magnetic forces between particles [Vicente et al. 2000], [Phenrat, Saleh, et al. 2007]. For example, two magnetic dipoles (head-to-tail configuration) with a material's magnetization at saturation M_s develop a magnetic potential Φ_m of the form (μ_0 the vaccum magnetic permeability):

$$\Phi_m = -\frac{\pi \nu_0 M_s^2 d_p^3}{9(2d/d_p + 2)} \approx -\frac{\pi}{18}\mu_0 M_s^2 d_p^3$$

1.3.2 Consequences on deposition

From these fundamental considerations, let us get back to the consequences of these mechanisms on particle deposition.

1.3.2.1 Particle adsorption

Whatever their range of action, attractive forces between suspended particles and surfaces are the leading mechanism for particle attachment by *adsorption*. From section 1.1, we know that several hydrodynamic mechanisms (advection, diffusion, interception) are expected to put particles in contact with elements of surface.

In the case of repulsive particle-particle interactions, a model for the adsorption of a single layer of particles on a flat surface was presented by Langmuir in the 1920s, assuming independent particles arriving at a series of independent adsorption sites on a surface. If additional steric and repulsions effects are considered, the distribution of particles on a surface becomes dependent on the history of the deposition. RSA (Random Sequential Adsorption) models are commonly used to answer these questions [Evans 1993]. On the case of attractive particle-particle interactions, deposition is not limited to a single layer of particles anymore and particles can stack on top of each-other by a *ripening* mechanism [Tosco and Sethi 2010]. Finally, it is worth noting that direct applications of these principles exist, like colloidal lithography [Michel et al. 2002].

It is worth noting that the adsorption of a particle is not only ruled by the way it approaches a surface; other adsorbed particles also impact the flow in return. A telling illustration is the shadow effect [Ko and Elimelech 2000], stating that the presence of a particle on a surface creates an area behind it inaccessible to the flow and other particles.

Other important hydrodynamic effects like the shear imposed by the flow on particles are expected to have a large effect on deposition. Indeed, the attachment (or later detachment) of a particle is at all times conditioned by a balance between the adhesive forces keeping it at the surface and the forces working against this stable position (like drag forces). Note that detachment mechanisms are not considered in this work, as they are irrelevant in all studied cases. A good review on this topic was made by [Henry 2018].

1.3.2.2   From attachment to clogging

For particle of negligible size before the pore space, these attachment events do not alter the porosity of the system. For particles of larger size however, the adsorption of a particle can affect the geometry of the pores. It can repeat until clogging mechanisms become plausible again, in accordance with the previous section.

A telling example comes from [Wyss et al. 2006], where the authors study multiple single-pore parallel channels. They work at particle to pore size ratios making bridging events unlikely, and still observe the progressive clogging of all channels over time. The mechanism they highlight is the irreversible sticking (short-range attractive Van der Waals forces mostly) of particles getting close enough to the walls of the pores. As a result, the probability of clogging events is not purely geometrical anymore. It relates to the fraction of particles susceptible to attach and reduce the pore space; i.e. particles passing at a distance from the surfaces compatible with short-range attractions and attachment events.

Similarly, groups like [Dersoir et al. 2015] focused on colloid attachment up to the formation of clogs. More precisely, they observed how the formation of clogs is impacted by the shape and size of the entrance of 2D model single pores. A pore with a smooth geometry and smooth surface is for example less subject to clogging, as less particles intercept its surface.
Both studies show the importance of the relative sizes in the system even for these non purely geometrical clogging events. For example, they find that the number of injected particles leading to a clog goes in (pore size/particle size)$^\alpha$ ($\alpha = 4$ for [Wyss et al. 2006], 7 for [Dersoir et al. 2015]).

1.3.3   Modeling

The transport and deposition of particles over the depth of porous media raises important questions of predictability: how deep will the particle flow? How will the flow in depth react to their deposition? To answer such questions, a large modelling effort exists in this field.

1.3.3.1 Transport equations & mechanistic

The transport of passive particles in porous structures is commonly described using the advection-dispersion equation. For mass transfers (like it is the case for particle transport), it links the evolution of the particle concentration over time to the spatial evolution of this concentration due to dispersion or advective flow.

It derives from the continuity equation (1.12), with n the concentration of particles in suspension and $\vec{j}$ the total flux of particles, that is the sum of the fluxes in and out of the considered elementary volume.

$$\frac{\partial n}{\partial t} + \vec{\nabla}.\vec{j} = 0 \tag{1.12}$$

Due to dispersion (similarly for diffusion, depending on the scale), a flux $\vec{j_D} = -D\nabla n$ arises from Fick's first law; with D the dispersion coefficient. In addition, an advective flux $\vec{j_A} = \vec{v}n$ arises from the flow at average velocity $\vec{v} = \vec{q}/\epsilon$. (1.12) therefore reads (1.13), rewritten as (1.14) in the simplified case of a 1D transport along the x axis.

$$\frac{\partial n}{\partial t} + \vec{\nabla}.(\vec{v}n - D\vec{\nabla}n) = 0 \tag{1.13}$$

$$\frac{\partial n}{\partial t} + v\frac{\partial n}{\partial x} - D\frac{\partial^2 n}{\partial x^2} = 0 \tag{1.14}$$

Neglecting mechanical dispersion over depth ($D \to 0$), this expression simply describes the evolution of the front of propagation of the suspension. Additional terms can also be considered to account for interactions between the particles and the porous system. A standard way is to consider a change of phase: particles move from the liquid phase (i.e. the suspension) to a new phase not subject to the flow. For instance, particles subject to biological or chemical degradation, like dissolution, pass to a void phase (i.e. become passive elements in the liquid phase). In other cases, particles get stopped in the system by diverse mechanisms as size-exclusion clogging or surface adsorption. Since they are immobilized and do not participate to the flow, they form a *solid* phase just like the porous matrix itself. To take this phase change into account, a term is added to Eq.1.14: the exchange rate of the concentration s of the new phase, $\partial s/\partial t$. Eq.1.14 becomes:

$$\frac{\partial n}{\partial t} + v\frac{\partial n}{\partial x} - D\frac{\partial^2 n}{\partial x^2} = \frac{\rho}{\epsilon}\frac{\partial s}{\partial t} \tag{1.15}$$

With ρ the fluid density and ϵ the porosity. The exchange rate is usually expressed for a given individual mechanism of phase change. A way of describing it, natural and common to all publications on the topic, is to say that the amount of particles passing to the new phase is proportional to the amount of particles present in the suspension: $\partial s/\partial t = kn$, with k a kinetic constant for dimensionality. Then, depending on the mechanism, the exchange rate also depends on other parameters gathered in a *exchange*

function F. The main examples to date are listed in Table 1.1.

$$\frac{\rho}{\epsilon}\frac{\partial s}{\partial t} = knF \tag{1.16}$$

Mechanism	F	Parameters
Degradation	-1	-
Linear deposition	1	-
Saturating adsorption	$1 - s$	s: surface coverage
Ripening [Tosco and Sethi 2010]	$1 + A_{rip}s^{\beta_{rip}}$	A_{rip}: fitting coefficient
		β_{rip}: fitting exponent
Straining [Bradford, Simunek, et al. 2003]	$(1 + x/d_{50})^{-\beta}$	x: depth in the porous medium
		d_{50}: median pore size
		β: fitting exponent

Table 1.1: Exchange function F for various deposition mechanisms.

The transport equations 1.15 and 1.16 form a system of coupled equations that does not have analytical solutions in most cases. Multiple modeling tools and approaches have, in consequence, been developed; like [Tosco and Sethi 2009] whose software performs numerical iterative solving of the coupled transport equations and the evolution of the porosity $\epsilon(s)$, permeability $K(s, \epsilon)$ and flow $q(n, s, K, \epsilon)$.

In addition, several mechanisms can be simultaneously at stake in a real system. A standard practice in this case is to assume additivity of the exchange rates of all individual mechanisms: $\partial s^{tot}/\partial t = \Sigma \partial s_i/\partial t$. Couplings between mechanisms are traditionally neglected, despite their plausible role in the events actually happening during transport and deposition. For studies considering detachment mechanisms, particles get resuspended in the bulk phase, hence the addition of similar terms of opposite sign $\partial s/\partial t = -k_{detach}n$. Note that detachment effects are not further detailed since most of them are out considered in this work.

1.3.3.2 Single collector model

All the mechanisms previously describe can be summarized by a particle entering the pore space, being transported from the suspension to the surface of the porous medium, and eventually stopping at the surface. The simplest way to model these events is to reduce the system to an element of fluid flowing towards a simple surface. Such model system is classically called in the literature a *single collector* and takes the form of a sphere placed in an infinite laminar flow.

The transport from bulk to surface is usually describes through the notion of *single collector contact efficiency* η_0, which represents the probability of a particle entering the system to reach the surface. It was introduced by [Yao et al. 1971] as the number of

particles reaching the surface N_s, divided by the number of particles entering the area equal to the projection of the collector (collector radius a_c, velocity v, concentration C_0).

$$\eta_0 = \frac{N_s}{vC_0(\pi a_c^2)}$$

The efficiency historically depends on three mechanisms leading to a "near-contact" event, as illustrated in Fig.1.6: (i) sedimentation, when a particle denser than the fluid settles on a surface, (ii) interception: when a particle follows a streamline passing at a distance from the surface comparable with the particle size, and (iii) diffusion: when the thermal movement derives a particle from its streamline and brings it closer to the collector surface.

For instance, Yao's formulation is a polynomial function of the particle to collector size ratio N_R, the Peclet number N_{Pe}, the porosity of the surface (via the *porosity number* A_S) and settling to fluid velocities ratio N_G (keeping their notation):

$$\eta_0 = 4.04 A_S^{1/3} N_{Pe}^{-2/3} + 3/2 A_S^1 N_R^2 + 1 N_G^1$$

Over time, several authors proposed corrections and extensions of the original model, to take into account more deposition mechanisms like surface adsorption, as well as fitted coefficients adapted to specific systems. The main examples are listed in Table 2.1. Note that with the number of mechanisms taken in account over the years increasing, so do the number of empirical fitting parameters defined in each model.
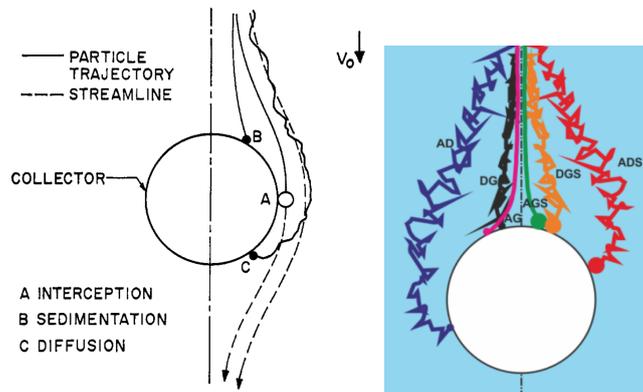
Figure 1.6: (left) Adapted from [Yao et al. 1971]: basic transport mechanisms in water filtration.
(right) Adapted from [Messina, Marchisio, et al. 2015]. Coupling of two transport mechanisms: A for advection, D for diffusion, G for gravity and S for finite size steric effects (punctual particles on the left; finite-size particles on the right).

Variations of the collector model have also been proposed, like Happel's model [Nelson and Ginn 2005] accounting for a fluid shell around the surface of the collector. Later,

Authors	Date	Mechanisms	Details
Yao et al.	1971	4	Porosity dependent variable, convection to diffusion, size ratio, gravity
Rajagopalan and Tien	1976	5	All above, and London forces
Tufenkji and elimelech	2004	6	All above, and Van der Waals forces
Ma et al.	2009	6	As above
Nelson and Ginn	2011	7	All above and additional gravity term
Ma et al.	2013	7	As above
Messina et al.	2015	7	As above

Table 1.2: Successive models of single collector efficiency. Refere to references for exact conditions of application.

[Ma et al. 2009] introduced a collector made of two touching hemispheres, to account for the confined porosity at the contact point between model grains.

Of course, additional corrections are applied to the single collector model to account for the more complex reality of porous media - since real systems are obviously not limited to a model flow towards a single sphere. [Messina, Tosco, et al. 2016] predicted for instance the limits of the upscaling from single collector efficiency calculations. Still, calculated values for η_0 are often corrected by a additional fitting parameter ($\eta = \alpha\eta_0$) to match the particle deposition measured in column experiments. As the efficiency η describes a probability of deposition, it is also used to predict (or fit) the kinetic constants $k = f(\eta, v)$ presented in the transport equations.

1.4 Advances in experimental methods

The aim when studying flow and transport in porous media is often to acquire a measure of the spatial organization of the system. That includes the structure of the porosity (pore size and orientation, permeability, etc.), as well as organization of the particles flowing or interacting with this porosity (position, number, behavior). The spatial resolution offered by a given technique is in general a good descriptor of the amount of information the technique will provide on the system. For this reason, the following section will present the most important techniques in the field, ordered by spatial resolution capability.

1.4.1 External observations

Historically, filtration problems led to very simple case studies. One could directly observe by eye the external aspect of a porous filter and infer conclusions on its state. For example, a cake forming at the surface indicates a need for replacement or cleaning. Still, no information can be gathered from the inside of the filter and only empirical conclusions can be drawn, like an estimation of the filter lifetime.

This limitation results from a simple fact: most porous media (from rocks to industrial filters) are made of non-transparent materials making impossible any internal observation.

A powerful technique introduced to gather more information consists in injecting a fluid or a suspension through a porous system and measuring a property of the fluid/suspension at the outlet of the system. The measured property can be the acidity, the ionic strength, the concentration in a specific ion or type of particle, etc. The difference between inlet (known injected fluid) and outlet provides knowledge on what happened inside the medium. When solutes or particles are injected, they are expected to exit the system some time later, i.e. to *break through* the system. The curve showing their concentration as a function of time (or injected volume) are therefore called break-through curves (BTC).

These curves are spatially limited since they only provide information at a single location outside the system. Still, they are at the basis of numerous discoveries in the field of particle transport, including most of the mechanistic models presented in Table 1.1, section 1.3. Note that this absence of internal validation of the mechanisms left several empirical fitting parameters in the corresponding models. Important works applied to colloidal particles include [Elimelech 1991], [Johnson and Elimelech 1995] or [Bradford and Leij 2018].

1.4.2 Partial internal observations

The will to increase the understanding of the events happening internally led to a different approach: the introduction of sensors along the media. An example is [Faber

et al. 2016] (see Fig.1.7.a). Through large-scale engineered setups, a discrete number of pressure sensors is distributed along a column containing a porous medium. By measuring effluent concentration, pressures and velocities over time, internal information is gathered at selected locations.

This approach is mostly feasible on media built for that purpose (model bead/grain packs) or naturally accessible (soils probed by drilling wells). Other materials make it more difficult, like rocks. At lab scale, the *sample cutting* technique can then be used. The sample is fractured or cut to access for instance the distribution of particles over the porosity at the final state of an experiment, like in [Cipolla et al. 2008] (see Fig.1.7.c) or [Xu et al. 2006]. The method is destructive and dependent on the opening protocol (particles can move during this step), therefore applied when most other techniques fail.

Similarly, a porous medium can be sampled at one or more location for imaging purposes. While a standard 3D medium can not be imaged as a whole, samples or sections taken in it can be observed by microscopy (standard or SEM). [Xu et al. 2006] used for example camera observations of strained colloids to back the mechanisms postulated from BTC studies. [Crist et al. 2004] or [Ochiai et al. 2006] (see Fig.1.7.b) also provided interesting observations using fluorescence or light-transmission imaging on thin samples to study the trapping of colloids at air-water interfaces in pores.

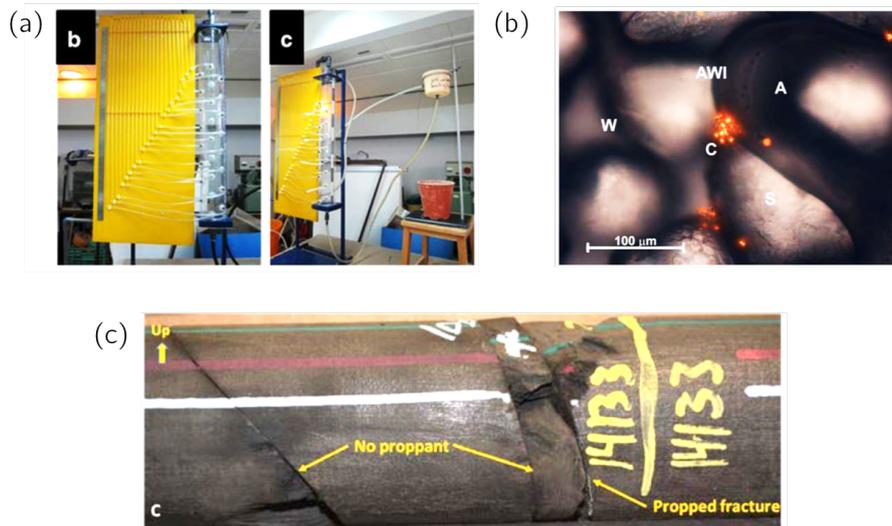Figure 1.7: (a) From [Faber et al. 2016]. Lab-scale column experiment with discrete pressure measurements. (b) From [Ochiai et al. 2006]. Deposited colloids at the grain scale. W: water, A: air, C: colloids, S: grain, AWI: air-water interface. (c) From [Cipolla et al. 2008]. Sample (rock) cut to assess the presence of particles in fractures. *Proppants* refer to millimetric particles injected in fractured rocks.

1.4.3   Complete internal observations

More intricate techniques have also been used to bypass the non-transparency preventing the direct observation of most samples. Those are mostly non-invasive techniques based on the emission/reception of electromagnetic radiations.

A first example is [Djehiche et al. 2009] (reference in French) with the use of gamma rays to study local porosity fluctuations due to deposition. The use of X-rays via X-ray micro-Computed Tomography (μ-CT) also developed a lot recently to perform 3D reconstructions of porous media, thanks to improvements in resolution capabilities and data-processing. In particular, studies were able to map, in 3D, the distribution of particles in complex structures after deposition events, as in [Hamamoto et al. 2016] or [Mikolajczyk et al. 2018] (see Fig.1.8.a). The spatial resolution of a few microns at best (for centimetric samples) offered by standard μ-CT machines sometimes make people turn to synchrotron light sources; based on the same principle but using higher energies to reach nanometric resolutions. While the space resolution of tomography techniques improved a lot in the last decade, temporal resolution (i.e. the time needed to perform a single scan of a sample; of the order of minutes) is still too weak to allow rich dynamic studies.

Less commonly, a 2D use of X-ray (radiography) is performed on porous media. The passage from 3 to 2 dimensions allows a higher time resolution, in the detriment of spatial precision as only a planar projection of 3D events is accessible.

(a)   (b)
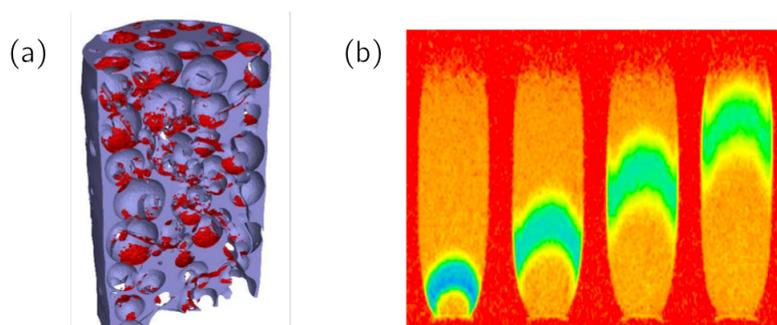
Figure 1.8: (a) From [Mikolajczyk et al. 2018]. Sedimented (red) particles in porous ceramic material by μ-CT. (b) From [Lehoux et al. 2016]. Dispersion front of nanoparticles (green/blue) in decimetric bead-packs, mapped by 2D MRI.

Then, MRI (Imaging by nuclear magnetic resonance (NMR), see chapter 2 for technical details) is a method which led to significant progress. It is based on the change in properties of protons present in the system (usually the protons of water), to provide internal intelligence in 1D, 2D or 3D on the pore size, presence of particles, solute concentrations, multi-phase behaviors, or even velocity fields. The typical resolution of MRI pictures is of the order of 1/100 of the NMR probe (cm to dm) encompassing the sam-

ple, that is roughly 1/100 of the sample's size. Telling examples include [Amitay-Rosen et al. 2005], [Lakshmanan et al. 2015], [Lehoux et al. 2016] (see Fig.1.8.b) or [Jiang et al. 2017]. More general overviews of the MRI capabilities in porous media have been proposed by [Lamrous et al. 1989] and [Britton 2011].

As for μ-CT, the choice in image dimensionality (1D, 2D, 3D) defines how quick an image can be obtained. With a standard line acquisition of 1 line per second in a $100 \times 100 \times 100$ voxels^3 volume, a line is imaged in 1 second, a plane in 1.7 minutes, and the whole volume in 2.8 hours. In the end, a trade-off is necessary between dimensionality, imaging time, artifacts levels and signal to noise ratio.

Confocal microscopy is a different promising technique. It has been recently applied to 3D porous media thanks to very specific conditions: a matching of the optical indexes of the porous structure and the invading fluid to make the system transparent. It has been for now mostly applied to the 3D characterization of porous media and to multiphase flows [Datta et al. 2014], [Shah et al. 2017], without any flowing suspension.

1.4.4 Reduced model systems

3D porous media like packs of beads or sand grains are model systems for more complex real media like soils. Because these media remain challenging to study precisely, a large fraction of the literature on the fundamentals of particle transport turned to models at the scale of a single pore or a few pores, typically tens to hundreds of microns large. Because the flow in these geometries involves microliters of fluid, the techniques are referred to as *micro-fluidic* or *milli-fluidic*.

Those systems are created specifically to allow imaging by microscopy: they consist in 2D features observable directly from a top or bottom view. In addition, they are made transparent, in glass or PDMS, potentially surface-treated to trigger specific hydrophilicity or affinity with suspended particles. By design, real-time dynamics of flowing particle and particle-medium interactions events can be observed directly. Interesting results on single pores came for instance from [Dersoir et al. 2015] (see Fig.1.9.a), who highlighted in particular the influence of the length over which particles accumulate on the formation of a clog. Studies a slightly larger scale (2D arrays of obstacles) were made by [Auset and Keller 2006] (see Fig.1.9.b) on how surface roughness increases particle stoppage and system clogging. Besides pure clogging, the distribution of particles on top or around of the pores has also been studied, for example by [Agbangla et al. 2012] who showed the accumulation of colloids in clogging clusters or non-clogging dendrites depending on the ionic strength conditions (see Fig.1.9.c).
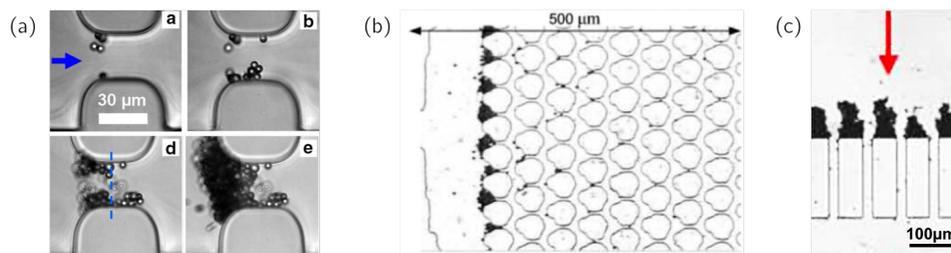
Figure 1.9: (a) From [Dersoir et al. 2015]. Micronic colloids adsorbing and accumulating at the entrance of a single model microfluidic pore. (b) From [Auset and Keller 2006]. 2D clogging experiment on rough pillars. (c) From [Agbangla et al. 2012]. Micronic particles forming dendrites in presence of salted fluid.

1.4.5   Conclusion

We went through diverse techniques, each offering different elements of observation of particles flowing in porous media. They mainly differ by the spatial and temporal resolutions they allow, from indirect localized measures at the outlet of a sample to real-time dynamics in model 2D systems.

Fig.1.10 presents an arbitrary classification of these techniques as a function of the resolution they offer. On the graph, the size of the dots is a qualitative estimation of the representation of each technique in the literature. Ideally, all innovations tend to move these dots towards to upper-right corner of the graph: spatial resolution allowing to image individual particles or pore feature, coupled with temporal resolution allowing a full understanding of the dynamics. Of course, we keep in mind that good temporal and spatial resolutions are subjective parameters depending for instance on the experimental flow-rate and scales.

In particular, real-time characterization of particle-media interactions is for now limited to studies in model 2D systems, providing results often difficult to link to the reality of more complex 3D porous media. It shows a lack of precise internal direct observation techniques, leaving open numerous questions on the exact internal deposition mechanisms of common particles. Beyond the fundamental scope of this work, an important side goal is to show how methods not commonly used to study particle transport in porous media can provide interesting new observations. The next chapter on the Materials & Methods will give an overview of such capacities.
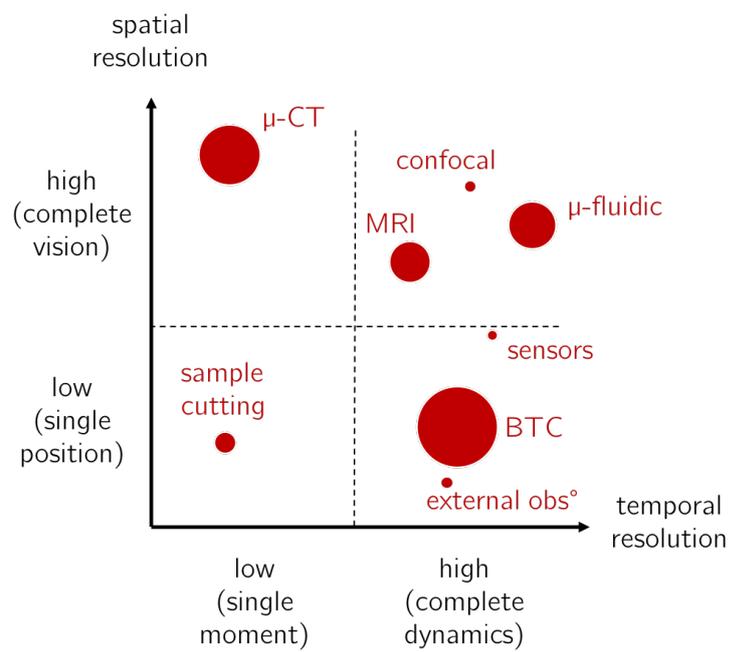
Figure 1.10: Distribution of common techniques used to study porous media. Marker sizes are arbitrary indicators to the abundance of the studies in the literature.

Scope of this work

From our general and scientific introductions of the topic, one point is clear: the interactions between suspensions of particles and porous structures are numerous, complex, and often intertwined. This work aims at drawing a modest overview of the most important of these interactions by building a framework where interactions can be easily understood and compared. From the state of the art, three types of interactions appear key:

1. The geometrical interactions between the particles and the medium, via its pore size distribution. As tackled in the previous section, such questions are commonly approached by a ratio comparing the size of the suspended particles to the size of the pores. It naturally gives a sense of the chances for a particle to be bigger or smaller than the paths inside the porous structure, and therefore clog or pass, respectively. We define and fix the **confinement ratio** $\mathcal{C}$, with d the particle diameter and w the characteristic pore size:

$$\mathcal{C} := \frac{\text{particle size}}{\text{pore size}} = \frac{d}{w}$$

2. The particle-particle interactions are relevant to assess the likelihood for a particle to adsorb to another particle. A generic way to do so is to compare the main forces bringing particles together (attractive) and the main forces turning particles away from each-other (repulsive). It is here important to note that the terms attractive and repulsive carry here a broad meaning, beyond their connotation from the DLVO theory.

   Examples of forces include Van der Waals forces, that always constitute short-range attractive contributions. On the opposite, drag forces usually tend to keep particles at a distance thanks to viscous forces; they are considered repulsive in this scope. Finally, dipole-dipole interactions (magnetic or electrostatic in particular) can either have an attractive $(+)$ or repulsive $(-)$ behavior depending on the conditions. Overall, the attraction/repulsion balance defines the aggregation tendency of a suspension, i.e. its instability. We define and fix the **instability ratio** $\mathcal{I}$:

$$\mathcal{I} := \frac{\text{particle-particle attraction}}{\text{particle-particle repulsion}} = \frac{E_{att}^{pp}}{E_{rep}^{pp}} = \frac{E_{VdW} + E_{EL(+)} + E_{mag(+)} + \dots}{E_{drag} + E_{EL(-)} + E_{mag(-)} + \dots}$$

3. The particle-surface interactions echo the particle-particle interactions for a particle approaching an element of surface of the porous matrix. In that case, a similar comparison of the attractive and repulsive forces at play relate to the affinity of the particles with the medium. We define and fix the surface **affinity ratio** $\mathcal{A}$:

$$\mathcal{A} := \frac{\text{particle-surface attraction}}{\text{particle-surface repulsion}} = \frac{E_{att}^{ps}}{E_{rep}^{ps}} = \frac{E_{VdW} + E_{EL(+)} + E_{mag(+)} + \dots}{E_{drag} + E_{EL(-)} + E_{mag(-)} + \dots}$$

Particle confinement, suspension stability and surface affinity are chosen as the three pillars of this work. They can be seen as three dimensions of a space we want to characterize: a *particle deposition phase diagram*.
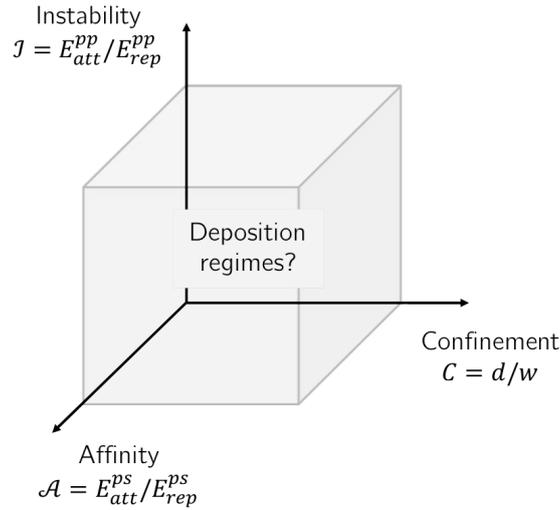
Chapters overview – exploring the deposition phases

From there, let us see how the results chapters presented in this work relate to the variation of those three parameters.

Chapter 3

To begin with, we consider the case of neutral particles flowing through a porous structure. They are chosen of size $d_p \approx 10 \ \mu$m and without surface charge or magnetic components, i.e. they do not display any significant electrostatic or magnetic behavior. Therefore, inter-particle and particle-surface attractive interactions are limited to weak

short-range effects; and drag and inertial effects are supposed predominant: particles are subject to pure hard-sphere contacts and bound/roll on each-other and on the surfaces of the system. That is equivalent to consider that drag forces are the predominant repulsive forces preventing particles to attach, which is here synonym of $\mathcal{I} \to 0$ and $\mathcal{A} \to 0$. The particle confinement is varied by changing the geometry of the pores, so that $\mathcal{C}$ becomes the parameter of interest of this first study. With E_{VdW} the depth of the Van der Waals potential well and E_D the drag work, our set of parameters reads (1.17). It corresponds to the first results chapter of this work: the exploration of the impact of the confinement ratio on the deposition of non-reacting particles.

$$\begin{cases} \mathcal{C} = \frac{d_p}{w} \in [0;1] \\ \mathcal{I} = \frac{E_{VdW}}{E_D} \to 0 \qquad (1.17) \\ \mathcal{A} = \frac{E_{VdW}}{E_D} \to 0 \end{cases}$$
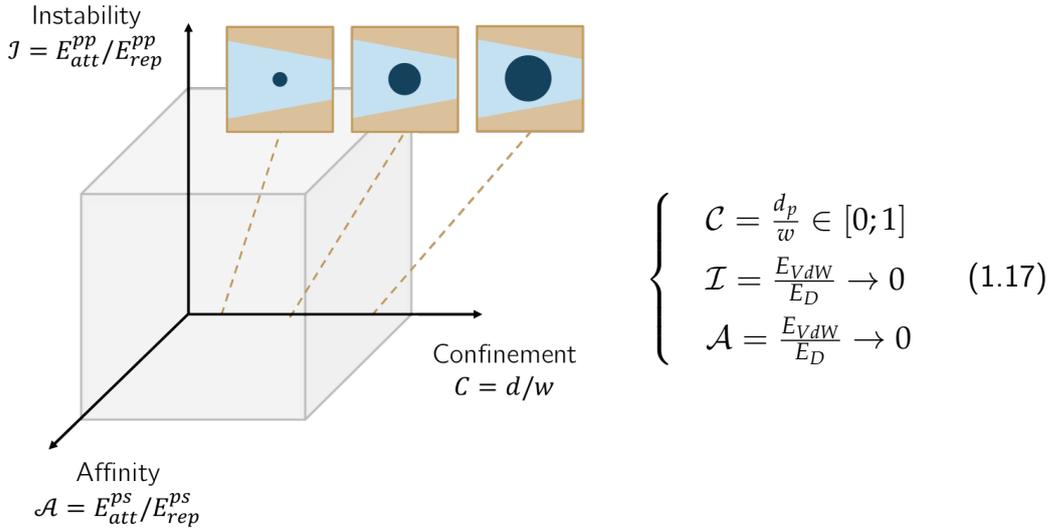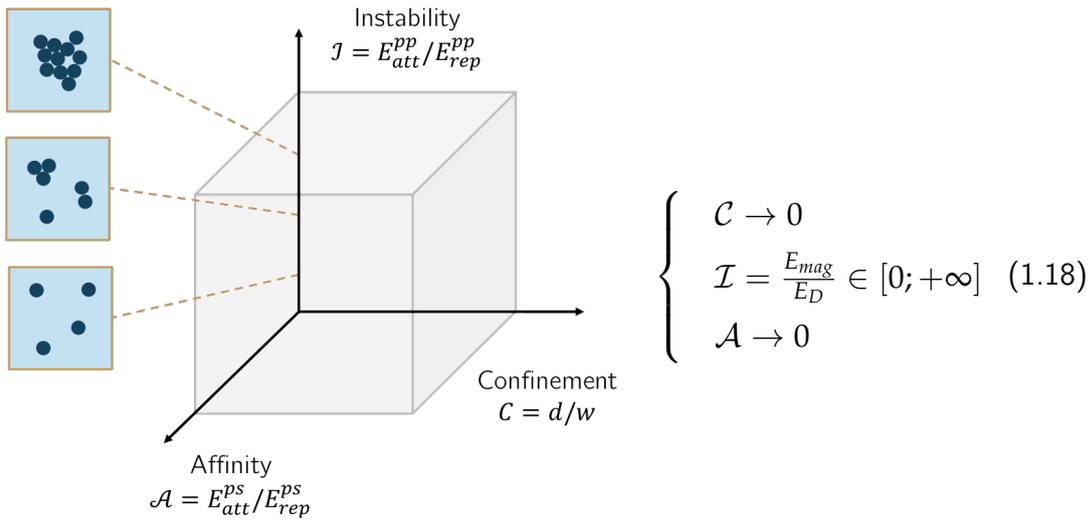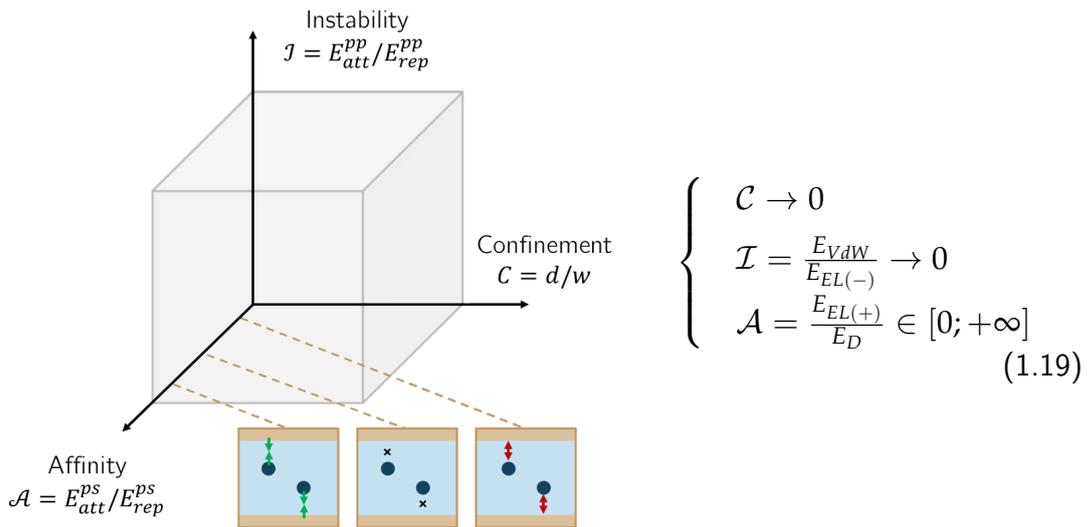
Chapter 4

Then, we consider the case of particles displaying a high aggregation tendency because of their magnetic nature, which is here synonym of suspension instability. Depending on the flow conditions and drag applied on adjacent particles, attractive or repulsive behaviors dominate: this study is an exploration of the $\mathcal{I}$ axis of the diagram. To limit the study to this axis, the particles are chosen of size small before the pore spaces ($\mathcal{C} \to 0$), and neutral towards the surfaces of the system ($\mathcal{A} \to 0$). The parameters at play write as (1.18).

Chapter 5

From there, the last parameter of interest is featured. We take the case of un-confined ($\mathcal{C} \to 0$) charged particles. The particles being of similar charge, they are subject to electrostatic repulsive forces overcoming the Van der Waals short-range attraction between them. They are therefore kept at a distance, i.e. stabilized ($\mathcal{I} \to 0$). They interact with the surface of the porous system they flow through, chosen of opposite

$$\begin{cases} \mathcal{C} \to 0 \\ \mathcal{I} = \dfrac{E_{mag}}{E_D} \in [0; +\infty] \quad \text{(1.18)} \\ \mathcal{A} \to 0 \end{cases}$$

charge. As a result, strong attractive electrostatic forces arise between the particles and the surfaces. Our set of parameters corresponds here to (1.19).

$$\begin{cases} \mathcal{C} \to 0 \\ \mathcal{I} = \dfrac{E_{VdW}}{E_{EL(-)}} \to 0 \\ \mathcal{A} = \dfrac{E_{EL(+)}}{E_D} \in [0; +\infty] \end{cases}$$
$$\text{(1.19)}$$

Chapter 6

To go further, we will finally study more precisely the effect of a coupling between particle-particle and particle-surface attractive interactions. This last chapter will complete our exploration of the deposition phase diagram via characterization of the $\mathcal{A}/\mathcal{I}$ plane and conclude this work.

Now that the scope of our studies is set, let us detail the general materials used along the work as well as the most important techniques we implemented.

Chapter 2

General Materials & Methods

Even though several quite different studies have been done in this PhD project, most of them share common materials, material characterization methods and experimental setups. This part aims at presenting their general scope to give a broad idea of the experimental approach chosen here.

First, we will present the materials, including the various porous media and suspensions of particles used throughout the projects. Then, we will focus on confocal microscopy applied to 3D index-matched porous media. Later, we will detail the second most important technique we used: Nuclear Magnetic Resonance (NMR) applied to the 1D imaging of 3D porous media. Last, other important but less critical techniques will be briefly presented: imaging by Scanning Electron Microscopy (SEM), imaging by fast-camera, and zeta-potential measurements.

2.1 Materials

This section includes all the components of the generic system used in several studies of this work: a porous structure, a fluid, particles suspended in the fluid, and a setup to flow them in controlled conditions. The section only aims at building an overview of the materials used across the PhD work. The detailed specifications for each element is further discussed in the corresponding study or chapter.

2.1.1 Porous media

A multitude of porous media can be used to perform transport studies. Therefore, the criteria motivating the choice of porous materials are presented before the description itself.

2.1.1.1 Motivation

A porous matrix suitable for the present project needs to fulfill the following criteria:

- Ease of creation. As each experiment requires its own medium and the media are not to be cleaned and reused, new matrices have to be easily producible on demand. As all experiments have to be conducted in identical conditions, all matrices also need to be interchangeable and therefore have repeatable characteristics.

- Dimension. Following the statements made in the state of the art section, a greater fundamental interest is found in studying 3D realistic structures compared to 2D model systems.

- Scale. The ability to deduce average trends from the measures made on the samples is crucial. Put another way, it means that a given porous medium has to be made of enough individual pores (with a distribution of sizes, shapes, orientations) to be able to say that, on average, each section of the medium is representative of all the possible outcomes (particle deposition, interactions, etc.). The point here is to avoid the limitation of model individual pores, which usually offer results difficult to generalize.

- Connectivity. To allow the free flow of liquid suspensions without deforming the material, the pore network has to be connected. Moreover, a constant permeability along the medium is needed to ensure a flow independent of the depth into the sample.

- Controlled structure. The understanding of the fate of flowing elements in the matrices is eased by knowing the boundary conditions of the liquid domain, i.e. by knowing the organization and characteristic sizes of the pores.

47

For these reasons, the selected candidate is a 3D porous structure made of grains packed together in a controlled way in a column. There are easy to produce and their structure has been extensively studied. This choice applies for all studies presented in the following chapters, except Chapter 4 where simple flow experiments were conducted in 2D microfluidic channels.

2.1.1.2   Random close packs

In order to create pack of grains as controlled as possible, the grains are in addition chosen spherical and monodisperse. This defines most of the expected structure, but one key parameter: the porosity.

For monodisperse spheres [Nolan and Kavanagh 1994], various types of packing can be achieved depending on the method used to create the pack (see Table 2.1). Experimentally, a perfect crystalline arrangement is difficult to form, especially as the container (column) imposes complex boundaries conditions to the beads. On the contrary, loose packings are not stable and not suitable for handling. For this project, random close packings (RCP) were therefore selected. They offer a good stability and can be made easily and in a reproducible way.

Model	Void fraction ϕ	Solid fraction $1 - \phi$	Comments
FCC or HCP lattice	0.26	0.74	Crystalline arrangement
Random close pack	0.36 to 0.38	0.62 to 0.64	Vibrated bed
Random poured pack	0.38 to 0.4	0.60 to 0.62	Beads poured
Random loose pack	0.40 to 0.41	0.59 to 0.60	Hand packing

Table 2.1: Various packings of spherical mono-disperse beads.

Moreover, the structure of their porosity is interesting compared for example to a very dense pack (see Fig.2.1). In a FCC pack, all pores have a complex geometry but are identical. At the pore scale of an RCP though, void elements have various shapes, sizes and orientations. This, in addition to the fact than each bead is on average in contact with 6 neighboring beads ([Roux et al. 2009]; reference in French), leads to a diversity of spatial configurations that will be helpful to fully explore the interactions. The more configurations, the more likely it is that all possible types of local interactions are observed (differently oriented surfaces, various particle arrival trajectory). Still, at the scale of the sample (hundreds of beads at least), this diversity is averaged and provides a global description consistent between all created samples. These average descriptors include the porosity ϕ, the pore size, the number of beads per column diameter, the number of contact points between beads, etc.
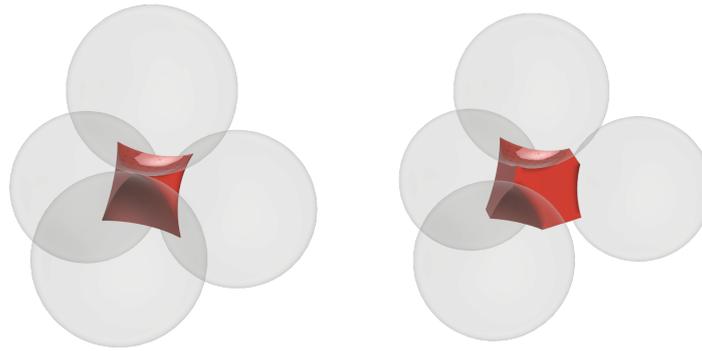
Figure 2.1: Illustration of the pore space (red) between 4 beads in a FCC pack (left) and a RCP (right).

2.1.1.3   Beads

Table 2.2 sums up the most important properties of the beads used to make the packs. To ensure the cleanliness of the beads, the following cleaning procedure is applied: each rinsing step consists in immersing the beads in a solvent, shaking vigorously for 60 seconds, letting sit for 15 minutes, shaking again and removing the supernatant.

1. Three successive rinses in tap water, to remove dirt and dust.
2. Three successive rinses in isopropanol to detach eventual organic deposits at the surface of the beads.
3. Three successive rinses in acetone to further clean the surfaces.
4. Four successive rinses in deionized water to remove traces or solvents.
5. Air drying in an dust free environment.
6. Shaking and sonication to break potential clusters of beads formed at drying.

Used in chapter	Supplier	Reference	Charac. size	Material	Main properties
3	CVP France	-	310 to 770 μm	Glass	spherical, monodisperse $\pm$ 5%
5, 6	Mo-Sci. Corporation	GL0179B6/63	63 $\pm$ 3 μm	Borosilicate	spherical, monodisperse, high purity

Table 2.2: Beads used to form the 3D model porous media. See Fig.2.2 for an illustration of the second type of beads.
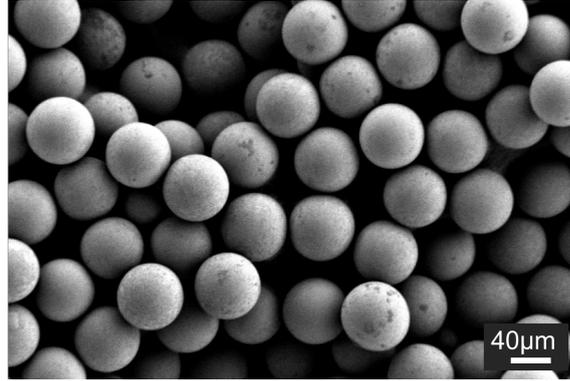
Figure 2.2: SEM imaging (1 kV) of dried borosilicate beads (63 μm diameter), illustrating their sphericity and mono-dispersity. On the right view, a larger distribution of pore throats is visible.

2.1.1.4 Making RCP

The pluviation method is chosen to create the random close packings of spheres. It allows to fill a column in a smoother way than the standard pouring methods, where beads are directly poured in the empty container. While the principle of this method is used in many applications, this variation was developed for the purpose of this work. The final result is a stable saturated porous medium ready to be used for flow studies.

The method requires the following elements: a column (shallow geometry, open at its two ends), spherical monodisperse beads of adapted size, working fluid in which the experiments will be performed. A good criterion to define an adapted bead size is to consider that the pack will be on average uniform over the depth of the column if at least 15 beads fit in the column characteristic width, i.e. $d_b \gtrsim 0.26\ R_C$ (see 2.1.1.5).
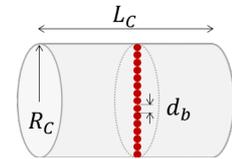
The key steps are illustrated in Fig.2.3 and detailed in Appendix 7.3.

2.1.1.5 Characterization

The previous allegations on the structure of a pack of monodisperse beads at RCP are here verified. Even though this point will be readdressed in the following chapters, Fig.2.4 presents two types of model porous media used in this work: a centimetric cylindrical NMR column filled with sub-millimetric beads; and a millimetric square glass capillary filled with micrometric beads.

On both examples, the random nature of the packs appear clearly, since no major ordered arrangement of beads is visible. As only 2D cuts of 3D packs are presented, disks that appear smaller than the average correspond to sections of beads higher or lower in

Loaded syringe needle ——

Inlet tubing ——

Capillary ——

Dense foam ——

Epoxy glue ——
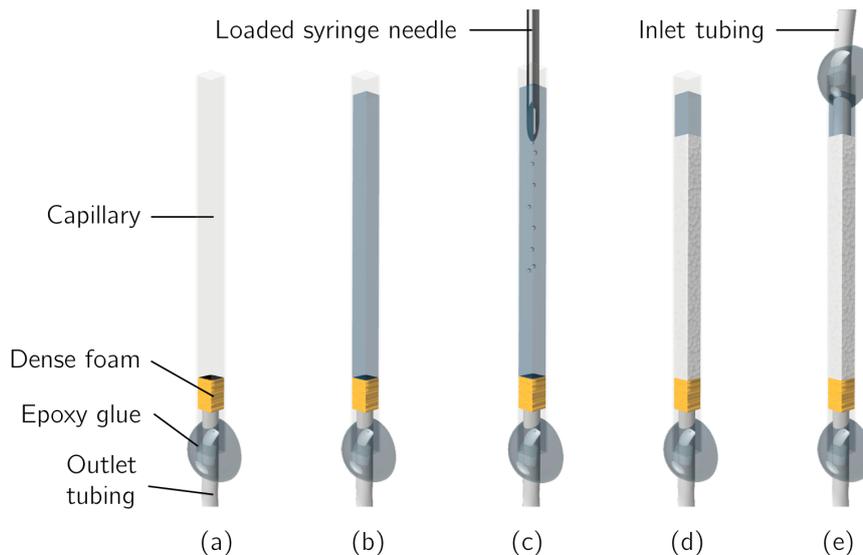
Outlet tubing ——

(a) (b) (c) (d) (e)

Figure 2.3: Illustration of the main steps of the pluviation method, in the case of a square capillary. (a) Stop foam and tubing mounted at one end of the capillary, (b) Capillary saturated with water from the the outlet, (c) Pluviation from a syringe loaded with particles in water, (d) random close packing, (e) sealed system.

the sample. A negligible number of non-spherical beads are present. Some small dark spots inside beads (i.e. inside the gray disks) correspond to core impurities, impossible to wash out. They do not impact the surface properties of the beads, but can distort the optical index uniformity of the pack.

It is also important to note than the beads composing the packs are not sintered (which can be the case when standard making methods are applied; see Appendix 7.3). A sintering step (i.e. heating the beads until their fusion temperature so that they slightly melt into each-other) is useful to form a very stable medium. A downside is that is changes dramatically the pore size distribution of the pack: all contact points between beads are replaced by smooth surfaces resulting from the melting. For this reason, and to keep a pore size distribution as large as possible, this method was not considered in this work.

2.1.2 Particles

The key general information for all particles used in this work is provided in Table 2.3. The clogging agents being tens of micron large, they are cleaned according to the same cleaning procedure as the beads composing the porous media. All other particles are bought or received suspended in water, so no additional cleaning or sorting is performed on them.

For the smallest particles, an estimation of the Hamaker constant H can be useful later in this work. Some tabulated values of interest are $H_{PS-PS} = 6.5 \times 10^{-20}$ J for
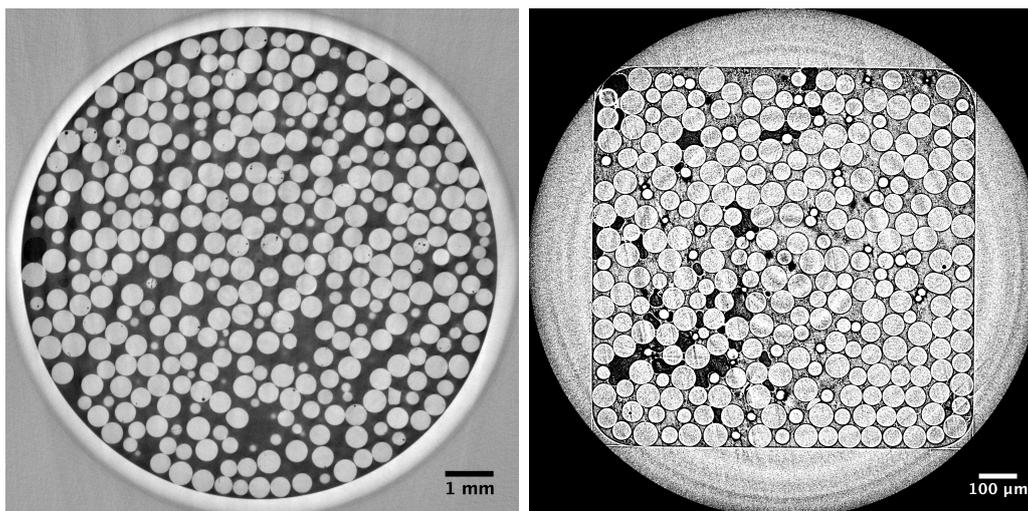
Figure 2.4: Examples of beads at RCP. (left) μ-CT cross-section of a pack of 400 μm polystyrene beads (light gray disks) in a 9.8 mm glass column (large disk).
(right) Synchrotron Soleil - Anatomix line. Cross-section of a pack of 60 μm borosilicate beads (light gray disks) in a 1.0 mm square glass capillary (square outline). Dark stains are trapped air bubbles that appear during the handling of the sample.

polystyrene, $H_{w-w} = 4.3 \times 10^{-20}$ J for water, or $H_{SiOH-SiOH} = 1.2 \times 10^{-20}$ J for silica.

When the systems get more complex (mix of solvents to saturate the porous media for instance), tabulated values are not available anymore and precise values of H are difficult to estimate. Unfortunately, most of the studies of this work fall in this category. For now, only the order of magnitude of this parameter will therefore by remembered: 10^{-19} to 10^{-20} J.

2.1.3   Injection fluids ans setups

2.1.3.1   Working fluids

Since all applications listed in the introduction section operate in aqueous conditions, water is the natural choice as the solvent of reference in this work. Still, the fluid saturating the porous media (referred to as *working fluid*) is key to create optimized experimental conditions and has to be tuned accordingly.

Two different working fluids are considered:

- A fluid to match the density of polystyrene particles and create conditions where sedimentation can be neglected (see Chapter 3).

- A fluid to match the optical index of glass beads to create transparent conditions;

Usage	Supplier	Reference	Used in chapter	Charac. size	Material	Main pties
Clogging agents	-	-	3	41 μm	polystyrene (PS)	spherical, monodisperse, neutral
Adsorbing colloids	ThermoFisher Scientific	F8765	6	1.0 μm	PS latex	amine functionalized, spherical, monodisperse, fluorescent
Adsorbing nanoparticles	BioPal Molday ION^{TM}	CL-50Q02-6A-51	4, 5	35 nm	PS latex	amine functionalized, spherical, monodisperse, fluorescent
nZVI aggregates	Politecnico di Torino (DIATI)	-	4	10 $\pm$ 8 μm	nZVI*	aggregates, polydisperse

Table 2.3: Particles used in suspension for the transport and deposition studies. (*: nano Zero Valent Iron)

see section 2.2 of the current chapter for more details. This fluid is also tuned in terms of ionic strength by controlled addition of dissolved salts (see Chapter 6).

The immersion of particles in a given working fluid also defines the stability of the suspension. Table 2.4 presents the balance $a^4\Delta\rho g/k_B T$ between the gravitational and diffusive forces acting on the particles. The ratio reflects the need to care about settling in our experiments.

Particles	Chapter	Ratio	Conclusion
Positive 35 nm nanoparticles	5	10^{-7}	Very stable
Positive 1 μm colloids	6	10^{-1}	Stable
nZVI clusters in water	4	10^{1}	Critical; quick settling
nZVI clusters in glycerol	4	10^{0}	Limit; need to maintain a flow in the system to prevent particle accumulation.

Table 2.4: Ratio $a^4\Delta\rho g/k_B T$ between the gravitational and diffusive forces for several experimental cases; and estimation of the stability of corresponding suspensions.

2.1.3.2 Pumps & tubing

Injection protocols are important to deliver fluid or suspensions in the samples with the right timing and rate. In all studies, syringe pumps (PHD 2000 Dual from Harvard Apparatus) were used with different syringes and flow-rates, pointed out in each study.

The tubings used along studies also differ by their length and sizes, but are chosen in inert polymers (poly-ethylene (PE) or PTFE) to ensure that no particle adsorbs at their surface. When nanoparticles are used, syringe filters are added after the syringe to remove potential particles/dirt exceeding 1 μm in size.

2.1.3.3 Microfluidic channels

Systems much simpler than the 3D packs previously described are also punctually considered in this work. They are reduced to the simplest expression of a porous medium: individual pores or arrays of a few pores in a single straight channel. In practice, the *microfluidic devices* used here are made at Harvard University's Center for Nanoscale Systems (making: E. Stolovicki). The channels are designed (see Fig.2.5.a) with a single inlet and outlet, a main channel, and a central feature. The central feature is made of a single constriction formed with two half-disks (see Fig.2.5.b) or several obstacles in parallel and/or series (see Fig.2.5.c).

The drawings are casted in PDMS using a MLA150 Maskless Aligner, with a submicron feature resolution. This means that the drawn features are expected to be reproduced in PDMS with a roughness smaller than a micron. For more details on the casting process, refer to [Gale et al. 2018].

The strength of this technique is that many different variations of the designs can be created simultaneously. In other words, many geometries (constrictions with various opening, obstacles with various diameters, etc.) can be tested easily. In this work, such devices are only used in Chapter 4 for the study of nZVI particles.

Such channels are very useful to observe, from above, events happening in 2D. With the adequate lighting, the contrast between the transparent fluid and the flowing particles is expected to be good and to allow a correct imaging of the particles dynamics by a confocal microscope as well as by a standard camera.
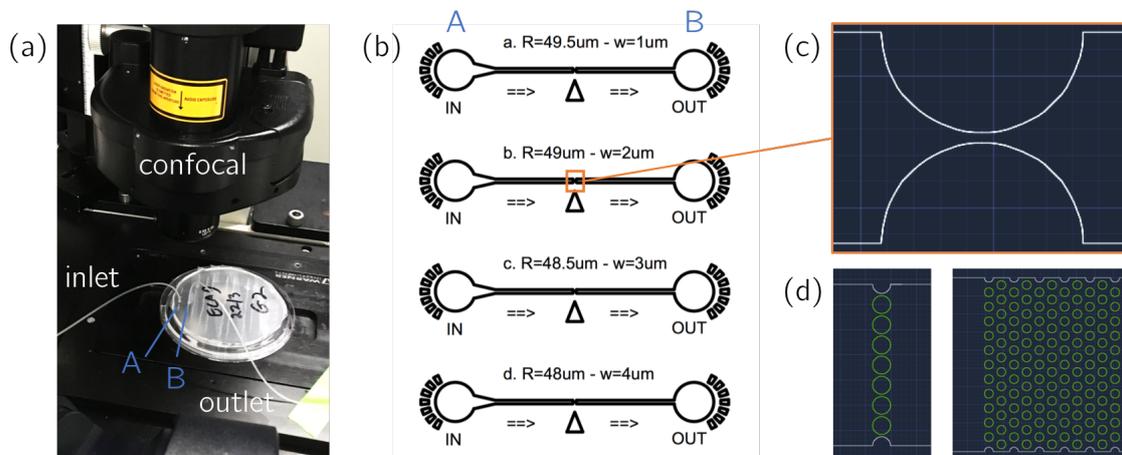
Figure 2.5: (a) Picture of the central part of the setup: the PDMS *wafer* including the channels, positioned on the confocal stage and connected to inlet/outlet tubings. (b) Overview of microfluidic channels as designed in the drawing software. View of 4 complete channels, each including a inlet and outlet (A and B) linked by a straight channel containing a feature at its center. (c) Zoom on the central feature (orange square): a simple constriction of 2 μm. (d) Examples of other central features, as 1D or 2D arrays of pillars.

2.2 Confocal microscopy for porous media

Confocal microscopy (common contraction of *confocal laser scanning microscopy, CLSM*) is an optical imaging technique able of capturing images at selected depths in a 3D sample, and eventually to rebuilt 3D structures from the 2D slices). It is extensively used in life science, especially in micro- or cell-biology and has been more recently applied to studies in material science. It is a derivation of standard fluorescence microscopy and therefore relies on the presence of fluorophores in the sample, i.e. fluorescent dyed molecules that can be excited by a specific light source and emit light in response.

2.2.1 The confocal effect

Instead of illuminating the whole sample at once like in standard microscopy, only a specific depth within the sample is targeted. Modern microscopes use laser sources with a wavelength adapted to the fluorescence of the samples. The laser light allows uniaxial lighting through the sample, with a sharp focus point (see the red path on Fig.2.6): only the fluorophores at this focus point are excited.

In addition, an objective is used to achieve an optical focus plane at the same depth. This way, only the emitted signal from the excited fluorophores can reach the detector (see plain green path on Fig.2.6): a specific optical section is selected. The coincidence of the two focal planes led to the term *confocal*. Note that since the wavelength of the returning light is longer than the laser wavelength (lower energy photon), a dichroic mirror is used to dissociate excitation and emission light paths.
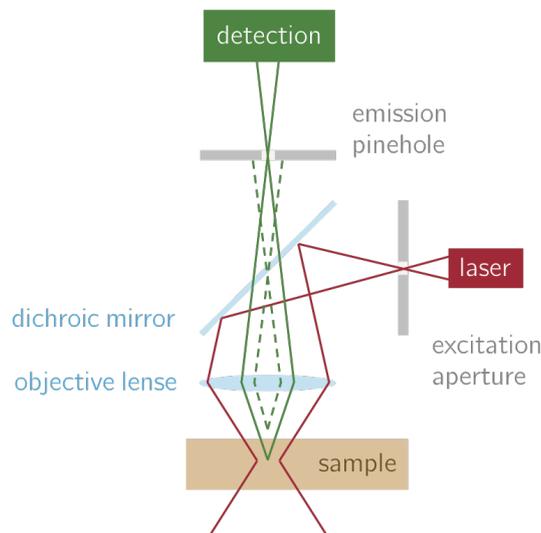

Figure 2.6: Scheme of principle of a confocal microscope, with the excitation and emission systems.

Now that the principle is explained for a single point in space, obtaining 1D, 2D or 3D images is just a matter of displacing this point to explore the space. This is achieved by

a set of rotating mirrors able to move the confocal point and scan the sample. The fact that the main optics are not moving is key is the reduction of noise. In addition, it shows that the time resolution of confocal microscope is not limited by the lighting process or the photon detection, but by the displacement frequency of the mirrors. Conventional mirrors have a line scanning frequency of ≈ 500 Hz, which means each line is scanned in 2 ms. For a 2D image of 1024 lines (standard resolution), it results in a frame rate of 0.5 fps (frame per second). That is too slow to observe, for instance, the trajectories of colloidal particle flowing at a decent velocity in a porous system. More advanced technologies - like the *resonant* scanners (mounted on piezoelectrics) used in this work - go up to 8 kHz and 8 fps for 1024 lines.

2.2.2 Additional features

2.2.2.1 Pinhole

Let us discuss further the notion of *single point excitation*. It is known that a single source (laser) point creates a local 2D diffraction pattern called Point Spread Function. As illustrated in Fig.2.7.a, a radial profile of this function exhibits a main peak (Airy pattern) followed by smaller peaks. Its diameter can be estimated by (2.1), with λ the excitation wavelength, NA the numerical aperture, M the magnifying factor of the objective, and α a factor accounting for the magnification of other optical components specific to the microscope ($\alpha \approx 3.6$ for Leica systems).

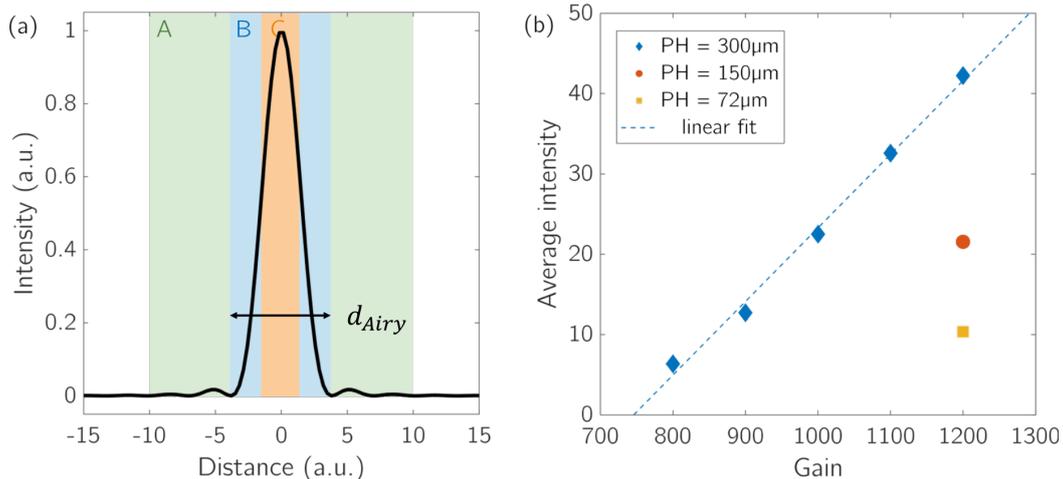$$d_{Airy} = \alpha M \frac{1.22\lambda}{NA} \tag{2.1}$$

Figure 2.7: (a) Schematics of the standard Airy pattern of a single light point. d_{Airy} indicates the size of the main Airy peak.
(b) Average intensity acquired from a homogeneous sample of fluorescent dyed fluid (Rhodamine B in water), for different gain and pinhole (PH) values.

The depth of the imaged section can be adjusted by tuning the fraction of the Airy pattern reaching the detector. To do so, the opening of the detection pinhole (PH, see Fig.2.6) can be adjusted. The basic setting is to set $PH = d_{Airy} = 1$ Airy unit, in which case only the signal from the main peak is detected (best signal to noise ratio). In case of weak signal, one can choose to increase the pinhole opening to extend the amount of light detected. On the opposite, one can focus the study on a thinner section of the sample by artificially reducing the size of excited area. Those three cases correspond to letters B, A and C respectively on Fig.2.7.a.

In the end, an estimation of the thickness dz of sample from which signal is actually acquired is given by (2.2), with n the optical index of the medium.

$$dz = \sqrt{\left(\frac{0.88\lambda}{n - \sqrt{n^2 - NA^2}}\right)^2 + \left(\frac{14nPH}{NA}\right)^2} \tag{2.2}$$

2.2.2.2 Gain

For a fixed value of pinhole, the gain (i.e. sensitivity) of the detector can also be tuned to improve the signal. Usually, the intensity of the signal is proportional to the gain (see Fig.2.7.b, blue diamonds), but the signal to noise ratio is not. Note that the same figure (square and disk markers) confirms that for an equal gain, a decrease in pinhole reduces the intensity of the signal proportionally.

The user can increase the gain to see more signal, with the risk of saturating some or all pixels of the detector, that is loosing the quantitativity of the signal. Having a constant gain value along an experiment of particle deposition can be challenging. Indeed, to see the very first particles depositing (low fluorescence), a high gain is needed. Then, as deposition occurs over time, a lower gain is needed since the many deposited particles can easily saturate the signal.

2.2.2.3 Multi-channels acquisition

After the confocal effect itself, the greatest strength of confocal microscopy is the ability to monitor several channels simultaneously. For standard biology applications, it translates in the ability to distinguish for instance the signal from different parts of a cell (nucleus, fibrin filaments, etc.) by staining them with fluorophores reacting the different excitation wavelengths.

Fig.2.8 highlights an application of this principle in the scope of the present work. The *bright-field* channel (a) is the image provided by a white light source, in addition to the laser source(s). As the light is not focused, the resulting signal is not limited to a specific thickness and can appear messy. In our case, this channel is mostly used to position the sample correctly. Then, a first laser can be used to excite specific particles
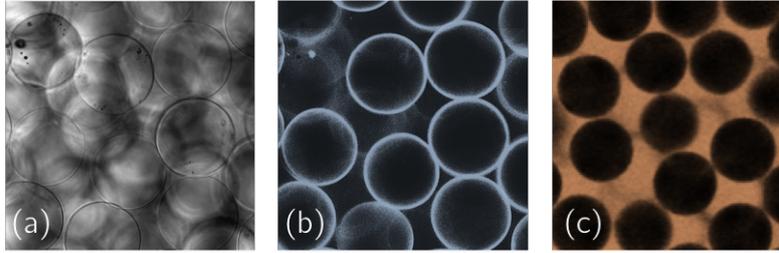
Figure 2.8: Three different channels that can be observed simultaneously; example of a pack of glass beads (for scale, disks are ≈ 60 μm in diameter). Note that all colors are artificial: the detected signal is an intensity, unrelated to the color of the excitation or emission lights.
(a) Bright-field channel (no fluorescence). (b) Fluorescent particles adsorbed at the surface of the beads ($\lambda_{ex} = 515$ nm). (c) Fluorescent dyed fluid (Rhodamine B, $\lambda_{ex} = 355$ nm).

(here adsorbed, (b)), in which case only the particles appear while the glass beads and pore space remain black. Finally, a second laser can be used to excite a fluorophore dissolved in the flowing fluid (here with the Rhodamine B dye, (c)). The fluid (pore space) appears bright, while the beads and particles remain black. The combinations of these channels help decoupling and understanding the various components of the system.

2.2.2.4 Tile-scans

A last feature worth mentioning for this work is the frame-stitching technique, called *tile-scans*. In standard mode, the field of view is defined by the objective, which can be limiting for studies over large samples. For a $10\times$ magnification with the specifications of the microscope, a single image can cover ≈ 1 mm at the maximum, roughly one tens of the length of the samples used in chapter 5 for instance.

To image larger distances, successive images (in 1D along one given axis, or in 2D along a pre-defined grid) are taken automatically. A short overlap between the frames then allows to rebuilt the larger pictures, from algorithms build-in the software of the microscope or open-source. The principle is explained in Fig.2.9.

2.2.3 Towards index-matched porous media

Of course, the whole process requires certain properties from the studied sample. First of all, the laser light needs to penetrate the sample in depth, which implies sample's transparency. Then, the laser light must not be subject to diffraction or optical aberrations. The main cause of diffraction is the presence of interfaces in the sample, defined by transitions from a given optical index to another. Let us take the example of stacked glass beads (in air). The "sample" appears overall clear, but the optical index of glass ($n_D^{glass} \approx 1.46$) is much higher than the one of air ($n_D^{air} = 1$). As a result, each element
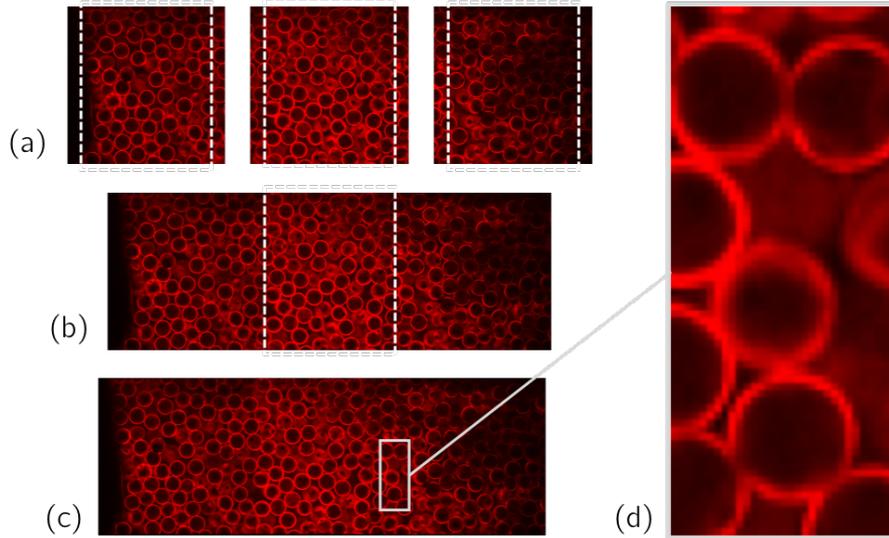
59

Figure 2.9: Principle of tile-scans. (a) Individual frames, including 5 to 10% overlap (outside white dashed lines). (b) Computing overlaps to adjust frames relative positions. (c) Final continuous frame. (d) Zoom on the stitched area, showing no significant error in reconstruction.

of surface of each glass bead will diffract the laser light: light is dissipated and no signal is detected. This principle is also mostly valid for glass beads immersed in water: the difference of indexes $\Delta n_D = n_D^{glass} - n_D^{wat} = 1.46 - 1.33 = 0.13$ is still too high to allow a straight light path: only a fraction of the light would reach the detector and the image would look blurry. Of course, the thinner the sample, the less material is crossed and the less diffraction happens. Therefore, such non-optimal settings can still be used to observe very thin samples, or close (tens of microns) to the surface of thicker samples.

To look in the depth of millimetric samples, the constituents of the system need to be *index-matched*, that is have a uniform optical index (typically $\Delta n_D \leq 0.1$). For this work, packs of glass beads are a good choice of porous media for their transparency, surface properties, purity and ease of use. The challenge is then to find a fluid with a similar index.

Since no common solvent has the same index as glass, a solution is to mix two compatible fluids to achieve the right index. In our case, given the applications of this work, we want to keep water as one fluid. Three other criteria are imposed for the other solvent: miscible to water, transparent and with a high index. Among the common solvents, DMSO (dimethyl sulfoxide) and glycerol are meeting those specificities. DMSO is finally chosen as its viscosity is much closer to the one of water ($\mu_{gly} = 1.2$ *Pa.s* $= 1200\mu_{wat}$ while $\mu_{DMSO} = 2.0\ 10^{-3}$ *Pa.s* $= 2\mu_{wat}$, at 20°C).

The same principle can be extended to more fluids, to tune better the viscosity,

wettability or polarity of the mix. [Datta et al. 2014] proposed a mix of 55.8% DMSO, 21.4% benzyl alcohol, 12.4% water and 10.4% ethanol; for beads of index $n_D = 1.467$. Such precisions was not needed for this work (see next subsection).

[LeBel and Goring 1962] showed that the refractive index of a mixture of DMSO and water evolves linearly with the fraction of the components. From Equation (2.3) we deduce that the fraction of water needed to have $n_D^{mix} = n_D^{beads}$ is $\phi_{wat} = 0.13$ ($\phi_{DMSO} = 0.87$).

$$n_D^{mix} = \phi_{wat} n_D^{wat} + (1 - \phi_{wat}) n_D^{DMSO}$$
$$\phi_{wat} = \frac{n_D^{mix} - n_D^{DMSO}}{n_D^{wat} - n_D^{DMSO}} \tag{2.3}$$

In practice, the refractive index of the glass beads varies (± 0.02), due to impurities in the core of the beads and batch variability. Still, direct observations validate that our choice of fluid is good enough to picture several layers of beads and reach 300 to 400 μm in depth (before the image gets blurry). [LeBel and Goring 1962] also studied the viscosity and density of the DMSO-water mixtures. From their work, we note that the viscosity of our fluid is estimated at $3.3 \ 10^{-3}$ Pa.s and the density at 1.1 g.cm^{-3}.

Material	n_D (20C)
Air	1.00
dH_2O	1.33
Glass Beads	1.46
DMSO	1.479
Glycerol	1.473
Polystyrene	1.59

Table 2.5: Useful refractive indexes

As a final comment, we see in Table 2.5 that the index of polystyrene is much higher than our index-matched system. Now, most particles of interest that were described in section 2.1 are made of polystyrene. It implies that, by stopping a large number of these particles in the system, we expect a degradation of the confocal imaging. Chapter 6 will reveal how critical this effect can be.

2.3   MRI – Nuclear Magnetic Resonance Imaging

The use of *Nuclear Magnetic Resonance* (NMR) and *Imaging by NMR* (MRI) for the study of porous media is not new but remains challenging. Instruments can be of quite large scale (like a medical MRI machine), and experimental setups have to be designed with care since no metallic part can be approached to the strong magnetic field surrounding the apparatus. Still, it is a powerful technique to gather information on the composition of materials. Here below are recalled some key principles of MRI (see the reference book [Callaghan 2007] for more details).

This technical section on NMR can be skipped without loosing any understanding of the results in further sections. It is presented in detail because it is an fairly original resource for the characterization of porous media and particle transport. The only key point to note is that we are able to measure the solid fraction along the samples, with a resolution of 60 μm.

2.3.1   From proton spin to magnetization

NMR uses a strong magnetic field to act on specific isotopes, but only the ones having a spin different from zero are sensitive to the magnetic field and can therefore be studied. The most commonly used are ^1H, ^{13}C and ^{19}F (all three have a spin number $I = 1/2 \neq 0$). Still, for reasons of specific operating conditions, each NMR probe (and therefore experiment) can target only one type of isotope.

A positive spin number provides each nucleus a spin vector of amplitude $S = \bar{h}\sqrt{I(I+1)}$ (with $\bar{h}$ Planck's constant), making the nucleus a magnetic dipole with a magnetic moment $\vec{\mu} = \gamma \vec{S}$. The higher the magnetic moment, the stronger the experimental signal will be. For this reason nuclei with a high gyromagnetic ratio γ are preferred, which explains the wide use of proton NMR/MRI: $\gamma(^1H)$ is for example 285% greater than $\gamma(^{13}C)$.

In this work, a proton-specific system was used. In addition from being the most common, it is specially convenient since water molecules are composed at 67% of protons; and most applications targeted by the present work are in aqueous conditions. When looking at a simple sample of water at rest, the magnetic moments of all protons are oriented randomly. The sum of these moments is therefore $\vec{0}$. Now, when the sample is set inside a magnetic field $\vec{B_0}$, it gets polarized - which means the moments of the protons get oriented in the direction of the field. The sum of the moments (*magnetization*) is then different from zero. Its absolute value reads

$$M_0 = NB_0\gamma^2\bar{h}^2/4k_BT \qquad (2.4)$$

With N the number of protons oriented along $\vec{B_0}$. Here, the study is focused on the

density of protons (i.e. their number N). From the previous expression, it seems clear that a measure of M_0 is sufficient to access this information; which is the aspect we will now detail.

2.3.2 From proton density to solid fraction

Because the amplitude of M_0 is negligible before B_0, it cannot be measured directly. A second magnetic field B_1 (*rotating field*) is introduced, perpendicular to $\vec{B}_0$ and applying radio-frequencies (RF) impulsions to disturb the orientation of the magnetization.

The steps presented here-below to access M_0 define a *double spin-echo* sequence, which is a reduced part of the standard *CPMG* sequence. The RF impulsions and the impulsions used to acquire the signal (read-out; *RO*) are summed up in Fig.2.10 (top left), along with an illustration of the main steps (see Fig.2.10.(i) to .(vi)).
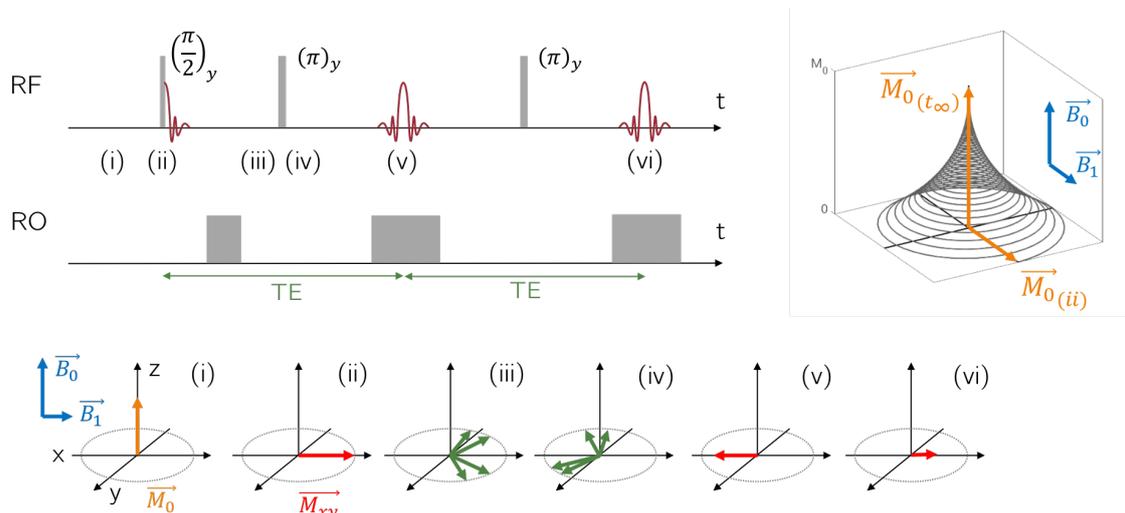

Figure 2.10: Illustration of a Double spin-echo NMR sequence. See text for details.

We fix z as the B_0 axis and xy as the transverse plane. A measure coil is placed in this plane, which means only the xy component of the signal is accessible. The sequence of events goes as follows:

- A RF pulse brings the spins out of equilibrium. It decreases the longitudinal magnetization M_z and creates a transverse magnetization component M_{xy}. Here, a $(\pi/2)_y$ pulse is applied, which completely rotates $\vec{M}$ in the xy plane ($M_z = 0$; see (i) to (ii)).

- Right after, the magnetization start relaxing towards its equilibrium position, as illustrated by the 3D plot showing the trajectory of $\vec{M}$ as it relaxes. Again, this movement can be easily decomposed in a growing longitudinal component M_z and a fast decaying transverse component M_{xy}. These two evolutions are characterized

by two *relaxation times* T_1 and T_2 respectively. They are are the basis of the dense field of *relaxation NMR* that will be not be detailed here.

- The transverse relaxation is not identical for all spins: field heterogeneities intrinsic to $\vec{B}_0$ create a distribution of spin phases leading to a *spin defocusing*: some relax faster than others (see (iii)). After a time $TE/2$ (6 to 9 ms in this work), a RF $(\pi)_y$ pulse is used to flip the spins around the y axis (see (iv)). It boils down to a compensation of the retardation between spins and allow to refocus them at a time TE (see (v)), after which the spins go out of phase again. This new alignment of the magnetization is called an *echo* and corresponds to a non-zero measurable signal (see red oscillating RF signal). In this same time, M_0 relaxed longitudinally with the characteristic time T_1: the projected value M_{xy} measured at (v) is $M_1 = M_0 exp(-TE/T_1)$, a fraction of the total magnetization.

- The same principle can be applied a second time (and more for a CMPG sequence) to create a second echo and access the value $M_2 = M_0 exp(-2TE/T_1)$ (see (vi)).

- These two measures give access to the total magnetization:

$$M_0 = M_1^2/M_2$$

Note that the sequence can be repeated over time to accumulated more signal and reduce the signal to noise ratio. For the system to be at rest at the beginning of the sequence, waiting a time TR is required for M_{xy} to be back to zero (i.e. $\vec{M}$ fully relaxed, in equilibrium along $\vec{B}_0$). For pure water, it is usually taken at $TR = 5T_1 \approx 15$ s for the relaxation to be over. This time is large before TE (milliseconds) and limits the number of measures possible in an experiment. For instance, repeating the sequence 4 times (which was done here) already takes one minute.

In the end, the knowledge of M_0 also gives the measure of the proton density N via (2.4). From there, measuring the volumetric liquid fraction ϕ_l of the sample is straightforward. The proton density of a block of solid (without protons) is zero. The proton density of a block of pure water has a maximum value N_{max}. Therefore, an unknown sample of magnetization M_0 and proton density N has a liquid fraction $\phi_l = N/N_{max}$. It finally leads to a measure of the volumetric solid fraction $\phi_s = 1 - \phi_l$:

$$\phi_s = 1 - N/N_{max} = 1 - M_0/M_{0,max}$$

Note that the value of $M_{0,max}$ was available in all experiments of this work. Indeed, pure fluid is always present on top of the porous samples and is imaged to serve as the reference signal for $\phi_s = 0$ (pure fluid).

2.3.3 Gradients for 1D imaging

From a single measure over the sample (which would give an average solid fraction value), the aim now is to divide the sample in as many regions as possible and perform a measure for each region; it is the principle of imaging (MRI). To do so, a third magnetic field (*gradient field* or *Read-out* (RO, see Fig.2.10) is introduced in the system. Technically, that means having in the NMR probe an additional coil for each dimension one is willing to image. One gradient is present in our machine, hence the will to use it to perform 1D imaging. That means an average value of solid fraction can be measured in each section of a sample along a given axis.

In practice, the gradient field encodes the positions in the sample in wave vectors k in the Fourier space. To rebuilt the expected profiles in the temporal space, an inverse Fourier Transform is done on the raw NMR signal.

2.3.4 Complementary information

2.3.4.1 Apparatus

We use a Minispec machine by Bruker (MQ20 ND Series) with a 0.5 T permanent magnet (20 MHz) and a 4 T.m^{-1} vertical pulsed gradient unit. The samples were vertically divided in 512 areas. It corresponds to 512 pixels over the 30 mm of field of view, i.e. a spatial resolution of 59 μm. These settings are chosen to provide the best signal to noise ratio (SNR$\approx$ 80).

2.3.4.2 Flow impact on the measure

A redundant question in MRI is the possibility to measure proton activity while they are in movement. That is the case for instance when the fluid in the sample is flowing at a velocity non-negligible before the time needed to run an NMR sequence (several seconds). Despite the existence of correction procedures to account for proton displacements, it was easier in this work to limit measurements to steady states. The method used to achieve these steady states is detailed in section 3.1.

2.3.4.3 Apparatus impact on the measure

On a different topic, the NMR probe has its own signal that has to be taken into account (see Fig.2.11). First, even though the field of view of the acquisition was set to 30 mm, the probe actually only provides a stable measure over a $\approx$ 10 mm area. Out of the 512 pixels chosen for our studies, only the ones in depths where the probe signal is at least at 90% of its nominal value are considered (see red markers). In addition, the probe (series of capacitors) is not perfectly homogeneous and provides a non-constant transfer
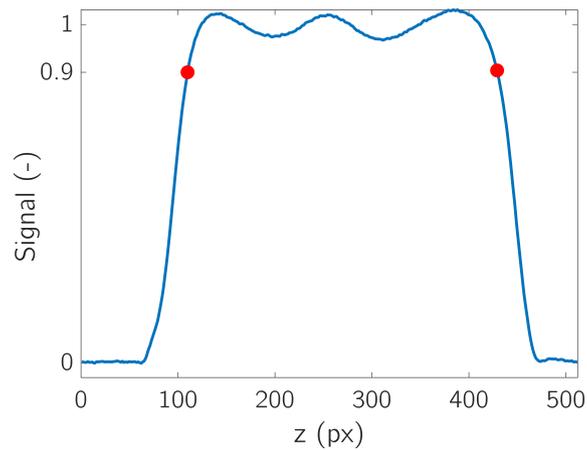
Figure 2.11: NMR probe signature profile along depth (in pixels). Red markers define the area where the signal is at least at 90% of its nominal value.

function along depth, even in the restricted area we just defined. To compensate this effect, the *signature* profile of the probe is measured and is strongly repeatable. All profiles presented in this work have been cut outside of the red markers and normalized by this signature profile.

2.4 Secondary methods

2.4.1 X-ray microtomography

Microtomography by X-rays (or micro-computed tomography, μ-CT) is a powerful imaging technique. It uses X-rays ($\lambda \in [0.01 - 10]$ nm) to study a physical (opaque) body without altering its structure or composition. Hard X-rays pass through relatively thick objects (sub-centimetric here) without being much adsorbed or scattered and can therefore go through a sample towards a photon detector. Depending on what is traversed and most especially the density of the components, their properties (energy, phase) will vary and carry information on the matter. These properties variations provide contrast is the resulting image.

Usually, a centimeter size cylindrical sample is chosen and mounted straight on a rotating support. At a given starting position, a radiography of a sample is taken. Then the sample it rotated of a small angle around its main axis and the process is repeated. Many cross-sectional scans (projections) of the samples are acquired, as a signature of the complete 3D structure. The real volume is then rebuilt based on operations like the Radon transform (now fully automated in μ-CT softwares).

For this work, we used a Ultratom scanner from RX Solutions at Ecole des Ponts ParisTech (Champs-sur-Marne, Paris, France; P. Aimedieu). The main specifications are provided in Table 2.6. In chapter 3, a good contrast in the images was possible thanks to the large difference in density of all constituents (1 g.cm^{-3} for water, 2.2 g.cm^{-3} for silica and 1.04 g.cm^{-3} for polystyrene). This difference could be increased by replacing water with air (drying), assuming that the porous media and deposited particles would not move during the drying process. In addition, note that a voxel size around 5 μm allows to see 40 μm particles with a reasonable resolution.

X-ray source	Hamamatsu L10711-23 (max 160 kV, 200 μA, min spot size 250 nm)
Imager	Paxscan Varian 2520V (1920×1560 px^2, pixel size 127 μm)
Energy	55 kV
Current	90 μA
Frame-rate	0.5 fps
Voxel size	5.3 μm

Table 2.6: Main μ-CT settings used in this work.

2.4.2 Scanning Electron Microscopy (SEM)

The few images presented in this work are done on a Zeiss SEM (Ultra55 and Supra55VP) using an Inlens detector, at the Center for Nanoscale Systems (CNS) at Harvard Uni-

versity). Energies in the range of 1 kV were used, on samples of a few mm^3, with a resolution down to 10^1 nm. See section 5.1.1.2 for view of the best resolution achieved in this work: fully resolved nanoparticles (35 nm in diameter) on a borosilicate surface.

Samples susceptible to *charge*, i.e. to store electrons by lack of conductivity are coated with a conductive layer of Pt/Pd (2 to 5 nm) using a Sputter coater apparatus, also at CNS. Our silica beads in particular required this additional step.

2.4.3 Fast-camera imaging

The microfluidic devices can easily fit on the stage of the confocal setup that we previously detailed. In addition, because they are two-dimensional and transparent, fast-camera imaging is also well suited to their study. Here, experiments were conducted with an imaging speed in the range of 2×10^3 to 10^4 frames per second. Such high speed is achieved at the price of a lower spatial resolution than for confocal imaging: 1.5 μm.px^{-1}.

The properties of the model used here are detailed in Table 2.7.

Supplier	Fastec Imaging
Model	HiSpec 1
Light sensitivity	3200 ISO monochrome
Speed	Up to 10^5 frames per second
Resolution	Up to 1280×1024 px^2 (500 fps)

Table 2.7: Main fast camera settings used in this work.

2.4.4 Zeta potential

To assess the stability or properties of suspensions of charged particles, a measure of the Zeta potential ζ [mV] is common. Its definition follows our previous considerations on the DLVO theory. We mentioned the Outer Helmholtz Plane and the diffusive plane defining the ionic atmosphere on top of a charged surface. An additional (intermediate) plane, called the shear plane, corresponds to the film of liquid mobilized when the surface is set in relative motion with the fluid. The value of potential at this location is the Zeta potential.

Here, we accessed the DelsaNano C Particle Size and Zeta Potential Analyzer (CNS, Harvard University). The apparatus has a theoretical potential range of $[-100; +100]$ mV, for concentration of $[0.001; 40]$%. In practice, the measures are found reliable on the lower side of the concentration range only.

The technique is based on a measure of the electrophoretic mobility of the particles in the fluid, i.e. their migration due to local charge gradients. To induce this mobility,

the sample (cuvette containing the suspension) is connected to two electrodes imposing an electric field in it.

Setting our approach

Now that the scope and methods of study are defined, let us get to the hearth of the matter. In section 1.4.5, three key parameters were introduced: the geometrical confinement of particles in the porosity, the stability of the suspensions, and the affinity between the particles and the surface of the system.
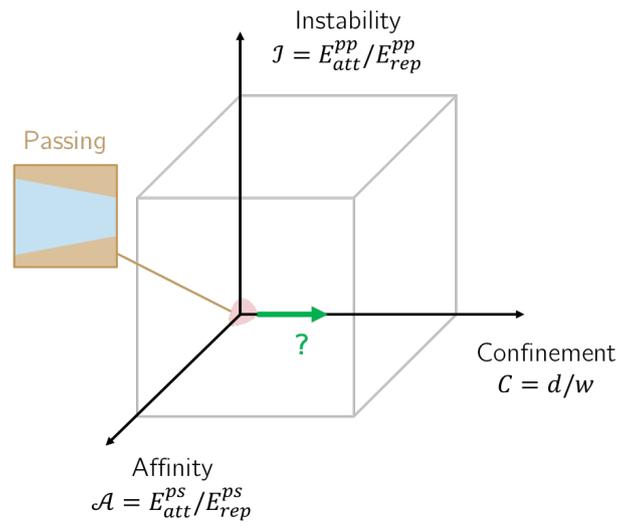
As a foundation for the following results chapters, we tackle here the case of non-confined, non-interacting stable suspensions flowing through porous matrices. In others words, we consider particles small before all pore throats, independent, and limited to hard-sphere contacts with the surfaces. It corresponds to $\mathcal{C}$, $\mathcal{I}$, $\mathcal{A} \to 0$.
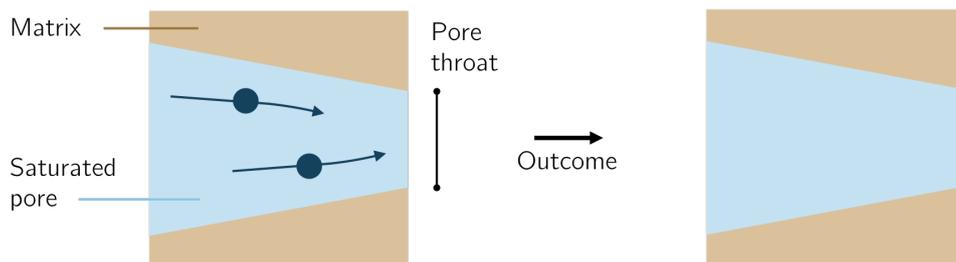
Such particles flow freely from pore to pore and are not subject to any deposition mechanism in the porous system. They are *passive*. Their flow may be complex and relates to some effects presented in state of the art (migration, interception with the surfaces, etc.) but the outcome of their passage in the system is straightforward: no stoppage event implies no alteration of the pore space. Equivalently, the final state of the medium is equal to its initial state, hence no particle present on the "outcome" scheme here-above. This state defines the reference point of our studies, to which we will come back along the work.

From this origin point, a first natural question is to wonder how the simple outcome of passive particle is modified by an increase in particle confinement. Answering this question, illustrated on the diagram here-after (see green arrow), is the objective of the first results chapter.

Instability
$$\mathcal{I} = E_{att}^{pp}/E_{rep}^{pp}$$

Passing

Confinement
$$C = d/w$$

?

Affinity
$$\mathcal{A} = E_{att}^{ps}/E_{rep}^{ps}$$

Chapter 3

Non-interacting particles at variable confinement

Particles with no attractive or repulsive interactions between themselves (hard spheres contacts) and between them and the surfaces of the porous media are considered. The absence of significant attractive or repulsive interactions is ensured by focusing on non-colloidal particles, tens of microns large. In addition, iso-dense conditions are created, which prevents the settling of the particles over the duration of the experiments. In these conditions, $\mathcal{I} \rightarrow 0$ and $\mathcal{A} \rightarrow 0$.

About the confinement $\mathcal{C}$ at the heart of this study, the exploration of a large range is achieved by varying the average pore size. For the particles to explore a large variety of pore configurations, they need to flow in media composed of enough pores. Given the size of the particles, it implies centimetric media. Such scale excludes microscopy studies that have a limited field of view, and motivates the method preferred here: imaging by NMR.

3.1 Specific Material & methods

3.1.1 Materials

3.1.1.1 Porous media

As detailed in the main Materials & Methods section, our reference in terms of 3D porous systems consists in beads packed at Random Close Packing. Precisely, we use here commercial spherical monodisperse glass beads (CVP France) sieved manually. Six batches were selected with different average diameters ranging from $d_g = 310$ μm to $d_g = 770$ μm, and a residual polydispersity of $\pm 5\%$ resulting from the sieving process. The beads are packed in cylindrical columns with an inner diameter of $W = 10$ mm, which ensures at least $W/d_g^{max} = 13$ beads per diameter of column: enough to avoid edge effects. For cleaning procedure, see section 2.1.

3.1.1.2 Suspensions of particles

The particles used are commercial spherical Polystyrene (PS) beads with a unique average diameter $d_p = 41$ μm indicated by the supplier. This material is used for its low density ($\rho_{PS} = 1.05$ g.cm^{-3}), which will be useful to neglect gravitational effects. In addition, they are manually sieved between 32 and 50 μm (i.e. $\pm 20\%$ around d_p) to prevent the presence of any outlier in the size distribution, which could have an important impact on our confinement-based study. To avoid confusion, these suspended beads are refered to as the *particles*, and the beads making the porous media as *grains*.

Our choice to vary the grain sizes with a single particle size, instead of varying the particle size with a unique grain size, can seem uncommon. It is justified by the will to keep suspensions of particles as reproducible as possible, especially in terms of average inter-particle distance in suspension, since the latter is expected to play a non-negligible role in clogging/bridging events. Put another way, using a unique particle size allows to use the exact same suspension for all experiments.

Given the grains and particles sizes, the range of confinement ratios of the study can be deduced by comparing the unique particle size to the range of grain sizes: $\mathcal{C} \in [0.3 - 0.8]$.

To focus on the pure effect of particle deposition by size-exclusion, we choose to neglect the effect of gravity (sedimentation) in this study. For this assumption to be valid, a fluid with the same density as our particles is made, by diluting deionized water (density $\rho_w = 1.00$ g.cm^{-3}) with glycerol (density $\rho_w = 1.26$ g.cm^{-3}). From the relation $\rho_{mix} = \rho_{PS} = \rho_g x + \rho_w (1 - x)$, the adequate weight fraction in glycerol x is deduced: $x = (\rho_{PS} - \rho_w)/(\rho_g - \rho_g) = 0.19$. The mix is adjusted to ensure no visible sedimentation or creaming occurs over up to 6 hours (longer than our experiments). The calculated viscosity of the mix [Cheng 2008] is $\eta = 1.6$ $mPa.s \approx 1.6\eta_w$, which is not

73

expected to modify significantly the flow in the porous system compared to pure water.

3.1.2   Methods

3.1.2.1   1D proton density profiles

To follow the evolution of the system as particles clog inside, 1D profiles are performed by MRI along the main axis of the samples (see Chapter 2 for technical details). The main components and specific dimensions of the setup are detailed in Fig.3.1, as well as the main direction (x) of the study: from the surface of the sample, towards downstream.
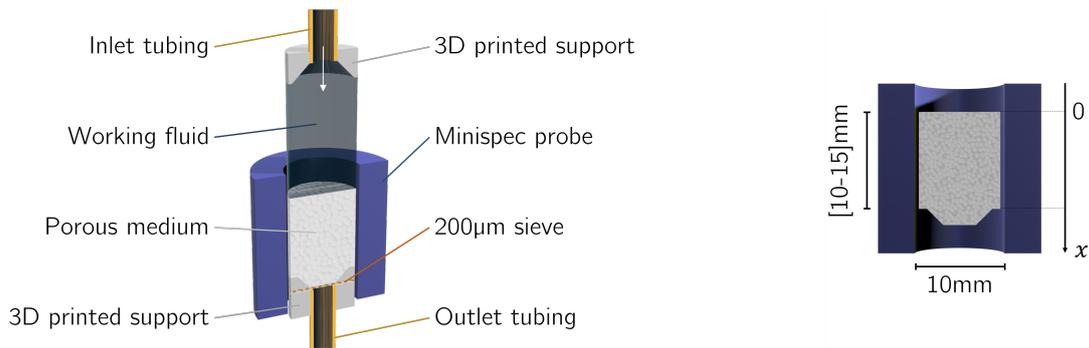
Figure 3.1: Illustration of a porous sample in a glass column with inlet and outlet tubings; positioned in the NMR probe. Right scheme shows characteristic sizes and origin and direction of the main axis (depth, x). Flow goes top to bottom.

As a reminder, this method gives direct access to the solid fraction ϕ_s as a function of the distance along the main axis of the system (depth, x). For ease of understanding of the results presented later, depth is defined in units of grain diameters d_g.

From Fig.3.1, we also note that both the sample and pure working fluid (on top of the sample) are placed inside the NMR probe. Let us first focus on the transition between those two media. When it is imaged, profiles like the ones presented in Fig.3.2are observed.

Before the transition (negative x, pure fluid) a solid fraction of zero is expected. After the transition (positive x, porous medium) a large solid fraction is expected. Indeed, on the profiles ϕ_s goes from 0 to 0.60, which corresponds to a reasonable value for a random close packing. The transition between pure fluid and porous medium is not perfectly straight but extends from approximately $-2d_g$ to $0d_g$. This is due to the non-perfect flatness of the surface of the pack of bead. See Fig.3.8.b for a visual confirmation.

Looking deeper in the sample (over 25 grain diameters), the value $\phi_s = 0.60$ is constant, which shows the homogeneity of the packs.

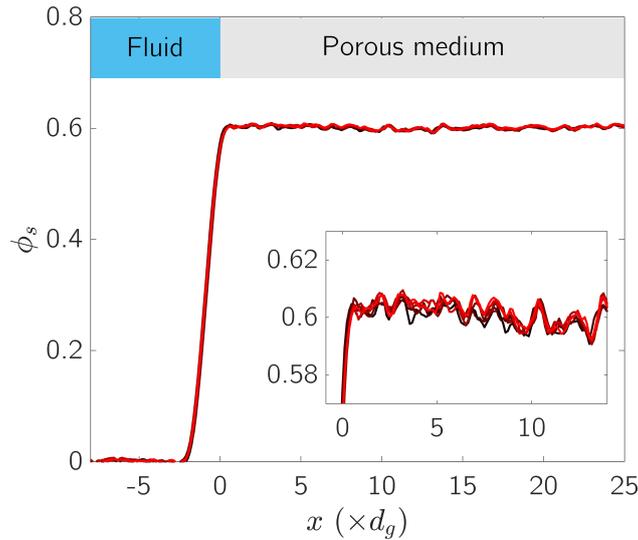Moreover, a close-up (Fig.3.2, insert) highlights three important points about:

Figure 3.2: Solid fraction profiles as a function of depth, and close-up around $\phi_s = 0.60$. Negative depths are filled with pure working fluid; positive depths with porous medium. 6 profiles are presented, separated by a rinsing step with pure working fluid.

- The variations around the average solid fraction value: $\phi_s = \bar{\phi}_s \pm 1.6\%$, which is a measure of the heterogeneity of the sample.

- The repeatability of the measure: the six curves presented correspond to six acquisitions separated by injections of pure fluid in the system. Since only fluid is injected, the medium is expected to stay identical, and the profiles to repeat: that is what we observe. With ϕ_s varying of 0.005 at most between acquisitions, our measure has a repeatability above 99%.

- The impact of the grain size on the profiles: for all acquisitions, constant up and downs in the signal are visible and correspond to the period between successive layers of grains. For instance, roughly five periods can be counted between 0 and $5d_g$ (hence one period per d_g). This is characteristic of some order in the local arrangement of the grains in the pack, and proves the stability of the pack over multiple acquisitions.

3.1.2.2 Injection setup & Automation

It has been shown in the General Material & Methods section that the presence of a flow can significantly impact the NMR signal. This impact is possible to quantify, at the price of a larger noise in the measurement. Since this study focuses on the clogging state of the porous media over the injections of particles, and not on the complex flow dynamics, we chose not to go in this direction and to carry out an indirect method; i.e. only image the system when the fluid is not in movement.

For the media to be imaged at steady state, one way is to inject the suspensions of particles by pulses instead of continuously. To do so, cycles of four steps are performed, using the setup presented in Fig.3.3:

1. Injection of a constant volume of suspension.

2. Injection of pure working fluid to make sure all deposited particles are stable and all non-deposited particles passed the porous medium, i.e. exited the system.

3. Waiting period for the flow to stop and the system to reach steady conditions.

4. NMR sequence to picture the current state of deposition.
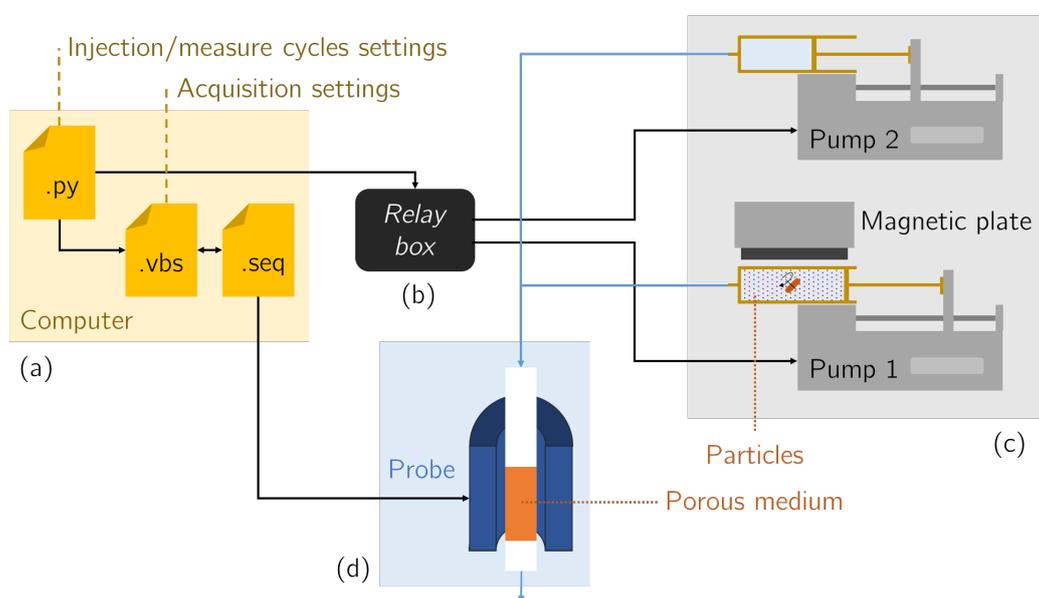
Figure 3.3: Overview of the setup. Scripts (a) control a relay box (b) automating the injection cycles (c), before the actual NMR imaging in the probe (d).

The setup is fully automated. A Python script controls a relay box (refer to C. Courrier, Navier Laboratory, for details on the circuits boards) triggering the two syringe pumps (suspension and working fluid). Once the injection cycle is over, the script calls the right NMR sequence and exports relevant times and data.

This setup implies that the pumps are at rest during the imaging, which introduces a risk of particle sedimentation. Despite the theoretical density-match of the particles, additional measures are taken to prevent it: a magnetic stirrer is inserted in the syringe containing the suspension and is activated by a magnetic plate placed on top of it.

Thanks to this full automation, up to 30 successive cycles of injection can be performed easily. To study as many steps of deposition as possible, the more injection cycles

the better. Still, the number of cycles is limited by the capacity of the syringes fitting on our syringe pump (140 mL). After this volume, replacing the syringe would cause variations in the internal pressure and eventually displace particles.

Table 3.1 summarizes the important parameters set for this study.

Part	Parameter	Notation	Value
Pump	Flow-rate	Q	640 mL.h^{-1}
	Injection time	t_{inj}	$\in [10; 30]$ s
	Flush time	t_{flush}	$\in [30; 90]$ s
	Stabilization time	t_{stab}	10 s
Minispec	Relaxation time	TR	15 s
	Acquisitions	-	30
	Echos	-	2

Table 3.1: Important parameters in the NMR study.

3.1.2.3   X-Ray Micro-tomography

For details about μ-CT imaging, refer to Chapter 2. All parameters are set here as presented in the main Material & Methods section.

3.2   Clogging dynamics at variable confinement

3.2.1   Confinement effect on deposition

Depending on their confinement in the pore space, particles are expected to clog, bridge or pass through the porosity. To build a better understanding of these mechanisms, three main cases are defined and explored: low, intermediate and critical confinement.
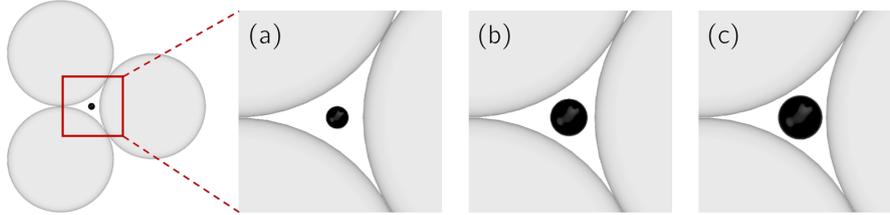
Figure 3.4: Illustration of the three main confinements of this study. Comparison between particle size and three grains in dense hexagonal packing, for (a) $\mathcal{C}=0.40$, (b) $\mathcal{C}=0.66$, (c) $\mathcal{C}=0.78$.

3.2.1.1   Low confinement

The first interesting case consists in studying the $d_p = 41$ μm particles in a porous system made of grains of average diameter 612 μm. The confinement ratio is $\mathcal{C}= d_p/d_{pore} = 0.40$, which means the average particle size is 40% of the maximum sphere fitting between grains ideally packed in a tetrahedron.

The evolution of the solid fraction over depth is presented in Fig.3.5. ϕ_s follows the same initial profile as for the reference case studied in the previous section: zero on top of the porous medium ($x < 0$) and small fluctuations around 0.6 in the porous medium ($x \geq 0$). Over cycles of injection (successive curves from black to red), a small increase of the solid fraction appears near the entrance of the bead pack. At a depth of $1d_g$ for example, ϕ_s grows from 0.62 to 0.66 (6% increase) in 8 cycles. In the same time at a depth of $20d_g$, it increases of 2%, just higher than the noise of our measure. Overall, we can conclude that some particles deposited, preferentially near the inlet.

To illustrate this case, μ-CT images near the inlet ($x \approx d_g$) are acquired at final state (after the last cycle) and presented in Fig.3.6. Local 3D views (see (a)) show how particles are deposited between the grains. It is clear that individual particles are clogged in pore throats smaller than their own size, close from the contact points between grains. Despite several particles clogged next to each-other, no obvious case of bridging is observed. A larger view (see (b); cut in yz plane, x being the depth) shows a larger diversity of configurations. While most of the pore space appears free
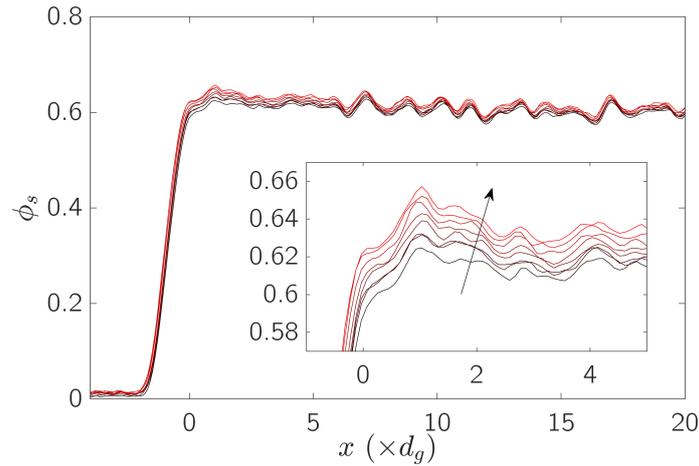
Figure 3.5: Solid fraction profiles over depth and 8 cycles of injection, for $\mathcal{C}=0.40$. Lowest darkest profile is the initial state; successive cycles follow the black arrow.

of particles, sparse clusters of particles appear in addition to individually clogged particles. In some places, where the apparent pore space is restricted, the clusters even completely fill pores. Further interpretation is tricky since we are looking at a 2D cut of 3D distributions, but it already gives a sense of the clogging mechanisms in such porosity.
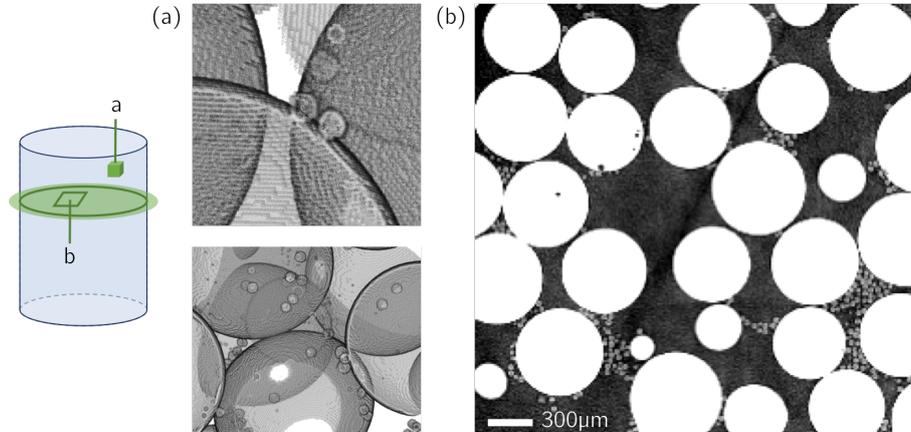
Figure 3.6: μ-CT views at $\mathcal{C}=0.40$ at final state. Left scheme shows where data have been extracted from. (a) 3D views of particles clogged between grains. White pixels are data missed in the 3D reconstruction. (b) 2D yz cut (see left illustration) of the system: grains in white, particles in light gray.

As a tack-away, all these observations confirm expected behaviors: clogging events occur in narrow pore throats, in a scattered manner while being more frequent near the entrance of the system.

3.2.1.2 Intermediate confinement

Let us now challenge these observations by increasing the confinement ratio to $\mathcal{C} = 0.66$. The same experiment is performed (see profiles on Fig.3.7) and shows a significantly different outcome. The initial state of the system is the same as previously, with an average solid fraction in the bead pack of 0.61. This highlights once again the repeatability of the preparation of our porous media. Then, over cycles of injection, clogging occurs and ϕ_s increases (see arrow (A)). The preferential increase near the inlet is even more obvious than before, with a clear decreasing slope over time appearing in the profiles between 0 and $20d_g$.

The phenomenon is completed by a second observation we did not witness before, at the entrance of the porous system (see arrow (B)). In an area originally filled with pure fluid, ϕ_s rapidly grows. It corresponds to particles accumulating at the surface of the porous medium, which means they are not penetrating the system anymore.
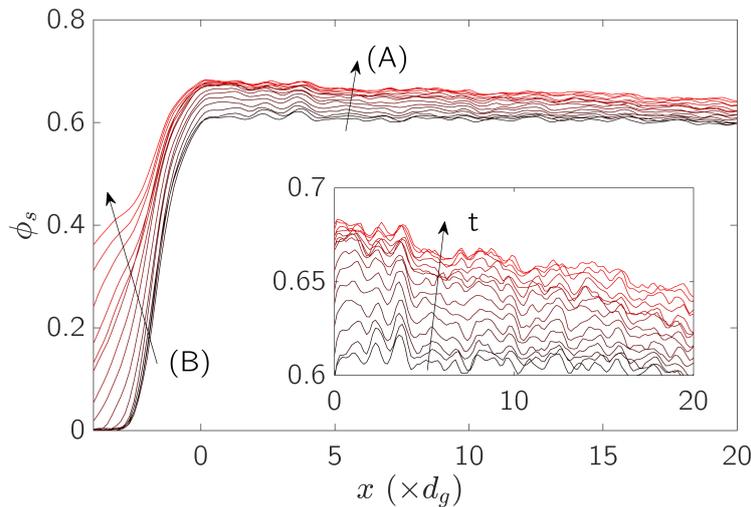
Figure 3.7: Solid fraction profiles over depth and over 30 cycles of injection, for $\mathcal{C} = 0.66$. Arrows (A) and (B) highlight the *in-depth* and *surface* deposition mechanisms respectively.

Like before, the distribution of particles can be checked by microtomography imaging (see Fig.3.8) on the sample at final state. On local 3D views (see (a)), pores appear largely filled with clogged particles stacked on top of each-other. A 2D cut of the system, this time in the xy plane, confirms that two distinct types of deposition occurred.

First, particles clogged in depth and formed localized clusters, following the mechanism previously revealed. These clusters fill a greater fraction of the pore space than in the case $\mathcal{C} = 0.4$ case, which is consistent with a greater increase in solid fraction. Then, on top of the pack of beads, a large number of accumulated particles is visible. They form a *cake*, that will be further characterized in subsection 3.2.3.
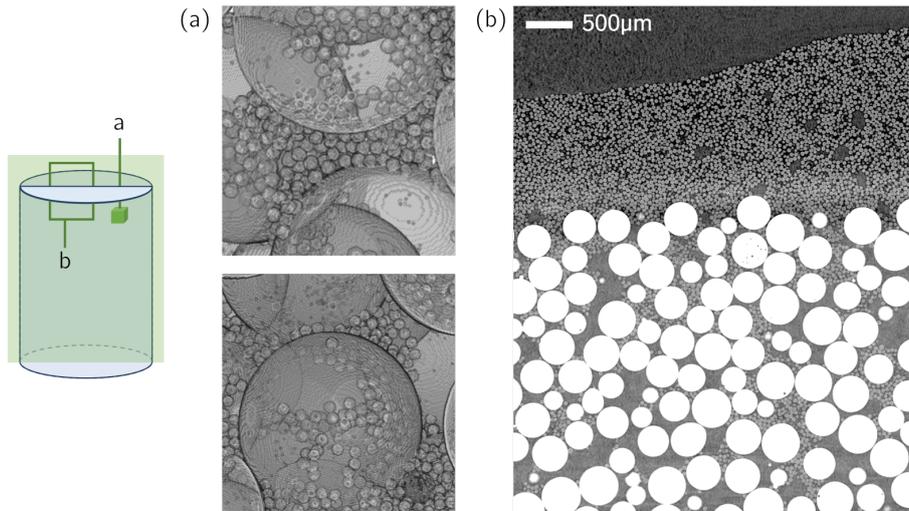
Figure 3.8: μ-CT views at $\mathcal{C}= 0.66$ at final state. Left scheme shows where data have been extracted from. (a) 3D views of particles clogged between grains. (b) 2D xy cut (see left illustration) of the system: grains in white, particles in light gray.

3.2.1.3   Critical confinement

Increasing again the confinement of the particles to $\mathcal{C}= 0.78$, the previous phenomena are expected to intensify. Looking at the solid fraction profiles (see Fig.3.9), the accumulation of particles near the top surface is obvious. The concentration of deposited particles decreases fast with increasing depth: no change in solid fraction is detected deeper than $x \approx 10d_g$. This confinement is referred to as critical since particles do not penetrate deep in the system but form a large cake on top of the grains after just a few cycles of injection.
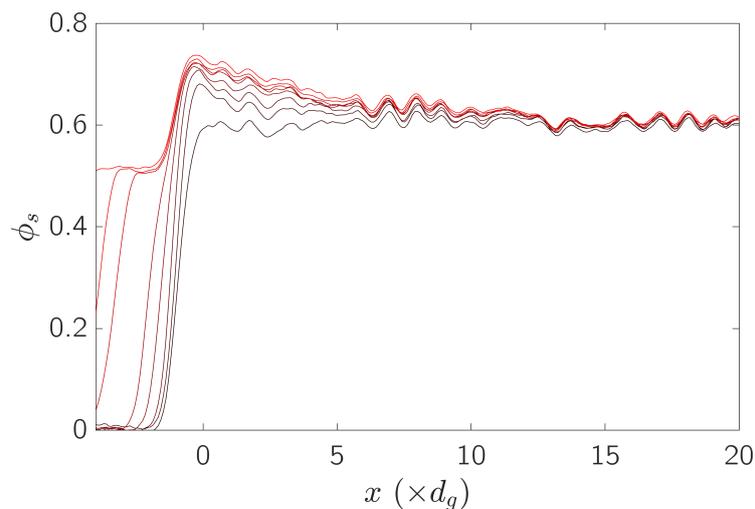
Figure 3.9: Solid fraction profiles over depth and 8 cycles of injection, for $\mathcal{C}= 0.78$.

81

Now that the global description of the distribution of particles as a function of the confinement has been done, we can focus on the dynamics driving the clogging *in depth* and the surface *caking*.

3.2.2 In-depth deposition dynamics

3.2.2.1 Cluster size distribution

The mechanisms driving in-depth deposition can be described by further analyzing μ-CT images. We look back at a case where deposition occurs only in depth: the low confinement example at $\mathcal{C} = 0.40$. On several images (yz cuts) at depths in the range $[d_g; 4d_g]$, we measure the average dimension of each cluster (apparent diameter d_c) and deduce their size distribution. The distribution is normalized by the size of a single particle d_p, as presented in Fig.3.10.(left). It shows an original distribution of sizes, with two main behaviors:

- Roughly 10% of the clusters show up at $d_c/d_p = 1$, which corresponds to deposits made of single particles.

- Then, most clusters have a diameter of $4d_p$ or more. Since the number of particles per cluster goes in first approximation in d_c^3, these clusters contain hundreds of stuck particles. Therefore, they gather almost all the clogged particles.
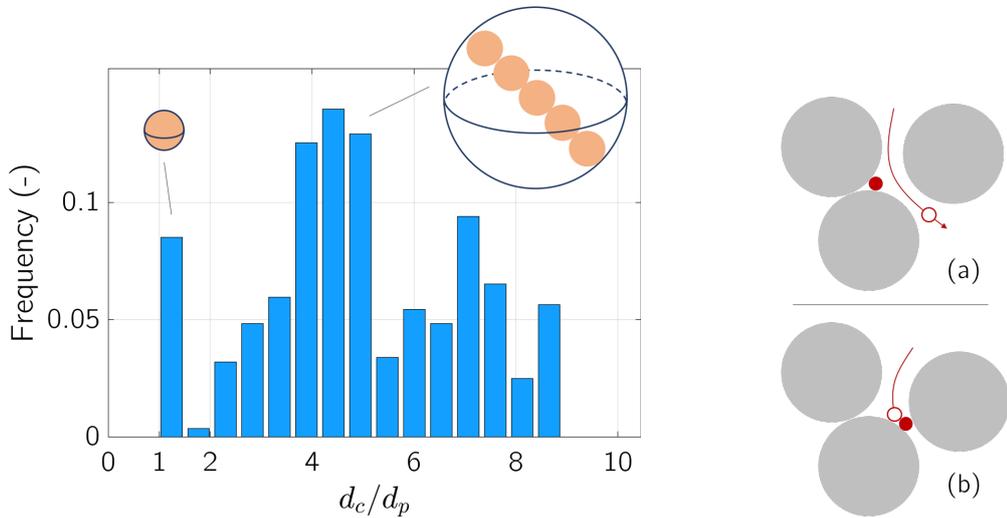

Figure 3.10: (left) Cluster size distribution from sample at $\mathcal{C} = 0.40$, $x \in [d_g; 4d_g]$. Peak at $d_c/d_p = 1$ highlights individually clogged particles; higher peaks denote large clusters.
(right) Illustrative scheme of how a clogged particle can induce or not further clogging.

This observation leads to a better description of the deposition mechanism. To begin with, the first particles block when they are dragged by the liquid through sufficiently

narrow pore throats. They partially fill the most probable inter-grains sites but do not likely alter significantly the flow through the porous medium, since fluid can still easily pass around the spherical shape of the clogged particles. Then, other particles therefore follow a similar path, arrive close to the blocked particles, which triggers two cases.

On the one hand, if the first deposited particle does not form a significant obstacle for following particles (see Fig.3.10, right, case (a)), it does not trigger further clogging events. This effect can explain the peak around 1 in the cluster size distribution.
On the other hand, if the first deposited particle forms a significant obstacle, following particles get stopped with a probability close to unity (see case (b)). This process goes on until the newly created cluster of particles reaches a size at which it is significantly affecting the flow, by loss of permeability. At the pore scale, it means most of the flux gets diverted to other pores. It also explains why the cluster size stopped growing, as it has reached its critical size.

3.2.2.2   Density of blocked particles

Let us confront these assumptions by looking at the evolution of NMR profiles over deposition. We consider a case where in-depth deposition is clearly visible: $\mathcal{C} = 0.66$. From the generic solid fraction ϕ_s, it would be interesting to get a better appreciation of the physical situation. For instance by knowing the solid volume of deposited particles in the 40% void space constituting the porous medium. To do so, we define the density of blocked particles n as the number N_b of blocked particles in a slice of elementary thickness (arbitrary), divided by the maximum number N of particles fitting in that slice. More precisely, the volume of blocked particles can be deduced from each NMR profile by subtracting the first profile (initial state, ϕ_s^0), according to:

$$\phi_s = \phi_s^0 + V_b / V_{tot}$$

$$V_b = \Delta\phi_s V_{tot}$$

With V_b the volume of blocked particles. Introducing V_p the volume of a single particle, the density of blocked particles writes:

$$n = \frac{N_b}{N} = \frac{V_b / V_p}{V_{max} / V_p} = \frac{V_{tot}}{V_{max}} \Delta\phi_s$$

Where V_{max} is the maximum volume of particles fitting in the pore space. It is equal to the void volume of the slice $(1 - \phi_s^0) V_{tot}$ multiplied by the solid fraction of the pack made of deposited particles ϕ_s^{dep}. The latter is calculated from μ-CT images (by comparing the area occupied by deposits to the area of the pore) at $\phi_s^{dep} = 0.50$. Hence the final expression:

$$n = \frac{\Delta\phi_s}{(1 - \phi_s^0)\phi_s^{dep}} \tag{3.1}$$

This density equals zero at initial time ($\phi_s = \phi_s^0$) and can reach unity if the gain in solid fraction $\Delta\phi_s$ goes to $(1 - \phi_s^0)\phi_s^{dep}$, i.e. 0.2. n is computed as a function of depth and shown in Fig.3.11 (left). The 13 first successive cycles of injection are presented to focus on in-depth deposition and neglect for now the impact of caking. From there, more injected particles lead to a higher density at all considered depths. The increase in density seems to be gradual and regular with the injections.

Note that the increase in density at depths below zero have to be treated with care. Their shape results from the subtraction between the profiles in the transition area between the pure fluid and the porous medium (see Fig.3.7, around $x = 0$). Since the solid fraction profiles are sharp in this region, more noise is introduced.
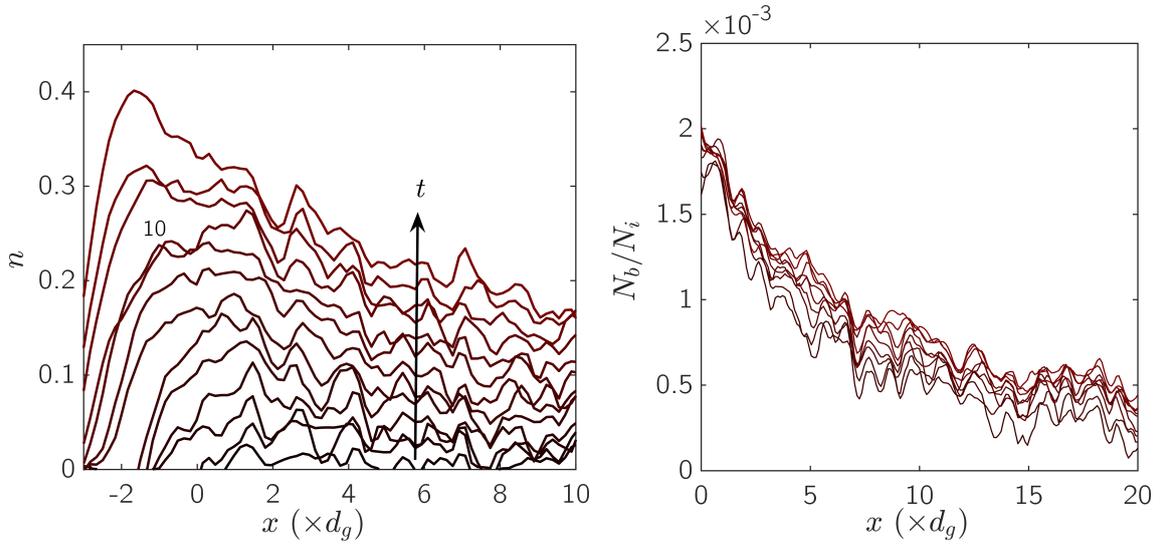
Figure 3.11: In-depth deposition dynamics for the 13 first cycles at $\mathcal{C}=$ 0.66. (left) Density of blocked particles versus depth; cycles go from bottom to top. (right) Number of blocked particles over number of injected particles versus depth for each cycle.

To better understand the evolution of the deposition over the injections, the number of blocked particles can also be rescaled by the number of injected particles since the beginning of the experiment. The result is presented in Fig.3.11 (right) and shows that all profiles collapse to a single master curve. It means that each new injection of particles leads to the same number of blocked particles. In other words, the density of blocked particles increases linearly with time and injections. This conclusion is valid (at least) until the last profile presented, that is until $n \approx 0.4$.

The fact that linearity can prevail even though such a high fraction of the system is filled with particles is surprising, since one can expect previously stopped particles to impact the deposition of arriving ones. On the opposite, our result shows that in this regime, particles go on discovering and populating new clogging sites regardless of the particles already clogged.

From μ-CT and NMR observations, we can state that clusters are essentially independent. They grow faster than our NMR time resolution, that is they are likely to go from initiation to saturation (i.e. reach the point where flow is deviated) between two successive injections. Consequently, the evolution of the blocked density that we are monitoring is essentially due to the creation of new clusters but is consistent with the mechanisms we inferred.

3.2.3 Caking dynamics

3.2.3.1 Cake initiation

In-depth clogging of particles happens until a critical situation where particles do not enter the porous medium anymore and start accumulating over the surface of the system. This moment corresponds to the initiation of the cake. To have a sense of this transition, the density profiles for all 30 cycles (and not only until the 13th) are shown in Fig.3.12, for the same example at $\mathcal{C} = 0.66$. From the regime described here-above, the deposition then changes drastically. In-depth ($x > 0$) profiles start superimposing, which means that the deposition inside the porous system becomes negligible. In addition, the profiles for $x < 0$ grow fast and form a peak way above the maximum density achieved in depth at $n = 0.9$, close to a completely caked surface.
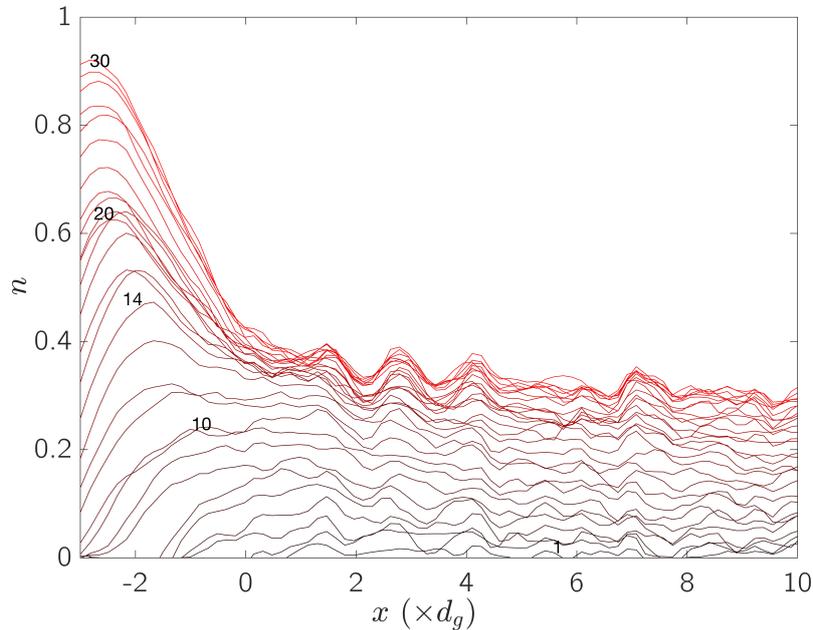

Figure 3.12: In-depth deposition and caking dynamics for the 30 cycles at $\mathcal{C} = 0.66$: density of blocked particles versus depth

The transition between predominant in-depth and surface deposition occurs for a value of n of the order of 0.4. This means accumulation diverges when a given number of clusters is created in a layer, and can be seen as a *percolation* effect. Before percolation,

flow paths are still available and in-depth clogging can still happen. At percolation, the density at the entrance reaches a value where particles are more likely to stack on top of each-other, which degenerates into a cake. Consequently, the porous medium near the entrance is never filled at more than 40% of its theoretical maximum capacity.

3.2.3.2 Cake description

The packing density of the cake is further characterized. From Fig.3.9, the solid fraction in the cake can be read directly by looking at the steady value reached above the porous medium: $\phi_s^{cake} = 0.52$ at $x = -3d_g$. An estimation can also be made by looking at the μ-CT images in the cake, visible on Fig.3.13. The solid fraction of the pack of particles is extracted by thresholding the image and measuring the surface fraction occupied by particles. The value found is $\phi_s^{cake} = 0.54$, slightly higher than the first estimation at 0.52 (likely due to the threshold value) but consistent with it. Moreover, these values are close to 0.50, as reported in the literature for loose non-vibrated random packs (see [Torquato 2002]). This value also is very similar to the one found in the deposited clusters ($\phi_s^{dep} = 0.50$), which is not surprising since the accumulation there is driven by the same physics despite the different geometry.

Note that these packs (cake and deposited clusters) show a density lower than the one achieved for the pack of grains by the pluviation method. Indeed, the particles are here more concentrated than the pluviated grains, therefore more likely to form bridges, which leads to more defects in the packing and a lower density.

This regime of dense surface accumulation is irreversible in the studied conditions. No case has been identified where further injection and accumulation of particles could modify enough the local pressures or velocities to generate un-clogging events.
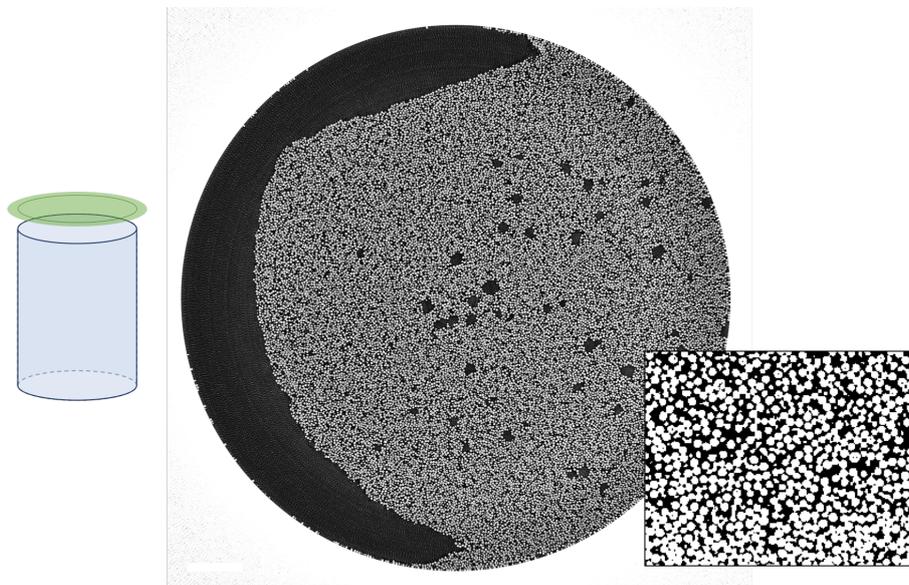
Figure 3.13: μ-CT view (2D yz cut) of the cake on top of the sample at $\mathcal{C} = 0.66$: particles appear in light gray. Void (air) appear in black, and show that at this height in the sample the cake forms a dome not filled the full width of the column. (insert) shows an example of thresholded (i.e. binarized) image used to calculate the solid fraction of the pack of particles.

3.3 Predicting clogging dynamics

3.3.1 Probabilistic approach

3.3.1.1 Description & parametrization

For modeling purposes, we represent the porous medium as successive identical layers of thickness e. For this thickness to be representative of the clogging events in the system, it seems natural that it is linked to the average pore size. As the average pore can be estimated as a fraction of the grain size, the value is fixed at $e = d_g/2$.

Overall, the linearity of the deposition dynamic in the in-depth regime confirmed that each particle entering a partially clogged layer will have the same probability to meet a free site in this layer (and the same probability to get stuck in it). This boils down to a constant probability p to stop in the layer and a constant probability $1 - p$ to progress to the next layer. Describing p as a constant value, whatever the position, can be further understood by considering that, on average, a particle either participates to the filling of a new cluster, or is deviated to the next layer.

3.3.1.2 Modeling

Now, let us define $f(i + 1)$ the probability for a particle to get stuck in the $(i + 1)^{th}$ layer. Naturally, the probability to clog on layer 2 is p times the probability to pass the 1st layer, $1 - p$: $f(2) = p(1 - p)$. More generally, the probability to clog in layer $i + 1$ depends on the passing the i first layers: $f(i + 1) = p \sum_{j=1}^{i} f(j)$, which rewrites as $f(i + 1) = pf(i)$. By recurrence, this results in the natural relation $f(i + 1) = p(1 - p)^i$. To the continuum limit, we define P the probability density function to get stuck at the depth x. The sum over depth writes $eP(x) = p(1 - \int_{0<u<x} P(u)du)$. The expression $\frac{p}{e} exp(-x\frac{p}{e})$ is proposed and we verify that it is indeed solution of the equation:

$$ 1 - \int_{0<u<x} \frac{p}{e} exp(-\frac{up}{e}) = 1 - \left[-exp(-\frac{up}{e}) \right]_0^x = exp(-\frac{xp}{e}) = \frac{e}{p}P^*(x) $$

This solution is held, hence the expression of $P(x)$:

$$ P(x) = \frac{p}{e} exp(-x\frac{p}{e}) \tag{3.2} $$

Equation 3.2 highlights a characteristic variable with the dimension of a distance: $\lambda = e/p$. It can be seen as an intrinsic penetration length, function of the porous structure and confinement ratio. Our model is therefore similar to previous filtration models where λ^{-1} is named the *filter coefficient* (see section 1.3). Despite this similarity, it is key to note that the present model takes into account both the clogging of the pore and the evolution of the flow path. While common filtration models assume a low

density of deposit (i.e. far from percolation), this appears to be valid up to large cluster concentrations for which a significant part of the medium is clogged.

Since expression 3.2 describes the probability of clogging as a function of depth, the number of particles blocked over depth is equal to the probability over each slice $eP(x)$ times the number of injected particles N_i. Hence the derivation of the density of blocked particles:

$$n = N_b/N = ePN_i/N$$

$$n(x) = p\frac{N_i}{N}exp(-x\frac{p}{e}) \tag{3.3}$$

Over depth, n has a maximum value reached at $x = 0$, at percolation just before the caking start. We note that value n_c. It is associated with the maximum number of particles that can be injected in the system, deduced from $n_c = pN_c/Nexp(0)$:

$$N_c = n_c N/p$$

This critical number of injected particles increases when p decreases and tends to infinity when $p \to 0$. It is consistent with the fact that particles with a infinitely small probability to clog will have a infinite penetration length (i.e. pass through the medium).

The evolution of n can also be clarified in terms of temporal dynamics. Since the experiment is not purely continuous in time (successive cycles of injection and imaging), a normalized time is defined as the ratio between the number of injected particles and the critical number of particles: $t = N_i/N_c$. Following this definition, the experiment ranges from $t = 0$ to $t = 1$ at percolation. Expression 3.3 then rewrites as 3.4. Interestingly, n increases linearly with time in this model, for any depth or clogging probability. That is in agreement with the experimental conclusions made on Fig.3.11: in-depth deposition repeats over time independently of the state of the system, until percolation.

$$n(x) = tp\frac{N_c}{N}exp(-x\frac{p}{e}) \tag{3.4}$$

Finally, the variations of n are computed and summed up in Fig.3.14 as a function of x, t, and p. Looking at a first value of probability (color mapped surface, $p = 0.2$), the previous conclusions are visible: critical value of n at $(x = 0, t = 1)$ and repeating exponential decay in depth for all times. As observed experimentally, for higher p values particles accumulate closer to the surface and percolation is reached for a smaller critical number of injected particles.
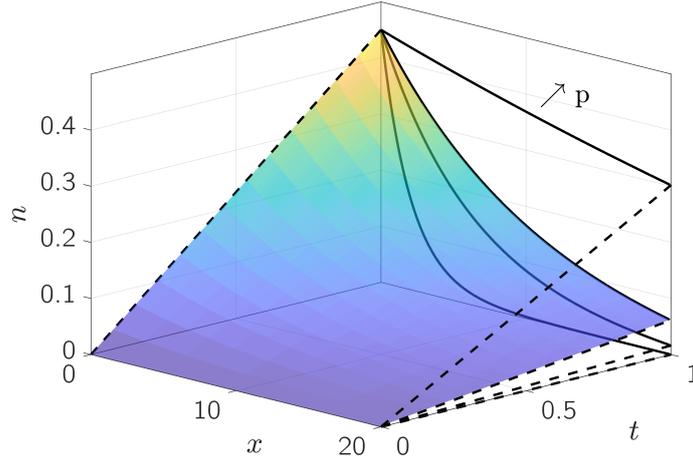
Figure 3.14: Computed density of blocked particles n as a function of depth and normalized time, for 4 values of p (from bottom to top): 0.5, 0.2, 0.1 and 0.02. Surface plot ($p = 0.1$) is color-coded in n. Dashed lines show the time evolution at $x = 2d_g$ and $x = 20d_g$. Plain line show final particle distribution over depth ($t = 1$).

3.3.2 Experimental validation

3.3.2.1 Data fit at high confinements

Let us now compare the model predictions with the NMR results presented in section 3.2. The only remaining unknown is the link between the clogging probability p and the confinement ratio $\mathcal{C}$. A high confinement is naturally related to a high probability of clogging, but no model relation has been proposed. Therefore, the experimental data (profiles over depth for various times) are fitted with our model by adjusting p.

In Fig.3.15, selected profiles at extreme depth and times are presented for 3 values of confinement. As mentioned before, a time rescaled by the time needed to reach percolation is introduced to compare experiments. To do so on our data set, the time of percolation / critical number of injected particles has to be known. It means that the rescaling can be done only for experiments where the clogging density n reaches n_c. In theory, n_c is reached for any confinement value if enough particles are injected. Still, experimental constraints (duration of the experiment) led to cases where n remains low at the end of our test (see Fig.3.5 for example, $\mathcal{C} = 0.40$). Therefore, model/data comparison is presented for higher values of $\mathcal{C}$: 0.56 (see crosses), 0.66 (see circles; same data as Fig.3.7) and 0.78 (see diamonds; same data as Fig.3.9).

The linearity of the deposition over time is confirmed for all values of confinement. Likewise, the predicted particle distribution in depth falls decently on the experimental points. Variations are visible between the modeled and data slopes but all trends are correctly caught.

A better understanding of the fits comes from a plot of the fitted p value for each value of $\mathcal{C}$ (see Fig.3.16). As expected, the clogging probability increases for increasing con-
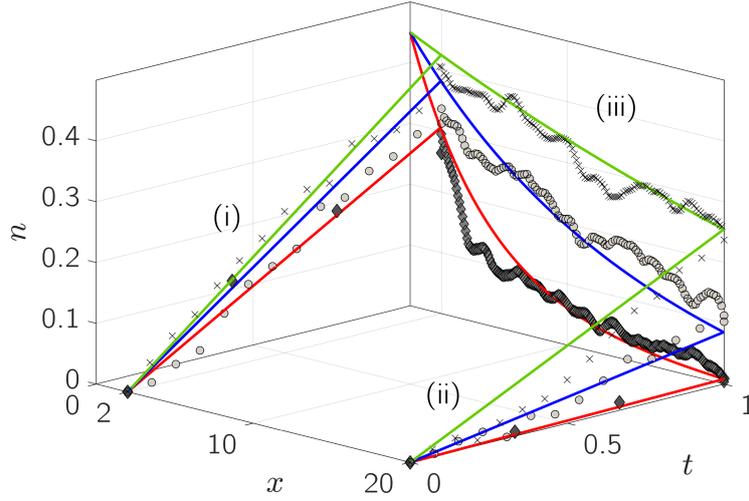
Figure 3.15: Experimental (markers) and model prediction trends (lines) of n versus depth and time. Three confinements are presented: $\mathcal{C} = 0.78$ (filled diamonds), $\mathcal{C} = 0.66$ (circles) and $\mathcal{C} = 0.56$ (crosses). (i,ii) Time evolutions at $x = 2d_g$ and $x = 20d_g$ respectively. (iii) Final particle distribution over depth ($t = 1$).

finement (see plain diamonds). More surprisingly, it follows a linear trend in logarithmic scale , which suggests a relation of type: $p(C) = exp(\alpha C + \beta)$ with α and β constants to define. At complete confinement, no particle is expected to enter the system hence a clogging probability of 1. From $p(\mathcal{C} = 1) = 1$ (see blue star), we deduce $\beta = -\alpha$ and Eq.3.5.

$$p(C) = exp(\alpha(C - 1)) \tag{3.5}$$

3.3.2.2 Predictions at all confinements

The resulting fitted model ($\alpha = 10.9$) follows the blue dashed line. It can be used to predict the clogging probability for any value of confinement, especially for cases where the critical number of injected particles could not be experimentally measured. Back to our example at $\mathcal{C} = 0.40$ (Fig.3.5), the model predicts a clogging probability $p = 1.1$ 10^{-3}. An estimation of the critical number of particles to inject to achieve percolation in this case is given by $N_c = n_c N / p$, as well as an estimation of the advancement reached at the end of the experiment $t = N_i / N_c$. Here, injection went on until $t = 0.35$, which means 200% more particles needed to be injected to reach percolation and initiation of the caking regime.

3.3.3 Conclusion & openings

The latter example illustrates how the knowledge of the confinement ratio of a system is enough to predict how many particles can be injected in the porous medium before complete clogging. That is a key information when trying to assess the efficiency or
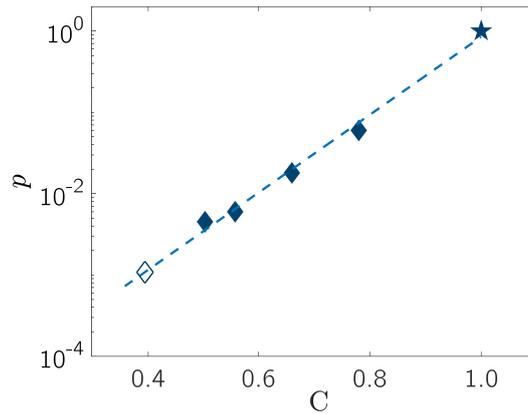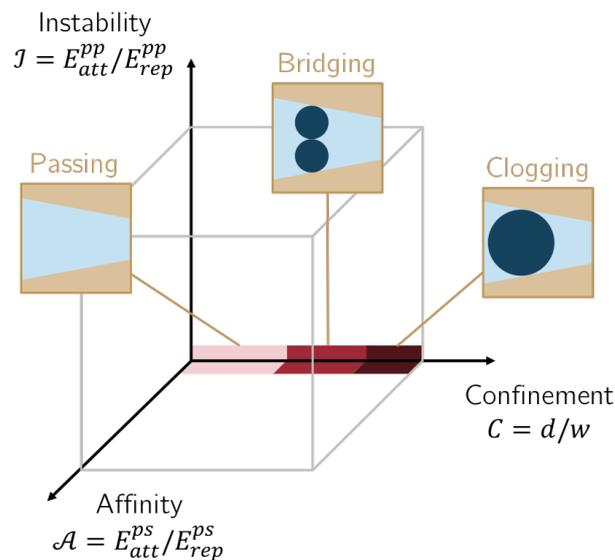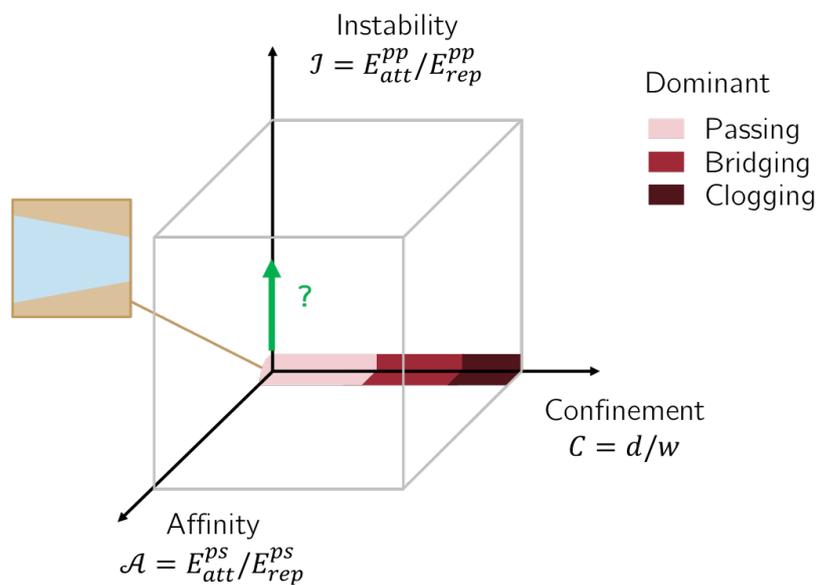
Figure 3.16: Clogging probability as a function of the confinement ratio. Filled diamonds are data points. The filled star shows the theoretical point of total clogging probability at maximum confinement. Empty diamond is extrapolated from exponential model (dashed line).

longevity of filtration systems for instance. Likewise, the penetration length λ, inversely proportional to the probability p, helps evaluating how deep a filtration system needs to be to capture particles. Overall, the main characteristics of such systems (dimensions of the medium, porosity, etc.) can be directly estimated from $\mathcal{C}$ and p. These results also provide insights on more complicated cases, like the competition between particles of different sizes (i.e. a system with a distribution of confinement ratios).

More generally, we explored in depth the behavior of non-interacting particles in variable confinement conditions. Two deposition mechanisms are identified and added on our phase diagram: geometrical stoppage by *bridging* and *clogging*. The study also validates that a confinement ratio given by the ratio between a particle size d and a pore size w, $\mathcal{C} = d/w$, is well suited for our description.

Transition : on particle aggregation

Instability
$$\mathcal{I} = E^{pp}_{att}/E^{pp}_{rep}$$

Dominant
- Passing
- Bridging
- Clogging

Confinement
$$C = d/w$$

Affinity
$$\mathcal{A} = E^{ps}_{att}/E^{ps}_{rep}$$

Back to the case of passive particles, at the origin of our diagram, the next natural question is: what behaviors arise when the stability of the suspended particles is challenged?

Chapter 4

Unstable particles at low confinement

The particles used here are much smaller than the pore size. With a size of the order of $d = 100$ nm in pores of approximately 10 μm, the confinement ratio is $\mathcal{C} = 10^{-2} \ll 1$. The particles are also chosen inert towards the surfaces of the porous system. The only particle-surface attractive interactions are the short-range Van der Waals forces, easily overcome by the drag in conditions of continuous flow. Therefore, $\mathcal{A} \rightarrow 0$.

Now about the parameter of interest, $\mathcal{I}$. To develop strong inter-particle attractive interactions, the usual option is to turn towards suspensions of charged colloidal particles that are not stable is specific conditions (see chapter 6). A second option is to use particles having a natural magnetization ensuring strong attraction as soon as particles approach each-other.

Indeed, we focus heree on ferric particles acting as magnetic dipoles attracting each-other in a common head-tail configuration. The related magnetic attraction potential reads (see [Phenrat, Saleh, et al. 2007]):

$$E_{mag}(d) = \frac{8\pi\mu_0 M_s^2 d_p^3}{9(\frac{d}{d_p} + 2)^3}$$

With μ_0 the magnetic permeability in the vacuum, M_s the specific magnetization of the material in Amperes per meter, d_p the particle diameter and d the distance from one surface at which the potential is evaluated. With $\mu_0 = 4\pi \times 10^{-7}$ Tm.A^{-1}, $M_s \approx 600$ kA.m^{-1} for the iron-based particles and $d \approx 100$ nm, the order of magnitude of E_{mag} at $s = 100$ nm is 10^{-17} J. This value is larger by two orders of magnitude than the standard Van der Waals energies, which means that magnetic forces are clearly dominant in this system. A illustration of this point is provided in Fig.4.1, where the attractive contribution between a particle and the surface Φ_{PS} (Van der Waals only) is seen negligible before the inter-particle magnetic attractive well Φ_{PP}.
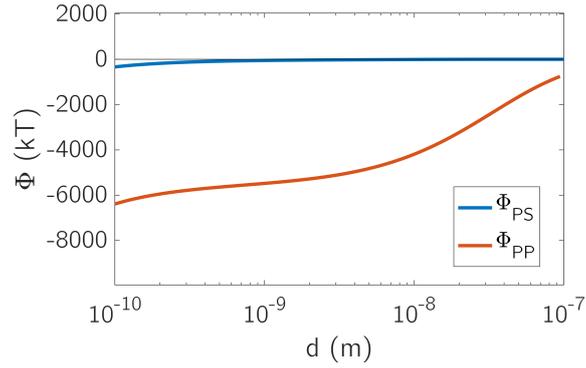
Figure 4.1: Particle-particle and particle-surface potentials in the case of magnetized particles ($M_s = 600$ kA.m^{-1}, $d = 10^{-9}$ m).

So far, only the mechanisms working for particle aggregation have been described. Let us now focus on the disruptive forces at play and first consider a straight large pore throat and laminar conditions.

There, two particles small before the pore and flowing close to each other follow streamlines a similar or equal velocity. Consequently, they are not subject to important velocity gradients and the drag force applied on the system of two particles is low. It writes $W_D = 6\pi\mu\Delta v d_p^2$, with Δv the velocity differential between the two particles, here tending to zero; hence $W_D \to 0$. It is the only force in this system susceptible to *de-stabilize* the particles by tearing them apart. Overall, attractive forces dominate by far and aggregation is likely: $\mathcal{I} \ll 1$.

Larger entities (clusters) can be formed, up to a point where they become of non-negligible size before the pore throats. Then, our conclusions on the drag work may not be valid anymore. The clusters are forced to evolve at a distance from each-other so that a non-negligible velocity differential appears between them, inducing shear when they happen to intercept one another. In the end, the growth of the clusters is limited by the energetic competition described by $\mathcal{I}$.

Because of these complex behaviors liked to the particle sizes, a direct observation of the particles is here essential to describe the situation. Moreover, aggregation is in itself a complex mechanism so the suspensions are studied in porous systems reduced to their simplest form: straight channels with controlled constrictions imitating pore throats.

4.1   Specific Material & methods

4.1.1   Suspensions of particles

4.1.1.1   nano-Zero Valent Iron particles

For this study, a very specific kind of particles are used: nano-Zero valent Iron particles (nZVI), as presented in chapter 2. They differ from the polystyrene spheres considered previously in many ways, but one property is here onf utmost importance: they are not engineered to be monodisperse model particles. Instead, their are made at industrial scales for efficiency purposes, in particular in the field of soil remediation. Therefore, their size distribution is not expected to be model at all. The point of this chapter is to use this heterogeneity of properties as a feature.

These particles are usually referred to as *nano*particles, even-though the order of magnitude of their size ranges from 1 to 10 μm. SEM images (see Fig.4.2) are useful to understand the several scales involved.

As produced industrially, single nZVI particles fall in the $[10 - 100]$ nm size range. They are composed of spherical iron particles, and less spherical iron oxides particles (see platelets on Fig.4.2.b). These particles are subject to strong attractive magnetic forces, hence a large instability in suspension. After sedimenting for example, aggregates are quickly formed: from just a few particles (see picture (d)) to micrometric clusters (see picture (c)). Even though the latter are more stable than single particles, they can still agglomerate in much larger (millimetric) structures when a large quantity of particles is left settling and dried; like for SEM imaging (see picture (a)).

Ideally, nZVI particles are stabilized to sub-micronic sizes when injected underground for remediation purposes, to ease their transport far in the soils. Still, their unstable nature make them strongly subject to clogging problems in the porosity of soils, which makes this study directly interesting to applied questions; in addition to the fundamental questions that they raise on the clogging of clusters.

4.1.1.2   Towards stable suspensions

The original nZVI aqueous solution (as provided by the supplier) is diluted to reduce the mean inter-particle distance and therefore the risk of aggregation. In addition, if aqueous conditions, the high density of the iron $\rho_{Fe} = 7.87$ g.cm^{-3} make the particle sediment quickly. We recall the settling velocity from section 1.3 $v_t = \Delta \rho g d_p^2 / 18\mu$, here estimated at ≈ 4 μm.s^{-1}. The height of the present pore is 20 μm, which means particles could sediment in just a few seconds.

For this reason, the dilution fluid used is glycerol ($\rho_{gly} = 1.26$ g.cm^{-3}, $\mu_{gly} = 1.4$ Pa.s). The difference in density with the iron is still important, but the high viscosity of glycerol drastically decreases the sedimentation of the particles. We now estimate v_t at
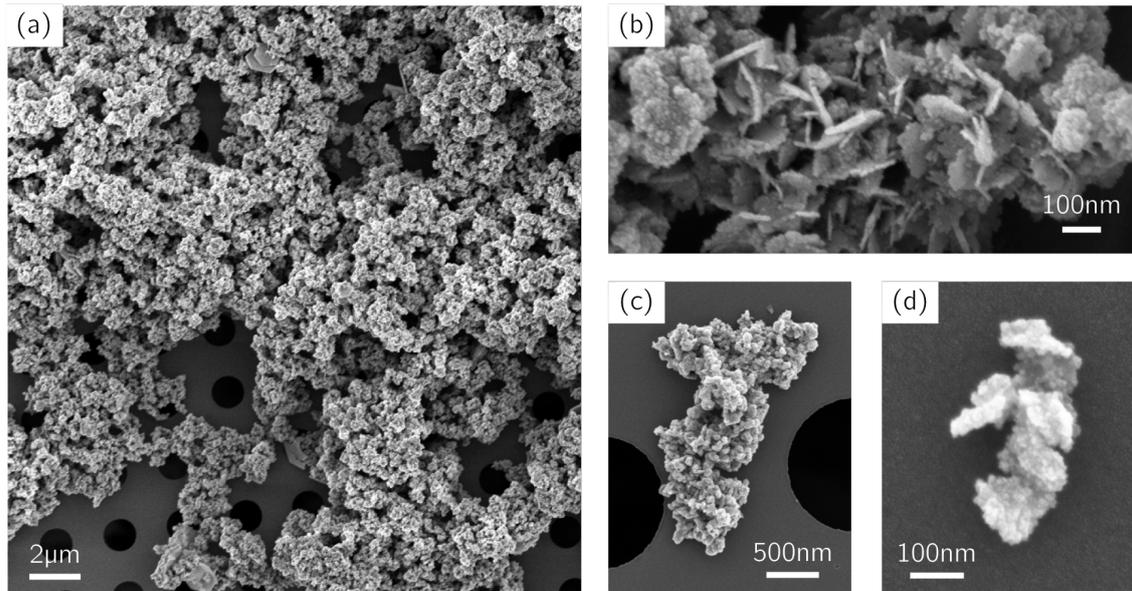
Figure 4.2: SEM imaging of sedimented nZVI particles, coated with a 2 nm Pt/Pd coating. (a) Portion of a large millimetric aggregate. (b) Closer view on the components of the aggregate: spherical bodies (iron particles) and platelets (likely iron oxides). (c,d) Micrometric and sub-micrometric clusters. Micronic dark circles are holes in the sample holder we used and are not relevant to the study.

3 nm.s^{-1}, a thousand times smaller that the previous value.

Because particles are initially in water, the resulting mix is of the order of 90 vol% glycerol and 10 vol% water+nZVI. All suspensions presented in the next sections are made using this mix as working fluid.

4.1.2 Experimental setup

4.1.2.1 Microfluidic channels & injection

As mentioned, the aim here is to focus on complex suspensions of attractive particles interacting with porous media reduced to a few pores. Microfluidic channels are made according to section 2.4.

The dimensions on the channels, and in particular of the constriction / spacing between obstacles are chosen so that the larger nZVI clusters have a significant change of clogging. Since nZVI clusters are expected of the order of 10 μm, the constrictions are made between 2 and 20 μm. Depending on the number of obstacles, the width of the channels varies between 100 and 400 μm. The height of the channels is imposed for all variations at 20 μm. This theoretical value can in practice vary of $\pm 20\%$ due to the making process.

Selected microfluidic devices are connected to a flow-rate driven pump set at $Q = 25$ nL.h^{-1}. For a reference rectangular channel of cross section $S = 100 \times 20 \ \mu m^2$, the estimated average flow velocity is $v = Q/S = 3.4 \ \mu$m.s^{-1}. Still, the flow-rate announced here is very close to the lower capacity of our pump and a significant (but repeatable) error is expected on the velocity value. Luckily, in any experiment, the real velocity can be computed directly from the videos and is therefore know at all times. This possibility also compensate the lack of precision in the channel's height.

Given the size of the channels, only a few microliters are needed per experiment. For for accuracy on the volume dispensed, a specific syringe is used: a 100 μL borosiliacte syringe by Hamilton (1.46 mm inner barrel diameter, model 710 N SYR).

4.1.2.2 Imaging

Two imaging techniques were used to observe the particles: confocal imaging to observe the particle deposition over long times (with a poor temporal resolution, $\approx$ 3 fps) and fast-camera imaging to follow the trajectories of particles over short times (thousands of fps). Refer to section 2.4 for details.

4.2 Single-pore clogging

By nature, the suspensions of particles that we consider here are complex. Their dynamics of transport and deposition are expected to be affected by a large number of parameters including the size, shape and concentration of the particles. To better understand the effect of each parameter separately, let us before hand treat a few simpler theoretical cases.

4.2.1 Towards suspensions of aggregates

4.2.1.1 Elementary particles

To begin with, we consider the theoretical case of a suspension of elementary (nZVI for instance) particles only. They form a model distribution of monodisperse particles with a unique characteristic size d, and flow towards a single pore of size w. In accordance with our previous results, the confinement ratio $\mathcal{C} = d/w$ plays here a major role. The outcome of this particle trying to pass through the pore is obvious:

- $d/w < 1$ leads to passing: all particles pass the pore.

- $d/w \to 1$ defines an intermediate case where several particles reaching the pore in the same time can bridge. The likeliness of such event decays with decreasing particle size, and increases with particle concentration.

- $d/w > 1$ leads to clogging: any arriving particles gets geometrically stuck and the suspension instantly cakes upstream of the pore.

Theses cases are illustrated in Fig.4.3.(a), (b) and (c) respectively. Overall, the outcome of a monodisperse suspension passing through a single pore is completely predictable and driven by $\mathcal{C}$. The same remains valid for any arrangement of pores with the same unique size. If one pore clogs, they all do, and vise-versa.
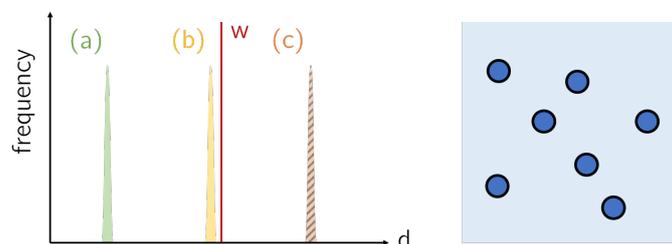
Figure 4.3: Schematic particle size distributions compared to a single pore size w. The distributions are narrow around a single value d (i.e. monodisperse): (a) $d < w$, (b) $d \to w$, (c) $d > w$.

4.2.1.2   Ideal distribution of clusters

We consider now that the elementary particles are suspended in conditions such that they can get close to each-other, which triggers aggregation. Depending on the concentration, solvent and driving forces (diffusion, flow, etc.), clusters of elementary particles are created, so that a distribution of sizes appears in suspension. This is still a theoretical case, and we consider all clusters spherical and described by a unique characteristic dimension (their diameter) d.

The outcomes function of $\mathcal{C}$ (passing, bridging, clogging) still apply, but they are now a matter of probability since the pore can either clog or stay open depending on the size of the particle arriving at it first.

Let us consider that the distribution of cluster sizes follows a normal law, with an average cluster size d_{av} and a standard deviation σ. The shape of the cluster sizes distribution is given by

$$f(d) = \frac{1}{\sqrt{2\pi}\sigma} exp\left(\frac{-(d - d_{av})^2}{2\sigma^2}\right)$$

We fix the value of a unique pore size w. From the basic properties of the normal distribution, the fraction of particles bigger than w is:

$$\theta = \frac{1}{2} erfc\left(\frac{w - d_{av}}{\sqrt{2}\sigma}\right)$$

With $erfc$ the complementary error function. It means that there is a probability θ that a cluster picked randomly in the distribution is larger than the pore and clogs. From there, the question of interest is: can we predict the clogging probability and conditions of this system? To answer this point, p is introduced as the probability for the pore to be clogged after N randomly picked particles tried to pass it:

$$p(N, \theta) = \sum_{k=1}^{N} \theta(1 - \theta)^{k-1} = 1 - (1 - \theta)^N$$

If all clusters are larger than the pore size (i.e $\theta = 1$; see Fig.4.4.c), the system will be automatically clogged after the passage of 1 particle ($p(1) = 1$). If, for instance, half of the distribution is larger than the pore size (i.e. $w = d_{av}$; see (b)), $\theta = 0.5$ and the system has a 50% chance of clogging at the first particle passing. After the attempts of 10 particles, this probability rises to 99.9%.

Note than similar results can be derived for log-normal distributions of spherical clusters, which tend to be more realistic for real suspensions of clusters (large clusters tend to be less represented than small ones; see after). Beyond the mathematical formalism and the simple example of a normal distribution, the point here is simply to show that single pore clogging remains fully predictable for known suspensions of
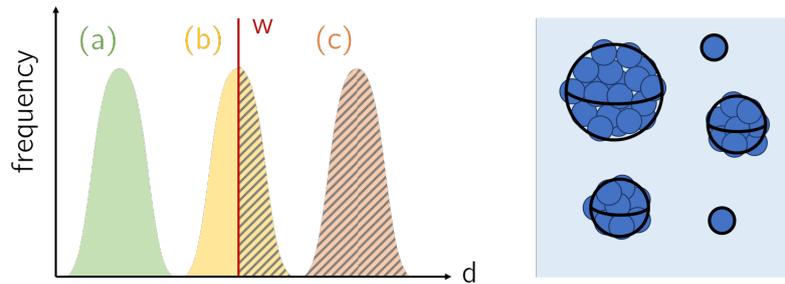
Figure 4.4: Schematic particle size distributions compared to a single pore size w. The distributions are large around a mean value (i.e. polydisperse in size): (a) all particles $< w$, (b) some particles $< w$, (c) all particles $> w$.

spherical clusters.

4.2.2   Clogging of suspensions polydisperse in shape

4.2.2.1   Suspension characterization

In addition to polydispersity in size, let us now consider that the clusters arriving in front of the single pore also have non-spherical shapes. It implies that the clusters have non-equal dimensions and therefore a main axis and an orientation. Compared to the previous case this orientation is an additional unknown variable, which makes a simple predictive model more complex to build. Instead, we propose to get back to an experimental study and use the nZVI particles, which size distribution fulfill those criteria.

Indeed, the coexistence in suspension of *elementary* nZVI particles (roughly 1 μm^3 in volume) and much larger clusters creates a broad distribution of sizes. Of course, the exact distribution strongly depends on the mixing procedure applied to the suspension. If the aggregates are torn apart enough (sonication, high-shear mixing), they break down into smaller aggregates. On the opposite, if no shear is applied and particles gather (by sedimenting for instance), much larger clusters can be formed. To get a sense of the particle sizes, we look under a microscope at a dilute suspension of nZVI particles settled on a glass cover (see Fig.4.5). The mixing procedure applied here is 30 minutes sonication and 2 minutes high-shear mixing.

The stretch in particle sizes and shapes is striking. Selected examples highlighted in Fig.4.5.b. show particles ranging from $1\mu m^2$ to nearly $700\mu m^2$ in projected area. Their projected aspect ratio AR (a standard measure defined as the larger visible dimension of the body divided by the smaller visible dimension) ranges from 1 to nearly 5. It is here critical to note that on all views presented in this section, only two out of three dimensions of the particles are visible, hence the notions of *projected* areas and AR.

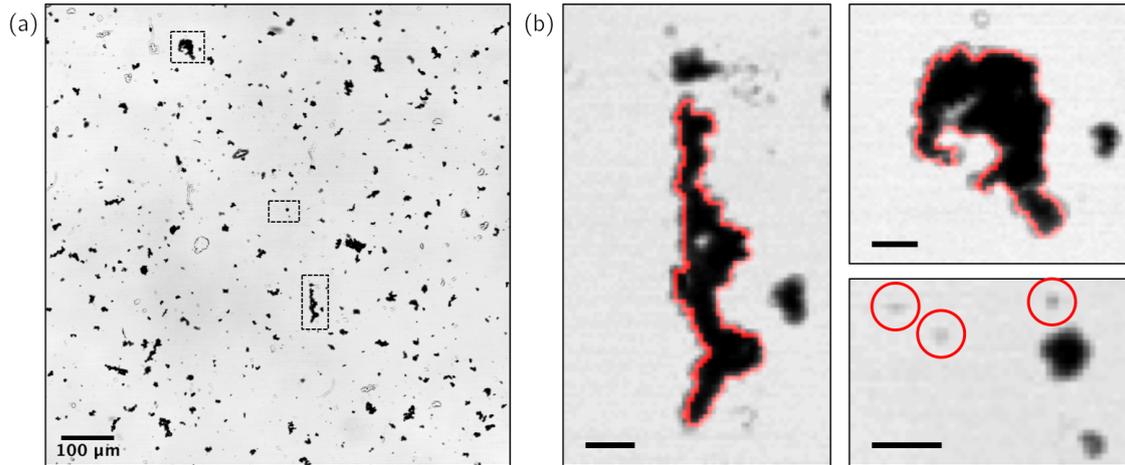These particles have a given size distribution when observed in static conditions like

Figure 4.5: (a) Microscope imaging of a suspension of nZVI particles settled on a glass slide. Particles appear in black. (b) Focused views on selected particles (from rectangular selections in (a)). The longest particle has a projected surface of 496 μm^2 and an aspect ratio $AR =$ 4.66 (longest dimension to the shortest; from red contour). The largest one is 672 μm^2, with $AR = 1.59$. The 3 small circled particles are roughly 1 μm^2, with $AR \approx 1$. Scale bars are 10 μm.

here. Still, their size distribution when observed dynamically (i.e. when being transported in fluid) is more relevant. The two distributions are not identical for several reasons. First, the clusters can flatten (deform) when settling, which increases their projected size. Most importantly, the particles are made of numerous elementary particles able to move or rotate around each-other. It gives the clusters flexibility and the ability to adopt different conformations depending on their environment. It is natural to expect that in flow conditions, clusters will tend to curl on them-selves to reduce drag forces. As a consequence, particles with smaller aspect ratios are expected to be seen in-flow (see section 4.3 for validation).

The assumption is verified by injecting the same suspension in a 100×20 μm^2 channel (length considered infinite), observed by microscopy (see Fig.4.6, left). As before, an estimation of the size and shape of each particle is made by measuring its area and aspect ratio AR. The distributions of AR, A and AR versus A are computed for more than 3000 particles and provided in Fig.4.6 (right). The frames used for this analysis are extracted from the main movies at a time interval insuring that a given particle is not counted twice.

Under these conditions, the average area is 18 μm^2, with 50% of the particles smaller than 7 μm^2 and 90% smaller than 39 μm^2. Since most particles are small and very large particles are rare, the distribution could be described as log-normal. About the aspect ratio: most particles show an AR close to unity ($\in [1 - 1.5]$). 20% of them really appear non-spherical with an aspect ratio above 2. From the 2D distribution, area and
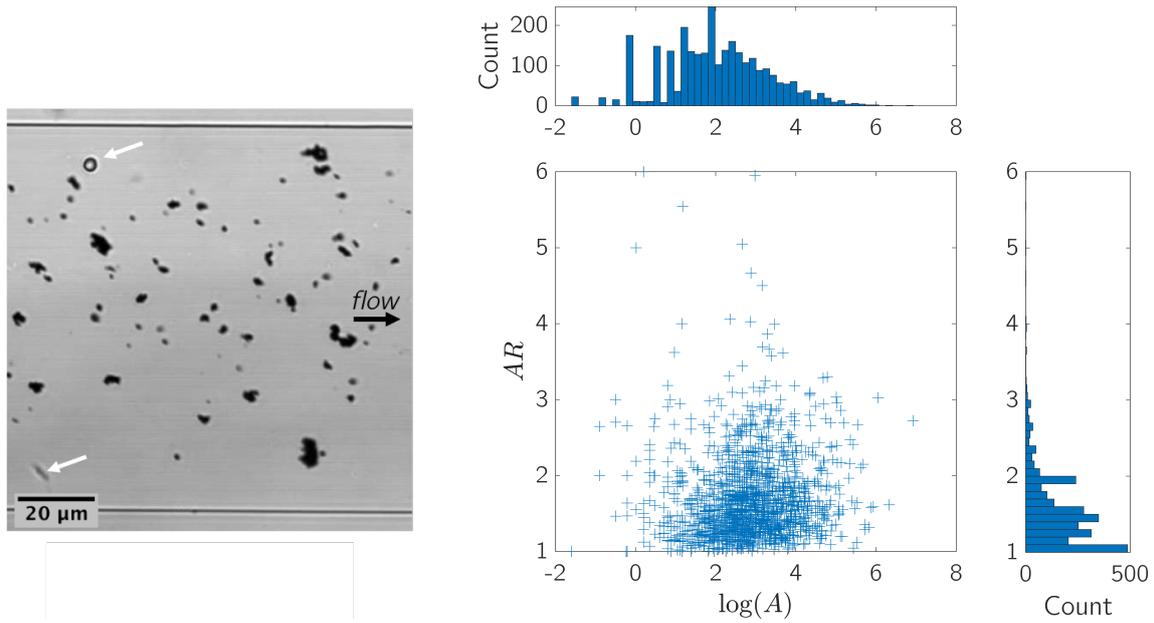
Figure 4.6: (left) nZVI particles flowing in a straight rectangular channel ($20\mu m$ in height), between the two horizontal black lines. Objects pointed by white arrows are fixed on the channel bottom and do not participate to the flow. (right) 2D distribution of the projected aspect ratio versus the projected area. Each marker is a measured particle.

aspect ratio do not seem correlated. It means that small particles can be elongated, while large ones can be spherical. This is not surprising given the many conformations the elementary particles can take. As expected, this distribution is significantly different from the previous one: both maximal area and maximal AR are much lower than before.

4.2.2.2 Flow towards constrictions

Let us now observe these particles in a channel with confined areas. Fig.4.7 shows the example of particles flowing towards four constrictions ($w = 6.0$ μm) in a 100 μm wide channel. Note that all presented particles have a dimension equal or larger to w. Several interesting conclusions can be made:

- In the straight part of the channel, all particles flow straight, following the expected streamlines. Still, their shape and size evolve slightly: they rotate on themselves around various axes. This is especially visible for particles with a large AR like (d), which seems to rotate along the y axis.

- When approaching the constrictions, particles follow a curved trajectories towards the closest opening, which is also expected from the streamlines.

- Then, particles pass or clog depending on their size and orientation. Among the particles appearing significantly larger than w, some clog (see (a)) and some find a way to pass (see (d)).
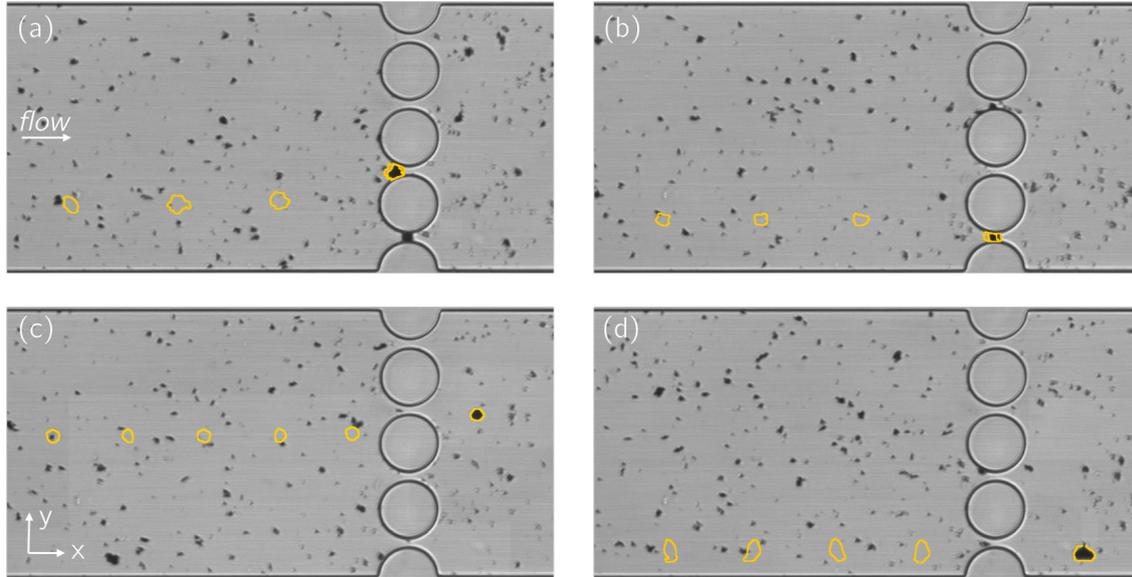
103

Figure 4.7: $100\mu m$ wide channel with 4 pores ($w = 6.0\mu m$; spacing between 2 pillars). Superposition of 5 successive positions (orange contours, $303ms$ between each) of 4 particles appearing larger than the pores. (a,b) Clogging particles. (c,d) Passing particles.

The ideal at this point is to build a better comparison between the particle and pores sizes, through confinement ratios. The following assumption is made: on these projected 2D views, any particle can be approximated by an ellipse and described by a minor and major axis. If a is the major axis and b the minor axis, $a > b$ by definition. The aspect ratio of the particle is $AR = a/b$ and its area $A = ab$. Naturally:

$$a = \sqrt{A * AR}$$
$$b = \sqrt{A/AR}$$

From there, it is interesting to see the previous 2D (see Fig.4.6) as a distribution of b versus a. More precisely, the confinement ratios $\mathcal{C}_a = a/w$ and $\mathcal{C}_b = b/w$ are defined and used (see Fig.4.8). Again, interesting conclusions arise:

- By definition, no particle can fill the $b > a$ region (see dark plain line).

- The further from the $a = b$ line, the higher the aspect ratio $AR = a/b$. This view confirms that, whatever the particle size, the maximum aspect ratio reached in the suspension is constant around 3. In other words, no particle is detected in under a line a slope $1/3$.

- A majority of particles fall in the $(a/w < 1 \cap b/w < 1)$ region: 80% of them more precisely. Since both visible dimensions are smaller than the pore, and despite the lack of information on the last dimension, a large probability of passing is expected.

104

- The remaining 20% have either one or two visible dimensions larger than the pore: $(a/w \geq 1 \cap b/w < 1)$ and $(a/w \geq 1 \cap b/w \geq 1)$. These are expected to clog with a fairly high probability.
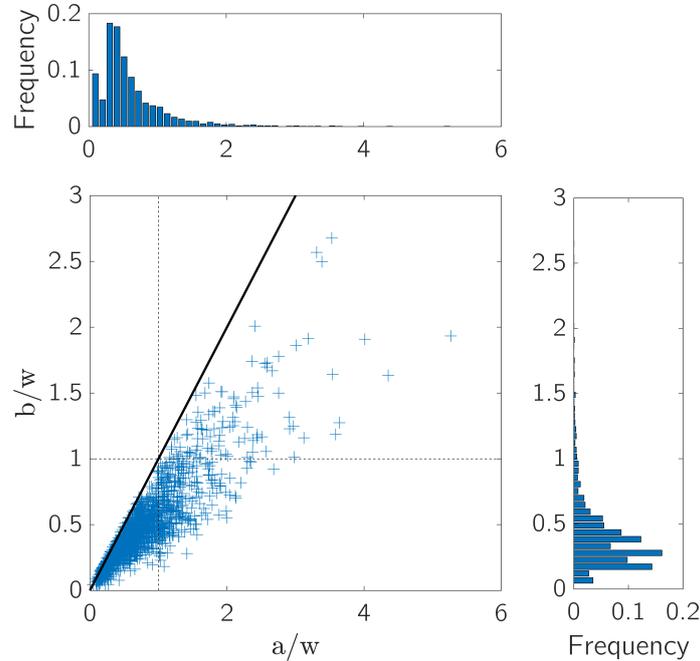

Figure 4.8: 2D distribution of the major and minor axis. Each cross is a measured particle; and separate 1D distribution for each.

4.2.2.3 Clogging efficiency

Now, clogging or passing events can be compared to the size of the particles via a and b. A mapping of the ≈ 3000 events is provided in Fig.4.9. On the map, the outcomes gather in three surprisingly well divided regions:

(A) For $(a/w < 1 \cap b/w < 1)$, all particles pass the pore. It is logical since no visible dimension exceeds w, with one additional information: none of these particles have a third dimension (c) large enough to question the conclusion of passing or clogging.

(B) For $(a/w \geq 1 \cap b/w < 1)$, 98% of the particles also pass and the 2% clogging are right at the border with the next region. This result is unexpected since all these particles have (at least) one dimension larger than w. It means that this larger dimension is far from critical for clogging.

(C) For $(a/w \geq 1 \cap b/w \geq 1)$, the results are more contrasted: 50% of the tracked particles clog. It is not possible to identify a sub-region where passing is predominant over clogging, or vis versa. This tends to show that beyond the definition
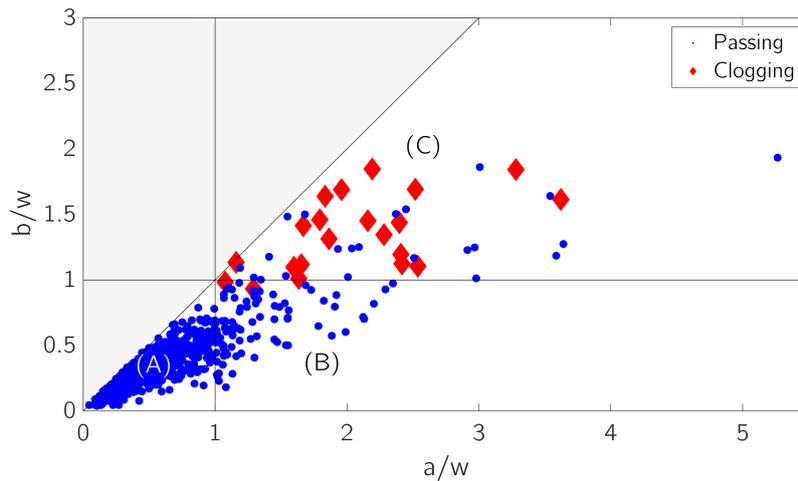
Figure 4.9: Mapping of the passing (blue dots) or clogging (red diamonds) particles as a function of minor and major axes confinement. Light gray area is excluded by definition.

of this region ($b/w \geq 1$), the sizes have no particular effect on the clogging probability.

These results raise fundamental questions on the mechanisms leading to the passage or clogging of non-spherical particles. Even-though these questions are at this point unanswered, it is already interesting to note that the knowledge of the shape distribution of a suspension can be enough to estimate a clogging probability per domain of the distribution.

Let us now focus on the mechanisms leading to these surprising domains, and more precisely on the characteristics of the flow surrounding the suspended clusters.

4.3   Clogging & anti-clogging mechanisms

4.3.1   Preferential orientation

4.3.1.1   Case of clusters with one large dimension

A first phenomenon helping particles to pass while having dimensions larger than the pore is their change in orientation when approaching the constriction. Fig.4.10 (top) presents a telling example of such mechanism. From high-speed imaging, relevant frames (on average 1 out of 500) are extracted to follow a large particle over time. The trajectory of the particle mostly follows a streamline but the orientation of the particle varies over time. Interestingly, the shape taken by the particles are sometimes clearly incompatible with a passage event (i.e. the visible projection is too large to pass the pore). At the constriction point, the visible size of the particle is just slightly smaller than the pore.
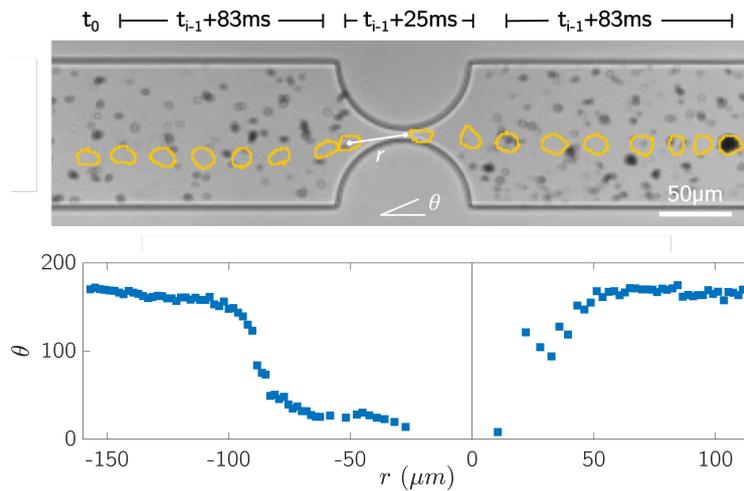
Figure 4.10: (top) Successive positions of a particle (orange) flowing from left to right, superposed to the frame showing the particle at its latest position. (bottom) Orientation of the particle as a function of the distance r between the centroid of the particle and the center of the constriction.

To better see the effect of orientation, the angle θ of the particle with regards to the horizontal axis is computed. It is plotted as a function of the distance of the centroid of the particle to the center of the constriction (see Fig.4.10, bottom). The effect is clear: the particle starts from a position oriented in the flow direction, rotates to pass the pore, and rotates again after passage. The rotation aligned the smaller dimension of the particle with the confined dimension of the pore, which explains the passage.

In the region where particles have one visible dimension larger than w, roughly 100% of the particles passed. We can therefore suppose that this mechanism is a general

mechanism for particle showing a dimension larger than w.

4.3.1.2 Case of clusters with two large dimensions

Now, let us look at the case of clusters with two out of three dimensions larger than the pore. Fig.4.11 and Fig.4.12 show respectively two clusters of this kind, one clogging and one passing. The two clusters seem to share very similar sizes and shapes (two similar dimensions, larger than the third one) but face different outcomes.
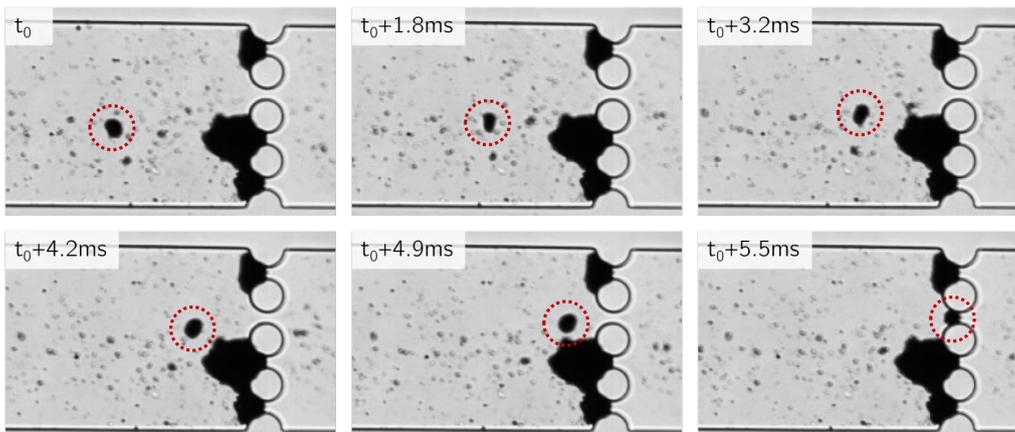

Figure 4.11: Cluster with two dimensions larger than a (8 μm) pore, at 6 successive times; clogging the pore.
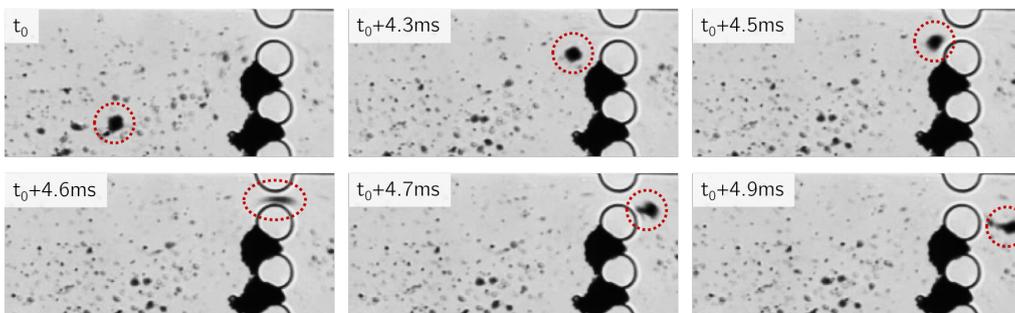
Figure 4.12: Cluster with two dimensions larger than a (8 μm) pore, at 6 successive times; passing through the pore by reorientation.

In the first example (Fig.4.11), the large "flat" cluster initially in the xy plane rotates on itself far from the constriction, which allows to observe its third dimension smaller then the pore size. Still, when approaching the obstacle, the cluster rotates back to its orientation parallel to the channel and fails to pass.
In the second example (Fig.4.11), the cluster stays flat when approaching the constriction before suddenly rotating and passing the pore. At passage, the third dimension much smaller than the pore is visible.

Together, these two examples show the complexity of the clogging conditions in that case. It can partially explain that in the $(a/w \geq 1 \cap b/w \geq 1)$ domain, passing and clogging events co-occur. To go further, it is interesting to highlight that the instantaneous particle reorientation, and therefore its passing or clogging, is likely strongly dependent of the local flow conditions imposed by the particle and channel geometries.

4.3.1.3   Shear impact on cluster orientation

To ease the understanding of the flow around the complex shapes of the clusters, a simple description is introduced. Each particle is approximated by a 3D box of ordered dimensions a, b, and c. A random particle with $a \neq b \neq c$ is then seen as a common rectangular parallelepiped. The following additional assumption is made: each particle has a shape falling in one of the three categories listed in Table 4.1.

Dimensions	Description
$a \approx b \approx c$	cube
$a \approx b > c$	sheet
$a > b \approx c$	rod

Table 4.1: Common shapes best describing boxes of dimensions a, b and c in various conditions.

The case of a cubical cluster (a fortiori spherical) is easy to treat, since it can be described using a unique characteristic dimension. If this dimension is smaller / respectively larger than w, the cluster passes / clogs.

To better visualize the two other cases, illustrations of relevant views are presented in Fig.4.13. Before all, the distribution of velocities in the considered geometry needs to be precised. Since the laminarity of the flow was proved previously, we assume a Poiseuille flow at the two most interesting locations in the system: in the straight section of the channel (far from the constriction) and at the constriction. In the straight part, the clusters are of negligible size before the width of the channel, but not before its height. Consequently, the shear rate $\dot{\gamma}_z$ in the z direction is more important than the shear rates in the x and y directions. At the constriction, the situation is reversed due to the geometry of the pore: the shear $\dot{\gamma}_y$ along y is greater. Now, we can easily assume that a cluster subject to uniaxial shear will tend to rotate to minimize it. Fig.4.13 illustrates this principle.

A rod-like body with a single dimension larger than w is first considered. It has a greater probability to have its larger axis in the x or y direction to minimize $\dot{\gamma}_z$. Then:

- From configuration (a_1), the passage of the rod is favorable and does not require any rotation. No common hydrodynamic effect is expected to induce its rotations to a clogging position.
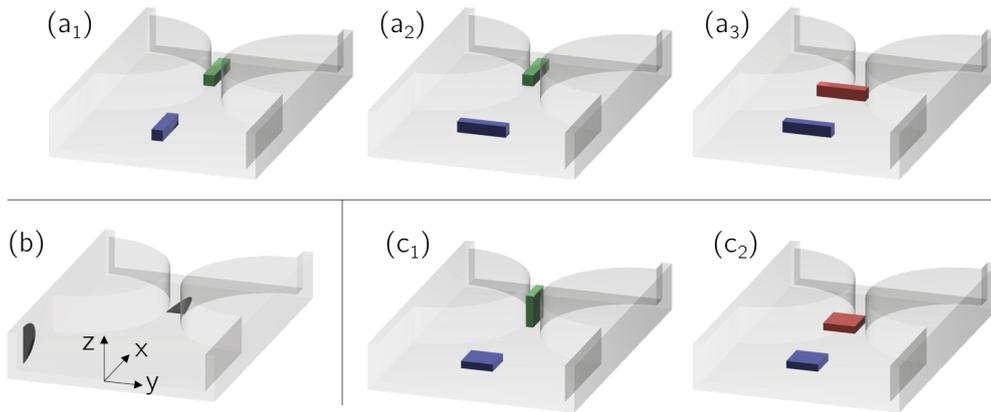
Figure 4.13: Illustration of the favorable conformations of a rod (a) and a sheet (c) in the channel geometry considered experimentally. Blue bodies show positions in the channel; green show bodies passing the pore; red show clogging bodies. (b) illustrates the axes system and the theoretical shapes of the velocity profiles along z in the straight part of the channel and along y at the constriction. Flow goes in the x direction.

• From configuration (a_2), a rotation along the z axis is needed for the rod to pass. Such event is likely, since the largest side of the body remains in the xy plane and it minimizes $\dot{\gamma}_y$ at the constriction. This is especially true since, at the approach of the constriction, the transition between maximum $\dot{\gamma}_z$ and $\dot{\gamma}_y$ is gradual as the channel shrinks along y.

• Overall, all favorable configurations in the straight channel are likely to lead to a passage event.

Moving to a sheet-like body with two dimensions larger than w, a single position minimize $\dot{\gamma}_z$: flat in the xy plane.

• From this configuration, the cluster can first keep minimizing $\dot{\gamma}_z$ and end up clogging the pore (see (c_2)).

• Or, the cluster can follow the gradual transition in maximum shear at the constriction and pass (see (c_1)).

• Overall, all favorable configurations in the straight channel can lead to a passage event, but at the cost of rotation conditioned by the competition between local shear rates.

Even-though this interpretation remains conceptual, it is natural and tends to validate the experimental findings. For rod-like bodies, all favorable configurations lead to a passing cluster. This tends to explain the passing-rate of roughly 100% in the domain

$(a/w \geq 1 \cap b/w < 1)$ of our previous diagram (see Fig.4.9). For sheet-like bodies, passing/clogging are both likely; hence a contrasted clogging probability in the domain $(a/w \geq 1 \cap b/w \geq 1)$.

Note that an important assumption made to draw this comparison with the experimental results is that (i) a cluster measured as having a single dimension a larger than the pore (apparent flat rod with $a > b$ on the images) has indeed a third dimension c comparable to b; (ii) similarly a cluster measured as having two dimensions $a \approx b$ larger than the pore has a smaller third dimension. In other words, the assumption is that the clusters tend to flow "flat" and minimize $\dot\gamma_z$.

This assumption is confronted to the many experimental observations. In a large majority of cases, a particle with two similar large dimensions seems to stay flat. Still, since it is not rotating, its third dimension is not visible and cannot be proved to be smaller than the two others. Luckily, a fraction of these clusters pass the pore (see Fig.4.12 for instance); which means the third dimension was indeed smaller for them, and that they were flowing flat in the xy axis, validating our assumption.

4.3.2   Cluster disintegration

4.3.2.1   Observations

Re-orientation was introduced as a first phenomenon leading to the passage of particles having dimensions larger than the pore. A second interesting mechanism has the same effect: the desegregation of clusters when passing constrictions.

From Fig.4.14, the effect is made clear on the example of a cluster with a particularly anisotropic shape. The cluster is first seen as a single body far from the pore (see (A)). Then, as it enters the constriction, the head of the cluster (i.e. the upstream part) detaches from the tail (see (B)). While the head passes the pore as a whole, the tail again spreads in at least three separate smaller bodies (see (C)).

The cartoon in Fig.4.14 proposes an explanation of this phenomenon. Before the pore, the upstream and the downstream parts of the cluster have a significantly different width, roughly by a factor of 2. In the straight channel, this has no impact since all parts of the clusters are subjects to the same velocity and drag. That is not true anymore when approaching the constriction: as the head is more central in the expected parabolic Poiseuille flow, it tends to accelerate more than the tail. The resulting shear is enough to break the bond between the two parts, and the head flows ahead (see (ii)).
Then, during the passage of the pore, the tail rearranges to reduce the drag applied on it (see (iii)). What happens next is not exactly visible but can be inferred from the same principle as before the constriction. Indeed, the sub-parts of the tail located closer to the center of the pore are subject to a greater velocity than the others sub-parts, and
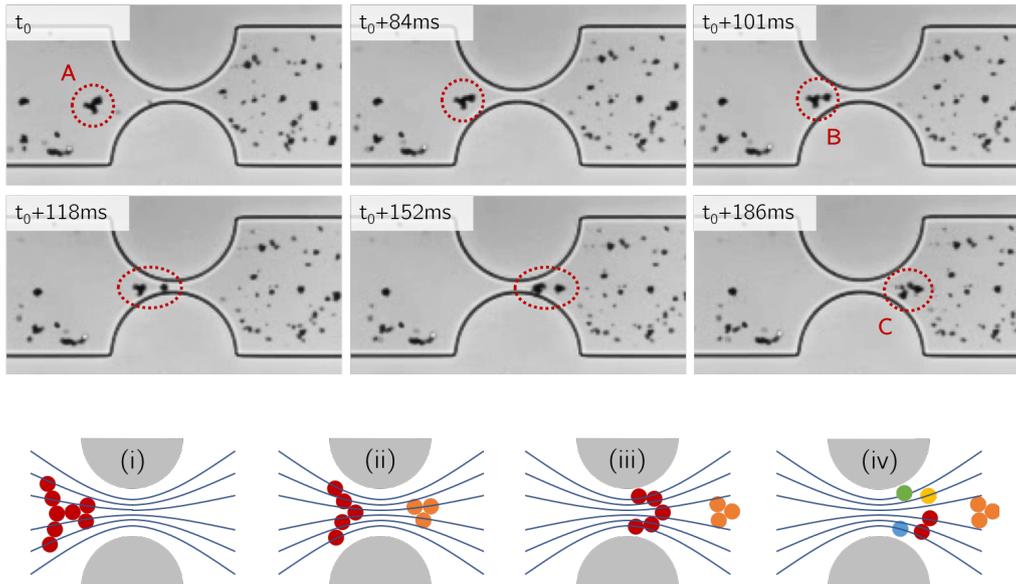
Figure 4.14: (top) Anisotrope cluster passing through a constriction, at six successive times. Flow goes from left to right. A: cluster as a single body, B: two parts separating, C: downstream part separating in several sub-parts. (bottom) Illustration of the mechanisms leading to progressive disintegration.

this velocity difference can again create shear conditions enough to break their bonds (see (iv)).

One can now wonder why this effect has not been observed for the large clusters previously presented. A plausible answer comes from the density of the clusters, in terms of packing of the elementary nZVI particles. In all previous examples, the clusters appeared filled and smooth, which is representative of a dense packing. As more density is also synonym of more cohesive bonds between elementary particles the conditions for these clusters to loose their integrity were never met experimentally. On the contrary, in loose clusters, elementary particles only form a limited number of bonds, which explains their tendency to desegregate. This principle is visually validated on other examples of disintegrating clusters, like the ones presented in Fig.4.15.

4.3.2.2 Further characterization

An easy estimation of the density of 2D shapes is the *circularity C* and its inverse commonly called the *compactness K* . They write:

$$C = K^{-1} = \frac{4\pi * \text{area}}{\text{perimeter}^2}$$

On the examples of Fig.4.15, $C = 0.38$ and 0.37 respectively. In comparison, the cluster on Fig.4.11) has a circularity of 0.89. Despite this significant gap, this measure is not
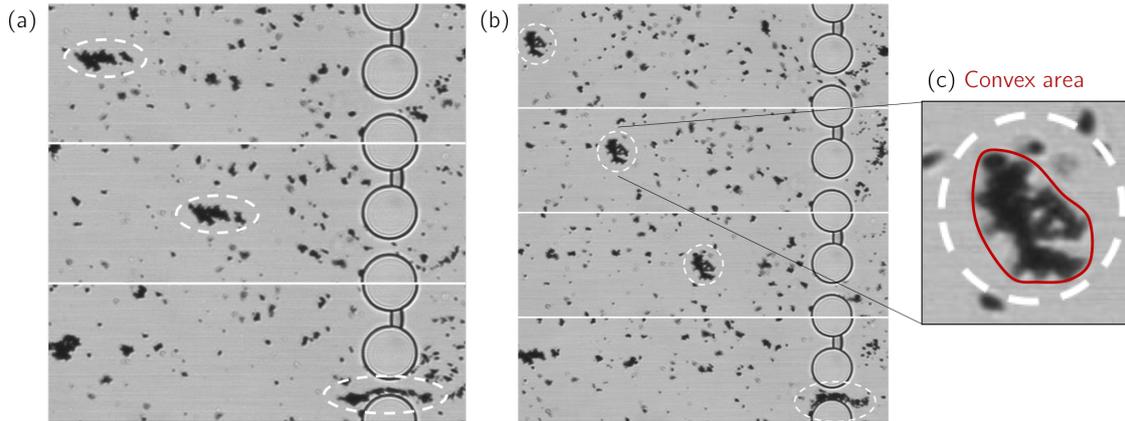
Figure 4.15: (a,b) Two examples of large loose clusters disintegrating when passing a constriction. 3 (for (a)) and 4 (for (b)) successive times are presented from top to bottom. (c) Illustration of the definition of the convex area.

fully satisfying for systematic characterization, since a low circularity can also be found for dense objects (in the sens of elementary particles bounds) with elongated shapes. For example, a dense rod on dimensions $b \times nb$ will have a circularity $\pi n/(n+1)^2$ that tends to zero for large n.

A second measure, the *solidity*, is more difficult to access directly from images but is much more robust to assess the density of a cluster. It writes as the ratio between the area of a body and its convex area, i.e. the area of the smallest convex shape containing the body. On our examples, the loose clusters have a solidity of 0.73 and 0.72 respectively; the dense cluster of 0.97 and the theoretical $b \times nb$ dense rod of 1.0, which is consistent with their densities.

A natural question is then to ask if this mechanism has a significant impact at the scale of a distribution of clusters. Let us consider a distribution of ≈ 4000 clusters of average solidity 80%, with 32% of them having one dimension larger than a single constriction $w = 8$ μm and 6% two dimensions larger. It is already important to note that not a single clogging event was observed in this experiment. The solidity and projected areas of the clusters are computed before (upstream) and after (downstream) passage of the pore, and reported in Fig.4.16.

The difference between the distributions before and after is striking. In particular, almost all upstream particles having an area above 60 μm^2 are not found downstream (see region (A)), i.e. likely broke. This threshold interestingly corresponds to a characteristic dimension of the order of $\sqrt{60} \approx 8$, the size of the pore. In the opposite, all smaller particles upstream flow downstream, a priori unaffected by the passage (see region (C)). Finally, a new category of particles appear after the passage of the pore (see (B)): small clusters with a low solidity. Still, looking at the 1D distributions, it appears that most
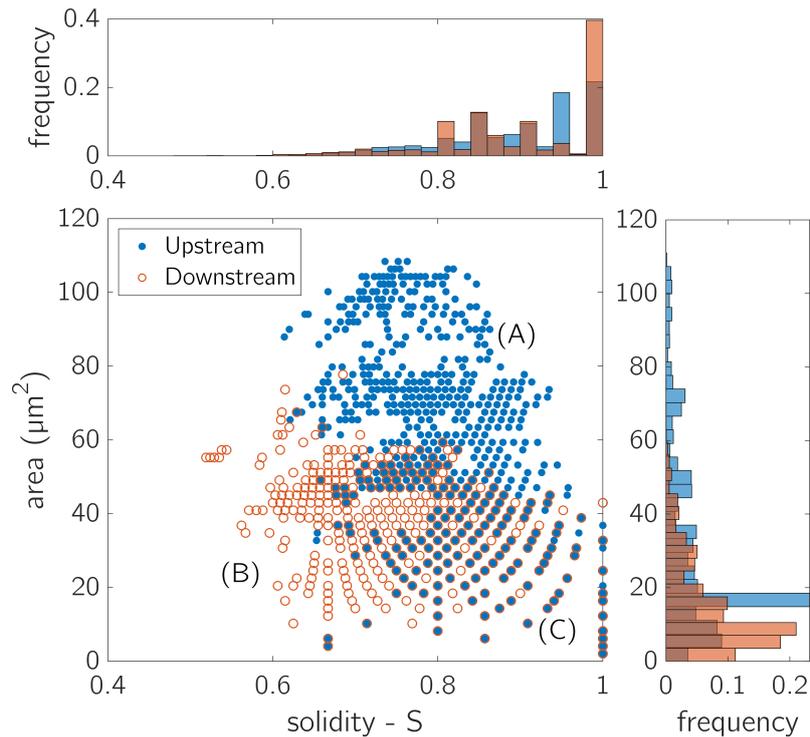
Figure 4.16: 2D distribution of the area and solidity of clusters before (upstream) and after (downstream) the passage of a 8μm pore. Side distributions use the same color code (upstream, blue; downstream, orange).

downstream particles actually have a solidity of 1, which is less surprising for particles of such small size (average area 7.3 μm^2 downstream, compared to 14.7 μm^2 upstream).

In the end, it makes no doubt that the passage of the pore combined to the de-segregation of clusters played a major role in this experiment. Of course, the fact that some clusters simply reoriented themselves to present a smaller projected area can not be excluded, but images clearly highlight disintegration as a predominant mechanism.

4.3.3   Conclusion & openings

From the several cases explored in the first section, the dynamics of single-pore clogging appear much more complex to predict in suspensions polydisperse in size and shape than in suspensions monodisperse or size-polydisperse.

Still, the present results made clear that it is wrong to consider clusters with a dimension larger than a given pore as ultimately leading to clogging events. At least two mechanisms prevent clogging events, namely the reorientation or re-structuring/de-structuring of the clusters. To take in account these effects, a first step is to better characterize suspensions in terms of aspect ratio or solidity in addition to the standard size measurements usually carried.

Of course, local geometry is not enough to fully predict those dynamics. Flow properties (flow-rate, local velocity field) and particle properties (cohesive forces) are required to assess the exact conditions of favorable cluster orientation or particle unbonding. Beyond our qualitative conclusions, these studies can pave the way to more general models balancing the drag and magnetic cohesive forces in such systems, and refine the transport modeling of such suspensions.

In addition, such results could benefit from a closer connection with previous works on the stabilization of nZVI suspensions [Tiraferri et al. 2008], and on the hydrodynamic description of polydisperse suspensions (in particular via the particle hydrodynamic radius ; [Phenrat, Kim, et al. 2009]).

Strictly speaking, the present study does not involve a modulation of the stability of the suspensions: a unique type of particles is used, in constant conditions of solvation. Still, the mechanisms we observed (reorientation of clusters keeping their integrity, disaggregation) result from a direct competition between the cohesive forces at the origin of the clusters and the local drag forces. By varying the pore sizes and confinement conditions, we explored the main scenarii, from dominant cohesion to dominant drag. For that reason, the identified mechanisms give indirectly an overview of the regimes found along the instability axis of our diagram.
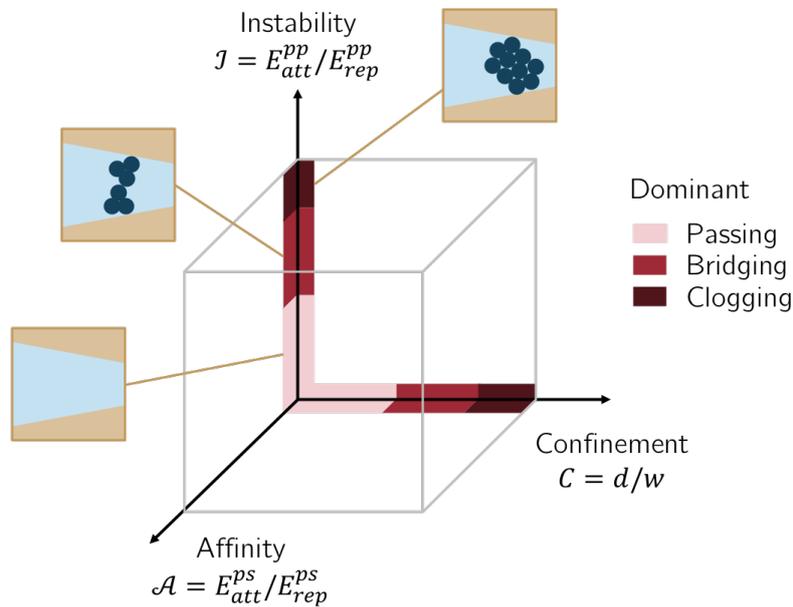
Transition : introducing surface affinity

The study originally focused on elementary particles expected, by their size, to evolve in completely unconfined conditions. The formation of large irregular clusters showed that the instability of a suspension can lead to the same fundamental mechanisms as initial high confinement conditions: bridging and clogging.
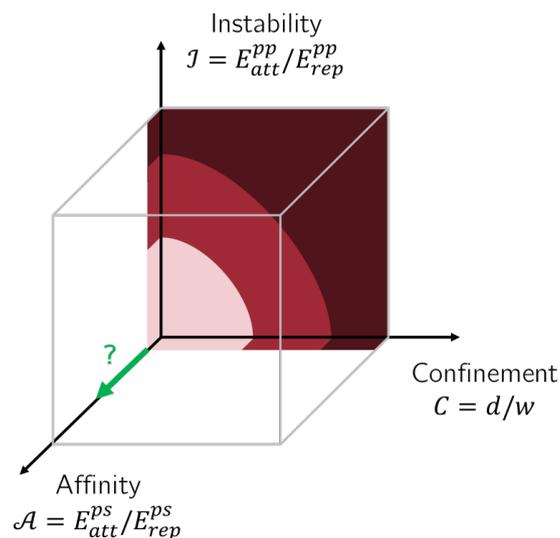
That conclusion is clear on our updated diagram: continuous domains of passing, bridging and clogging are drawn. This continuity has not been verified experimentally but results from the following thought: cohesive particles forming clusters susceptible to bridge pores will likely clog the same pores if the size of the elementary particles is increased. On the opposite, suspended particles at intermediate confinement, also susceptible to bridge, will without doubt clog if allowed to adsorb to other particles of their kind. This symmetry is a validation of the $\mathcal{I}/\mathcal{C}$ panel filled here-above.

Despite this continuity, a clarification is needed. The boundaries of the bridging domain at high confinement and high stability does not depend on the flow conditions. Indeed, we know from section 1.2 that the bridging probability of particles arriving simultaneously at a constriction is in first approximation independent on the velocity conditions.

On the opposite, the boundaries of the bridging domain at low confinement and high instability strongly depends on the local velocities and shear rates, as they are the driven forces of cluster disintegration (and orientation to a lesser extent).

Such differences do not appear on the diagram to ease its reading but are important to keep in mind.

Before going further, we recall that our recent focus on clogging made us put aside the large majority of small nZVI clusters, or even elementary particles, never affected by the pore size reductions. They acted here as passive particles because of their low affinity with the PDMS surfaces. Still, similar particles (with surface charges and/or magnetic properties) are likely to develop a strong affinity with other types of surfaces. From unconfined, stable, passive conditions to physico-chemical interactions with the surfaces: that is the next interesting topic we will now tackle.

Chapter 5

High surface affinity at low confinement

The goal of this part is to understand the effect of interactions between suspended particles and the surfaces of a porous matrix. We neglect here the geometrical size-exclusion interactions ($\mathcal{C} \to 0$). Neither do we describe the geometrical physical interactions with the surface, like bouncing or sedimentation. We focus on particle-surface physico-chemical interactions and consider more precisely the most relevant ones in the world of colloidal transport: electrostatic interactions.

Let us recall the forces at play to evaluate the particle-surface affinity $\mathcal{A}$. Short-range (tens of nanometers) Van der Waals forces are always present and attractive. In addition, the development of electrostatic potentials depends of the surface charge density at the surface of the medium (q_{pm}) and at the surface of the particles (q_p). Depending on the sign of these charges, two cases appear (see Fig.5.1 for illustration).
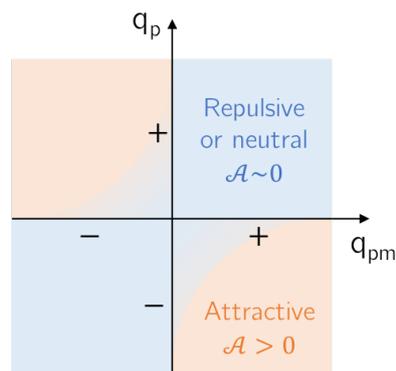
Figure 5.1: Illustration of the dominant repulsive (blue) or attractive (orange)behavior as a function of the sign of the porous medium surface charge q_{pm} and the particle surface charge q_p.

- If medium and particles are of same charges (both positive or negative; $q_p q_{pm} > 0$), electrostatic interactions are repulsive. Assuming high enough charge densities, they overcome the Van der Waals attraction. In other words, all particles

approaching the surfaces are repelled and are not expected to adsorb. There is synonym of no affinity: $\mathcal{A} \to 0$.

- Now, it their charges are of opposite sign ($q_p q_{pm} > 0$), an attractive electrostatic well adds to the Van der Waals well. There is no electrostatic repulsion, and particles are expected to adsorb the the surface of the medium when approaching it at a distance of the order of the Debye length. Other repulsive forces can play a role, like drag forces, but generally the particle-surface affinity is present: $\mathcal{A} > 0$.

Note that for the two cases, particles all share the same surface charge, so that they naturally repel each-other ($q_p^2 > 0$). Again assuming a high enough surface charge density, it creates a good suspension stability and $\mathcal{I} \to 0$.

In this chapter, we want to tackle the most interesting case of a high particle-surface affinity; hence a medium and particles of charges of opposite charge and of high enough amplitude to trigger adsorption.

5.1 Specific Material & Methods

5.1.1 Materials

5.1.1.1 Porous media & working fluid

The potential of confocal imaging to study the deposition of small particles has been proven already. It is the selected method for this study, and justifies the use of the model porous matrices previously introduced: packs of glass beads index-matched with the DMSO:dH_2O working fluid (WF). As a reminder from the general Material & Methods chapter, the specifications of these systems are as follows:

- Composition: monodisperse borosilicate spheres of diameter $d_g = 63$ μm.

- Media dimensions: $1 \times 1 \times 10$ to 20 mm^3 square capillaries, hence on average 16 to 20 beads diameter per sample's height/width.

- Organization: RCP (Random Close Packing; $\phi_0 = 0.62$), with a complex pore size distribution. An order of magnitude of the average pore size is given by the diameter of the maximum sphere that can fit between a tetrahedron of such spheres: $d_{50} = d_g/6 \approx 10$ μm.

- Surface charge: strongly negative (SiO^- groups).

- Working fluid: 90:10 DMSO:dH_2O at saturation. Low Reynolds laminar flow.

Since direct imaging of the porous media will be performed, checking their stability over time is straightforward. For instance, some defects in the RCP are easy to identify and do not move at all over the complete experiment. See for example Fig.5.5, 1.8 mm in the sample.

5.1.1.2 Charged nanoparticles

As stated before, we build here a system at low confinement, that is where the size of the particles is negligible before the average pore size. we choose in this part to work with particles several orders of magnitude smaller than the size of the grains. The selected particles have a diameter $d = 35$ nm $\ll d_{50}$ (confinement ratio $\mathcal{C} \approx 4\ 10^{-3} \ll 1$) and properties summed up in Table 5.1. Most notably, these nanoparticles (NP) have a high positive surface charge, so that we expect strong electrostatic attractive forces between them and the surfaces of our porous matrices.

Size. To estimate the mean particle size, the NP are imaged under SEM (dispersion on a clean surface, drying, 1 nm Pt:Pd coating). Clusters of NP are observed and allow a measure of the particle size distribution (see Fig. 5.2). The measured size (60 nm) is higher than announced by the supplier (35 nm) by a factor 1.7. This difference may be explained by a possible swelling of the particles in the working fluid, even if the

Supplier		BioPAL Inc.
Reference		Molday ION EverGreen
Catalog	#	CL-50Q02-6A-51
Mean size	d	35 nm (supplier), 60 nm (measured)
Composition		8 nm magnetite core, 27 nm Dextran shell
Density	ρ_p	1.25 g.cm^{-3}
Functionalization		Amine groups ($C6$)
Zeta potential	ζ_p	+31 mV
Fluorescence	λ_{ex}	505 nm
	λ_{em}	515 nm
Nb of particles	N	6.4 10^{16} g^{-1}

Table 5.1: Nanoparticle properties (source: biopal.com)

dry conditions of SEM imaging makes it unlikely. More likely, due to the small scale of the imaging and the SEM electron beam energy used, particles may have started to slightly melt (i.e. appear bigger and lose their sphericity) under SEM imaging conditions.

In the end, all nanoparticles are still significantly smaller than the average pore size. Consequently, we conclude that the low confinement conditions are valid using these particles.

(a)

(b)
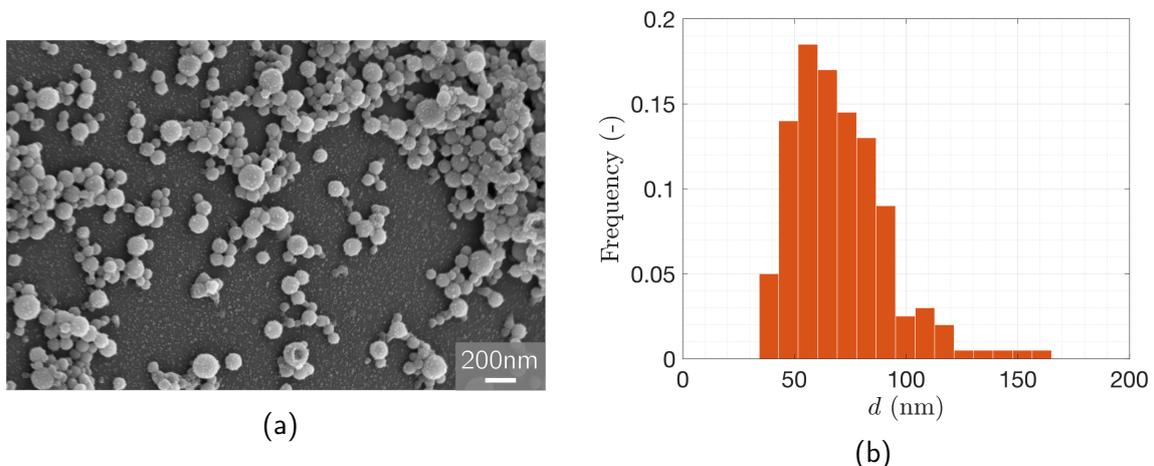
Figure 5.2: (a) SEM imaging ($EHT = 3.0$ kV, InLens) of NP dried on a flat silica surface. (b) NP size distribution extracted from (a): main peak at 60 nm $\pm$ 30 nm.

Concentration. Strong NP/surfaces attractive interactions are expected, but only a small fraction of the suspended particles flow close to the surfaces (the majority of them being in the bulk pore space). Given the target timescale of the experiments (hours) and the surface to cover, a quite high concentration of suspended particles has to be used. Still, we want the concentration low enough so that all particles can still be considered

independent and non-interacting in the flow. To comply with these two conditions, we make a suspension at 6.4 10^9 part.μL^{-1}, that is a volume fraction of $n = 1.4\ 10^{-4}$ vol%. To verify that particles can be considered independent in such conditions, we also estimate the mean inter-particle distance in the ideal gas model: $< r >= (\frac{1}{n})^{1/3} = 540$ nm, significantly larger than the size of the particles. It is commonly assumed that at that scale the electrostatic forces do not extend further than the size of a particle, from the surface of the particle itself. Particles here can therefore be considered as non-interacting in the flow at the working concentration.

Diffusion. As the diffusive behavior of the NP will play a major role in the experiments, we estimate here the diffusion coefficient of the particles based on Stokes-Einstein equation.

$$D = \frac{k_B T}{3\pi\mu d}$$

Where $k_B = 1.38\ 10^{-23}$ J.K^{-1} is the Boltzmann constant, T is taken as the room temperature (293 K), $\mu = \mu_{WF} = 3.3$ mPa.s. The resulting value of the diffusion coefficient in this system is $D = 1.3\ 10^{-14}$ m^2.s^{-1}.

5.1.2   Methods

5.1.2.1   Confocal imaging

As described in section 2.2, the complete device is imaged using the *Tile Scan* method. The fluorescent channel is set to the fluorophore of the NP: excitation at $\lambda_{ex} = 505$ nm and acquisition around the emission peak $\lambda_{acqu} \in [515; 550]$ nm.

The aim is to image a large portion of the samples (full width, 1 mm, over full depth of the medium, $\approx$ 10 mm), and to follow over time the evolution of the fluorescence signal (i.e. the presence of particles). The time required to perform a complete scan over the medium is a few minutes. Depending of the flow-rate used for the experiments, this can be a long time compared to the characteristic evolution time (adsorption) of the system. It means that by the time our scan goes from the entrance to the deepest parts of the system, significant deposition events may have happened and distort our observation of the phenomena. To avoid this, a way has to be found to stop the evolution while imaging. It can be achieved by flushing all suspended particles before imaging, which is possible by alternating pulses of NP suspension (to trigger adsorption events) and pulses of pure working fluid (to rinse) and then image (see Fig.5.3). To validate this approach, we also check by direct observation that the flushing step does not detach particles: while injecting pure fluid in a system where particles are already adsorbed, the fluorescence signal is constant.

Moreover, as the particles themselves are smaller than our imaging resolution, we expect the suspension to provide an average fluorescence intensity related to the NP concentration. Then, if adsorption occurs at the surface of the silica beads, the fluorescence signal will come from both suspended particles and adsorbed particles. The flushing method we just described is also an efficient way to avoid such issues by preventing the presence of suspended particles. Another interest of this method is that the imaging time can be decorrelated from the actual injection time.
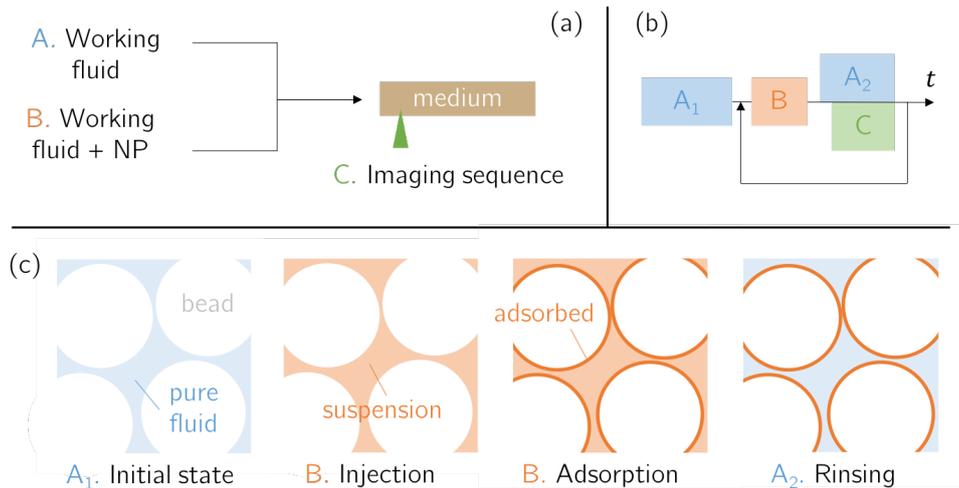
Figure 5.3: (a) Simplified injection setup including the three main components: rinsing fluid A, suspension B, imaging C. (b) Sequence of a full cycle. (c) Illustration of the state of the medium at different steps.

5.1.2.2 Injection cycles

Based on the alternating pulses of particles and rinsing fluid, the volume of each pulse of particles V_{inj} is constant and fixed to allow a significant number of particles to adsorb between each acquisition. In other words, it is fixed so that the observed fluorescence signal after a given cycle is significantly different than after the previous cycle, i.e. particles adsorbed significantly. The fixed value is $V_{inj} = 20$ μL (≈ 5 PV; *pore volumes*: the volume of pores in the whole medium).

Then, pulses of working fluid are injected to rinse. The volume of these pulses is also fixed and chosen arbitrarily by checking the time at which the fluorescence in the pore space completely vanishes, i.e. no particles are present in suspension anymore. As a rule of thumbs, 10 PV is a careful choice, to flush but also to ensure the stability of all adsorbed particles.

The injected volume V_{inj} is constant over the experiments. The flow-rate however is not, because it is a parameter we choose to vary along the study to see the effect of the flow velocity on the adsorption. In consequence, the time needed to perform one

injection varies accordingly: $t_{inj} = V_{inj}/Q$. This time and others are summed up in Table 5.2. The total time per cycle t_{cyc} equals the sum of the injection time, the flushing time, a stabilization time of 5 s between the end of the injection of the imaging, and finally the imaging (TileScan) time. The latter can vary depending on the length of the porous media (i.e. the number of tiles to image) but is of the order of 1 to 5 minutes. The total time per experiment t_{exp} corresponds to a certain number of successive cycles. It is illustrated here on the example of 10 cycles ($t_{exp} = 10t_{cyc}$) done experimentally. In the end, single experiments range from 50 min to almost 9 hours, which highlights the large difference in timescales when working with flow-rates covering several orders of magnitude.

Flow-rate Q (μL.min^{-1})	Injection volume V_{inj} (μL)	Injection time t_{inj} (min)	Cycle time t_{cyc} (min)	Exp. time t_{exp} (hours)
1.3	20	15.4	51	8.5
13	20	1.5	9.5	1.6
130	20	0.15	5.5	0.90
208	20	0.096	5.3	0.88

Table 5.2: Injection time settings for various flow-rates.

Now that the system is well defined, experimental results will be presented first at the global scale of the porous media, before focusing on the local expression of nanoparticle deposition.

5.2 Adsorption over depth

We described how nanoparticles are injected at the inlet of our porous system. Let us now study the result of these cycles of injection on the distribution of adsorbed particles.

5.2.1 Deposition towards saturation

5.2.1.1 Early deposition

We first inject a single pulse of particles at $Q = 13$ μL.min^{-1} ($v = 0.55$ mm.s^{-1}) and observe the resulting confocal image (see Fig.5.4, top).
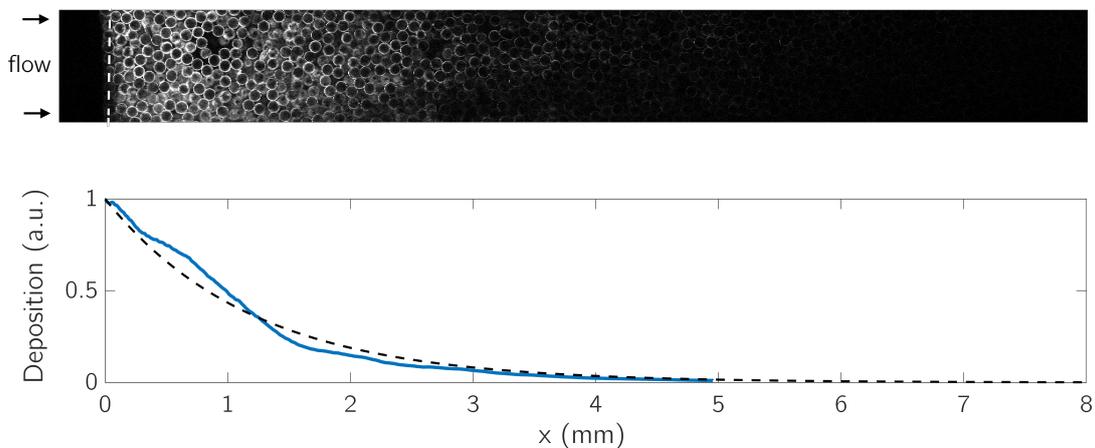
Figure 5.4: (top) Raw confocal image after injecting 1 pulse of particles. Brightness is proportional to the amount of adsorbed particles. Scale is the same as on the bottom plot. (bottom) Profile resulting from the protection of the top image. Dashed line shows the best fit in $y(x) = exp(-x/x_0)$, with $x_0 = 1.2$ mm the characteristic spreading distance of the particles.

The flow being left to right, several points can be made:

- Overall, the image is composed of dark areas (no fluorescence, i.e. no adsorbed particles) and bright areas (containing adsorbed particles).

- At the inlet (far left, dotted white line), a sharp transition from dark to bright highlights the transition between the inlet tubing (no beads, particles cannot adsorb) and the porous system (particles meet surfaces and can start adsorbing). Given the brightness of the signal, it is clear that many particles adsorbed on these very first beads.

- Looking further in depth (to the right), the fluorescence signal seems to fade. This area corresponds to the section over which particle adsorbed.

- Looking even deeper, the medium appears completely dark: no particle reached these depths.

To get a better sense of the distribution of deposited particles along depth (x), the fluorescent signal from the confocal image is summed over the width of the sample. We end up with a saturation profile over depth (see Fig.5.4, bottom). The profile confirms the observations made of the image: the deposition is maximal near the entrance and vanishes in depth.

As a particle enters the system, it has a given probability to encounter a surface and adsorb to it. If it does not adsorb, it can explore further the medium. Therefore, the observed distribution results from the spreading of the particles from the entrance to deeper areas driven by successive events of adsorption or passage to deeper pores.

5.2.1.2 Further deposition

Several additional cycles at the same flow-rate are performed, and the distribution of adsorbed particles after each of them is acquired (see Fig.5.5). The fluorescence spreads further and further as we keep injecting, which means the nanoparticles explore and adsorb to deeper sections of the system. Interestingly, the intensity of fluorescence near the entrance does not evolve with further injections and seems to reach a saturation. To verify it, the profiles over depth are computed from each image. As expected, the cumulated signals exhibit a clear saturation value which is used to normalize the profiles to unity (meaning saturation) and end up with Fig.5.6.
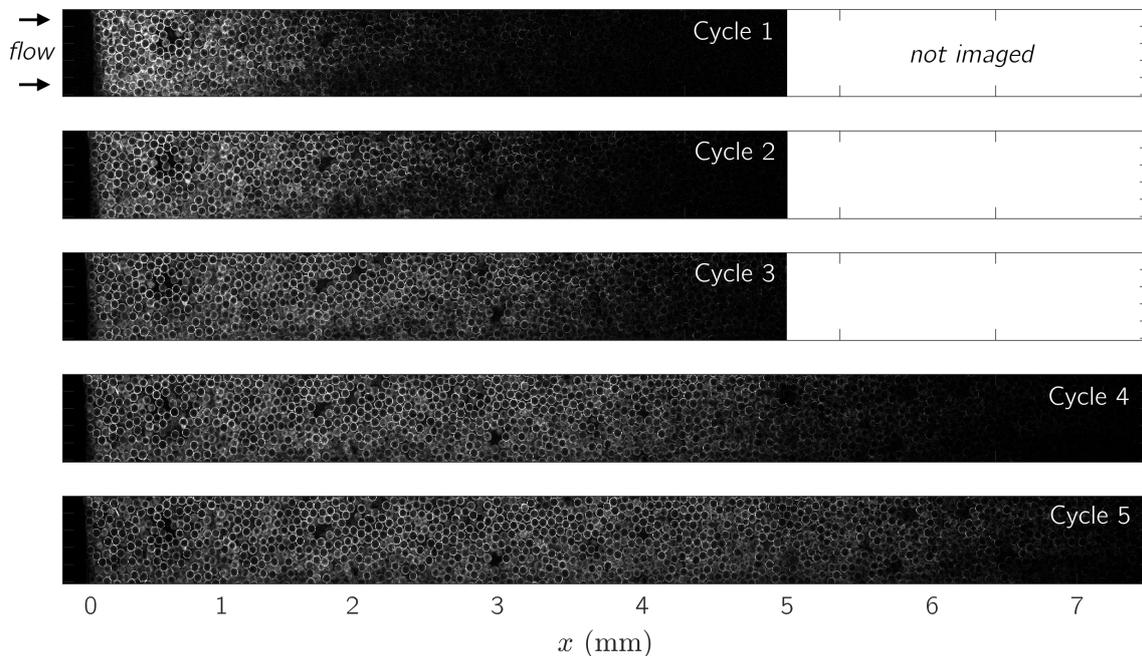
Figure 5.5: Raw confocal images after the injection of 1 to 5 V_{inj}. As the fluorescence spreads to deeper regions we have been imaging deeper in the system, from 5 mm initially to 7 mm.

Note that cycles 8 and 11, corresponding to $8V_{inj}$ and $11V_{inj}$, have been done
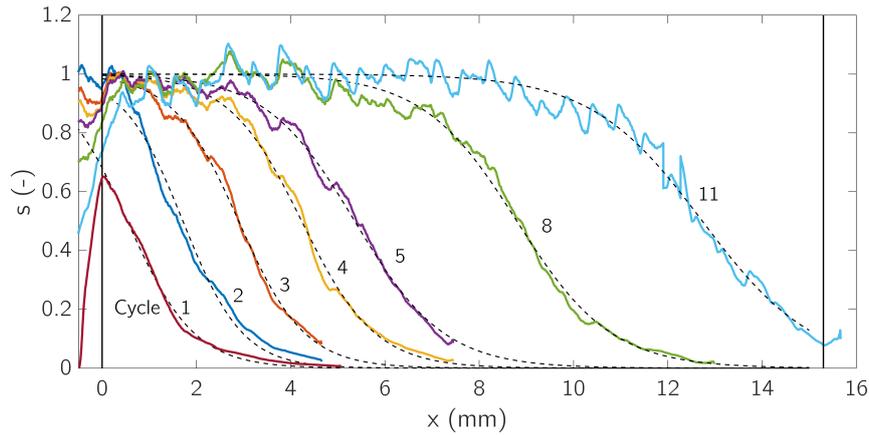
Figure 5.6: Saturation profiles over depth of porous medium after the injection of 1 to $5V_{inj}$, and $8V_{inj}$ and $11V_{inj}$ to show the state of deposition after a much longer time. Dashed lines are sigmoidal fits in $1/1 + exp(-(x - x_c)/x_0)$; see modelling section. The two vertical lines indicate the limits of the sample: entrance at $x = 0$ mm and end of the bead pack at $x = 15.3$ mm.

experimentally to have a measure of the state of deposition long after the dynamics already acquired. As a result, data for $[6 - 7]V_{inj}$ and $[9 - 10]V_{inj}$ are not available.

The existence of a saturation is explained by the repulsive interactions between particles. When a particle approaches a surface, two cases prevail: (i) the closest element of surface is free of particles and the arriving one can adsorb, or (ii) a particle is already adsorbed there and repels the arriving one to a further location ($\mathcal{A} > 0$, $\mathcal{I} = 0$). As particles keep adsorbing, less and less sites remain free. At some point, all arriving particles are repelled: a maximum coverage (saturation) is reached. Then, when new particles enter already saturated areas, they just keep flowing as passive tracers to unsaturated surfaces downstream.
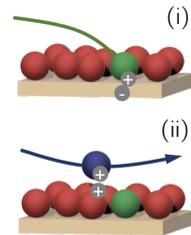
Taking a closer look at Fig.5.6, it appears that consecutive profiles have very similar shapes, or more precisely seem to be the same profile shifted in depth. This means that the same dynamic of adsorption is repeating over depth as we keep injecting, in other words is identical whatever the section considered in the system, as long as saturation has been achieved at the entrance of this section. To challenge this observation, all profiles (reaching saturation, which excludes the first one) are rescaled in depth by the characteristic depth covered between each cycle x_c. We define $X = x - ix_c$, with i the cycle/injection number and rescale each profile to get Fig.5.7. For simplicity, the origin of the rescaled depth is chosen at $S(X = 0) = 0.5$. All profiles collapse on a single master curve (see dashed line on Fig.5.7). This fact proves that all profiles reaching saturation can be described by the same dynamics, and validates the assumption of a stationary propagation of the adsorption front in depth.
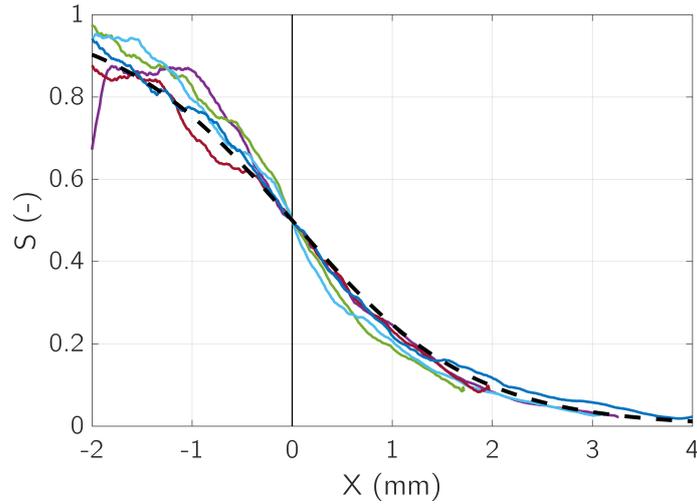
127

Figure 5.7: Profiles from Fig.5.6 rescaled in depth by the characteristic distance covered by particles between cycles.

5.2.1.3   Modeling

At first, all the surfaces of the system are free of particles. A particle entering the system has a probability p of approaching and adsorbing to a surface. Assuming a characteristic exploration depth per time step l (for instance the average pore size), we can quantify the process of exploration and adsorption over depth. From a probability p to adsorb in the first pore ($1 - p$ to pass), a particle has a probability $p(1 - p)^{k-1}$ to adsorb in the kth pore. Over depth, the amount of deposition s is proportional to that probability (and to the number of injected particles). From the same passage to the continuum as in section 3.3, s rewrites as:

$$s(x) \propto p e^{x \ln(1-p)}$$

That remains valid until all particles do not share the same adsorption probability p anymore, that is until the presence of other (deposited) particles affects arriving particles. It is considered true as long as particles are sparsely distributed on the surfaces, i.e. the saturation is low.

For that reason, none of our experimental profiles can be fitted with this model: after the first cycle, the saturation is already significant at the entrance of the system. Still, this first profile is actually fairly well described by an exponential decay (see Fig.5.4, bottom, dashed fit). It shows that despite the non-independence of particles at such saturations, the model is still a good first approximation.

To go further on the dynamics at all cycles, we define from now the amount of deposition $s(x, t)$ as the number of adsorbed particles to the maximum number of surface adsorption sites. It is natural to see the gain in deposition ∂s per time unit as proportional to the fraction of surface sites still available $(1 - s)$ and to the number of particles available in suspension n. It writes as $\partial s = kn(1 - s)\partial t$, with k $[s^{-1}]$ a kinetic

constant added for dimensionality and characteristic of the adsorption kinetic. Note that the previous case of deposition far from saturation ($s \ll 1$) leads to $\partial s = kn\partial t$; that is a constant gain in adsorption independent on the state of deposition.

In the general case (up to saturation), the fact that the differential equation for $\partial s / \partial t$ (also called *adsorption rate*) depends on s and on the number of suspended particles n prevents a straightforward resolution. From section 1.3 we also know that the concentration of suspended particles follows the advection equation, hence the following coupled system:

$$\begin{cases} \frac{\partial n}{\partial t} + v \frac{\partial n}{\partial x} = -\frac{\partial s}{\partial t} \\ \frac{\partial s}{\partial t} = kn(1 - s) \end{cases} \tag{5.1}$$

To solve System (5.1), it is useful to recall that all profiles collapse on a single master curve characteristic of the propagation of a stationary wave of adsorption events. The same change of variable done previously can also be done by replacing the characteristic deposition distance x_c by time multiplied by a velocity. We thus introduce $X = x - v_1 t$ $[m]$, function of x and t, where v_1 $[m.s^{-1}]$ is the velocity of propagation of the adsorption wave.

From the change of variable, the corresponding adsorbed and suspended saturations S and N are also introduced: $s(x,t) \rightarrow S(X)$ and $n(x,t) \rightarrow N(X)$. (5.1) leads to (5.2).

$$\begin{cases} \frac{\partial n}{\partial t} = \frac{dN}{dX} \frac{\partial X}{\partial t} = -v_1 \frac{dN}{dX} \\ \frac{\partial n}{\partial x} = \frac{dN}{dX} \frac{\partial X}{\partial x} = \frac{dN}{dX} \\ \frac{\partial s}{\partial t} = \frac{dS}{dX} \frac{\partial X}{\partial t} = -v_1 \frac{dS}{dX} \end{cases}$$

$$\begin{cases} \frac{dN}{dX} = \frac{u_1}{u - u_1} \frac{dS}{dX} = \alpha \frac{dS}{dX} \\ \frac{dS}{dX} = -\frac{k}{v_1} N(1 - S) \end{cases} \tag{5.2}$$

Now, integrating dN/dX over X from $-\infty$ to X, and defining $\alpha = v_1/(v - v_1)$ leads to

$$N(X) = \alpha S(X) \tag{5.3}$$

The physical meaning behind (5.3) is that large adsorption requires large amounts of suspended particles, while limited adsorption only occurs where the number of suspended particles also goes to zero. α^{-1} denotes the variation between the fluid and propagation wave velocities. In these conditions, injecting (5.3) in (5.2) gives the rescaled adsorption rate $S'(X)$ (5.4), where $\lambda = v_1/k\alpha$ has the dimension of a distance. It is reduced to a first-order nonlinear differential equation which solves analytically (thanks to the

previous definition $S(0) = 0.5$):

$$S'(X) = -\lambda^{-1}S(1-S) \tag{5.4}$$

$$dS/S(1-S) = -dX\,\lambda$$
$$\left[ln(S) - ln(1-S)\right]_{0.5}^{S} = -\left[X/\lambda\right]_{0}^{X}$$
$$ln(S/(1-S)) = -X/\lambda$$
$$S = exp(-X/\lambda)/(1 + exp(-X/\lambda))$$

$$S(X) = \frac{1}{1 + e^{X/\lambda}} \tag{5.5}$$

Equation (5.5) describes the saturation over (rescaled) depth as a sigmoidal shape, which is consistent with the master profile on Fig.5.7. Best fit is obtained for $\lambda = 0.8$ mm (see dashed line). In the end, we were able to correctly and fully describe the dynamic of adsorption of consecutive pulses of particles, as the rescaled stationary propagation of the adsorption front.

Now that this principle is proved, the velocity of this front - that was for now introduced theoretically - can be further detailed.

We recall that, in this study, the injected volumes along the cycles replace the real time t. We can rewrite $v_1 t$ accordingly, with j the number of the cycle, Q the flow rate, S the section of the capillary and phi_0 the porosity:

$$v_1 t = v_1 \frac{jV_{inj}}{Q} = v_1 \frac{jV_{inj}S\phi_0}{v}$$

Remarkably, because all cycles lead to the same front propagation, the propagation between two cycles j and $j+1$ is a constant and writes $v_1 V_{inj}S\phi_0/v$. It implies that v_1/v also is a constant, that we call γ. In the end, we showed that the adsorption front velocity is proportional to the pore velocity, which was expected.

In the continuity, we note that α rewrites $\gamma/(1-\gamma)$. Likewise, λ rewrites

$$\lambda = \frac{1-\gamma}{k}v$$

5.2.2 Impact of the flow-rate

5.2.2.1 Flow-rates sweep

The previous sections taught us the propagation mechanism at a given injection velocity. These results can now be challenged by varying the flow-rate in the experiments. We explore a large range of Darcy velocity from 0.1 to 16 times the previous value of 0.55

mm.s^{-1}. For each value, an adsorption front is well visible and propagates in depth according to the same stationary description as before. Consequently, the same rescaling in X is performed and leads to profiles presented in Fig.5.8.
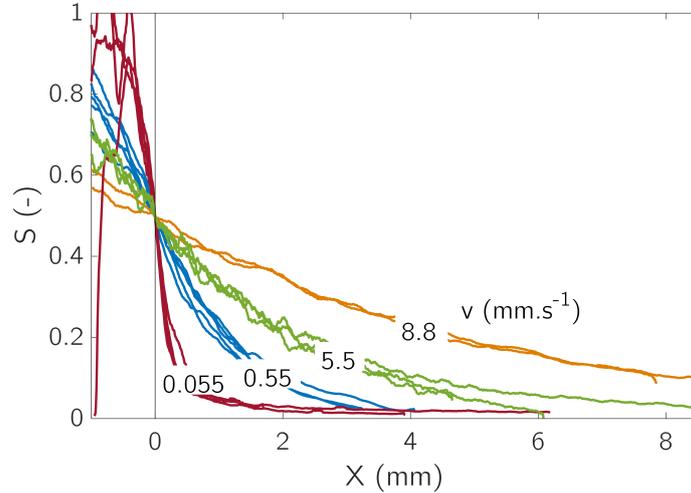

Figure 5.8: Saturation as a function of rescaled depth for four values of velocity over three orders of magnitude.

Variations in the shape of the rescaled profiles appear clearly at the different velocities. First, we can note that the fact that all curves meet at $S(0) = 0.5$ is imposed by the origin of the rescaled depth. Then, what is most interesting is the extent of the depth achieved in each condition. At the lowest velocity, the area saturated by particles is very narrow around 0. As larger velocities are used, this area is stretching, i.e. for a same pulse, particles are distributed along a larger depth.

This effect is explained as follows: at low flow-rate, a particle spends a relatively long time flowing along a given surface. When increasing the flow-rate, the particle travels the same given surface in a shorter time. Assuming that a particle attempts to adsorb the surface a given number of times per time unit, the number of attempts is inversely proportional to the flow-rate. Consequently, a pulse of particles will spread over a larger area at greater flow-rate. This notion of attempt frequency will be deeper discussed from local observations in section 5.3.

Equation (5.5) applies for all rescaled curves on Fig.5.8. It leads to an estimation of the previously introduced characteristic *exploration length* λ for each flow-rate, by fitting our sigmoidal expression. Results are presented in Fig.5.9, left. This length represents the extent of the area along which the particles are spread. For instance (see Fig.5.9, right), 50% of the particles deposit between $-\lambda$ and λ and 99% between -5λ and 5λ. Besides, it appears that the exploration length increases roughly linearly with increasing flow-rates. Despite the poor precision of our data, this confirms the behavior described previously and provides an estimation of the depth of porous medium

affected by additional pulses, as a function of the velocity. In first approximation, it tells that when the velocity increases of one order of magnitude, the particles spread over a distance also one order of magnitude bigger.
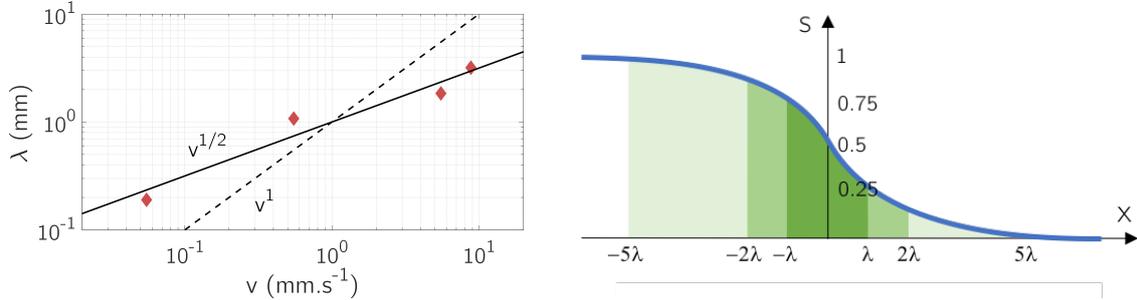

Figure 5.9: (left) λ fitted from Fig.5.8 for four different flow-rates. Two models are presented: $v^{1/2}$ and v^1; plain and dashed lines respectively. (right) Theoretical view of the fraction of deposited particles in sections around the origin of a sigmoid.

5.2.2.2 Towards a general master curve

To go a bit further, we would like to verify the dependence of λ with the velocity. We stated that $\lambda = v(1 - \gamma)/k$, hence expectations of $log(\lambda) = log(v) + $ cte. For validation, a curve of slope 1 is added on Fig.5.9(left) and does not follow the experimental results. Instead, the evolution of λ are well described by a line of slope 0.5, representative of a power law $\lambda \propto v^{1/2}$.

At the time of writing, this result remains unexplained. Our model predicts that for increasing velocities, the depth of sample 10λ over which the adsorption events spreads increases linearly. The experimental results tend to show that we are over-estimating this increase, and that an additional phenomenon slows down the spreading with increasing velocity.

Despite this lack of explanation, it is still interesting to apply the best fitted model $\lambda \propto \sqrt{v}$. More precisely, through Equation (5.5), we see that introducing the variable change $X^* \rightarrow X/\lambda$ would lead to a master curve independent on the flow-rate of the experiment. Indeed, introduced the rescaled depth $X^* = X/\sqrt{(v)}$ on the data from Fig.5.8 leads to Fig.5.10. All profiles, for all injection cycles and velocities, collapse of a single master curve. It means that through a double rescaling over time and flow rate, a global description of the shape and evolution of the adsorption front is achieved:

$$S(X^*) = \frac{1}{1 + e^{X^*}}$$

In the next section, we will challenge this general understanding by taking a closer look at the local mechanisms driving the adsorption, at the scale single beads or fractions
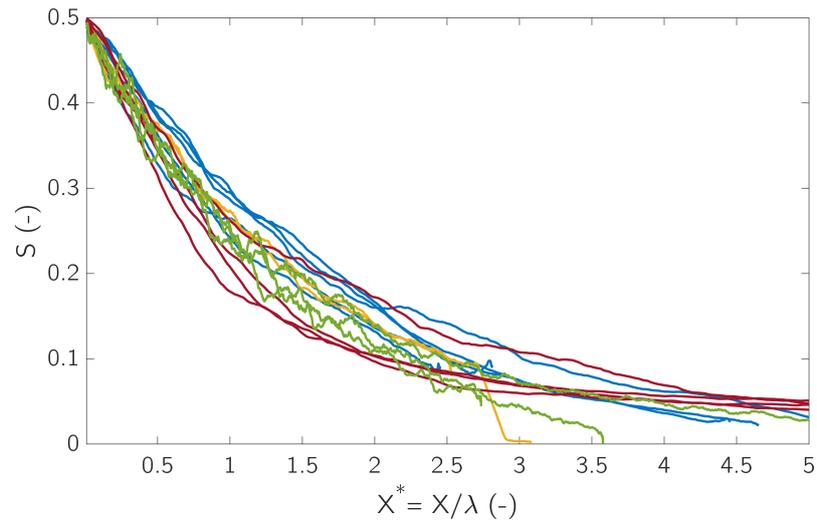
Figure 5.10: Saturation as a function of $X^* = X/\lambda$: all velocity profiles collapse to a single master profile.

of beads.

5.3 Local observations & dynamics

5.3.1 Heterogeneous local adsorption

Until this point, the confocal images were treated as a whole to extract precious deposition profiles over depth and time. From the same data, the resolution of this imaging allows us to take a much closer look at the system and study the local specificities of adsorption.

5.3.1.1 Observations a dual deposition

We first recall a typical global view, from an experiment at $v = 0.55$ mm.s^{-1} (see 5.11.a). A closer view (250×250 μm^2 window; see (b)) are selected and presented. On both, the fluorescence is relatively high which is synonym of advanced deposition. Still, two types of areas can be distinguished:

- Almost everywhere, the deposited particles outline the surface of the silica beads. This is expected since we are looking at 2D cuts of the 3D spherical beads: in this plane, the cross-section of the adsorbed surface is indeed a circle. These circles appear fairly homogeneous in intensity and can therefore be assumed to be homogeneously covered by particles.

  The inside of the circles does not appear fully dark, because the fluorescence signal is acquired over a finite thickness of sample, i.e. over a range of bead's sections (see Fig.5.12). In addition, note that the brightness of the global image has been increased to ease the observation.

- Some areas do not follow this description (see white arrows). They appear much darker than the rest of the frame and are of variable size.

These images tend to show that the deposition is not as uniform as the previous global study had us believe.

5.3.1.2 Identification of a dual porosity

A higher resolution shot of a similar area is presented in Fig.5.12. The dark areas appear clearly, as well as their positions compared to the position of the beads: they are regions corresponding to the *contact points* between adjacent beads (see in particular (b) on the image).

The positions of the areas are the contact points between beads, but their size is not limited to the "punctual" contact point. It is on average much larger, of the order of 10 μm. An explanation for this observation is that the particles do not adsorb in these specific areas, which therefore remain non-fluorescent and *excluded*.

We also note that the regions appear as ellipses of different orientations. It can be explained by the fact that contact points between beads are of random orientation in the
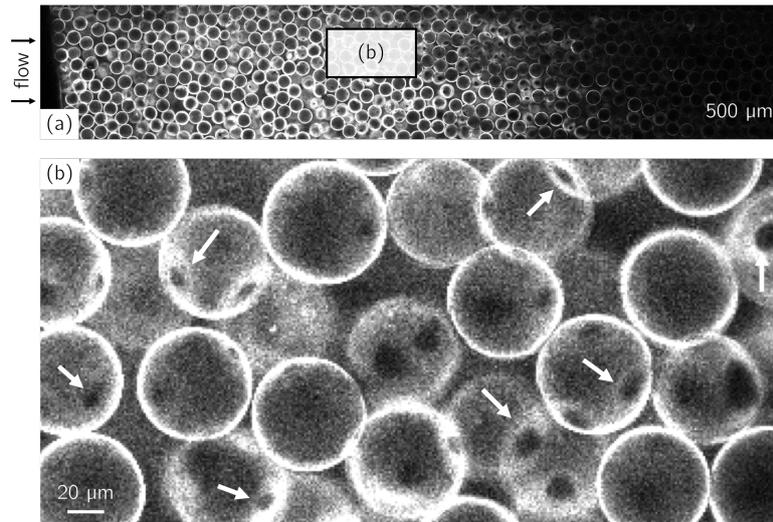
Figure 5.11: (a) Global view of the deposition state ($v = 0.55$ mm.s^{-1}; cycle number 3). (b) Selected window from the global view. White arrows pinpoint areas appearing darker than the average fluorescence signal.

porous medium. Indeed, we recall that confocal images result from the accumulation of the fluorescence signal over a thin thickness of sample (see section 2.2). The different orientations of a plane of contact between two beads, relatively to the plane of imaging, will therefore lead to a variety of observations (see Fig.5.12.a, .b, .c):

(a) When the imaging plane coincides with the mid plane between two beads, the excluded contact point appear as a perfect disk.

(c) When the contact point is perpendicular to the imaging plane, the average signal coming from the area only encompasses a thin section of the confined area, hence an apparent line.

(b) For intermediate (and most represented) cases, the contact point areas appear as a combination of the two previous cases: ellipses.

All these cases are observed experimentally. Remarkably, it demonstrates that the exclusion phenomenon is not limited to a specific orientation of the contact points in the system but apply to all of them.

We oppose these areas to the *bulk* surfaces more uniformly covered by particles. This duality is similar to a dual porosity, even-though all surfaces are continuous and smooth. What is more, the excluded areas correspond to the thinner pore throats of the system, as pore throats get thinner and thinner when approaching the contact point. It suggests that the exclusion may be due to the higher particle confinement there.

135
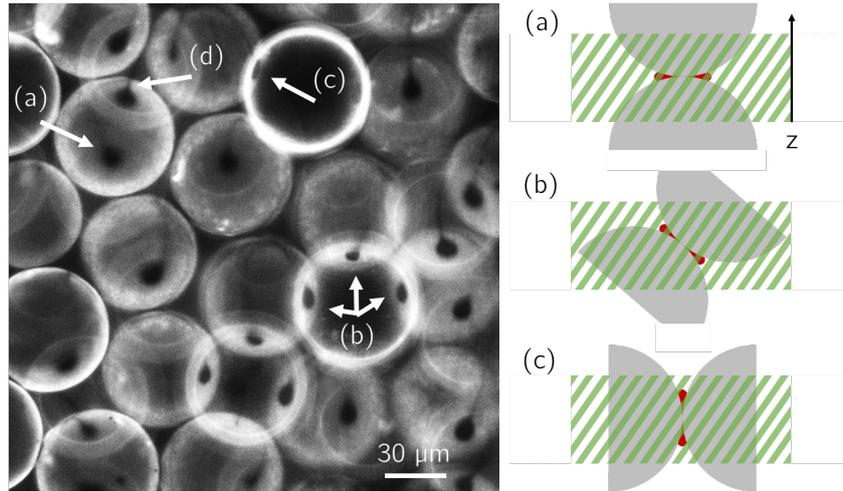
Figure 5.12: Confocal acquisition with a large depth of imaging (large pine-hole). Three types of darker areas are seen: (a) disks, corresponding to contact areas in the imaging plane, (c) lines, corresponding to contact areas perpendicular to the imaging plane, and (b) ellipses at intermediate orientations. (d) highlights a trail (dark line) behind a dark area.
Note that this image has been obtained by collecting the fluorescence signal from a thickness of sample three times larger than previously (confocal pinhole increased to 200 μm), hence a better contrast.

5.3.2 Confined areas characterization

Let us better describe the confined areas that we just identified. We can in particular attempt to further characterize them in terms of geometry and local hydrodynamics.

5.3.2.1 Geometrical characterization

First, it is interesting to understand what exactly are the ellipses observed experimentally in terms of surface on which particles can adsorb. From the experimental data, we can measure the size of the excluded ellipses, but this measure is only a projection of the surface actually excluded. More precisely, each dark area surrounding a contact point corresponds to a fraction of the surface of the grains in contact. One dark area corresponds to two caps of spheres, one on each bead (see Fig.5.13.a). The excluded surface S_{ex}, i.e. the surface of each cap, can be calculated using:

$$S_{ex} = 4\pi r_g^2 \left(1 - \sqrt{1 - \frac{(d_{ex}/2)^2}{r_g^2}} \right)$$

With $r_g = d_g/2 = 32$ μm the bead radius and d_{ex} the major axis of the excluded ellipses (see Fig.5.13.b). From the image presented in Fig.5.12, the *excluded diameter* d_{ex} is measured for each contact point. A distribution of excluded diameters is deduced (see Fig.5.13.c) and reveals a narrow peak centered around the average value $\bar{d}_{ex} = 14$ μm. It means that in these conditions, the excluded areas have an average diameter of

136

14 μm. It is much larger than the size of individual particles ($d_p = 35$ nm) and confirms that the exclusion is not really localized at the contact points but spreads further.

We can now use the main axis of the ellipses d_{ex} to estimate the excluded surface S_{ex}. The calculated value is: 3.1×10^2 μm^2. Normalized by the total surface of a spherical grain $S_g = 4\pi r_g^2 = 1.2 \times 10^4$ μm^2, we get an estimation of the excluded surface fraction per sphere, per contact point: $\sigma_{ex}^{cp} = S_{ex}/S_g = 2.6\%$.

This is valid for each contact point, and the average number of contact points per sphere in a random close packing is estimated in section 2.1 at 6. Consequently, the surface fraction per bead concerned by the exclusion phenomenon is of the order of

$$\sigma_{ex} = 6\sigma_{ex}^{cp} \approx 16\%$$
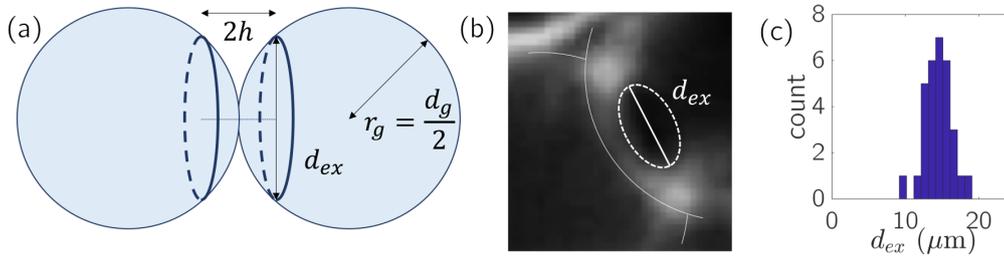
Figure 5.13: (a) Illustration of the two spherical caps surrounding a contact point, (b) Example of the measure of an excluded diameter between two beads, (c) Distribution of excluded diameters.

As the effect is valid on all grains, it is at least 16% of the total surface of the porous matrix that is concerned, which is significant. Even-though further characterization of the adsorption is needed, it already means that the deposition on a substantial fraction of the system may be driven by specific dynamics.

5.3.2.2 Time evolution

For now, we considered the excluded areas as static geometries. In reality, their size changes over time. By following a specific contact point over injection cycles (see Fig.5.14), the evolution over time is clear:

- At first, no deposition occurred so the excluded areas are naturally invisible (see cycles 2 and 3).

- As the *bulk* deposition progresses, the excluded areas are left behind (see white arrows). The overall fluorescence tends to saturate, in accordance with the saturation of the bulk surfaces. In the same time, the size of the confined ellipses decreases and tends to zero.
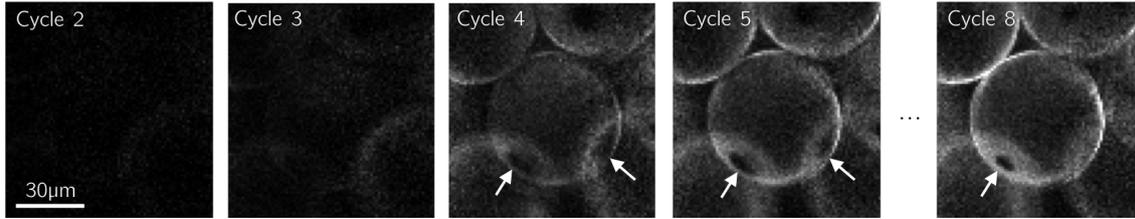
Figure 5.14: Selected area after five different cycles of injection, focused on the contact points between neighboring grains. White arrows highlight the areas around contact points, mostly free of fluorescence.

The fact that these areas fill up with time means that particles eventually access them and adsorb on the confined surfaces. The exclusion phenomenon is therefore not endless.

From Fig.5.14, and especially the contact points pointed by the right arrow, it is clear that the contact point areas tend to be fully covered at long times. What is more difficult to define is their state at early times. Indeed, to be able to define confined areas, the bulk areas need to be filled enough; i.e. the fluorescence needs to be high enough for the excluded zone to be visible. By the time we get a contrast good enough to identify excluded areas, they may have already be slightly filled.

On this example, the distinction becomes possible at cycle 4, where excluded zones of main diameter $d_{ex} \approx 20$ μm are present. This value is significant (one third of the bead's diameter): reported to the surface of the bead, it represents an excluded surface fraction $\sigma_{ex}^{cp} = 5\%$ per contact point and $6 \times 5 = 30\%$ of the total surface.

The main message here is that the confined regions evolve over time in a range of sizes from tens of microns to zero, when fully covered.

5.3.3 Coupled bulk/confined dynamics - single pulse study

5.3.3.1 At the scale of a tile

To have a better sense of the difference in deposition dynamics between bulk and confined areas, a new kind of acquisition is performed. A selected area at the entrance of the porous medium (500×500 μm^2; see Fig.5.15.a) is imaged in "real-time" (i.e. not using injection/rinse cycles between images). A single pulse is injected during 25 min at $v = 0.055$ mm.s^{-1}. The time resolution is pushed to one frame every 5 seconds (0.2 fps) which is enough to follow in detail the local deposition dynamics.

The process previously observed over cycles of injection repeats here: the area of study goes from empty to covered with particles (see Fig.5.15.b). Again, the confined areas start to be visible when the bulk deposition is already advanced (see 5 min) and then decrease in size.
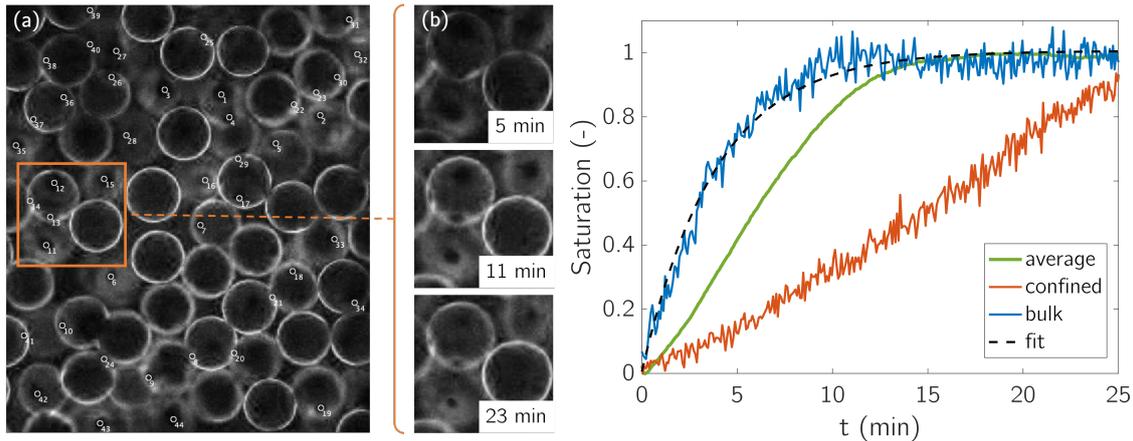
Figure 5.15: (left) (a) Selected $500 \times 500 \ \mu m^2$ window at the entrance of a porous medium, where a single pulse of particles is injected at $v = 0.055$ mm.s^{-1}. Dots highlight a manual selection of confined areas. (b) Zoom on the orange square from (a) at three times during the injection. (right) Saturation over time during the single pulse, for bulk and confined areas separately, and the frame average. For the bulk deposition, the fit previously presented in $1 - exp(-kt)$ is added and shows a good agreement with the data.

The fluorescence signal is summed over the window and presented over time (see Fig.5.15, right, green curve). It shows that the average deposition during the pulse increases sharply and tends to a saturation value. The question then is to know what are the contributions of the bulk and confined areas in this average deposition.

The decoupling is achieved by a manual selection of 50 bulk areas and 50 confined areas (see numbered circles on Fig.5.15.a). The average deposition dynamic in bulk and confined areas respectively is added to Fig.5.15.right : bulk areas are filled much faster than the average, and confined areas much slower. Note that all curves are normalized to their expected plateau values, to focus on a comparison of the dynamics. The analysis therefore remains qualitative but highlights a clear and interesting difference. We can now precise the analysis by focusing on a single contact point.

5.3.3.2 At the scale of a contact point

To directly link bulk and confined dynamics, we select a contact point area and look simultaneously at the deposition happening inside the "empty" area and next to it, in the bulk.

A linear section (see white line) is recorded for each time, which is equivalent to have a deposition profile of the contact point area. On a single line, this process is noisy due to relatively low image resolution at this level of magnification. To reduce the noise, the line is rotated all around the ellipse (0.5 degree
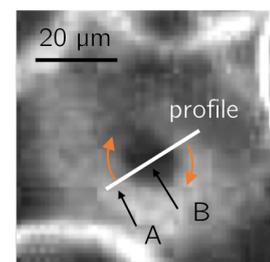
steps; see orange arrows). The resulting $360/0.5 = 720$ profiles
are then averaged in one profile (per time step) representative of
the average deposition radially around the contact point. The
profiles are presented versus the distance to the contact point, for increasing time (see
Fig.5.16 (left)) and versus time for different distances to the contact point (see Fig.5.16
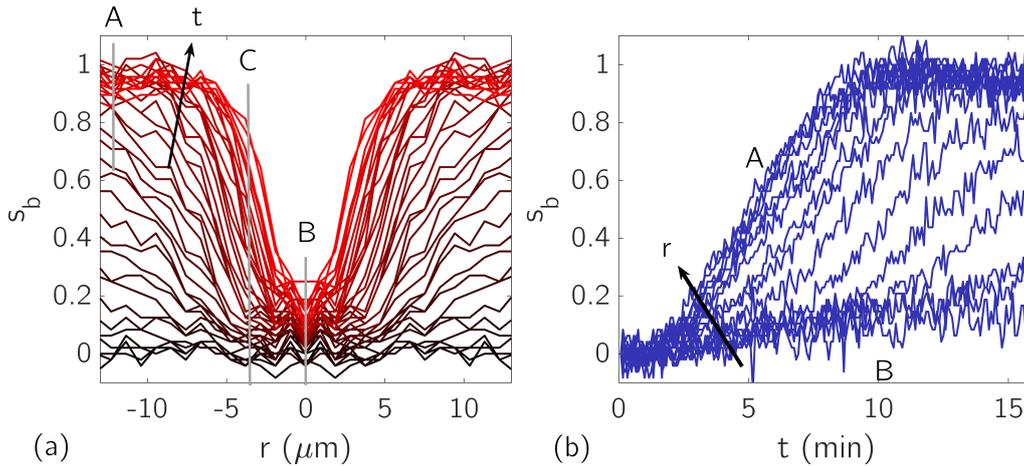(right)). Note that due to the radial averaging performed, the spatial profiles are sym-
metric around zero.

Figure 5.16: (a) Radial evolution of the saturation for various times
(every 50 seconds). A, B and C highlight three points of interest; see
text. (b) Same data set, transposed. Saturation as a function of time
for 20 positions between A and B.

Let us look first at point A, far from the contact point (see $r \approx -10~\mu$m). From the
profiles, the deposition there is fast and saturates. This saturation value is associated
with the bulk saturation (s_b) and fixed to unity. At the contact point (see B; $r = 0$), the
profiles confirm a much slower deposition reaching only 20% of the bulk saturation value
over the duration of the experiment. Finally, in the transition region (see C; $r \in [-7;0]$
μm), an intermediate dynamic is visible: the excluded area is progressively filled, from
the sides. This behavior is similar to the propagation of a radial front of adsorption,
from the bulk areas towards the contact point.

5.3.4 Deposition mechanisms

At this point it is important to remind that the notions of *confined* and *bulk* areas were
introduced for description purposes, but there is no physical boundary between them. It
simply is a continuous passage from large pore throats to the contact points.

So far, the take-away is that confined areas fill with some retardation. We will now
explain in more details this retardation.

5.3.4.1 Geometrical aspects

A first natural explanation is linked to the confinement itself. We adopt here a schematic but efficient framework. We consider that the concentration of particles arriving along the surfaces are constant. We also assume that the particles approach the surfaces at a given distance where they start to explore the surfaces and eventually adsorb. Far from the contact point, the number of particles available to explore an element of surface is constant. In consequence, deposition happens uniformly (see A on the scheme). This is not true when approaching the contact point. The finite distance that we introduced implies the existence of a region where the same number of particles available to explore is shared between twice more elements of surface (see B on the scheme). It is equivalent to say that a same number of particles is shared between more adsorption sites; hence a slower deposition rate.
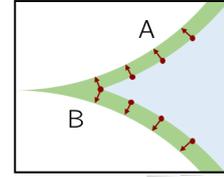
A second possible geometrical effect is worth noting. When particles approach a surface, they also approach previously deposited particles and get repelled by them to further elements of surface. When the surface considered in un-confined, the particles are brought to a nearby free adsorption site. On average, the number of adsorption attempts is therefore constant over the surface and only function of the current local coverage of the surface (see paths a_1 and a_2 on the scheme).
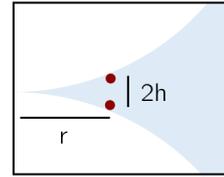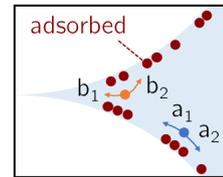
Now, when the same scenario happens close enough from a contact point, deposited particles can form a repulsive barrier preventing the exploration of the surface closer to the contact point (see paths b_1 and b_2 on the scheme). In that case, particles are more likely to move away from the confined region and the number of adsorption attempts is reduced towards the contact point. On average, the deposition there is therefore slower.

The length scale leading to such an effect can be estimated. An order of magnitude for the size of the entanglement is a few particle's diameters: $2h \approx 10^1 d_p \approx 0.4$ μm ($\mathcal{C} = d_p/h = 0.1$). Using the same geometrical framework as before (geometry of a cap of sphere; r_g the grain's radius), this value of h corresponds to a distance r from the contact point given by:

$$\frac{r^2 + h^2}{2r_g h} = 1$$

$$r = h\sqrt{\frac{2r_g}{h} - 1} \approx 3\mu m$$

$2r \approx 6$ μm defines the diameter of an area around the contact point where the mechanism of repulsion in confined conditions is plausible. The estimation remains rough and is

not observed directly, but is in the range of excluded diameters identified before ($[0-20]$ μm). To conclude, it can play a role when the excluded areas shrink to diameters of ≈ 10 μm but is not likely to explain the complete phenomenon.

5.3.4.2 Flow characterization

Besides pure geometrical aspects, let us now consider the local flow. Indeed, having different flow conditions between bulk and confined areas can be synonym of different mechanisms of approach of the surfaces.

Let us identify which transport mechanism dominates locally in this situation, in particular between advective and diffusive transports. The easiest way to do so is to calculate the Peclet number at the scale of the particles, as a function of the position near the contact point.

$$Pe = \frac{d_p v}{D}$$

The only unknown here is the local velocity. Because the flow is laminar, we know independently of the geometry that the velocity is maximal towards the center of the pore and tends to zero at the surfaces. We keep the average pore velocity used in the previous section, $v_0 = 0.55$ mm.s^{-1}, which is the slowest considered in this chapter. The Peclet number where the average velocity is reached (i.e. in the bulk space of the pore) is $Pe = 1.5 \times 10^3 \gg 1$. The particles there are transported by advection.

On the opposite, the no-slip condition at the wall imposes the existence of a distance from the surface where $Pe \ll 1$, i.e. where diffusion dominates. These two statements lead to the existence of a distance from the wall where an advection/diffusion transition occurs, at $Pe \approx 1$. At this location, the velocity is noted v_δ and is by definition:

$$v_\delta = \frac{D}{d_p} = 37 \mu m.s^{-1}$$

The corresponding distance, noted δ, can be seen as the thickness of a layer above the surfaces where diffusion prevails (*diffusive layer*). Unfortunately, the thickness of δ along the surface is not trivial to estimate because the exact flow field in such intricate geometry is experimentally unknown. In particular, it depends on the packing and the pressure gradient applied locally.

Additional studies on simulated flows have been done but did not raise precise conclusions. Fig.5.17 illustrates one attempt. A laminar cylindrical flow of imposed average velocity v_0 passes through a double obstacle made of two spheres (63 μm diameter) in contact. The velocity field at proximity of the contact point allows to identify color-coded
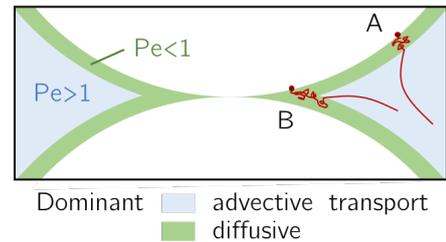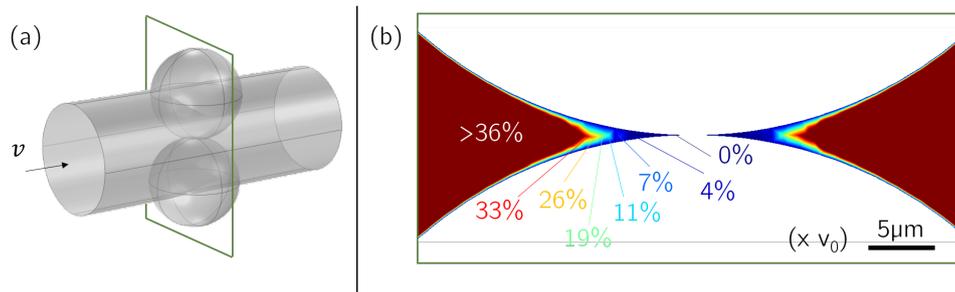
iso-velocity lines, in percents of v_0.

Figure 5.17: Finite elements simulation of the flow field around two beads ($\varnothing 63$ μm). (a) Overview of the system, (b) Mid-cut of the velocity map around the contact point. Colormap corresponds to iso-velocity lines, indicated in percentage of the imposed average velocity v_0.

In our example v_δ/v_0 is of the order of 10%, which corresponds to the color-code turquoise. Far from the contact point, the distance (δ) from the surface to this iso-line is reduced to a few tens of nanometers. It means that particles in this region diffuse over a narrow layer (a few times their size at most) before meeting the surface. As we look closer to the contact point, the diffusive layer widens and takes a maximum value in the contact point plane ($\delta \approx 6$ μm). Consequently, as particles flow closer to the contact points they encounter a thicker diffusive layer and take more time to explore the surface and eventually adsorb. For instance, a factor 2 in δ results in a average exploration time $t \propto \delta^2$ multiplied by 4.

As stated before, these considerations remain qualitative but provide coherent elements of explanation of the delayed deposition in confined areas.

In the end, we proposed a panel of mechanisms likely to play a role in the exact deposition dynamics in confined areas. Whatever the exact mechanism, the difference in dynamics and now been clearly proved and raises a last question: does is impact the global dynamics that we measured and characterized in section 5.2?

5.4 Overall dynamics characterization

The previous sections made clear that the dynamics of deposition are heterogeneous in our system. Section 5.2 focused on the global deposition trends (i.e. averaged fluorescence signal) while section 5.3 focused on the local discrepancies. The goal here is to combine these two visions to propose a final overview of the adsorption dynamics.

5.4.1 Propagation profiles in confined areas

5.4.1.1 Observations

As a starting point, we recall a confocal image already presented in section 5.2 ($v = 0.55$ mm.s^{-1}; cycle 3). It shows the global distribution of the adsorbed particles along several millimeters of sample. In addition, selected areas are magnified to show the eventual local heterogeneity in deposition (see Fig.5.18).
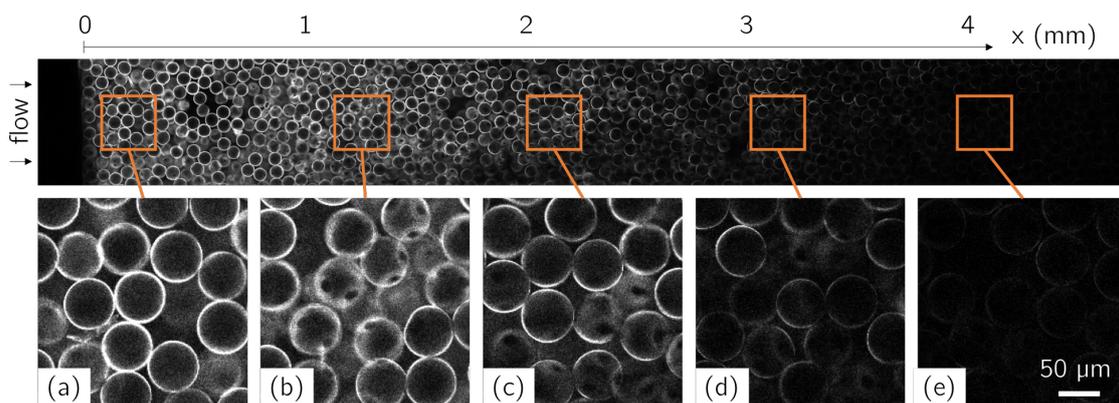
Figure 5.18: Selected areas along the depth of a sample where the global deposition ranges from saturated ($x \approx 0$ mm) to null ($x \approx 4$ mm). Example at $v = 0.55$ mm.s^{-1}; injection cycle 3.

The observations that we previously made over time translate here over space: at the tail of the deposition front (see (d)), the surfaces are hardly covered and the deposition appears low but homogeneous. When the deposition gets more advanced, the heterogeneity appears (see (c)) and gets more and more pronounced with increased coverage of the bulk surfaces. Finally, at locations where the front of deposition is already passed ($s = 1$; see (a)), the coverage is homogeneous again and 100% of the surfaces are fully covered.

5.4.1.2 Confined deposition profiles

From the global confocal signal, we deduced deposition profiles by summing the images over depth (see Fig.5.6 for example). Here, the aim is to apply the same principle to the

evolution of the confined areas over depth.

Unfortunately, no easy way has been found to isolate automatically the contribution from the confined and bulk zones. Therefore, for all positions for all acquired cycles, the contact points are manually identified. For each of them, the apparent excluded diameter d_{ex} is measured.

Like previously, the measure of the size of the excluded area gives access to a measure of the excluded surface per grain (of radius r_g), and to the local excluded surface fraction. We recall their expressions:

$$S_{ex} = 4\pi r_g^2 \left(1 - \sqrt{1 - \frac{(d_{ex}/2)^2}{r_g^2}}\right)$$

$$\sigma_{ex} = 6\frac{S_{ex}}{S_g} = 6\left(1 - \sqrt{1 - \frac{(d_{ex}/2)^2}{r_g^2}}\right)$$

More than the excluded surface, we are interested here in the saturation in the confined areas s_c, defined from zero to unity. When the excluded surface is maximal, the confined areas are free of particles, i.e. their saturation is zero. On the opposite, when the excluded surface is reduced to the contact point itself, the confined areas are saturated. It implies:

$$s_c = 1 - \frac{\sigma_{ex}}{\sigma_{ex}^{max}}$$

With σ_{ex}^{max} the maximal surface fraction concerned by the delayed (confined) dynamics. This maximum is achieved at the very beginning of the deposition, when the distinction between the two dynamics first occurs. The critical size for (visual) distinction of the heterogeneity was previously set at $d_{ex}^{max} = 20$ μm and is confirmed on the views here-above. Because our visualization of the phenomenon is limited by a good enough contrast (i.e. deposition), we assume that a slightly larger value (by 10%) is reasonable. Hence $d_{ex}^{max} = 22$ μm, and a value of σ_{ex}^{max} fixed at $\approx 35\%$. The meaning behind this number is that at the moment when the heterogeneity in dynamics starts, 35% of the surface of the system is affected by the delayed deposition dynamics. Even-though the deposition is at this moment far from saturation, it represents an impressively high fraction of the medium.

Back to our experimental data, the size of ≈ 950 contact points is measured over depth and cycles. The resulting values of confined saturation s_c are reported in Fig.5.19 (see markers). The manual acquisition combined to the diversity of configuration/orientation of the contact points leads to a large noise in the results.

Still, trends clearly stand out. For all cycles, the measures confirm a decay of the saturation of the confined areas at greater depths.
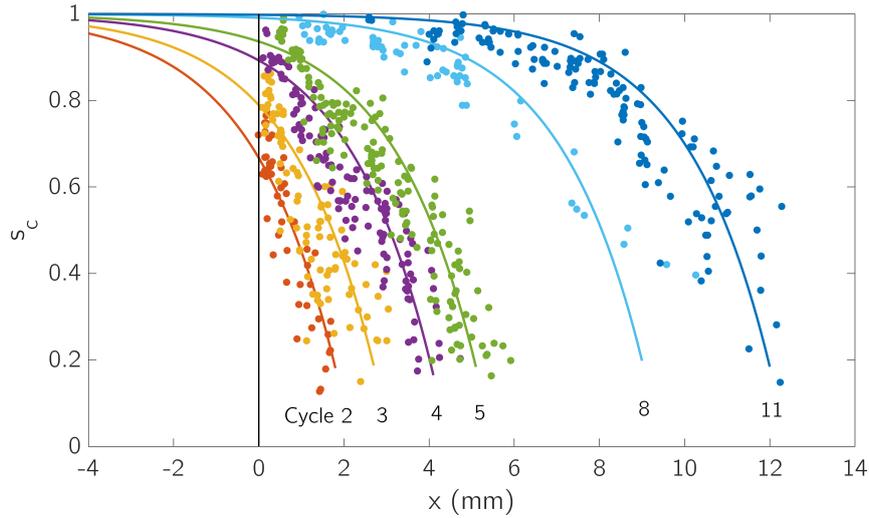
Figure 5.19: Saturation in confined areas s_c as a function of depth x. Disks are data points sorted by cycles of injection, lines are exponential fits $s_c = exp(-(x - x_r)/x_0)$.

All measured values of d_{ex} are smaller than the limit fixed at 22 μm. A direct consequence is that the profiles are not accessible for saturations below ≈ 0.2. In other words, we are not able to describe the saturation in confined regions when they do not stand out enough from the signal. Additionally, we note that all profiles drop quite sharply when s_c go to low values. It seems likely that these sharp slopes do not describe the very beginning of the deposition in the confined areas. This motivates our assumption to consider that a different early-deposition regime exists but that we do not access it experimentally.

In definitive, we have been able to extract the deposition dynamics in the confined regions only.

5.4.1.3   Towards decoupled bulk/confined dynamics

It is interesting here to recall what represent the profiles (saturation s versus depth for different times) initially presented in section 5.2. The global saturation s was obtained by summing the fluorescence signal over the width of the sample; therefore including the contribution of the bulk deposition and of the delayed confined deposition. We now have access to the deposition in confined areas separately; hence the question: can the two types of dynamic be fully decoupled?

As mentioned earlier, the separation between bulk and confined regions is a way of describing a phenomenon which actually is continuous and progressive. Still, it is useful here to see the medium as composed of two fully distinguished porosities: a large (bulk) filling faster than the other. We introduce the confined surface fraction f_c and the bulk surface fraction f_b. By definition, $f_b = 1 - f_c$.

146

The confined surface fraction f_c is the amount of surface ruled by the slower deposition. It is naturally equal to $\sigma_{ex}^{max} = 0.35$ introduced before. The complement, 0.65, is then assumed to account for the fraction of surface driven by the main dynamic. The global deposition is the weighted sum of each contribution. The only unknown here being the saturation in bulk conditions only, it is then isolated:

$$s = f_c s_c + f_b s_b = f_c s_c + (1 - f_c) s_b$$

$$s_b = \frac{s - f_c s_c}{1 - f_c} \tag{5.6}$$

Given the noise present in the experimental global profiles (see Fig.5.6) and the high variability of the confined profiles (see Fig.5.19), the operation (5.6) can not be applied directly on our data. Still, an overview of the decoupled dynamics is accessible by working of the model curves.

- For the global saturation s, our sigmoidal model in $1/(1 + exp((x - v_1 t)/\lambda))$ is used, with $t = j V_{inj} S \phi_0 / v$ (j the cycle number).

- For the confined saturation only, model curves in $s_c = 1 - exp((x - x_r)/x_0)$ are considered (see plain lines on Fig.5.19; and next subsection for a definition and discussion of the model).

Expression (5.6) is applied on those trends, which results in the decoupled dynamics presented in Fig.5.20.
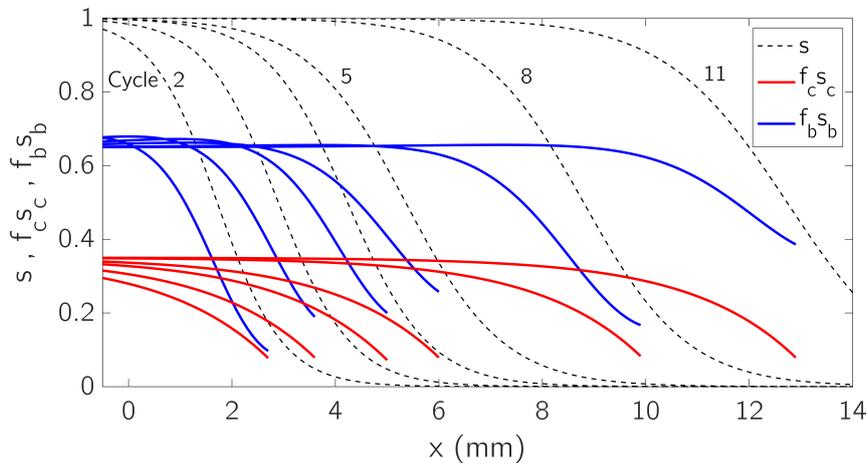
Figure 5.20: Decoupled confined (s_c; red lines) and bulk (s_b; blue lines) saturations. The global saturation is the sum of the two contributions (s; dashed lines, duplicated from Fig.5.6).

A first interesting note to take is that the confined dynamics follow quite well the propagation of the global deposition. In other words, the confined profiles s_c propagate in depth over the cycles in a way very similar to s. It means the deposition in confined

conditions follows the start of the deposition, or at least is triggered by the arrival of particles at a given depth of the system.

The profiles deduced for s_b naturally follow the same trend. The slope of the profiles (see blue lines) is increased: it is representative of the characteristic thickness of the front of deposition (λ) and therefore implies that the deposition in the bulk areas is actually confined to a narrower section of sample. Put another way, it means that the spreading of the particles was previously over-estimated because of the delayed deposition in the confined areas.

5.4.1.4 Confined front propagation

The fact that the dynamics in the smaller porosity also propagates as a front is challenged by applying the same change of variable as before: $X = x - v_2 t$. Because this front propagates with the global deposition front, the velocity v_2 is actually equal to the global front velocity $v_1 = \gamma v$.

Computing the rescaled depth for all data points (see Fig.5.21) reveals a single master trend. This result confirms the propagation of the confined deposition as a stationary wave following the advancement of the particles/bulk deposition over depth.
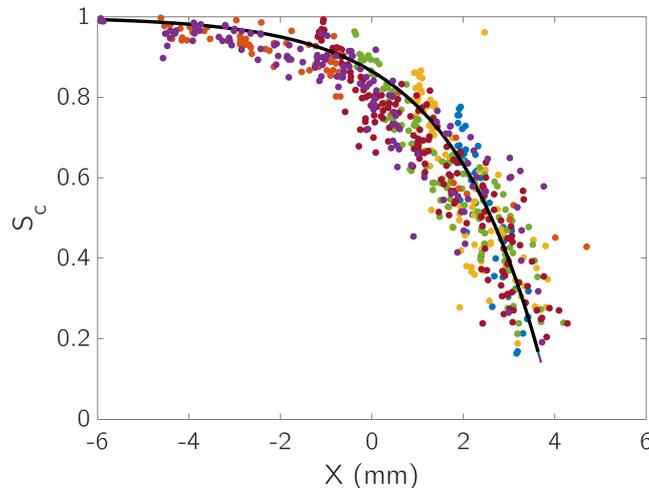
Figure 5.21: Saturation over rescaled depth. Profiles and data points from Fig.5.19 shifted according to variable change $x \rightarrow X$. The black line is the model in $S_c = 1 - exp(X/\lambda_c)$

Let us discuss further the shape of the profiles and master curve. Considering only bulk areas (section 5.2), the adsorption at a given time and space is limited by the amount of suspended particles available at proximity. It led to a relation in $\partial s/\partial t \propto n$.

Now considering only the confined areas, we proved that the adsorption starts with some retardation compared to the bulk. By definition, it also means that it starts after the passage of the pulse of suspended particles.

While a fraction of the suspended particles explores the bulk surfaces, another fraction enters the thicker diffusion layer along confined regions. Therefore, we can see this situation as the formation of a reservoir of particles diffusing for a longer time, exploring the space, and eventually adsorbing to free surface sites in the confined areas.
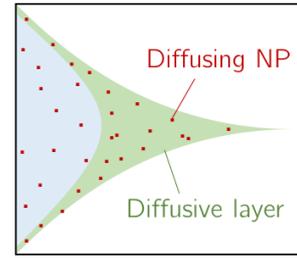
In addition, one can consider that the reservoir is re-filled at each new cycle of injection, which means that each injection adds a constant number of particles in the confined areas. Note that this assumption is motivated by the wave propagation of the deposition linked to the cycles. It seems valid only when the deposition is limited by the number of free surface sites to site and not by the slow diffusion of the first particles to the confined surfaces. In other words, is it expected to describe the reality of our system for $s \gg 0$ (that is for the flatest part of the dynamic).

In that case, the rate of deposition in the confined areas is proportional to the (constant) number of suspended particles in the reservoir and to the number of confined surface sites available. Defining k_c as the kinetic constant driving the adsorption event itself, it reads:

$$\frac{ds_c}{dt} = k_c n_c (1 - s_c) \tag{5.7}$$

(5.7) expressed regarding to the rescaled depth X rewrites as (5.8) and solves as follows:

$$\frac{dS_c}{dX} = -\frac{k_c n_c}{v_1}(1 - S_c) \tag{5.8}$$

$$\frac{dS_c}{1 - S_c} = -\frac{k_c N_c}{u_1}$$

$$-ln(1 - S_c) = -\frac{k_c N_c}{u_1}X = -X/\lambda_c$$

$$S_c = 1 - e^{X/\lambda_c} \tag{5.9}$$

In equation 5.9, λ_c is a characteristic length of spreading of the adsorption in confined areas over depth, echoing λ for the global case. The corresponding fit is presented in Fig.5.19 (see plain lines) and Fig.5.21 (dashed line, $\lambda_c = 2.0$ mm). This simple model correctly catch the trends of adsorption in confined areas, even-though the assumption of a constant number of particles in the confined zones has not been fully verified.

5.4.1.5 Perspectives

Overall, this result confirms our understanding of the process in this model dual porosity. The overall deposition, independent on the depth considered in a sample, is described

by the sum of two contributions for which we propose analytical solutions.

Interesting perspectives are still open. In particular, a study of the dynamics in the confined porosity as a function of the velocity would constitute as good complement. From our current understanding, the size and rate of coverage of the confined area is fully driven by the shape of the diffusive layer along the surfaces. As mentioned, the exact velocity and pressure fields remain unknown and prevent a full description of the situation.

For higher average velocities, one could expect the diffusive layer to be thinner and more concentrated around the contact points (transition velocity v_δ pushed closer to the walls). In consequence, the deposition in confined conditions would follow a similar dynamic but over a smaller surface fraction of the system.

5.4.2 Conclusions & discussions

5.4.2.1 Conclusion on high affinity and low confinement conditions

In the present chapter we focused on particles strongly interacting with the surfaces of the porous system but repelling each-other. To keep a very low confinement, we made the choice of nanoparticles. Even though they end up coverage the full surface of the porous system, their submicronic size and diffusive behavior led to an unexpected dual transport mechanism.

Over the porosity open to the flow (*bulk*), nanoparticles get efficiently in contact with the surface and adsorb until saturation is reached. This process keeps progressing in depth following the propagation of a stationary wave, with a characteristic depth of deposition driven by the velocity of the flow. On the contrary, the *confined* porosity can overall only be accessed by diffusive exploration of the nanoparticles. Since this porosity here represents up to 10% of the total surface, this retarded mechanism can have a large impact on the global propagation and adsorption of particles depending on the flow conditions.

In the end, only two mechanisms prevail along the axis accounting for surface affinity. Passing, repulsive (drag) forces dominate electrostatic forces; and adsorption when they do not. These trends are added to our diagram.
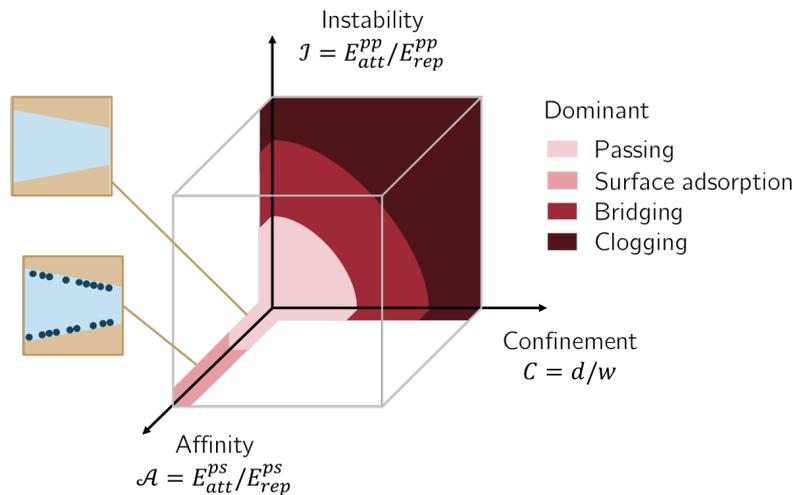
5.4.2.2 Openings - Importance of the pore size distribution

The interpretations of this chapter are strongly dependent on the specific geometry and confinement of the packs of beads we use. For generalization purposes, these points are further discussed.

In the case of nanoparticles and very low confinement in the complete porosity of the system, these results can be extrapolated to other types of porous media if we consider the following:

- The porosity smaller than the advection/diffusion layer is subject to slow, diffusion-driven adsorption.

- On the opposite, porosity larger than this critical layer is subject to quicker, mostly advection-driven adsorption.

For instance, as illustrated in Fig.5.22, considering rough surfaces instead of smooth beads like in our model can increase the actual fraction of pore size affected by slower dynamics. Systems with dual porosities can exhibit even larger opposite dynamics. It is the case for example for soil aggregates: millimetric grains form a first porosity and are themselves made of smaller grains aggregated together and forming a secondary porosity. These smaller grains are themselves rough or made of smaller entities, etc.

Pore size distribution

µm
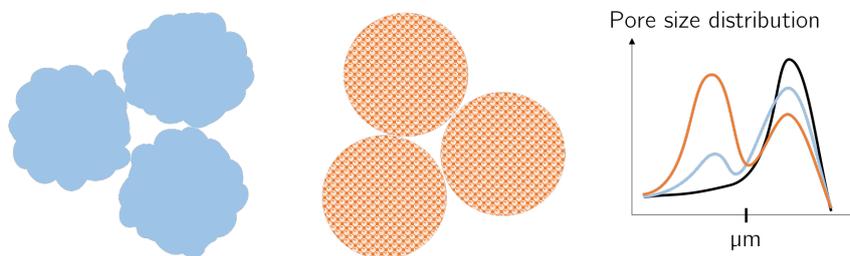
Figure 5.22: (left) Schematics of other systems likely affected by the phenomena described in this chapter: rough grains or multi-porous grains. (right) Drawing of the corresponding pore size distribution: our case in black, rough grains in blue and multi-porous grains in orange.

The $nZVI$ particles used in Chapter 4 are good examples. The pollutants targeted by these re-mediating particles are mainly submicronic, which means they can have a large diffusive behavior in low velocity systems. From the precedent SEM images of nZVI clusters, it is clear that their surface is very rough and multi-porous. On the one hand that is useful to maximize the surface where pollutants can adsorb. But on the other hand, it also increases the surface fraction that has to be explored by diffusion, and therefore the surface that will be covered according to a much slower dynamic.

Transition : on coupled mechanisms

Confinement / surface affinity coupling

So far, the particle deposition regimes for specific conditions of surface affinity and confinement have been studied. We described separately the confinement axis alone (passing, bridging, clogging regimes) and the surface affinity axis alone (passing, surface adsorption regimes). To have a complete understanding of the deposition mechanisms in the affinity/confinement ($\mathcal{A}/\mathcal{C}$) plane, one question remains: what can we expect from a coupling between these two parameters?
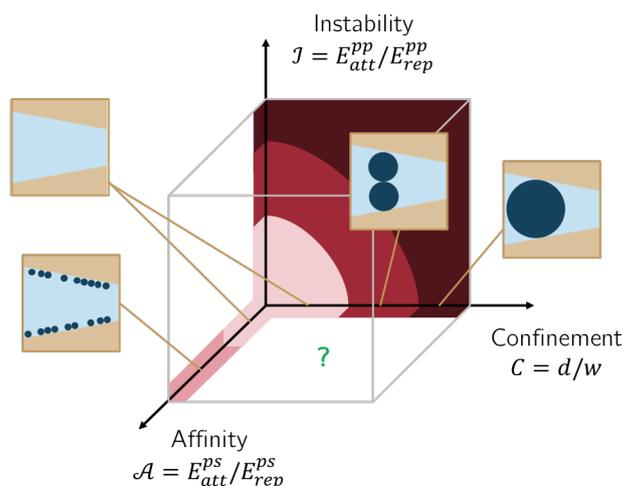
While it does not constitute a chapter on its own, some considerations help answer this question. To begin with, we highlight that the dual dynamic observed in chapter 5 is directly caused by the very low confinement conditions in this system. In other words, the nanoparticles are smaller than the inter-surfaces distance almost anywhere in the system. Let us take an arbitrary example: we look at what is happening at some distance from the contact point between two beads, where the surfaces are separated by 3 μm.
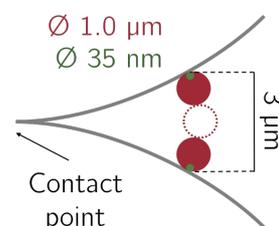
A nanoparticle ($d_p = 35$ nm) flowing in this "constriction" has a confinement ratio $\mathcal{C} = 10^{-2}$. Therefore, a particle adsorbing there will have no impact on the porosity and will not trigger bridging of clogging events. Now, we keep the surface affinity parameter constant ($\mathcal{A} =$cte) and increase the particle confinement ($\nearrow \mathcal{C}$). We consider 1.0 μm particles, subject at the same theoretical location to a confinement $\mathcal{C} = 0.33$. For them, a significant bridging probability exists.

No experimental study has been done in this work to specifically precise this point, but some SEM observations directly illustrate it. Fig.5.23 compares the distribution of particles near the contact point between two spherical beads (63 μm diameter) in two cases:

- On the left, nanoparticles are deposited quite uniformly on the surfaces and no distinction is visible between areas of inter-surface distance below or above 3 μm. As a side note, this view is a direct illustration of the results of chapter 5.

- On the right, 1.0 μm particles observed at a similar scale show a very different outcome. They easily form bridges that trigger their accumulation in a corolla at some distance from the contact point. We emphasis that this example is illustrative only, because we are not sure about which exact mechanisms led to this particle distribution.
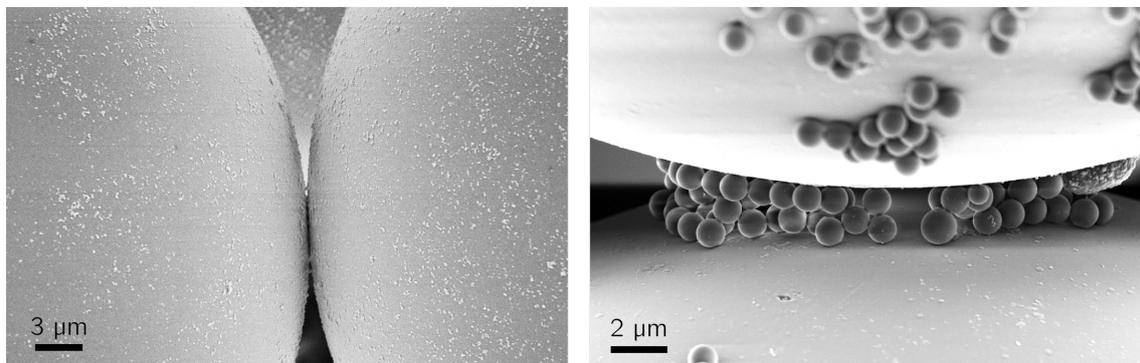

Figure 5.23: SEM imaging of 35 nm positively charged particles (left) and 1.0 μm nm positively charged particles (right) in the contact point area between two 63 μm silica beads.

These elements seem sufficient to assume that a coupling exists between high confinement promoting surface adsorption, and surface adsorption increasing the confinement in return. It allows us to infer a theoretical disposition of the deposition regimes in the surface affinity / confinement $\mathcal{A}/\mathcal{C}$ plane (see completed diagram here below):

- likely predominant passing at low confinement and low affinity,

- surface adsorption only at high affinity and low confinement,

- increased bridging probability at high affinity and high confinement.
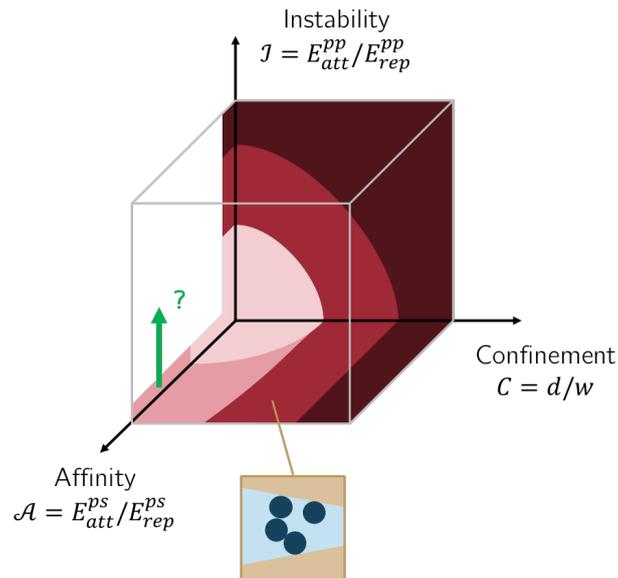
Surface affinity / particle stability coupling

From this updated diagram, on main challenge remains open: the deposition of particles having both a high affinity for the medium (high $\mathcal{A}$) and a significant tendency to adsorb to each-other (high $\mathcal{I}$).

So far, we showed that unstable particles tend to cluster, which triggers bridging and clogging in the absence of surface affinity. On the opposite, particles efficiently repelling each-other can adsorb to surfaces and form single layers. In the next chapter, the question will be: from a situation where surface layers are formed, how does the system react to a destabilization of the suspension?

Chapter 6

Particle-particle-surface interactions at low confinement

We focus now on micronic colloids, easier to observe than the previous nanoparticles. They are chosen of opposite charge than the surfaces of the porous matrix, to trigger surface adsorption events. Then, the particle-particle interactions are modulated via variation of ionic strength of the suspensions. In the continuity of chapter 5, the porous media (3D packs of spherical beads) and type of imaging (confocal) are conserved.

Comparing the particle size $d_p = 1.0$ μm to the average pore size $w \approx 15$ μm results in a confinement ratio $\mathcal{C} = 5 \times 10^{-2}$. This value confirms the low confinement conditions of the study. As in the previous chapter, the surface affinity ratio $\mathcal{A}$ here compares the particle-surface attractive electrostatic energy to the drag work applied on a particle attaching to the surface of the system. The charge of the particles is chosen to achieve $\mathcal{A} \gg 1$, i.e. favorable surface adsorption. Finally, the instability ratio $\mathcal{I}$ compares the inter-particle electrostatic forces to the drag work applied between two particles adsorbing in the flow. Via the modulation of the repulsion/attraction conditions, we will move from predominant inter-particle repulsion ($\mathcal{I} \ll 1$) to predominant cohesion ($\mathcal{I} \gg 1$).

6.1 Specific Material & Methods

6.1.1 Materials

6.1.1.1 Porous media & working fluid

This chapter reuses the porous media introduced in the previous chapter: 3D packs of borosilicate beads (63 μm) at random close packing in $1 \times 1 \times [10 - 20]$ mm^3 glass capillaries. Likewise, the saturating fluid is the same to keep the system index-matched: a 13:87vol% mix of dH$_2$O:DMSO.

6.1.1.2 Inter-particle interactions modulation

We recall from section 1.3 that the DLVO theory describes the force between charged surfaces interacting through a liquid medium: it can therefore be applied here to two interacting charged particles. We focus here on the medium-long range electrostatic forces and consider the short range Van der Waals forces as constant.

It has been shown that the characteristic thickness of the EDL is well represented by the *Debye length* $\lambda = \kappa^{-1}$. In a solution of ionic strength I and relative permittivity ϵ_r, at a temperature T, the inverse of the Debye length writes:

$$\kappa = \sqrt{\frac{\epsilon_r \epsilon_0 k_B T}{2 \times 10^3 \mathcal{N}_A e^2 I}}$$

With $\mathcal{N}_A$ the Avogadro number and e the elementary charge. In particular, $\kappa^{-1} \propto I^{-1/2}$ shows that an increase in ionic strength decreases the thickness of the EDL, i.e. the distance of repulsion between particles. The ionic strength itself derives directly from the ions in solution. For n types of ions, of concentrations $[c_1..c_n]$ and charges $[z_1..z_n]$, the ionic strength is defined as

$$I = \frac{1}{2}\sum_{i=1}^{n} c_i z_i^2$$

As only monovalent salts are used in this work, their case is considered more precisely. For a generic salt at concentration c, made of a cation of charge $z = +1$ and a anion of charge -1, $I = 1/2 * [c(+1)^2 + c(-1)^2] = c$. The ionic strength is directly measured by the salt concentration. It has the unit of a concentration: $mol.L^{-1} = M$.

6.1.1.3 Suspended colloids

Ideally, in the continuity of chapter 5, we could try to modulate the adsorption of the nanoparticles used in this thesis. The main reason preventing this choice is that even if

particles actually start adsorbing to each-other at higher ionic strength, our imaging resolution is limited in identifying it. Individual particles are smaller than the minimal pixel size (around 200 nm). The distinction between single layers of nanoparticles or stacks of nanoparticles could only be deduced from a variation in the fluorescence intensity.

A more direct way to access the particle distribution (layer or stacks) at the surfaces in to increase the particle size so that it becomes larger than the imaging resolution. Therefore, 1 μm colloids are introduced. We choose them in latex and with a positive surface charge theoretically easy to modulate. The main properties of these colloids are listed in Table 6.1.

Supplier		ThermoFisher Scientific
Reference		FluoSpheres^{TM} microspheres
Catalog	#	F8765
Mean size	d_p	1.0 μm (supplier), 1.0 μm (measured)
Composition		latex
Density	ρ_p	1.04 $g.cm^{-3}$
Functionalization		Amine groups
Fluorescence	λ_{ex}	505 nm
	λ_{em}	515 nm (yellow-green range)

Table 6.1: Colloids properties (source: thermofisher.com)

Size. The sphericity and monodispersity of the colloids announced by the supplier are verified experimentally. From SEM pictures of dried settled colloids (see Fig.6.1, left), a distribution of the measured particle diameters d_p is deduced (see Fig.6.1, right). The conclusions are that the particles are perfectly spherical (less than 1% of oblongue particles) with a monodisperse size $d_p = 1.0$ μm ± 80 nm.

Diffusion. As before, the diffusive behavior of the particles is evaluated by estimating the diffusion coefficient $D = k_B T / 3\pi\mu d$, with $k_B = 1.38 \ 10^{-23}$ J.K^{-1} the Boltzmann constant. Like in the previous chapter, T is taken as the room temperature (293 K) and μ as $\mu_{WF} = 3.3$ mPa.s. The diffusion coefficient is then calculated at $D = 4.4 \ 10^{-16}$ m^2.s^{-1}, which is very low compared to the previous nanoparticles. The particles are not expected to diffuse significantly in the experiments (see section **??** for a validation).

Zeta Potential The zeta potential of the colloids is given by the supplier in water: $\zeta = +30$ mV. A precise measurement in our working fluid was not possible by classical electrophoresis method, because of the difference in electrophoretic mobility between water and DMSO, which induces inhomogeneous migration of the suspension during the application of the electric field. In other words, in the case of this mix of solvents, the measure given by the apparatus is based on a coupled solvents/particles mobility and is
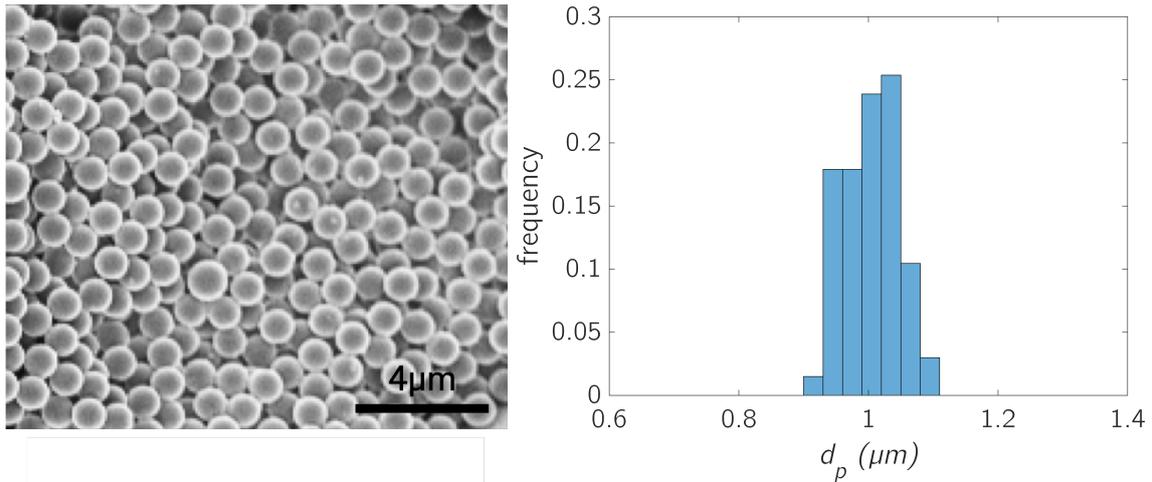
Figure 6.1: (left) SEM image of dried stacked colloids. (right) Distribution of colloid diameter d_p, over 100 particles extracted from SEM images like (left).

not representative of the particle only.

Still, considering (i) the value measured in pure DMSO ($\zeta = +12$ mV), and (ii) the low water to DSMO ratio of our working fluid, we assume a Zeta potential in the working fluid $\zeta \geq 12$ mV. Such positive values are consistent with colloids forming a stable suspension and favorably adsorbing to borosilicate surfaces. This stability is verified when injecting the suspension at the inlet of our a porous medium: only independent single colloids are observed. What is more, it gives an estimation of the values of the surface potential of the colloids, usually slightly higher than the zeta potential.

6.1.1.4 Suspensions used for the modulation

In theory, any salt can be used to vary the ionic strength of the solution. Here, the system imposes an additional constraint: a high solubility of the salt in both water and DMSO. Many studies performing ionic strengths modulation use potassium chloride KCl or sodium chloride $NaCl$, but those salts have a very low solubility in DMSO. It means that the concentration (and the ionic strength) of the fluid can be varied in a very narrow range. For this reason, sodium iodide NaI is chosen for this work. Its solubility in pure DMSO is 0.16 g.mL^{-1} (against 2.1×10^{-3} g.mL^{-1} for KCl) [Reynolds and Silesky 1960]. In the mix (13 vol% water), the solubility rises to 0.30 g.mL^{-1}. This value is verified experimentally by progressively adding sodium iodide to working fluid until some remains undissolved. The non-dissolution criterion chosen is that salt crystals remain suspended (settled) even a week after their addition. Over four different tests, the average solubility measured is $sol = 0.303$ g.mL^{-1} - the value expected from the literature.

From the maximum amount of salt that can be dissolved, the accessible range of ionic strength is calculated. Knowing the molar mass of the salt $M^{NaI} = M^{Na} +$

$M^I = 23 + 127 = 150$ $g.mol^{-1}$, the concentration (and ionic strength since the salt is monovalent) is $I = sol/M$. The maximum ionic strength achieved at salt saturation is $I = 2.0$ M. In the end, the ionic strength can be varied between this saturation value and the ionic strength of the pure fluid. We select six values over six orders of magnitude: $I = 2.0 \times 10^0$, 2.0×10^{-1}, 1.0×10^{-1}, 1.0×10^{-2}, 1.0×10^{-4} and 1.0×10^{-6} M. We assume here that the added salt has no other significant effect than the variation in ionic strength.

6.1.2 Methods

6.1.2.1 Confocal imaging & injection

At a given time during the experiments, the confocal fluorescent channel provides an image where all fluorescent components appear: both suspended and adsorbed particles. This can be an issue since particles flowing near a surface or near previously adsorbed particles can be interpreted on a picture as deposits. To distinguish suspended and adsorbed particles, the *time averaging method* is set (see Fig.6.2). When several images (5 to 10 in this work) are performed in a short time interval (of the order of 100 ms), adsorbed particles appear at the same position on all images but suspended particles appear at slightly different positions since they flow downstream. On the average image, the adsorbed particles therefore appear fully bright while the intensity of the suspended particles fades away. In the end, the deposits are selectively imaged.

In the precedent chapter, a large range of velocities has been explored. It implied the use of injection/rinse/imaging cycles to image the systems at comparable number of injected particles. That is not needed here as this study do not focus on the influence of the flow-rate. The injection of suspension is continuous over all the experiment.

A constant flow-rate is chosen at $Q_0 = 5$ μL.min^{-1}. The value is fixed arbitrarily for two reasons: (i) an average fluid velocity to be close to the velocities used in soil remediation applications ($v \approx 10^0$ mm.s^{-1}); as well as (ii) significant but progressive particle adsorption during the experimental imaging time (up to 10 hours). As before, the flow occurs in the square capillary over a surface $w^2 = 1$ mm^2 with an average porosity $\phi_0 = 0.4$, hence an average fluid velocity $u_0 = Q_0/w^2\phi_0 = 1.9 \times 10^{-4}$ m.s^{-1}. Like previously, local and global views of the particle deposition are confronted. To do so, several scales of studies are used (see Fig.6.3):

(i) the complete media, from inlet to outlet by the *tilescans* method, to assess the deposition dynamics over depth.

(ii) the fraction of media near the inlet, to picture the dynamics in a reduced region where the concentration of suspended particles is assumed constant (see below). This region is roughly 1×0.3 mm^2, i.e. the full width of the medium times ≈ 5 bead' diameters in depth.
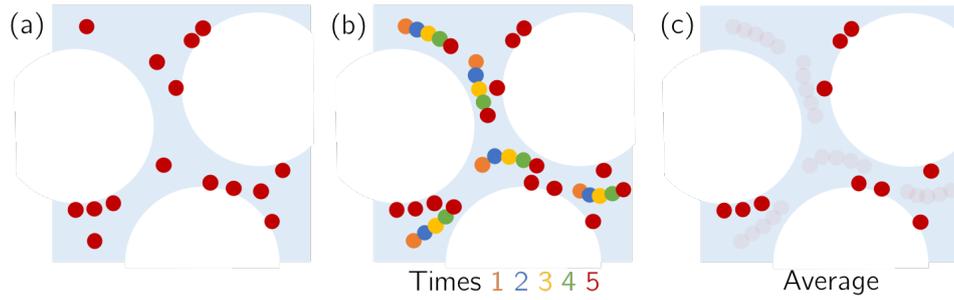
Figure 6.2: Illustration of the time averaging method; fluid in light blue, porous medium in white. (a) Image resulting from a single frame acquisition: suspended and adsorbed particles appear with the same intensity. (b) Superposition of 5 frames at 5 close successive times. (c) By averaging the frames from (b), suspended particles fades away and adsorbed particles stay bright.

(iii) local views of area $50 \times 50 \ \mu m^2$ to $150 \times 150 \ \mu m^2$, to present specific configurations of deposits.
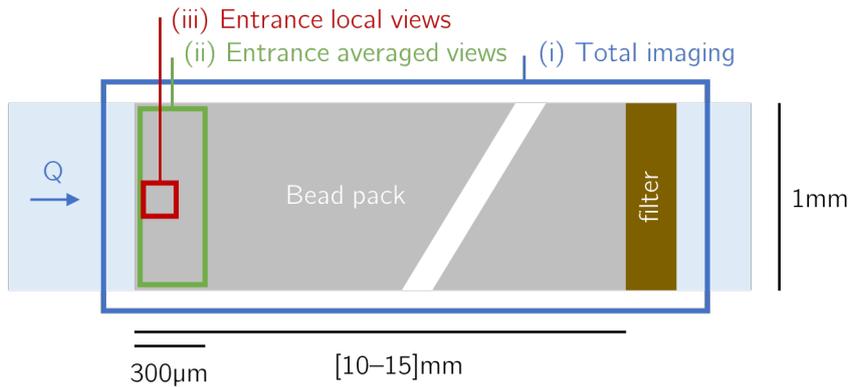
Figure 6.3: Illustration of the three views/scales used in this chapter: (i) global image of the system, given access to deposition over depth, (ii) focused view on a $\approx 300 \ \mu$m slice at the entrance of the system, (iii) local view to explore specific local dynamics.

In the first part of this chapter (sections 6.2 and 6.3), we will analyze the colloidal deposition dynamics at the entrance section of the system. The interest is that, there, the dynamics is expected to be easier to understand, since the concentration of suspended particles can be assumed constant. Two facts support this assumption. First, a constant concentration C_0 is imposed at the inlet, which means the concentration is at least constant at the very first layer of beads forming the pack. Then, the second part of this chapter (sections 6.4) will show that the deposition dynamics is uniform over a depth equal or lager to the chosen entrance section.

6.2 Surface-limited adsorption

6.2.1 Local surface adsorption mechanisms

6.2.1.1 Observations

We first consider the case of particles with a fully developed repulsive potential, to echo the case treated in chapter 5. In a $150 \times 150 \ \mu m^2$ window near the entrance of the porous medium, the amount and distribution of adsorbed colloids is followed over time (see Fig.6.4). At the beginning of the experiment, the surfaces of the borosilicate beads are free of adsorbed particles since no fluorescence is visible. After 40 min of injection, sparse bright dots appear: they correspond to individual colloids adsorbed on the surfaces. Adsorption goes on; in just 30 additional minutes the outline of the beads is clearly visible. From this point on, even 8 additional hours of injection only slightly change the state on deposition. The outline of the beads just becomes denser but its average thickness does not vary.
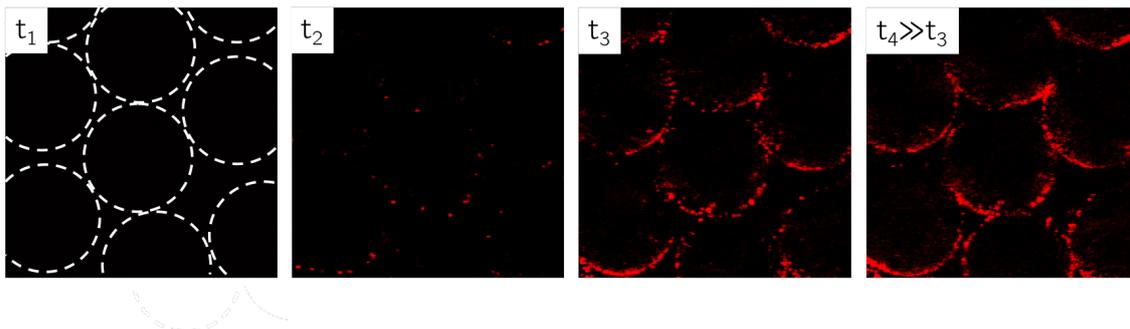
Figure 6.4: Confocal imaging over a $150 \times 150 \ \mu m^2$ window at 4 times, for $I = 1 \times 10^{-6}$ M; flow goes from bottom to top. Matrix (beads) and void space appear black; adsorbed colloids appear red. ($t_1 = 10$ min) Initial state; no adsorbed particles; white dashed show the position of the beads' surfaces. ($t_2 = 40$ min) Sparse adsorbed particles. ($t_3 = 70$ min) Non-uniform single layer visible at the surface of the beads. ($t_4 = 9$ h) Denser single layer.

The distribution of particles achieved at the end of the experiment (saturated state) is surprising. A single layer of particles is visible at the surfaces but a clear asymmetry appears between the bottom and the top of the bead. With the suspension flowing bottom to top, it means that the deposition is predominant on the upstream side of the beads.

6.2.1.2 Local particle trajectories

An explanation for this asymmetry comes from the *interception* mechanism expected to lead to adsorption events (see Fig.6.5). Assuming a purely advective approach of

the colloid, it will only interact (i.e. intercept) with the surface of a bead if it follows a streamline passing closer to the bead than its own radius (see (a)). If that is the case, it will naturally encounter first the upstream side of the bead. Interception does not necessarily lead to an adsorption event, but even if the particle bounces on the surface and flows downstream to intercept a new element of surface, the probability to adsorb upstream still remains higher. A second aspect is to consider (see (b)): previously adsorbed particles form a roughness on the surface than can divert the streamlines of arriving particles or the particles themselves by inter-particle repulsion. This effect is similar to the *shadow* effect [Ko and Elimelech 2000] and limits the accessibility of the downstream surfaces.
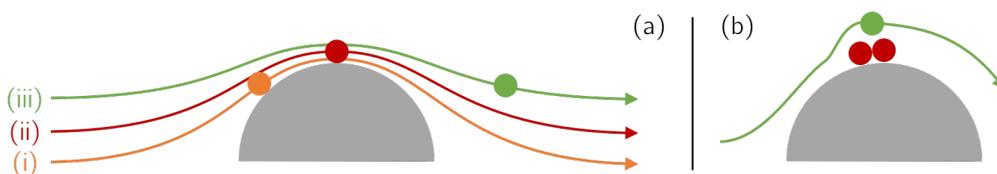
Figure 6.5: (a) Schematics of the interception mechanism. Following the streamline (i), a particle has high chances to intercept the upstream surface of a bead. That is valid until (ii): from this point on streamlines bring particles further than one radius to the surface and not interception event is triggered. (b) Schematics on how adsorbed particles can repel a particle away from the downstream surface.

The interception mechanism relies on particles following the trajectories of streamlines without disruptions. This fact is questionable given the non-punctual nature of the particles and the potential local velocity variations in this complex geometry. An experimental validation is proposed by following particles over time when they approach a surface with already deposited particles. Experimentally, we focus on a $50 \times 50 \ \mu m^2$ region and record the position of the suspended particles over time (i.e. we momentarily do not use the averaged images). Over a ≈ 60 s movie, the positions of the particles are color-coded and stacked to provide a view of their trajectories. They are observed along the surface of a bead facing a rather large pore throat (30 μm) to better assess the effect of the distance from the surface (see Fig.6.6, left).

Different behaviors can be distinguished. Far from the surface (see (a)), the colloids follow pretty straight trajectories and seem to follow a streamline. Getting closer from the surface (see (b)), the trajectories become more wiggly. Finally, at a distance from the surface comparable to a few colloid diameters, the trajectories show large fluctuations of amplitude comparable to multiple particle diameters (see (c)). Note that the surface they are running along is not flat but is simultaneously covered with adsorbed particles (see (d)).

Let us analyze the nature of these fluctuations. A first natural assumption is to call upon a random walk due to particle diffusion. A simple verification comes from an
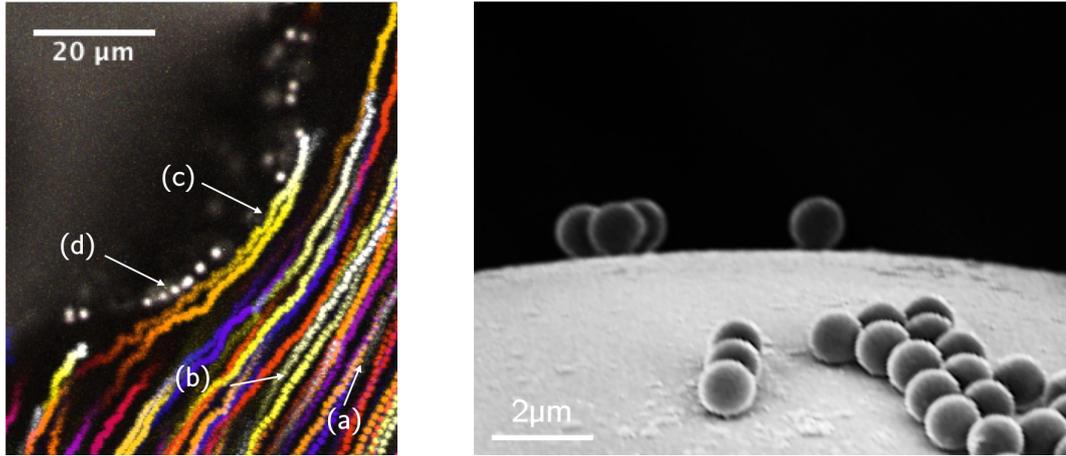
Figure 6.6: (left) Superimposed positions (i.e. trajectories) of colloids flowing far (a), near (b) or directly along (c)the surface of a bead on which other colloids adsorbed (d). Colors are added to differentiate particles. (right) SEM view of the surface of a bead with a few adsorbed colloids, to give a sense of the surface roughness created by the deposits.

estimation of the local Peclet number at the scale of the colloid $Pe = d_p v / D$. The diffusion coefficient is equal to 1.3×10^{-13} $m^2.s^{-1}$ and v is the local velocity which can be deduced from the average pore velocity $v_0 = 1.9 \times 10^{-4}$ $m.s^{-1}$ (see 6.1.2). Assuming a Poiseuille profile from the surface to the center of the pore, the velocity at a distance of 2 colloid diameters from the surface is $v(2d_p) = 2v_0(1 - (r_{pore} - 2d_p)^2 / r_{pore}^2)$, hence $v = 1.0 \times 10^{-4}$ $m.s^{-1}$. Back to the calculation of the local Peclet number, $Pe > 10^2$. Therefore, no significant diffusive transport is expected and the assumption is invalidated. Another way to visualize this is to consider the amplitude of the fluctuations. Looking at particle (c) for instance, the amplitude is estimated at $h \approx 2$ μm$= d_p$. By diffusion, such displacement can on average be achieved in a time $t \approx h^2 / D = 31$ s. This is very long compared to the timing observed here: h is traveled in the order of one second.

Since the fluctuations are not diffusive and the flow laminar, these variations are likely due to an effect of the local velocity field. More precisely to the fact that the flow is constantly disturbed by the continuous adsorption events. Indeed, each adsorbing particle creates an additional roughness at the surface of the porous medium. In response, the flow evolves to adapt to the roughness. The trajectories of the flowing particles are deviated which creates local instantaneous fluctuations. On top of that, the amplitude of the fluctuations is augmented by the repulsion between adsorbed and flowing particles, and between the flowing particles potentially approaching each-other when deviated from their original streamline. Since Fig.6.5 is already at the spatial and temporal limit of our imaging capacity, this point could not be studied in more details. As further tests, it would be very interesting to image with a better time resolution the flow and deposition of particles at the surface of a single bead places at the center of a capillary (similar to the single collector model), to have even more model flow and geometry.

To conclude on the surface approach mechanisms, we can state that they are not trivial but on average correctly described by an frequency of attempts of particle-surface collisions.

6.2.2 Global deposition dynamics

6.2.2.1 Experimental profile

To better evaluate the adsorption dynamics at the scale of many beads and not just a few, the field of view of the study is opened to all beads at the entrance of the porous medium. The fluorescence signal is cumulated over a ≈ 5 beads strip and cumulated over time (see Fig.6.7). From no deposition (i.e. no fluorescence), the number of adsorbed particles increases sharply and reaches a plateau value. As we know from chapter 5 and from the images that this plateau corresponds to a single layer of particles, the fluorescence signal F is the number of particles adsorbed at he surface S normalized by the maximum particle capacity of a single layer S_0. This ratio defines the surface saturation $F/S_0 = S/S_0 = s$, from zero to unity (plateau).
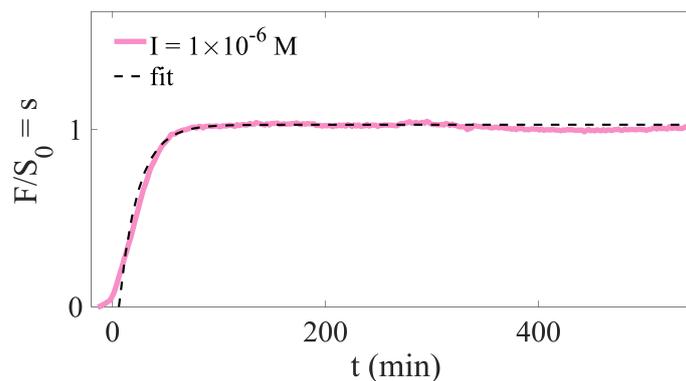
Figure 6.7: Cumulated fluorescent intensity F normalized by the maximum surface deposition intensity S_0, i.e. surface saturation s as a function of time t. Experimental data (pink) fitted by the surface deposition model $s(t) = 1 - exp(-kt)$ with $k = 5 \times 10^{-4} \ s^{-1}$ (black dashes).

6.2.2.2 Comparison with the adsorption of nanoparticles

As this situation echoes the previous case of suspensions of nanoparticles, it is interesting to compare the dynamics. The data set from the last chapter, used to compute depth propagation dynamics, can also be used to compute over time the amount of deposition at the entrance of the system (see Fig.6.8.c). The trend for the nanoparticles is identical to the one we just witnessed for micronic colloids: the saturation reaches a plateau over time, when the full single layer of particles is formed. The apparent dynamic is the same, but the particle distribution is very different. They result from separate

mechanisms, listed here-below and illustrated in Fig.6.8.(a) for micronic particles and (b) for nanoparticles.

- For the nanoparticles to approach the surfaces of the system, we showed that a diffusive transport through a more or less thick layer is required. It implies that, in the end, all surfaces are reached and the medium is covered at 100%. We also showed that diffusive transport mechanism does not significantly participate to the transport towards the surface for the 1 μm particles.

- For the micronic colloids, the interception effect (even when modulated by fluctuating trajectories) excludes in first approximation half of the surfaces.

- In addition, the finite size of the particles implies that a volume around the contact points are stericaly excluded. In the case of nanoparticles (35 nm), this limitation is not visible. But for 1 μm colloids, it represents another fraction of the surface of the beads which is not accessible to deposition events. Refer to Fig.5.23 for an SEM illustration of this steric effect.

Overall, similar conditions (repulsive particles forming a single layer of deposit) lead to very different outcomes depending on the particle size and type of transport towards the surfaces. More importantly, a difference in size of two orders of magnitude (from 10^1 to 10^3 nm), makes the maximum coverage of medium drop from 100% to less than 50%. This information is critical to correctly predict the surface fraction of a system subject to adsorption.
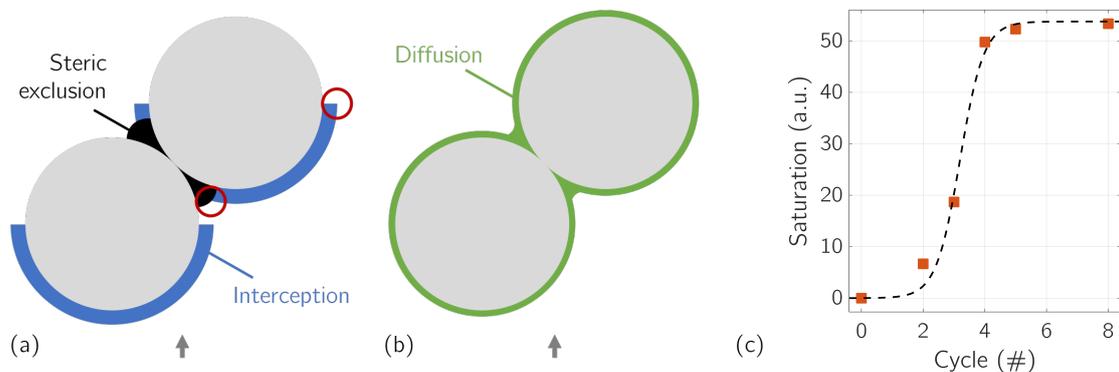

Figure 6.8: (a) Main surface approach mechanisms in the case of the micronic colloids. (b) Main surface approach mechanisms in the case of the nanoparticles from chapter 5. (c) Saturation over injection cycles from chapter 5.

6.2.2.3   Modelling the single-layer deposition

Back to the average dynamics at the entrance of the medium, the Langmuirian mechanism introduced before can also be tested here. It relies on the assumption that the

particles are transported to surface adsorption sites independently of other particles. This assumption seems invalid here since we clearly showed that a flowing particle can be impacted by previous deposits (see trajectories). The fluctuations in the particle trajectory also go against more basic hypotheses of the model: homogeneous surface and equivalence of all surface adsorption sites in particular. When the approach is valid, the predicted saturation over time writes:

$$s(t) = 1 - exp(-kt)$$

With k a kinetic constant characteristic of the adsorption dynamic. This exponential trend fits correctly the experimental measures (see Fig.6.7, dashed line) with $k = 5 \times 10^{-4} \ s^{-1}$, which shows that the model remains globally valid despite the complex way particles attempt to explore the surfaces.

The slight deviation from the model at $t \leq 0$ is attributed to the shape of the front of suspended particles at the beginning of the injection. Due to some dispersion, the front is not expected to be perfectly straight but to include a short area of lower particle concentration, leading to an initial lower adsorption rate.

To conclude, we validated that unconfined particles, attracted by the surfaces by repelling each-other form a saturated single layer at the surfaces. In addition, large differences in terms of actual surface coverage appear as a function of particle size and approach mechanisms. Let us now explore the effects of a modulation of the inter-particle repulsion using the $1 \ \mu$m colloids.

6.3 Modulated adsorption

6.3.1 Adsorption dynamics

The previous section treated the case of a suspension where no salt had been added ($I = 10^{-6}$ M). Let us now progressively increase the ionic strength and perform the same experiment.

6.3.1.1 Observations

At a slightly higher ionic strength ($I = 10^{-4}$ M), the situation is similar to the reference case (see Fig.6.9): sparse independent adsorption events (see t_2) are followed by the formation of deposits on the surface of the beads (t_3). A major difference is that the deposits are at some places not limited to a single layer of particles anymore. This observation is a logic consequence of the increase in I, since particle-particle adsorption are now more favorable.

Following this, one could expect that inter-particle bounding continues to go on top of the surface layer until, eventually, complete filling of the pore space. This does not seem verified: the deposits after a long injection time (9 h; t_4) remain thin regarding to the pore size.
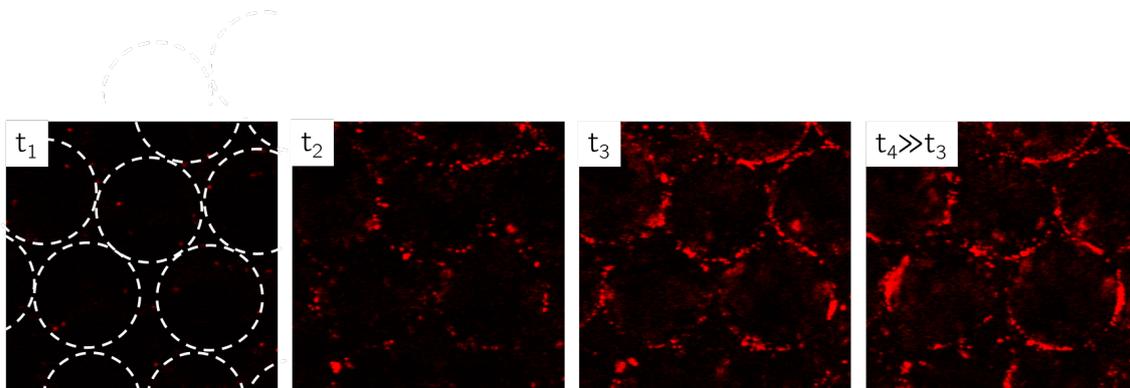
Figure 6.9: Confocal imaging over a 150×150 μm^2 window at 4 times, for $I = 1 \times 10^{-4}$ M; flow goes from bottom to top. Matrix (beads) and void space appear black; adsorbed colloids appear red. ($t_1 = 10$ min) Initial state; no adsorbed particles; white dashed bead outlines. ($t_2 = 40$ min) Some adsorbed particles, outlining the surfaces. ($t_3 = 70$ min) Deposits at the surface and on top of the surface. ($t_4 = 9$ h) Slightly larger deposits.

By increasing more the ionic strength, the deposition significantly increases (see Fig.6.10; example at $I = 1 \times 10^{-1}$ M). The adsorption of individual particles at the surfaces is soon followed by the adsorption of other colloids on top of them. Over time, a thick (and fairly uniform) layer of particles is formed. This further increase in

ionic strength made the particle-particle adsorption events more likely. Even though the spatial resolution is not good enough to clearly count individual colloids, the thickness of the deposits is of the order of 5 μm, i.e. 5 particles. Again, despite this important accumulation, the pore space is far from being filled at the end of the experiment (see $t_4 \gg t_3$).
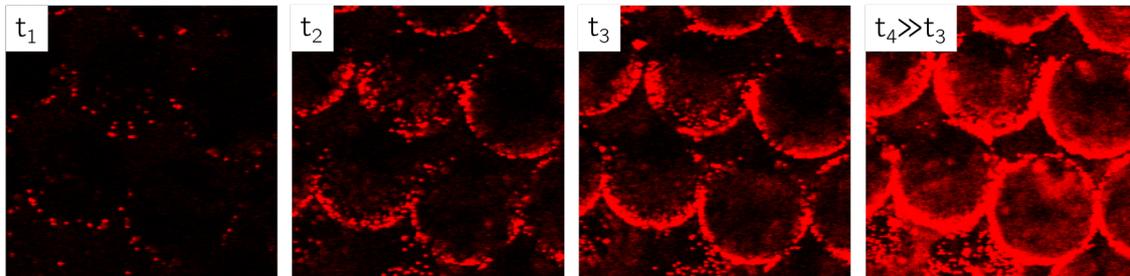

Figure 6.10: Confocal imaging over a 150×150 μm^2 window at four times, for $I = 1 \times 10^{-1}$ M; flow goes from bottom to top. Matrix (beads) and void space appear black; adsorbed colloids appear red. ($t_1 = 10$ min) Initial state; white dashed bead outlines. ($t_2 = 40$ min) Deposit close to a single surface layer. ($t_3 = 70$ min, $t_4 = 9$ h) Several layers of deposit.

With further increase in I, the situation gets trickier to study (see Fig.6.11 for $I = 2 \times 10^0$ M, at the dissolution limit of our salt). After an injection time ($t_2 = 40$ min) previously leading to an initiation of surface layer, the system is here largely filled with colloids. Quickly, the presence of so many polystyrene particles breaks the index-matching of the system and the images get blurry and saturated because of the diffracted fluorescence.In consequence, this condition of ionic strength is now considered as critical for our study capabilities and will be treated separately as an extreme case.
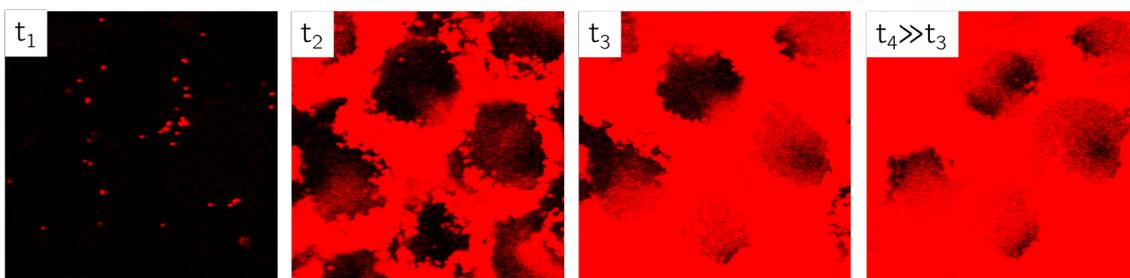

Figure 6.11: Confocal imaging over a 150×150 μm^2 window at four times, for $I = 2 \times 10^0$ M; flow goes from bottom to top. Matrix (beads) and void space appear black; adsorbed colloids appear red. ($t_1 = 10$ min) Initial state; white dashed bead outlines. ($t_2 = 40$ min) Dense deposit, filling the pore space ($t_3 = 70$ min, $t_4 = 9$ h) Blurred confocal image by the presence of too many non-index-matched particles in the void space.

6.3.1.2 Deposition dynamics over time

The global deposition dynamics become clearer when the number of adsorbed particles is computed over time along the entrance of the media. Six values of ionic strength are considered to encompass the several situations we just described. The amount of adsorbed particles F is, as before, normalized by the maximum number of particles fitting in a surface layer S_0 (estimated from the case at $I = 10^0$ M).
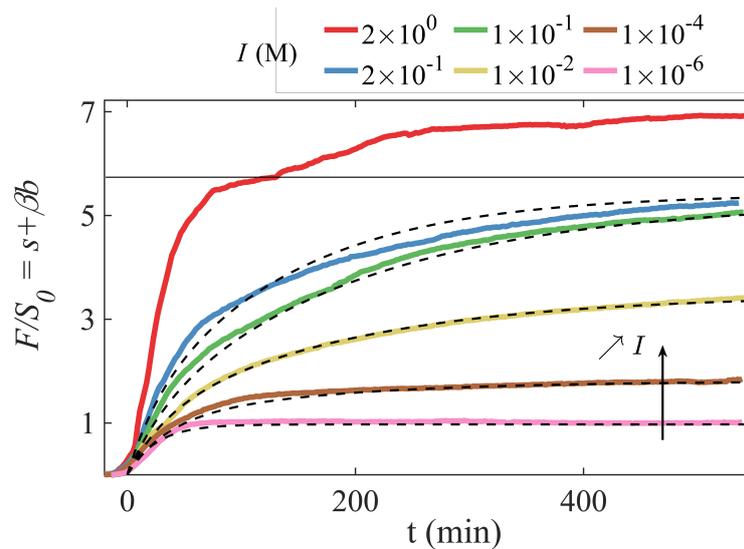

Figure 6.12: Cumulated deposition with regards to a saturated surface layer $F/S_0 = 1$, as a function of time t. Increasing ionic strengths from bottom to top. Horizontal line at $F/S_0 \approx 6$ indicates the deposition value where the confocal images before too blurred by the accumulated colloids to provide quantitative deposition measures.

   The main curves are gathered in Fig.6.12, including the profile already presented in Fig.6.7 corresponding the lowest ionic strength (lowest curve; pink). From there, higher ionic strengths lead to higher depositions. Cases have been mentioned where deposition is larger than a single surface layer, which implies that F/S_0 can take by definition values larger than unity. In particular, two cases prevail, below and above 10^{-0} M.

   From $I = 10^{-4}$ M to 2×10^{-1} M, the rate of deposition is at first large (sharp increase in F/S_0) and decays over time. After 9 hours of injection, the deposition is not exactly stopped but the profiles clearly tend towards a plateau value. A confrontation of these dynamics and of the previous direct images allows to draw interesting conclusions: the deposition slows down over time and stabilizes when a certain number of layers of particles is formed on top of the surfaces. That is surprising because a flowing particle can now in principle adsorb to any nearby adsorbed particle and new suspended particles arrive continuously. In consequence, adsorption should go on and an unlimited continuous deposition is expected. Note that this conclusion also confirms that the images at

$t_4 = 9$ h are representative of the final states of deposition in each condition of ionic strength.

The case $I = 10^{-0}$ M (red profile) corresponds to Fig.6.11. The deposition increases sharply before saturating. As seen from the images, this deposition value is not representative of the real deposition. Because of the large accumulation of non-index-matched particles in the pores, the acquired fluorescence signal is not qualitative anymore. This effect is assumed to be visible on the profile from the strange inflection point after one hour of injection. Still, we recall the main observation from the corresponding images: a large fraction of the pore space is in this case filled with adsorbed particles.

To account for deposition on top of the surface layer $s = S/S_0$, the particle saturation in the *bulk* phase (i.e. in the pore space on top of the surface layer), b, is introduced. It is defined as the number of particles adsorbed in bulk B divided by the maximum number of particles fitting in this space B_0 (equivalent to an average pore capacity, minus the surface layer). b is therefore a saturation between zero and unity. The global deposition is now a sum of the surface and bulk deposition components $F = S + B = sS_0 + bB_0$. We still consider it with regards to the surface saturation:

$$\frac{F}{S_0} = s + \frac{B_0}{S_0}b = s + \beta b$$

Where the factor β compares bulk filling capacity to the surface filling capacity. In other words, it means that the bulk deposition is equivalent to β times the surface deposition. In our specific system, given the particle to pore sizes ratio, the bulk represents a larger fraction of the pore space than the surface layer. β is therefore expected to be larger than one.

To deduce β from the experimental profiles, we need to identify a case where both the deposition F, the surface satuation s and the bulk saturation b are known simultaneously. Then $\beta = (F/S_0 - s)/b$. Unfortunately, when the bulk adsorption reaches saturation ($b = 1$, $I \approx 10^0$ M, assuming $s = 1$), our measure of the deposition is not quantitative. On the opposite, when our measure of F is quantitative, the fraction of bulk saturation b is unknown. In consequence, an estimation of the value of β is postponed to later sections, where the physical mechanisms of deposition are better understood.

6.3.1.3   Flow-rate influence on the deposits

It is now clear that the adsorption of particles in conditions of low inter-particle repulsion is actually limited to a fraction of the pore space, and that this fraction is a function of the ionic strength. Increasing ionic strengths make particles more and more likely to bound. This change in interactions likely affects the bounding dynamics but does not explain the existence of the saturation. Only one other parameter is susceptible to play

a role in particle adsorption: the local flow conditions, in particular the local velocities and velocity gradients.

The fact that velocity participates or not to the deposition state is verified experimentally. From the same experiment as before, at saturation, pure working fluid is injected at different flow-rates. At the same flow-rate Q_0 than the previous particle injection, no change in the deposition state is observed. In particular, no particle detachment is seen. Then, the flow-rate is raised to $4Q_0$: the deposition state evolves with the detachment of pieces of deposits, before stabilizing at a new equilibrium state. When the system is completely stable (i.e. after waiting several minutes), the operation is repeated at $8Q_0$ and $16Q_0$ (see Fig.6.13). Again, the distribution of deposited particles drastically changes. With increasing steps of flow-rate, the deposits on surfaces exposed to the flow are detached while the deposits near contact points remain.
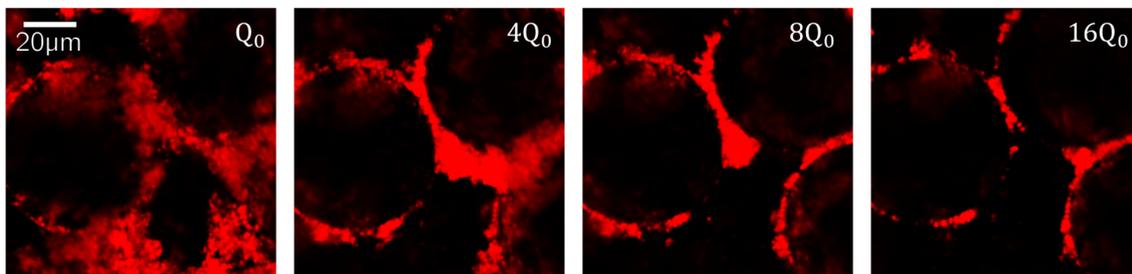
Figure 6.13: Selected 100×100 μm^2 window at the entrance of the system; $I = 2 \times 10^{-1}$ M. Pure working fluid is injected by steps at Q_0, $4Q_0$, $8Q_0$ and $16Q_0$, which modifies the shape of the deposits.

It has been shown in chapter 5 that, in the working conditions, the areas around contact points correspond to low velocity zones. We can therefore correlate the areas where the deposits remain to the areas of lower velocities. On the opposite, deposits in the areas of larger velocity are torn away from their location when the average velocity increases.

In the end, local velocity clearly rules the shape and extent of the deposits. The exact distribution of particles in given conditions of flow and ionic strengths result from an equilibrium between the cohesive (electrostatic) forces between adsorbed particles and the drag induced on the particles by the presence of local velocity gradients. Beyond some critical velocity, the drag force is so large that no adsorption is possible and deposition reaches a saturation value. More precisely, the equilibrium is driven by the following causality: as a deposit grows, the porosity decreases. Since the flow-rate is constant but the volume accessible to the flow is smaller, the local velocity increases. The drag force on the particles increases. The cycle goes on until the drag force takes over the cohesive force.

This only shows the existence of a saturation value reached when drag forces dominate inter-particle cohesive forces. It defines a binary regime: either cohesion predominates and adsorption events happen, either drag predominates and prevents further deposition. In such conditions, the probability of adsorption is unaffected until the equilibrium is reached, i.e. the rate of deposition is constant. This should result in a dynamic similar to the one shown in insert: a linear deposition until the critical velocity, and then a plateau value. It does not describe the progressive decay in adsorption rate observed experimentally.
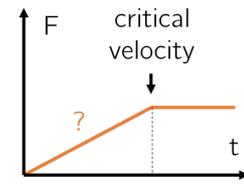
The decay of $\partial F / \partial t$ over time highlights an additional key point: the probability of adsorption is not constant but decreases as deposition occurs. The explanation sill comes from the effect of local velocity and appears through a model we will now detail.

6.3.2 Modelling the cohesion/drag coupling

6.3.2.1 Energies at stake

Let us precise the interactions taking place. As a particle approaches at a short distance from a previously deposited particle, it interacts with it through Van der Waals forces and electrostatic forces. The interaction is well represented by a potential $\Phi = \Phi^{VdW} + \Phi^{EL}$ function of the inter-particle distance, that we recall from sections 1.3 and 6.1. In particular, when the surfaces of the two particles are close enough (separation of the order of primary attractive well, a few nanometers), they adsorb to each-other.

The depth of the well, here called $\Delta\Phi$, defines how much energy has to come from disruptive forces to separate the two entities. It is a function of two parameters (the distance to the surface d_0 and the Debye length κ^{-1} and is calculated via $\Delta\Phi = | \Phi^{VdW}(d_0) | - \Phi^{EL}(d_0, \kappa)$. An example is provided in Fig.6.14, showing Φ as a function of the distance to the particle surface d. It was generated using the potential expressions from 1.3. With $d_0 = 2$ nm, $\Delta\Phi$ is given by the depth of the potential at this location (see depth of point A, at low ionic strength $I = 10^{-3}$ M for instance). With increasing ionic strength and decreasing Debye length, the potential deepens, which means that more energy is required for cohesive forces to be overtaken (see point B). Note that for short enough Debye lengths, the global potential Φ gets confused with the Van der Waals contribution only Φ^{VdW}.

From the cohesive forces, let us detail the main disruptive force in this study: the drag force applied on the newly attached particle. Indeed, the system can be reduced to a deposited particle delimiting the boundary of the system (velocity tends to zero) and a particle momentarily stopped at a distance $d_p/2$ from the boundary (non-zero velocity). The drag force is proportional to the particle size itself, to the fluid viscosity and to the velocity differential at the locations of the particles. It writes $F_D = 6\pi\mu d_p v_{d_p}$, with v_{d_p}
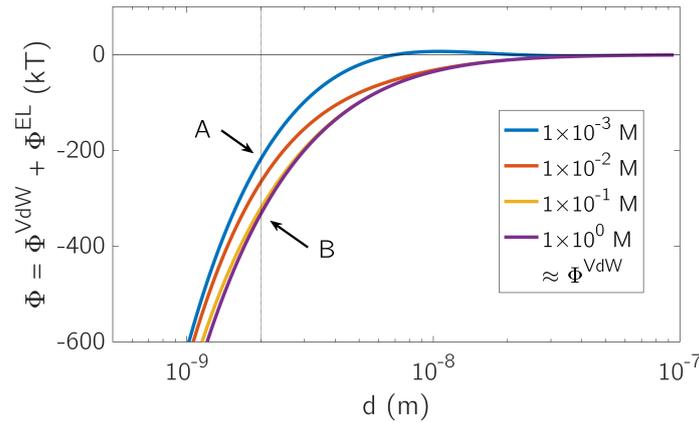
Figure 6.14: Global potential as a function of the distance to the surface d, for four values of ionic strengths. Calculated from potential expressions of 1.3. The vertical line corresponds to $d = d_0 = 2$ nm.

the velocity at a distance d_p from the surface. Assuming that the distance of application of the force is the particle size itself, it results in a work W_D expressed by:

$$W_D = 6\pi d_p^2 \mu v_{d_p}$$

The condition for the drag to prevent the adsorption of a particle is fulfilled when $W_D > \Delta\Phi$, i.e. where the left term increases with increases velocity and the right term decreases with increasing ionic strength. The critical velocity v_c at which the two energies are equal is extracted:

$$v_c = \frac{\Delta\Phi}{6\pi\mu d_p^2}$$

We can verify from this expression the effect of an increase in ionic strength. It is equivalent to a shortening in Debye length and a deepening of the primary well of potential energy $\Delta\Phi$, increasing proportionally the critical velocity. At higher ionic strength, deposition can progress further before v_c is reached: that is what we observe experimentally.

6.3.2.2 Evolution of the porosity

A key point to go further is to link the state of deposition to the velocity in the system. We consider a unique model pore and set its initial radius to R_0. We assume a uniform deposition around the pore, so that the pore radius goes from R_0 to $R < R_0$ over time (pore clogging corresponds to $R \to 0$).

By definition, the bulk deposition b can be expressed in 2D as the filled cross-section of the pore to its entire cross-section (see Fig.6.15.a). The choice of a 2D representation is motivated by the will to compare directly this model to the experimental data, that

are 2D cross-sections of the media. b writes:

$$b = \frac{\pi R_0^2 - \pi R^2}{\pi R_0^2} = 1 - \left(\frac{R}{R_0}\right)^2 \tag{6.1}$$

Now about the velocity; a Poiseuille profile is assumed from the center to the edge of the pore. Its expression is reminded from section 1.3: the velocity at a distance r from the central axis of the pore of radius R, with an average pore velocity $\bar{v}$, is $v(r) = 2\bar{v}(1 - r^2/R^2)$.

As the porosity is decreasing, the average velocity is increasing accordingly at constant flow-rate. The average velocity at a given time is linked to the average velocity at time zero v_0 by the equality of the flow-rates $\bar{v}R^2 = v_0 R_0^2$. In the end, the velocity profile in the pore of evolving radius R writes as (6.2). Note that this expression directly links the velocity profile in the pore and the state of deposition b, by injecting (6.1) in (6.2), $R = \sqrt{1-b}R_0$. It is not showed explicitly as a function of b because the further considerations are easier to develop in terms of pore radii.

$$v(r) = 2v_0 \left(\frac{R_0}{R}\right)^2 \left(1 - \frac{r^2}{R^2}\right) \tag{6.2}$$

If the critical velocity v_c is reached in the pore, it implies to existence of a critical radius R_c defined as follows: between the pore center and R_c, $v \geq v_c$; between R_c and the pore wall $v < v_c$. At the position $r = R_c$, $v = v_c$, hence from (6.2):

$$R_c = R\sqrt{1 - \frac{v_c}{2v_0}\frac{R^2}{R_0^2}}$$
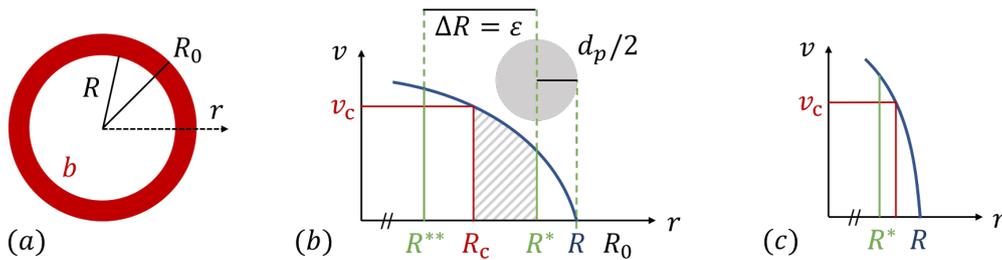
Figure 6.15: Notations used in the model. (a) Model circular pore, of radius R_0 initially and R over time, delimiting a deposition corolla b. (b) Schematics of the velocity profile near the pore wall, in the case $R_c \in [R^{**}; R^*]$. Dashed area is favorable for adsorption. (c) Velocity profile in the case $R_c > R^*$. No position is favorable for adsorption.

6.3.2.3 Towards an adsorption probability

Let us now assume that particles are uniformly distributed in the pore, in the range $r \in [0; R]$. Two conditions on their position are required for them to adsorb (see

Fig.6.15.b for an overview of the notations):

- be close enough from the surface to get in contact with it, in particular at the rhythm of the fluctuations of trajectories. This distance to the pore wall, of the order of a particle diameter but not precisely measured, in noted ϵ. It corresponds to a distance from the pore center $R^{**} = R - \epsilon$. In addition, because of their finite size, the particle centers are limited to a distance $d_p/2$ from the pore wall, i.e. $R - d_p/2$ from the pore center. This distance is noted R^*. Only the particles in the interval $\Delta R = [R^{**}; R^*]$ are at a position suitable for adsorption.

- be located further than the critical radius R_c from the pore center; that is be in a velocity region compatible with dominant cohesive forces.

This description allows to define a probability of adsorption. Three cases can be distinguished depending on the velocity profile in the model pore.

(i) If the velocity is lower than the critical velocity everywhere in the interval $\Delta R = [R^{**}; R^*]$, all particles in this area candidate for adsorption. The probability of adsorption p in this situation is the area corresponding to this interval divided by the cross-section where the suspensions is flowing. Therefore:

$$p_{v(\Delta R) < v_c} = \frac{\pi R^{*2} - \pi (R^* - \epsilon)^2}{\pi R^{*2}} = 1 - \left(\frac{R^{**}}{R^*} \right)^2$$

R^* and R^{**} are geometrical parameters independent of the state of deposition. As long as $v(\delta R) < v_c$, ΔR is a constant distance but the pore radius decreases. Consequently, ΔR represents a growing fraction of the pore size and this model predicts that the probability of adsorption increases as porosity decreases.

(ii) Then, when the critical velocity v_c is achieved somewhere in ΔR, only a fraction of the particles in this interval actually has an approach velocity compatible with adsorption. Equivalently, $R_c \in \Delta R$. The adsorption probability p is (see (b); dashed area):

$$p_{v_c \in v(\Delta R)} = 1 - \left(\frac{R_c}{R^*} \right)^2 = 1 - \left(\frac{R}{R^*} \right)^2 \left(1 - \frac{v_c}{2v_0} \frac{R^2}{R_0^2} \right)$$

The trend is here opposite to (i); p_2 is maximal for $R = R_0$ (initial state) and decreases with decreasing pore radius.

(iii) From there, the system reaches a point where the velocity in the complete interval ΔR is above the critical velocity, which means any particle attempting to adsorb will likely be dragged by the flow. That is equivalent to $R_c > R^*$ (see Fig.6.15.c). The interval of positions suitable for adsorption is reduced to zero, hence:

$$p_{v(\Delta R) \geq v_c} = 0$$

Regime (ii) well describes the behavior observed in the experimental profiles. It explains the progressive decay in adsorption rate by a reduction of the fraction of particles available for adsorption as the porosity increases, because of an increase in average velocity. Regime (iii) following regime (ii) is also coherent with the observations: when no particle fulfills the adsorption conditions anymore, deposition stops. In the following comments, we consider than our system falls in conditions of velocity field leading to regime (ii) and (iii). Still, regime (i) could be expected for different systems or flow conditions, in particular for larger pores or a lower flow-rate.

At this point, it is possible to express the adsorption probability as a function of the deposition itself (see (6.3)). The expression is not trivial but well presents the main trends of the deposition mechanisms (see Fig.6.16 for a representation of $p(b)$ for critical velocities in the range $[0; v_0/2]$). Indeed, for any value of critical velocity, p is maximal at the initial state ($b = 0$) and decays over time. It reaches $p = 0$ (i.e. deposition stops) at a value of bulk deposition b that corresponds to a saturation value b_{sat}. With increasing critical velocity (i.e. increasing ionic strength), the initial probability of adsorption is higher and the system reaches saturation at a higher value of b. As observed in the experiments, it means a thicker final deposit.

$$p(b) = 1 - \frac{R_0^2(1-b)}{(R_0\sqrt{1-b} - d_p/2)^2}\left(1 - \frac{v_c}{2v_0}(1-b)\right) \qquad (6.3)$$
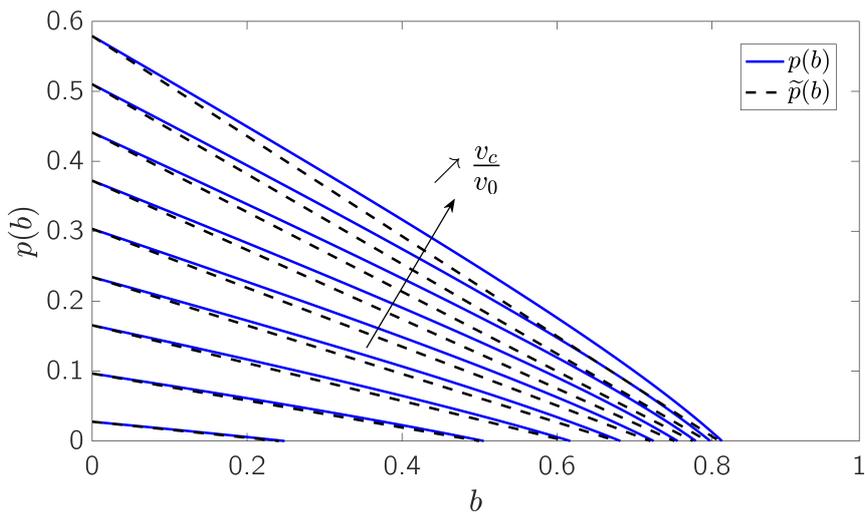
Figure 6.16: Adsorption probability as a function of the bulk deposition. Model expression (blue, plain) and approximated expression $\widetilde{p}$ (black, dashed); see 6.3.2.4.

6.3.2.4   Model simplification

In our description of the trends, it appears that the probability is easily described by an initial probability and a bulk deposition saturation value b_{sat}. Given the shape of the probability curves, it is tempting to define a simplified form of p, in particular via the function:

$$\widetilde{p}(b) = p_0 \left(1 - \frac{b}{b_{sat}} \right)$$

Where p_0 is the initial probability, deduced from (6.3) at $b = 0$:

$$p_0 = p(b=0) = \frac{R_0^2}{R_0^{*2}} \left(1 - \frac{v_c}{2v_0} \right)$$

Similarly, an expression of b_{sat} is extracted from (6.3) and (6.1). b_{sat} is reached at the transition between regimes (ii) and (iii), when the critical velocity is reached at the closest position from the surface, R^*. At this moment, the final (and minimal) radius R_{sat} of the pore is reached. R_{sat} and b_{sat} are expressed as follows:

$$p_{v(R^*)=v_c} = 0 = 1 - \left(\frac{R_{sat}}{R^*} \right)^2 \left(1 - \frac{v_c}{2v_0} \frac{R_{sat}^2}{R_0^2} \right)$$

$$\frac{v_c}{2v_0} = \frac{d_p R_0^2}{R_{sat}^3} \left(1 - \frac{d_p}{4R_{sat}} \right)$$

In cases where the saturation is reached far from a clogging state, R_{sat} remains significantly larger than a single particle size d_p, hence ($d_p/4R_{sat} \ll 1$) and equation (6.4). Combined with (6.1), it finally leads to b_{sat}.

$$R_{sat} \approx \left(\frac{2v_0}{v_c} d_p R_0^2 \right)^{1/3} \tag{6.4}$$

$$b_{sat} = 1 - \left(\frac{2v_0}{v_c} \frac{d_p}{R_0} \right)^{2/3} \tag{6.5}$$

We now have expressions for b_{sat} and p_0. The simplified form $\widetilde{p}$ is presented along p in Fig.6.16 (dashed lines). It is by definition a linearisation of the adsorption probability as a function of deposition. At low critical velocity (lowest curves), $\widetilde{p}(b)$ perfectly follows the dynamics of $p(b)$. For increasing v_c, the adsorption probability at initial state and final state of the system are perfectly described; but the probability decay over time is slightly overestimated.

We recall that this expression was obtained under the assumption that the pore size R remains significant before a single particle radius $d_p/2$, i.e. the pore is not close from clogging. In the end, the simplified form $\widetilde{p}$ is retained as it carries a strong physical meaning that we will now develop.

178

6.3.2.5   Model bulk deposition dynamics

Now that the saturation state has been described, it is useful to express the deposition over time $b(t)$. The adsorption rate $\partial b / \partial t$ is naturally proportional to the probability of adsorption on top of this first layer, $p(b)$. Since the adsorption in bulk is conditioned by the adsorption of particles at the surface, it is also proportional to the surface deposition s. With k' a kinetic constant characteristic of the frequency of the bulk adsorption attempts, considered constant in this study, the adsorption rate reads:

$$\frac{\partial b}{\partial t} = k' s p(b) = k' p_0 s \left(1 - \frac{b}{b_{sat}} \right)$$

The term $k' p_0$ can be rewritten as a global bulk kinetic constant k_b, characteristic of both the kinetics of the particle-particle approach events and of the probability for a particle approaching a deposited particle to actually adsorb.

Looking at the particle deposit as a whole, as a first approximation, it means that the process can still be considered as a Langmuirian process until a saturation value of deposited volume fraction b_{sat} is reached. It is now clear that $\widetilde{p}$ carries a natural description of a deposition towards saturation, with a given dynamic and a plateau value. Still, it is worth emphasizing that the expression in not only natural: it was derived in a way given access to precise formula for b_{sat} and p_0 as a function of the experimental conditions.

The bulk deposition is conditioned by the surface deposition. On the opposite, we assume that the dynamics of surface deposition are not affected by the particles depositing in bulk. Obviously, the presence of thicker deposits around the site can complicate the accessibility of surface adsorption sites, but we consider that, in standard conditions on ionic strength ($I < 10^0$ M), the filling of the surface layer occurs fast before the bulk deposition. These considerations will be validated with direct observations in the next section.

Assuming s independent of b allows to consider than the previous solution for the surface dynamics $s = 1 - exp(-kt)$ still holds. Using this expression, the bulk adsorption rate $\partial b / \partial t$ has an analytic solution (6.6); obtained after variables separation and integration from $t = 0$ to t and $b(0) = 0$ to b.

$$\frac{\partial b}{\partial t} = k_b \left(1 - exp(-kt) \right) \left(1 - \frac{b}{b_{sat}} \right)$$

$$\frac{b'}{1 - b/b_{sat}} = k_b (1 - exp(-kt))$$

$$-b_{sat} ln \left(1 - \frac{b}{b_{sat}} \right) = k_b \left(t + \frac{exp(-kt)}{k} \right)$$

$$b(t) = b_{sat} \left[1 - exp \left(\frac{k_b}{k b_{sat}} (1 - exp(-kt) - kt) \right) \right] \tag{6.6}$$

We verify $\lim_{t \to 0} b(t) = 0$ and $\lim_{t \to \infty} b(t) = b_{sat}$. This final expression is fairly simple considering the complex mechanism it is based on. Via k_b (therefore p_0) and b_{sat}, it depends on the initial pore radius, on the particle size, and more importantly on the critical velocity imposed by the ionic strength conditions.

In addition we note that the model for $s(t) = 1 - exp(-kt)$ is present in the final form of $b(t)$. When the filling of the surface layer is fast before the bulk dynamics ($s \to 1$), a simplified form of $b(t)$ is:

$$b(t) \overset{s=1}{\approx} b_{sat} \left[1 - exp \left(\frac{k_b}{k b_{sat}} \right) exp \left(-\frac{k_b}{b_{sat}} t \right) \right]$$

This model finally provides a fully analytical expression for the global deposition, accounting for surface and bulk adsorption mechanisms: $F/S_0 = s(t) + \beta b(t)$.

6.3.2.6 Numerical application & trends

Before moving to a direct comparison with the experiments, let us recall which parameters have already been calculated/estimated and which remain as fitting parameters.

- The Hamaker constant H, the contact distance d_0 and the surface potential Φ_0 have been calculated in section 2.1.

- The viscosity μ, average velocity v_0, particle size d_p and (variable) ionic strength I are imposed by the user, therefore known.

- The value for the average pore size is fixed at $R_0 = 15$ μm. This choice results from two facts. First, in an ideal packing of beads, the diameter of the largest sphere fitting between the beads is $1/6^{th}$ of the bead diameter. Here: $63/6 = 10.5$ μm, which is an underestimation since pores are larger in a RCP. Then, on our confocal images, sizes of 15 ± 10 μm are measured. The mean value 15 μm is coherent and retained.

- The kinetic constants k and k' are fitted parameters. The value k has already been deduced from the deposition at lowest ionic strength, via the model $s = 1 - exp(-kt)$. This value (5×10^{-4} s^{-1}) is kept for all other cases of I.

The main dependencies of the function defined in the model are also reminded:

$$v_c = f(\mu, d_p, H, d_0, \Phi_0)$$
$$b_{sat} = f(R_0, d_p, v_c, v_0, I)$$

$$k_b = f(p_0(R_0, d_p, v_c, v_0, I), k')$$

$$b = f(b_{sat}, k_b, k)$$

In addition to k', a single other fitting parameter remains: the bulk to surface ratio β. To estimate the coherence of the trends given by the model so far, we arbitrarily fix the values of those two unknown. We use $k' = 10^{-2}$ min^{-1} and $\beta^{arb} = 10$ to compute the evolution of the bulk deposition $b(t)$ and the global deposition $s(t) + \beta^{arb} b(t)$ (see Fig.6.17.a and .b respectively). Arbitrary ionic strengths are used for the computation: $[10^{-6}, 10^{-5}, 10^{-4}, 10^{-3}, 10^{-2}, 10^{-1}, 10^{0}]$ M.
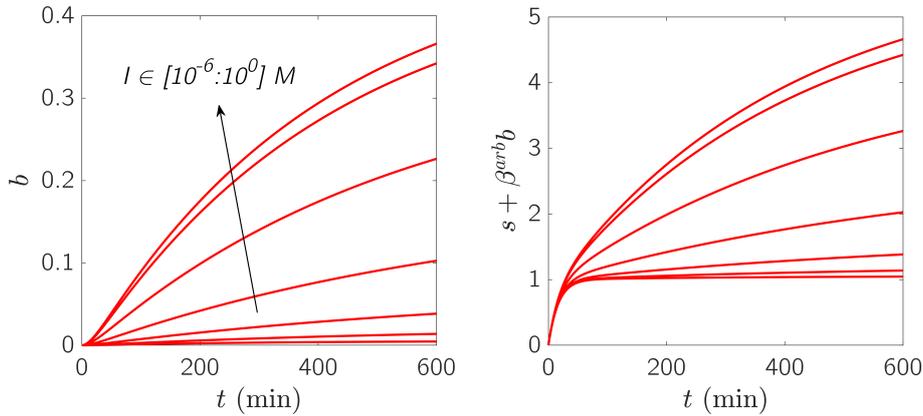
Figure 6.17: (a) Model trends of $b(t)$ for $I \in [10^{-6}; 10^{0}]$ and $k' = 10^{-2}$ min^{-1}. (b) Model trends of $s(t) + \beta b(t)$ for $I \in [10^{-6}; 10^{0}]$, $k' = 10^{-2}$ min^{-1} and $\beta^{arb} = 10$.

At low ionic strength (Fig.6.17.a, lowest curve) the model predicts no bulk deposition. As higher values are used (one curve per decade), the deposition increases fast before slowing down: there is a small difference between the two lowest decades, a large difference between the two middle decades, and again a small difference between the two highest decades. Note that the maximum value of b cannot be interpreted at this point, since the kinetics and amplitude of the curves depend on k', the value of which is for now arbitrary. An inflection point is also visible at early times ($t \approx 20$ min), attributed to the fact that $b(t)$ is at first limited by the creation of a surface layer of particles.

The surface and bulk impacts are logically combined in Fig.6.17.b. At early times, the surface deposition prevails. The trends are then the same than for $b(t)$ alone, simply shifted towards higher depositions.

6.3.2.7 Comparison to experimental data

Now that the trends are validated, the values of k' and β and fitted to the experimental profiles previously presented in Fig.6.12. The experimental value $I = 2 \times 10^{0}$ M is excluded from the comparison, for the reasons mentioned before (different regime of

particle accumulation).

Three calculated variables (H, d_0 and Φ_0) are adjusted around their calculated values to allow a better fit. In the three cases, the adjustment is in the range of the calculated expectations, which shows that the theoretical values were close to the reality of the system. The two fitting parameters k' and β are fitted, as summarized in Table 6.2, and finally lead to a comparison of the model and experiments (see Fig.6.18).

Parameter	Calculated value	Adjusted value	Fitted value
H	$[10^{-19} - 10^{-20}]$ J	5×10^{-20} J	-
d_0	$[1-5]$ nm	2 nm	-
Φ_0	$[12-30]$ mV	20 mV	-
β	-	-	9.5
k	-	-	5.0×10^{-4} s^{-1}
k'	-	-	4.2×10^{-4} s^{-1}

Table 6.2: Calculated, adjusted and fitted values of the model for the bulk deposition $b(t)$.
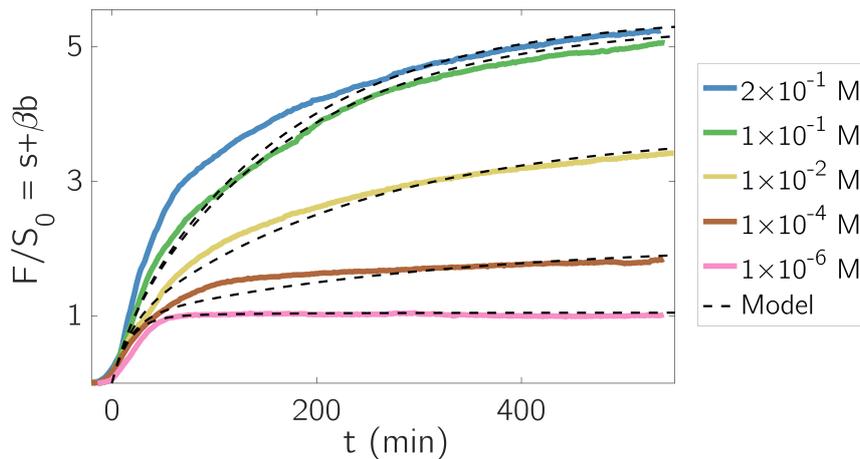
Figure 6.18: Comparison between model (dashed lines) and exprimental (plain lines) global depositions, over 5 orders of magnitude of ionic strengths.

The correspondence between modelled and experimental data is overall very good. In all cases, the asymptotic value $1 + \beta b_{sat}$ is well predicted in the full range of ionic strengths. The dynamics are also respected, with the good prediction of an adsorption rate decaying over time for all values of I. The experimental deposition tends to grow slightly faster than the prediction (most plain curves start higher than the model ones). This is explained by an effect neglected here: the deposition of some particles by bridging or clogging near the contact points of beads. This effect was assumed negligible from the images but is difficult to evaluate precisely.

Towards higher ionic strengths (especially at $I = 2 \times 10^{-1}$ M), the deposition at early times gets much faster than the model. It can mean that the same reason that made us exclude the case $I = 2 \times 10^{0}$ M can already have an impact here: the suspension starts to un-stabilize and some particle can cluster in-flow, triggering a different regime of accumulation (clusters adsorption to the surfaces in particular).

Despite this fact, the final state of deposition is still well predicted. The reason for it is that the saturation condition based on the local flow does not depend on the history of deposition.

6.3.2.8 Conclusions

Given the limited number of fitting parameters introduced in the model, the results are very promising. They provide an efficient way to predict the dynamics of deposition of a mechanism poorly explored for now: the accumulation of particles on top of a surface layer, limited by the evolution of the flow and porosity.

Beyond the exact dynamics, the fraction b_{sat} of the bulk space that can be filled before drag forces dominate inter-particle cohesion is particularly interesting. The experimental and modelled values of b_{sat} (see Fig.6.19) confirm that the final state of deposition in such systems can be quite easily estimated.
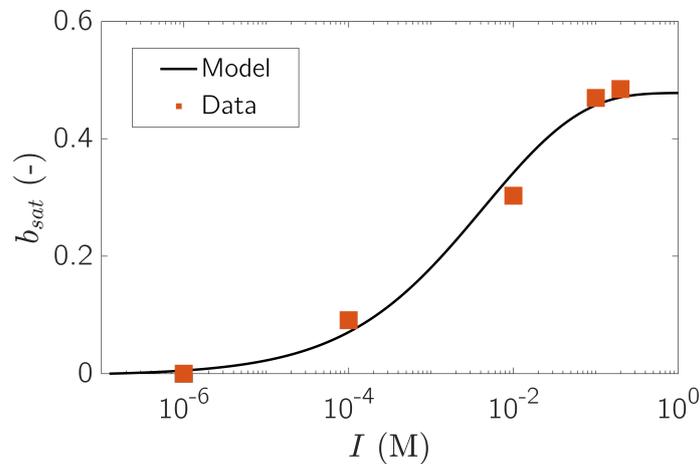
Figure 6.19: Model (line) and experimental (squares) values of the bulk deposition saturation, over ionic strength.

As a final note, we see here that the model predicts a plateau value for the bulk deposition for ionic strengths of 10^{0} M and higher. This prediction results from the fact that the surface charges of the particles cannot be screened further and further indefinitely: from some ionic strength value, the Debye length gets so small that the surface potential Φ is only described by the Van der Waals potential Φ^{VdW}. The

energy barrier to pass gets constant, so does the critical velocity and the bulk adsorption saturation value.

That is never observed experimentally, since such a situation also corresponds to the destabilization of the suspension and quick accumulation, like we observed at $I = 10^0$ M, until potential clogging of the system. Finally, we can state that in the large range of ionic strengths $[10^{-6} - 10^{-1}]$ M, the bulk saturation b_{sat} takes values from 0 to 0.5. It means that the bulk space gets filled from 0 to 50%, which is coherent with the observations.

This closes our study at the entrance of the porous media, and leaves two particularly important questions open: (i) does the drag/cohesion competition have other consequences in the system, and (ii) is our understanding of the deposition dynamics there enough to predict the dynamics deeper in the system?

6.4 Further consequences on deposition

6.4.1 Structure of the deposits

To begin with, let us evaluate how the drag-cohesion competition translates at a more local scale, in particular on the nature of the deposits.

6.4.1.1 Near-surface trajectories

To better assess the shape of the deposits created on the surfaces, local observations are performed in a case of high ionic strength $I = 2 \times 10^{-1}$ M, for which large deposits are expected (see Fig.6.20).

Around the bead, we can see a thick deposit fairly uniformly distributed along the surface; expect towards the middle of the view, where a cluster of particles clearly stands out. Such a cluster creates an obstacle to the flow and can lead to slightly modified deposition dynamics. Particle (a) for example, despite some fluctuations in its trajectory, clearly intercept the deposit and stops.
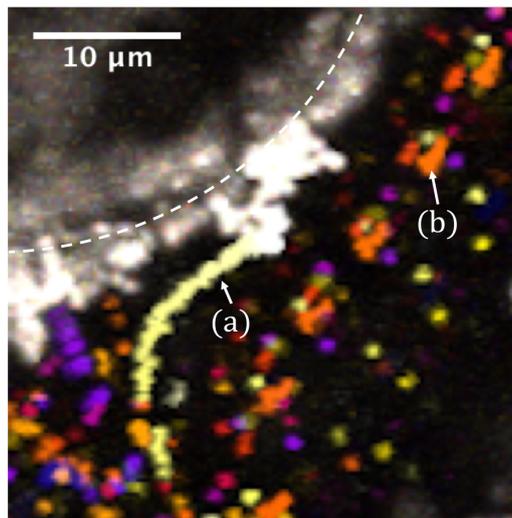
Figure 6.20: Particle trajectories (colors) and deposits (white) in a 35×35 μm^2 window, at $I = 2 \times 10^{-1}$ M.

Based only on the previous model, this is surprising. Indeed, we proved that the deposition is limited by a threshold on the local velocity, which creates deposits of uniform thickness on all surfaces. In fact, this is valid not only at the scale of a pore but also at the scale of any element of surface in the system, which makes the reality much more complex.

A direct consequence of the mechanism we described is that the thickness of the deposits is actually expected to follow the iso-critical velocity line along the surfaces. In other words, at each position, deposition stops where the critical velocity is reached.

Consider a typical velocity field between beads (see side-insert; each color gives an iso-velocity line): if the critical velocity corresponds to the color turquoise, deposition will favorably occur in the turquoise to dark blue areas. The thickness of these areas varies a lot, from very thin at the entrance to large in the regions pointed by gray arrows.

This explanation has consequences broader than the latter observation, but also explains that deposits can grow larger in some areas. Because these specific deposits clearly form a pack of colloids poking out the surfaces, they will be referred to as *clusters*.
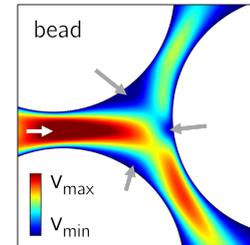
6.4.1.2 Critical cluster growth - Detachment

From this observation, one can wonder if these clusters grow in the same manner as the smooth surface deposits. To answer this question, one of them is followed over time (see Fig.6.21). In addition to the expected (rather smooth) surface deposits, a cluster A occupies a significant fraction of the cross-section of the pore. Its shape is odd and likely results from multiple particle interception events. The presence of this cluster may even explain that the surfaces at its proximity are mostly free of deposited particles; if most arriving particles intercept it rather than the surfaces. The fact that the cluster remains in this configuration shows that the velocity is low enough in this pore, at this moment.

As deposition goes on (see t_2), both A and the surface deposition grow, until A bridges the upper and lower sides of the cross-section. At t_3, A has detached from the lower side to move to a more stable position, in a lower velocity area near a contact point between two beads. In the same time, a new deposit B forms on the lower side, now fully accessible again. Finally, A and B reach an equilibrium size: t_4 corresponds to an equilibrium state.
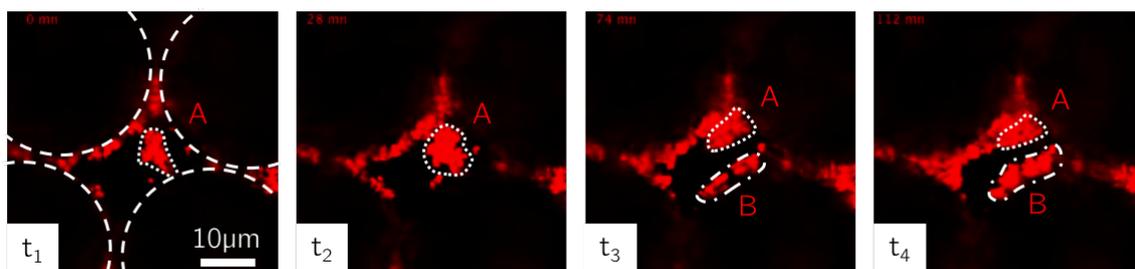
Figure 6.21: Example of cluster detachment at $I = 1 \times 10^{-2}$ M. Two interesting clusters of clusters are highlighted, A and B.

The growth of clusters can in the end appear more erratic that the model deposition described until now. Still, the size of the clusters and their structure/shape in the pore space is limited by the same principles as before: they rearrange to reduce the drag applied on them. When a cluster reaches a size critical for its cohesion, some particle-particle bounds are broken to allow the cluster to rearrange in a more stable configuration.

A second interesting case is observed (see Fig.6.22). At the same ionic strength $I = 1 \times 10^{-1}$ M, a pore is followed over time. The pore size is larger than average, which allowed the formation of a thick deposit (≈ 10 colloids high) at the surface of a bead facing the large pore throat. At t_1, the deposit has reached saturation and is not growing anymore. Some time later, it suddenly detaches from the beads, as a whole, and flows downstream. Due to its massive size, it quickly stops again in a constriction between two beads in the same pore.
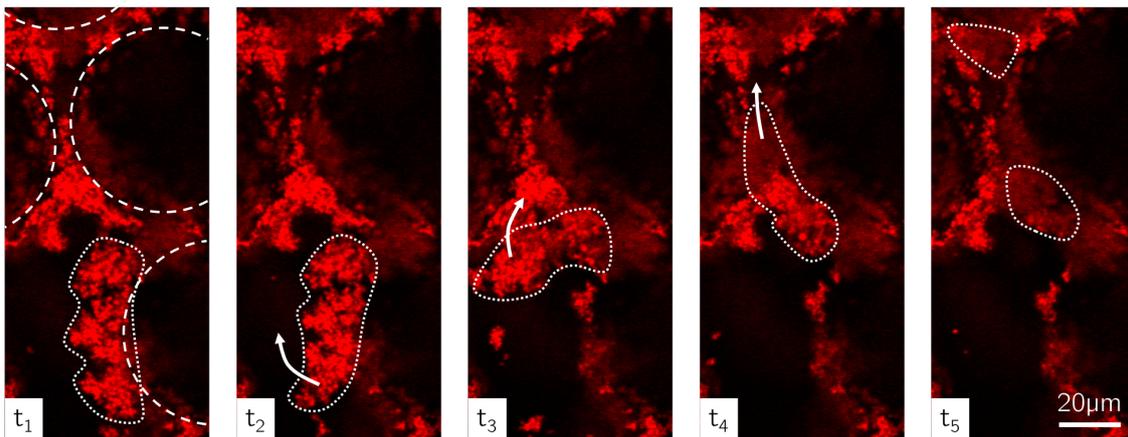
Figure 6.22: Example of cluster detachment at $I = 1 \times 10^{-1}$ M. At t_1, a large cluster is attached at the surface of a bead. From t_2 to t_4, it is detached by the flow and rotates/translates further in the system. At $t_5 \approx t_4$, it breaks is two and stops in a more stable position less than one bead diameter from the initial position.

In that case, the detachment event is not linked to the growth of the cluster itself because no particle adsorption has been observed between t_1 and t_2. Of course, particles could have adsorbed to the same cluster at a different depth, since we are limited to a 2D view of a 3D geometry.

Still, another explanation is plausible: even if the size of this cluster is constant, adsorption events elsewhere in the system modify the local flow conditions. At constant flow-rate, a decrease in porosity somewhere in the same cross-section increases accordingly the local velocity in the neighboring pores. In consequence, the drag force applied on the obstacle also increases and a cluster which was stable before is detached.

In addition, it is interesting to note that the cluster is detaching as a single block. This behavior is common to all detachment events observed in these systems; in other words no detachment of single particles were seen. This statement raises the question of which bounds break first when the drag forces are increased. From Fig.6.22, the cluster leaves behind it the surface of the bead mostly free of particles, but not completely. It means that most breaks occurred near the surface layer, but it is not enough to deduce

that particle-bead bounds are more likely to break than particle-particle bounds.

Overall, the phenomenon of detaching clusters remains marginal before all the particles deposited in stable positions from the start. It is validated by the fact that the previous model gave a great description of the deposition dynamics without taking in account this effect. Keeping this in mind, we will now focus on how the deposition near the entrance of the porous media translates deeper in the samples.

6.4.2 Adsorption in depth

On the same data set, we now open the field of study to the complete confocal acquisitions at the scale of the sample, of the order of 10 mm deep in the flow direction. The depth variable x is added to the time variable to study the dynamics over both dimensions. The summation of the full images over the sample's width gives access to 1D profiles over depth, for all acquired times (every 2 minutes for 9 hours). To ease the visualization, only a selection of these profiles are presented.

6.4.2.1 Low ionic strengths

For low ionic strengths from 10^{-6} to 10^{-4} M, the profiles have shapes similar to the ones presented on Fig.6.23. From no fluorescent everywhere ($F = 0$, lowest curves), the amount of deposited particles increases with time all along the 8 mm of porous medium. The profiles are fairly flat, which shows a uniform deposition. The deposition then reaches a saturation value (around $F = 400$) which, from the images of the previous section, corresponds on average to a single layer of particles at the surfaces.
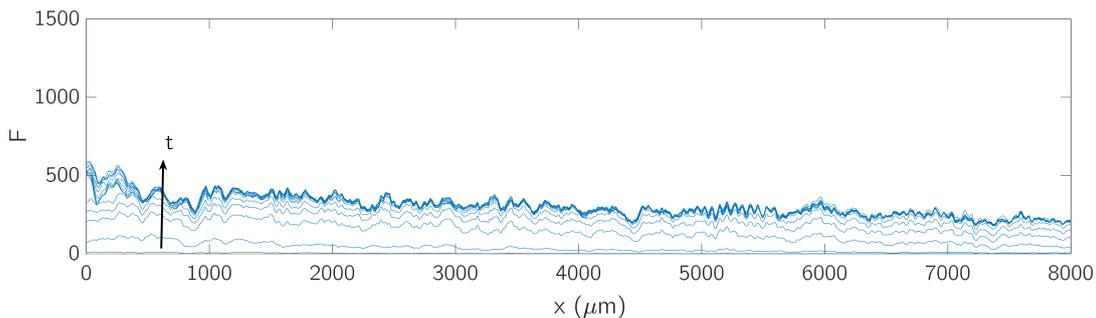
Figure 6.23: Deposition over depth for $I = 10^{-4}$ M, at successive times (bottom to top).

The situation can be explained as follows. Since only a surface layer is formed, arriving particles can flow to deeper sections of the system at anytime (before and after saturation). There, they meet surfaces free of adsorbed particles. Compared to the entrance (at initial state), the flow-rate and ionic strength are unchanged, and the pore geometry is similar. Therefore, the particles interact with these fresh surfaces the same

way particles interacted with the fresh surfaces at the entrance before. The dynamics of deposition are expected to repeat the entrance dynamics, which corresponds to the propagation of a single front of deposition just like in chapter 5.

A difference with chapter 5 is that, here, the colloids have from the start spread far in the system (i.e. particles reach the end of the sample even at the first profiles). While it is tempting to apply the same (sigmoidal) model as in chapter 5 to describe the evolution of the adsorption front, the flatness of these profiles makes is difficult. Indeed, the slope of the front is too small to allow a correct adjustment of the fitting parameters (in particular λ from $S(X) = 1/1 + exp(X/\lambda)$, the characteristic depth over which the deposits spread).

Still, the fact that the profiles tend to a similar saturation value for all depths proves that the single layer deposition identified at the entrance is valid everywhere in the system. In consequence and by similarity with chapter 5, the deposition is expected to propagate in depth with the same dynamics as long as particles are injected.

6.4.2.2   Higher ionic strengths?

We increase now the ionic strength. For intermediate values (10^{-2} to 10^{-1} M), the deposition profiles look like the ones presented in Fig.6.24.a. As before, adsorption spreads deep into the system, but its dynamics differ significantly. From now on, the confocal signal is normalized by the value corresponding to a saturated surface layer $S_0 = 400$.
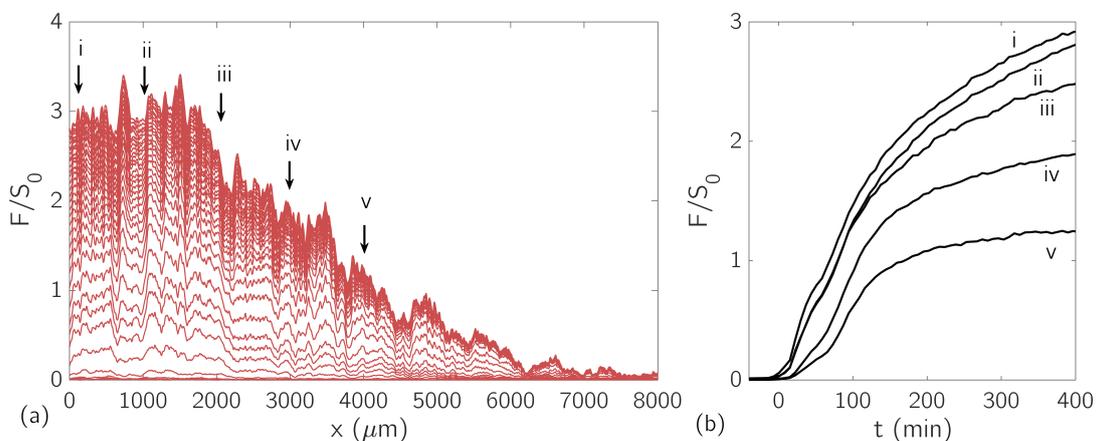
Figure 6.24: (a) Fluorescence over depth at $I = 10^{-2}$ M, every 7 minutes for 9 hours (from lowest to highest). (b) Fluorescence over time at selected depths i to v: entrance i, 1000 μm ii, 2000 μm iii, 3000 μm iv, 4000 μm v

A first visual conclusion is that the deposition is not uniform in depth. It is the highest near the entrance and decreases over depth. Almost no particle reaches depths of 7 to 8 mm, which is major difference with the previous case.

The trend near the entrance (position i) confirms a high adsorption rate decaying towards zero, which corresponds to a saturation value of $F/S_0 \approx 3$. We check that it is the same entrance saturation value as in the previous section. Deeper, the dynamics can be evaluated more precisely by plotting F over time at selected depths (see Fig.**??**.b). At all depths, F increases gradually towards a saturation value. This saturation value is much lower than at the entrance (especially visible for iii, iv and v).

It is surprising, because the expectations developed here above still hold. As long as the deposition at saturation at the entrance (surface and bulk this time) is lower than the whole pore space, particles can explore deeper sections of the material. There, they encounter less covered surfaces and can adsorb. Again, this corresponds to the propagation of a front of adsorption. In the end, profiles similar to Fig.6.23 with a higher plateau value seem plausible. How to explain then that the saturation values vary so much?

An element of answer lays in the confocal images themselves, to which we now come back to better understand what happens locally. A selection of frames corresponding to Fig.6.23 is presented in Fig.6.25. Let us note several observations:

- At t_1, the system appears globally free of particles. When zooming in of course (see (a)), individual deposited particles are visible in accordance with the previous study at the entrance.

- Over time, fluorescence increases roughly everywhere in the system, which means that deposition continues in a given area until saturation (see (a), (b), (c)) and propagates in depth in the same time.

- What is more surprising is the local state of deposition in depth, for example at location (d). The observations are contradictory:

    - Looking at the spatial distribution of particles only, there is definitely more particles adsorbed in (d) than in (a). The beads are quite well outlined, in a way similar to (b).
    - Now looking at the intensity only, the image in (d) appears much darker than (b), with a global brightness similar to (a).

At this point, it seems unlikely that what we are observing is due to the number of accumulated colloids only. What is more probable is that the gain of the confocal itself is decaying with increasing depth. This reason would explain that two similar states of deposition appear with different brightnesses.

On the technical side, we verified at multiple occasion that the confocal signal is in general reliable in depth. It was for example extensively used in chapter 5 to draw the nanoparticle adsorption profiles over depth. Another technical aspect could explain the decay in gain: if the capillary device is slightly tilted, the thickness of sample crossed
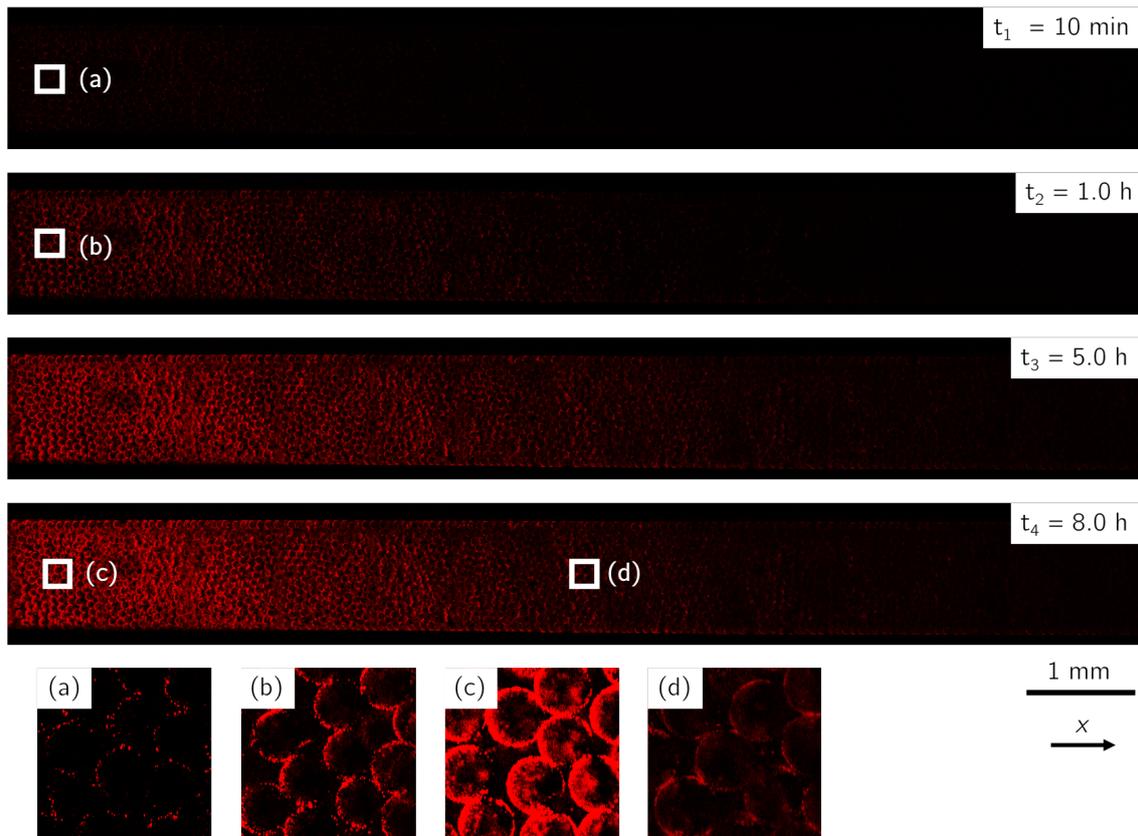
Figure 6.25: Confocal images of the full medium for an experiment at $I = 10^{-2}$ M, at four successive times. Views (a) to (d) precise the corresponding white square areas above.

by the laser beam to the focal point varies with depth. As long as adsorption is low, the system is well index-matched everywhere and no problem is seen (which explains the coherent profiles at lower I). With increasing adsorption (multilayers), the presence of many deposited particles can affect the fraction of light reaching the imaging plane. The thicker the section of sample, the less signal. Because the gain of the experiments is set at the entrance, a capillary tilted downwards (see insert) would explain a loss of gain in depth. For a unidentified reason, this situation seem to have happen for most of our experiments. The explanation is not fully satisfying because the loss in gain should in this case be proportional to the amount of adsorbed particles, but it is the best found at the time of writing.

As a final remark, even if these conclusions are true they do not cast doubt on the previous studies. They simply (and unfortunately) prevent strong comparison between locations spaced in depth. For future experiments, we note that an apparent flatness of the system may not be enough and has to be assessed and corrected with care.

6.4.2.3   Qualitative conclusions

Leaving aside the technical considerations, some qualitative conclusions on depth deposition can still be drawn. First, the fact that particles deposit deep into the sample proves that they can explore the sample, i.e. the upstream pores stay open in accordance with our saturation mechanism. Then, the fact that a saturation is reached at any depth tend to prove that the entrance saturation mechanism applies everywhere.

Imaging plane

Capillary
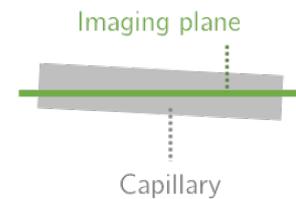
6.4.2.4 Critical ionic strengths

Keeping in mind the issues on the gain, we can still observe the fluorescence profiles at critical ionic strengths (see Fig.6.26 (top) ; for $I = 2 \times 10^0$ M). We recall that in theses conditions the deposition of colloids is fast and massive at the entrance of the system. It is clearly visible on the profiles: for $x \approx 0$, the signal saturates in less than an hour; as confirmed directly on the image (Fig.6.26 (bottom); see t_2).

Still, one important question remained from the study made at the entrance: is this massive deposition synonym of clogging of the porous medium? From $t_1 = 1$ h to $t_3 = 8$ h, fluorescence clearly spreads up to 3 mm deep, i.e. the deposition significantly progresses in depth. It implies that the passage of colloids towards deeper sections is still possible in this time frame, which proves that the system is not clogged.

In the end, we can infer that a bulk saturation mechanism can still apply in these conditions. While the pores get significantly filled, the local velocities increase accordingly and shape in return the deposits to maximize the open sections of the pores. In addition, the mechanism of cluster detachment observed previously is expected to play an important role here: successive detachment of pieces of deposits can in the end displace large quantities of particles to deeper sections of the system.

6.4.3 Conclusions & openings

6.4.3.1 Conclusion on particle-particle-surface interactions at low confinement

In this chapter, we studied the adsorption of particles in low confinement, high surface affinity and variable conditions of particle-particle interactions. A large panel of regimes has been explored.

First, when particles are still repelling each-other, a single surface layer of particles is formed and echoes the results from chapter 5. A major difference is noted: the surface fraction of medium actually covered varies greatly with the particle size; it is estimated at a value as low as 50% here. Then, we identified a regime of self-limited accumulation of colloids based on a local and instantaneous balance between the cohesion between
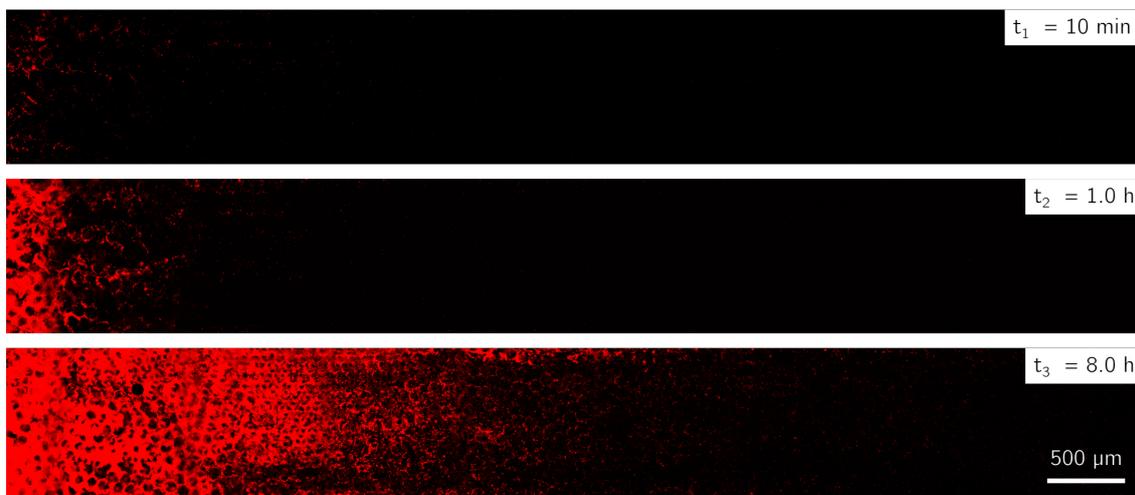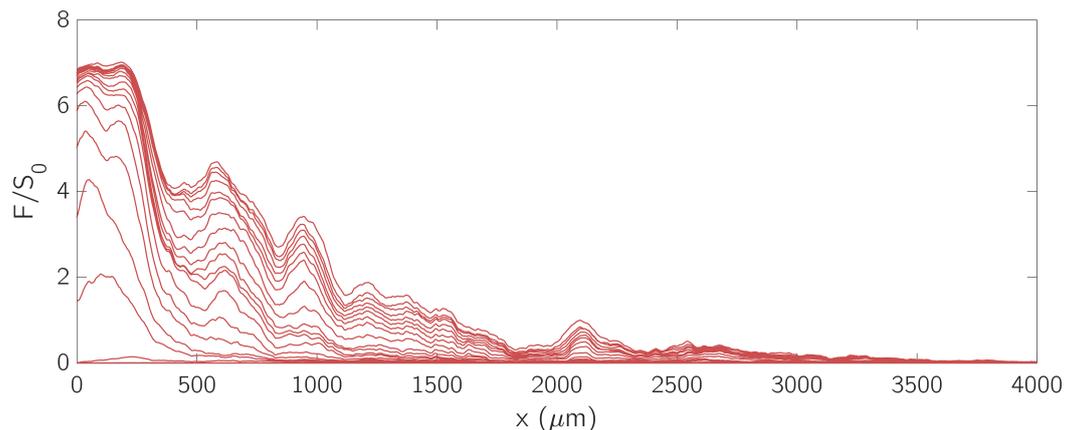
Figure 6.26: (top) Fluorescence over depth at $I = 2 \times 10^0$ M, every 25 min for ≈ 8 hours (from lowest to highest). (bottom) Corresponding confocal images at three selected times.

deposited particles and the drag forces imposed by the flow in the reduced porosity of the system. Finally, insights on the propagation of particles in depth thanks to this mechanism and to the detachment of clusters have been addressed. In particular, we show that clogging events can be delayed even in conditions of extreme deposition. These regimes are used to complete the deposition phases diagram.

6.4.3.2 Openings

The principle of self-limited deposition of colloids can have interesting applications. Let us consider first the case of a porous medium with a large pore size distribution. One can choose conditions of ionic strength to trigger the deposition of a controlled amount of particles at the surface of the pores. More exactly, deposition will go on in each pore until a critical velocity is reached locally. In principle, it leads to a medium with a unique final pore size; i.e. a passage from an heterogeneous to homogeneous system regarding pore sizes.
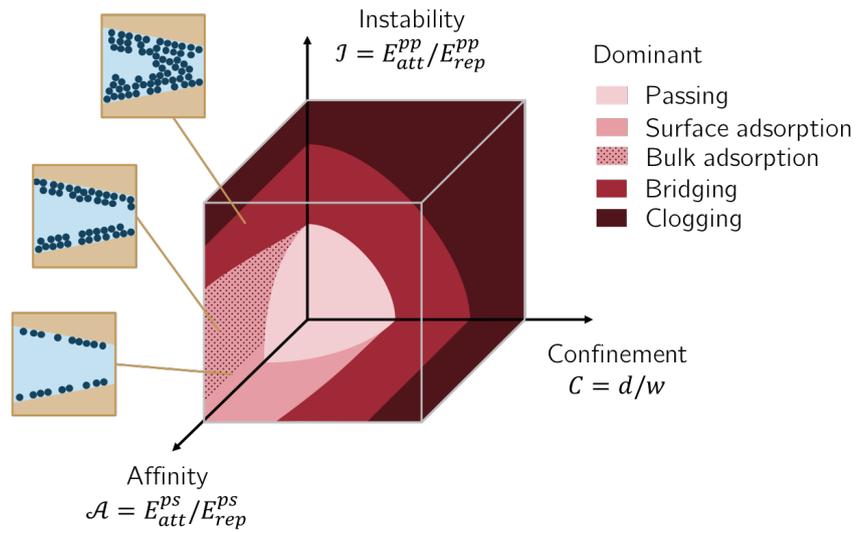
Similarly, the deposition of a controlled number of layers of particles at the surface of a medium can be used to create a secondary porosity in the system, defined by the size and packing of the deposits.

Perspectives & applications

Beyond the results presented for each specific case, the studies performed in this work also allowed to tackle interesting problems that could not be presented in depth in this work but have a real potential for further research. Four examples are now briefly introduced.

Bacterial accumulation in microfluidic channels

The first example results from a joint project with Prof. X. Wang from Harvard University, who provided the biological knowledge and samples on the study of biofilm growth in confined porous media (see [Wang et al. 2016] for context).

While accumulating in the porosity of matrices, the bacteria considered here grow and form a very interesting network (*biofilm*) in the pores. This film creates a secondary porosity with a permeability depending on their health, i.e. on the quantity of nutrients flowing to them through the film. Depending on the thickness and geometry on the film, as well as on the flow conditions, the supply of nutrients evolves locally and the bacterial growths reacts in response. It provides a great example of particle accumulation strongly coupled to the evolution of the local flow conditions. For further details, see Fig.7.1 (Appendix 7.1).

Fracture consolidation using confinement

A second study performed on the side of this work is a direct application of the results on the confinement-driven clogging dynamics. It deals with the study of particles flowing through collapsing fractures, which has large applications for underground *fracture propping* [Speight 2016]. Basically, sub-millimetric particles are distributed in newly created fractures. Under the stress imposed by the surrounding matter, fracture collapse on themselves and tend to eject the particles in the process. This problem is relevant to our topic because the very interesting phenomenon follows: the particles get trapped in the confined areas of the fractures and in their roughness. It can therefore be seen as clogging under conditions of confinement increasing with time, as the volume of fracture tumbles down. For further details, see Fig.7.3 (Appendix 7.1).

Nanoparticle capture using nZVI particles

A third project using the knowledge gathered on the clogging of pores by nZVI particles has been directly applied toward the actual use case of these particle: remediation. The efficiency of the deposited nZVI particle to catch pollutants has been assessed by injecting model *pollutants* in channels already affected by deposition events. As model pollutants, the amine-modified nanoparticles used in Chapter 5 are excellent candidates as they share multiple properties with positively charges contaminants usually targeted for removal by nZVI particles. A glimpse of the kind of experiments carried out is provided in Fig.7.2: the concentration of nanoparticles before and after a filter of nZVI particles are compared and related to an efficiency of removal. For further details, see Fig.7.2 (Appendix 7.1).

Colloidal transport in inverted RCP matrices

The last study ambitions to complete the conclusions of chapter 5 on the importance of low-velocity areas in the particle transport and adsorption dynamics.

In relies on a very interesting material created with the help of Prof. O. Pitois from Navier Laboratory. The material is a solidified hydrogel foam, i.e. a volume of hydrogel in which compacted bubbles of air (cells) are embedded. The compaction of the bubbles is of the order of 80%, which implies that all cells are deformed and share "flat" surfaces with the other cells they are in contact with. The hydrogel matrix surrounds the bubbles and leaves inter-cells openings at the place of the flat surfaces. In other words, the cells form a completely connected porosity in a block a gel. Note that the geometry of the pores is the exact opposite of the packings of beads studies in this work: the pores because the matrix, and vice versa.

For the purpose of transport studies, the porosity is then filled with water to work in saturated conditions. Remarkably, since the hydrogel is made at 75% of water, it is perfectly transparent when saturated with water (iso-index $n_D \approx 1.33$). In the end, the material can be easily imaged in depth and has a interesting uncommon pore geometry.

When flowing 1 μm positively charged colloids (low ionic strength conditions) in this system, they adsorb to surfaces as described in the first section of chapter 6. A major difference with the dynamics observed then in that the concave geometry of the cells create important areas of low-velocity. Consequently, particles tend to flow quickly from pore to pore through high velocity paths, and can only reach the majority of the surfaces through diffusive transport. For further details, see Fig.7.4 (Appendix 7.1).

Conclusion

In this work, we ran across multiple cases of complex interactions between suspensions of particles and porous matrices. To visualize our findings and put them in perspective, let us now emphasize the global particle-medium interactions diagram that was built along the chapters.
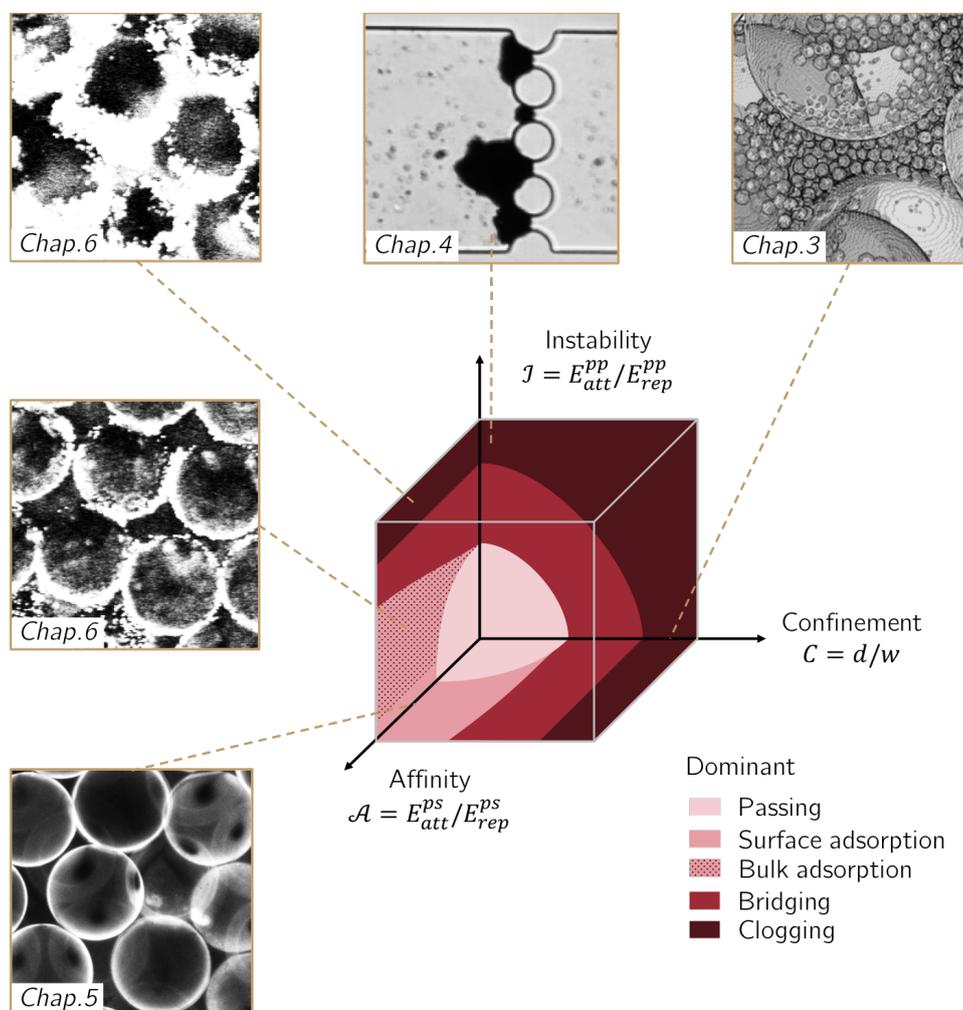
Scope of the results

To begin with, the general clogging mechanism was presented on stable monodisperse suspensions too large to develop impactful electrostatic interactions with the surfaces or between themselves. It allowed us to show that geometrical deposition in confined conditions is driven by the formation of pore size clusters, until percolation of the deposit and divergence of the deposition (caking). A simple predictive model is proposed to link the clogging probability of particles to their confinement.

Then, the predictable clogging mechanisms of model spherical particles were challenged by the study of more complex suspensions, polydisperse in size and shape, resulting from strongly unstable small elementary particles. These results highlighted behaviors like reorientation of desegregation, linked to a coupling between particle, flow and pore geometry. They provide new guidance on how current models can be refined to take these aspects into account.

From the case of strongly interacting particles, we moved to stable (repelling) particles with a high electrostatic affinity with the surfaces of the matrices. We verified important adsorption mechanisms like the formation of a single layer of particles at the surfaces of the system. In addition, a surprisingly important phenomena arose: the significant impact on the adsorption dynamics of the local velocity conditions and dominant particle transport mechanisms. Again, these results can directly help to refine predictive models based on surface deposition.

Finally, particle-particle and particle-surface interactions were combined to study the deposition of colloidal suspensions with a modulated stability. A broad range of deposition stages appeared: the formation of a single layer of particles validating our precedent results, the unexpected controlled accumulation of multi-layer deposits, up to clogging mechanisms; completing the discussion initiated in the first chapter.

Perspectives

Of course, the full understanding of more complex cases where all interactions coexist remains very challenging. When particles are attracted to each-other, subject to surface adsorption and expected to clog pores they interact with, it is clear that the standard assumption of independent deposition mechanisms does not hold anymore. A sense of such complex system was given by our confocal study of highly unstable colloids (chapter 6, highest ionic strength).

In the end, the present results can help to set new grounds for the understanding of more complex situations out of the direct scope of this diagram. A telling example is the case of suspensions made of several types of particles, in competition for all the mechanisms we listed so far. Here, the complicated deposition and accumulation dynamics can be approached using the same fundamental principles highlighted along this work: the evolution of the flow following clogging events, the evolution of the porosity

following adsorption events, or the lose of integrity of clustered particles depending on the shear conditions.

All the previous examples show that many interesting questions remain open around the large question of suspensions of particles interacting with porous media. On the technical side, it is clear that the development of direct dynamic observations techniques like the ones presented here is key to fully understand the fundamentals of the various particle deposition dynamics. On the applied side, the potential of those results is large both for the prediction of particle transport and deposition (soil remediation), and for the making of innovative systems using controlled particle stoppage as a feature (filtration systems, drug delivery).

Bibliography

Agbangla, Gbedo Constant, Eric Climent, and Patrice Bacchin (2012). "Experimental investigation of pore clogging by microparticles: Evidence for a critical flux density of particle yielding arches and deposits". In: *Separation and Purification Technology* 101, pp. 42–48. ISSN: 13835866. DOI: 10.1016/j.seppur.2012.09.011.

Alabi, Olusegun Olalekan (2011). "Fluid Flow in Homogeneous and Heterogeneous Porous Media". In:

Amitay-Rosen, Tal, Andrea Cortis, and Brian Berkowitz (2005). "Magnetic resonance imaging and quantitative analysis of particle deposition in porous media". In: *Environmental Science & Technology* 39.18, pp. 7208–7216. ISSN: 0013-936X.

Arbabi, Sepehr and Muhammad Sahimi (1990). "Critical properties of viscoelasticity of gels and elastic percolation networks". In: *Physical Review Letters* 65.6, pp. 725–728. ISSN: 0031-9007. DOI: 10.1103/PhysRevLett.65.725.

Auset, Maria and Arturo A. Keller (2006). "Pore-scale visualization of colloid straining and filtration in saturated porous media using micromodels: COLLOID STRAINING AND FILTRATION". In: *Water Resources Research* 42.12. ISSN: 00431397. DOI: 10.1029/2005WR004639.

Bacchin, P., P. Aimar, and V. Sanchez (1995). "Model for colloidal fouling of membranes". In: *AIChE Journal* 41.2, pp. 368–376. ISSN: 0001-1541, 1547-5905. DOI: 10.1002/aic.690410218.

Bear, Jacob (1972). *Dynamics of Fluids in Porous Media*. Elsevier.

Bradford, Scott A. and Feike J. Leij (2018). "Modeling the transport and retention of polydispersed colloidal suspensions in porous media". In: *Chemical Engineering Science* 192, pp. 972–980. ISSN: 00092509. DOI: 10.1016/j.ces.2018.08.037.

Bradford, Scott A., Jirka Simunek, et al. (2003). "Modeling Colloid Attachment, Straining, and Exclusion in Saturated Porous Media". In: *Environmental Science & Technology* 37.10, pp. 2242–2250. ISSN: 0013-936X, 1520-5851. DOI: 10.1021/es025899u.

Bradford, Scott A., Scott R. Yates, et al. (2002). "Physical factors affecting the transport and fate of colloids in saturated porous media: FACTORS AFFECTING THE FATE OF COLLOIDS". In: *Water Resources Research* 38.12, pp. 63–1–63–12. ISSN: 00431397. DOI: 10.1029/2002WR001340.

Britton (2011). "Porous Media Studied by MRI". In: *Encyclopedia of Magnetic Resonance*. Chichester, UK: John Wiley & Sons, Ltd, emrstm1263. ISBN: 978-0-470-03459-0. DOI: 10.1002/9780470034590.emrstm1263.

Brown, G. O. (2002). "Henry Darcy and the making of a law: HENRY DARCY AND THE MAKING OF A LAW". In: *Water Resources Research* 38.7, pp. 11–1–11–12. ISSN: 00431397. DOI: 10.1029/2001WR000727.

Callaghan, Paul T. (2007). *Principles of nuclear magnetic resonance microscopy*. reprinted. Oxford science publications. OCLC: 551122816. Oxford: Clarendon Press. 492 pp. ISBN: 978-0-19-853997-1.

Carman, P.C. (1997). "Fluid flow through granular beds". In: *Chemical Engineering Research and Design* 75, S32–S48. ISSN: 02638762. DOI: 10.1016/S0263-8762(97)80003-2.

Chen, Kai Loon and Menachem Elimelech (2008). "Interaction of Fullerene (C $_{60}$) Nanoparticles with Humic Acid and Alginate Coated Silica Surfaces: Measurements, Mechanisms, and Environmental Implications". In: *Environmental Science & Technology* 42.20, pp. 7607–7614. ISSN: 0013-936X, 1520-5851. DOI: 10.1021/es8012062.

Cheng, Nian Sheng (2008). "Formula for the viscosity of a glycerol water mixture". In: *Industrial and Engineering Chemistry Research* 47.9, pp. 3285–3288. ISSN: 0888-5885. DOI: 10.1021/ie071349z.

Cheremisinoff, Nicholas P. (1998). *Liquid filtration*. 2nd ed. Boston: Butterworth-Heinemann. 319 pp. ISBN: 978-0-7506-7047-0.

Cipolla, Craig L., Norman Raymond Warpinski, and Michael J. Mayerhofer (2008). "Hydraulic Fracture Complexity: Diagnosis, Remediation, And Explotation". In: *SPE Asia Pacific Oil and Gas Conference and Exhibition*. SPE Asia Pacific Oil and Gas Conference and Exhibition. Perth, Australia: Society of Petroleum Engineers. DOI: 10.2118/115771-MS.

Crawford, Christopher Blair and Brian Quinn (2017). *Microplastic pollutants*. OCLC: ocn949750262. Amsterdam: Elsevier. 315 pp. ISBN: 978-0-12-809406-8.

Crist, J. T. et al. (2004). "Pore-Scale Visualization of Colloid Transport and Retention in Partly Saturated Porous Media". In: *Vadose Zone Journal* 3.2, pp. 444–450. ISSN: 1539-1663. DOI: 10.2113/3.2.444.

Datta, Sujit S., T. S. Ramakrishnan, and David A. Weitz (2014). "Mobilization of a trapped non-wetting fluid from a three-dimensional porous medium". In: *Physics of Fluids* 26.2, p. 022002. ISSN: 1070-6631, 1089-7666. DOI: 10.1063/1.4866641.

Derjaguin, B and L Landau (1941). "Theory of the stability of strongly charged lyophobic sols and of the adhesion of strongly charged particles in solutions of electrolytes". In: *Progress in Surface Science* 43.1, pp. 30–59. ISSN: 00796816. DOI: 10.1016/0079-6816(93)90013-L.

Dersoir, Benjamin et al. (2015). "Clogging of a single pore by colloidal particles". In: *Microfluidics and Nanofluidics* 19.4, pp. 953–961. ISSN: 1613-4982, 1613-4990. DOI: 10.1007/s10404-015-1624-y.

Djehiche, Abdelkader et al. (2009). "Etude experimentale du depot de particules colloidales en milieu poreux : Influence de l'hydrodynamique et de la salinite". In: *Comptes Rendus Mecanique* 337.9, pp. 682–692. ISSN: 16310721. DOI: 10.1016/j.crme.2009.08.002.

Dong, K.J. et al. (2009). "DEM simulation of cake formation in sedimentation and filtration". In: *Minerals Engineering* 22.11, pp. 921–930. ISSN: 08926875. DOI: 10.1016/j.mineng.2009.03.018.

Dressaire, Emilie and Alban Sauret (2017). "Clogging of microfluidic systems". In: *Soft Matter* 13.1, pp. 37–48. ISSN: 1744-683X, 1744-6848. DOI: 10.1039/C6SM01879C.

Dullien, F (1979). *Porous Media Fluid Transport and Pore Structure*. 1st ed. Academic Press. ISBN: 978-0-323-15135-1.

Einstein, Albert (1905). "Uber die von der molekularkinetischen Theorie der Warme geforderte Bewegung von in ruhenden Flussigkeiten suspendierten Teilchen". In: *Annalen der Physik* 17.8, pp. 549–560.

Eker, Omer F., Fatih Camci, and Ian K. Jennions (2016). "Physics-based prognostic modelling of filter clogging phenomena". In: *Mechanical Systems and Signal Processing* 75, pp. 395–412. ISSN: 08883270. DOI: 10.1016/j.ymssp.2015.12.011.

Elimelech, Menachem (1991). "Kinetics of capture of colloidal particles in packed beds under attractive double layer interactions". In: *Journal of Colloid and Interface Science* 146.2, pp. 337–352. ISSN: 00219797. DOI: 10.1016/0021-9797(91)90199-I.

Evans, J. W. (1993). "Random and cooperative sequential adsorption". In: *Reviews of Modern Physics* 65.4, pp. 1281–1329. ISSN: 0034-6861, 1539-0756. DOI: 10.1103/RevModPhys.65.1281.

Faber, Suzanne et al. (2016). "Migration and deposition of fine particles in a porous filter and alluvial deposit: laboratory experiments". In: *Arabian Journal of Geosciences* 9.4, p. 293. ISSN: 1866-7511, 1866-7538. DOI: 10.1007/s12517-016-2309-x.

Gale, Bruce et al. (2018). "A Review of Current Methods in Microfluidic Device Fabrication and Future Commercialization Prospects". In: *Inventions* 3.3, p. 60. ISSN: 2411-5134. DOI: 10.3390/inventions3030060.

Ghidaglia, Claude (1996). "Transition in particle capture in deep bed filtration". In: *Physical Review E* 53.4. ISSN: 1063-651X, 1095-3787. DOI: 10.1103/PhysRevE.53.R3028.

Goldsztein, Guillermo H. (2005). "Volume of Suspension That Flows through a Small Orifice Before It Clogs". In: *SIAM Journal on Applied Mathematics* 66.1, pp. 228–236. ISSN: 0036-1399, 1095-712X. DOI: 10.1137/040616164.

Grahame, David C. (1947). "The Electrical Double Layer and the Theory of Electrocapillarity." In: *Chemical Reviews* 41.3, pp. 441–501. ISSN: 0009-2665, 1520-6890. DOI: 10.1021/cr60130a002.

Greenkorn, R. A. (1981). "Steady flow through porous media". In: *AIChE Journal* 27.4, pp. 529–545. ISSN: 0001-1541, 1547-5905. DOI: 10.1002/aic.690270402.

Gregory, John (1981). "Approximate expressions for retarded van der waals interaction". In: *Journal of Colloid and Interface Science* 83.1, pp. 138–145. ISSN: 00219797. DOI: 10.1016/0021-9797(81)90018-7.

— (1975). "Interaction of unequal double layers at constant charge". In: *Journal of Colloid and Interface Science* 51.1, pp. 44–51. ISSN: 00219797. DOI: 10.1016/0021-9797(75)90081-8.

Grolimund, Daniel and Michal Borkovec (1999). "Long-Term Release Kinetics of Colloidal Particles from Natural Porous Media". In: *Environmental Science & Technology* 33.22, pp. 4054–4060. ISSN: 0013-936X, 1520-5851. DOI: 10.1021/es990194m.

Hahn, Melinda W., Dean Abadzic, and Charles R. O'Melia (2004). "Aquasols: On the Role of Secondary Minima". In: *Environmental Science & Technology* 38.22, pp. 5915–5924. ISSN: 0013-936X, 1520-5851. DOI: 10.1021/es049746d.

Hamamoto, Shoichiro et al. (2016). "Pore network structure linked by X-ray CT to particle characteristics and transport parameters". In: *Soils and Foundations* 56.4, pp. 676–690. ISSN: 00380806. DOI: 10.1016/j.sandf.2016.07.008.

Helmholtz, H. (1853). "Ueber einige Gesetze der Vertheilung elektrischer Strome in korperlichen Leitern mit Anwendung auf die thierisch-elektrischen Versuche". In: *Annalen der Physik und Chemie* 165.6, pp. 211–233. ISSN: 00033804, 15213889. DOI: 10.1002/andp.18531650603.

Henry, Christophe (2018). "Particle resuspension from complex surfaces: current knowledge and limitations". In: *arXiv:1802.06448 [cond-mat, physics:physics]*. arXiv: 1802.06448.

Herzig, J. P., D. M. Leclerc, and P. Le. Goff (1970). "Flow of Suspensions through Porous Media. Application to Deep Filtration". In: *Industrial and Engineering Chemistry* 62.5, pp. 8–35. ISSN: 0019-7866, 1541-5724. DOI: 10.1021/ie50725a003.

Hillel, Daniel (1980). *Fundamentals of soil physics*. New York: Academic Press. 413 pp. ISBN: 978-0-12-348560-1.

Hogg, R., T. W. Healy, and D. W. Fuerstenau (1966). "Mutual coagulation of colloidal dispersions". In: *Transactions of the Faraday Society* 62, p. 1638. ISSN: 0014-7672. DOI: 10.1039/tf9666201638.

Ives, K.J (1970). "Rapid filtration". In: *Water Research* 4.3, pp. 201–223. ISSN: 00431354. DOI: 10.1016/0043-1354(70)90068-0.

Iwasaki, T., J. J. Slade, and Wm. E. Stanley (1937). "Some notes on sand filtration". In: *Journal (American Water Works Association)* 29.10, pp. 1591–1602.

Jenkins, Matthew C. et al. (2011). "Finding bridges in packings of colloidal spheres". In: *Soft Matter* 7.2, pp. 684–690. ISSN: 1744-683X, 1744-6848. DOI: 10.1039/C0SM00544D.

Jiang, Lanlan et al. (2017). "Behavior of CO 2 /water flow in porous media for CO 2 geological storage". In: *Magnetic Resonance Imaging* 37, pp. 100–106. ISSN: 0730725X. DOI: 10.1016/j.mri.2016.11.002.

Johnson, Philip R. and Menachem Elimelech (1995). "Dynamics of Colloid Deposition in Porous Media: Blocking Based on Random Sequential Adsorption". In: *Langmuir* 11.3, pp. 801–812. ISSN: 0743-7463, 1520-5827. DOI: 10.1021/la00003a023.

Katsube, T. J. and J. P. Hume (1987). "Permeability determination in crystalline rocks by standard geophysical logs". In: *GEOPHYSICS* 52.3, pp. 342–352. ISSN: 0016-8033, 1942-2156. DOI: 10.1190/1.1442308.

Ko, Chun-Han and Menachem Elimelech (2000). "The Shadow Effect in Colloid Transport and Deposition Dynamics in Granular Porous Media: Measurements and Mech-

anisms". In: *Environmental Science and Technology* 34.17, pp. 3681–3689. ISSN: 0013-936X, 1520-5851. DOI: 10.1021/es0009323.

Koivisto, Juha and Douglas J. Durian (2017). "Effect of interstitial fluid on the fraction of flow microstates that precede clogging in granular hoppers". In: *Physical Review E* 95.3, p. 032904. ISSN: 2470-0045, 2470-0053. DOI: 10.1103/PhysRevE.95.032904.

Kosvintsev, S. et al. (2003). "Sieve mechanism of microfiltration separation". In: *Colloids and Surfaces A: Physicochemical and Engineering Aspects* 230.1, pp. 167–182. ISSN: 09277757. DOI: 10.1016/j.colsurfa.2003.09.027.

Krishna, P and D Pandey (1981). "Close-Packed Structures". In: *International Union of Crystallography*.

Lakshmanan, S. et al. (2015). "Characterization of nanoparticle transport through quartz and dolomite gravels by magnetic resonance imaging". In: *International Journal of Environmental Science and Technology* 12.10, pp. 3373–3384. ISSN: 1735-1472, 1735-2630. DOI: 10.1007/s13762-015-0767-4.

Lamrous, O. et al. (1989). "Magnetic resonance imaging application to study of porous media". In: *Revue de Physique Appliquee* 24.5, pp. 607–612. ISSN: 0035-1687. DOI: 10.1051/rphysap:01989002405060700.

Larson, Ronald G. (1999). *The structure and rheology of complex fluids.* Topics in chemical engineering. New York: Oxford University Press. 663 pp. ISBN: 978-0-19-512197-1.

LeBel, R. G. and D. A. I. Goring (1962). "Density, Viscosity, Refractive Index, and Hygroscopicity of Mixtures of Water and Dimethyl Sulfoxide." In: *Journal of Chemical & Engineering Data* 7.1, pp. 100–101. ISSN: 0021-9568, 1520-5134. DOI: 10.1021/je60012a032.

Lehoux, A. P. et al. (2016). "Magnetic resonance imaging measurements evidence weak dispersion in homogeneous porous media". In: *Physical Review E* 94.5, p. 053107. ISSN: 2470-0045, 2470-0053. DOI: 10.1103/PhysRevE.94.053107.

Li, Yusong et al. (2008). "Investigation of the Transport and Deposition of Fullerene (C60) Nanoparticles in Quartz Sands under Varying Flow Conditions". In: *Environmental Science & Technology* 42.19, pp. 7174–7180. ISSN: 0013-936X, 1520-5851. DOI: 10.1021/es801305y.

Lozano, Celia et al. (2012). "Flow and clogging in a silo with an obstacle above the orifice". In: *Physical Review E* 86.3, p. 031306. ISSN: 1539-3755, 1550-2376. DOI: 10.1103/PhysRevE.86.031306.

Ma, Huilian et al. (2009). "Hemispheres-in-Cell Geometry to Predict Colloid Deposition in Porous Media". In: *Environmental Science & Technology* 43.22, pp. 8573–8579. ISSN: 0013-936X, 1520-5851. DOI: 10.1021/es901242b.

Manger, Edward (1963). *Porosity and Bulk Density of Sedimentary Rocks.*

McDowell-Boyer, Laura M., James R. Hunt, and Nicholas Sitar (1986). "Particle transport through porous media". In: *Water Resources Research* 22.13, pp. 1901–1921. ISSN: 00431397. DOI: 10.1029/WR022i013p01901.

Messina, Francesca, Daniele Luca Marchisio, and Rajandrea Sethi (2015). "An extended and total flux normalized correlation equation for predicting single-collector efficiency". In: *Journal of Colloid and Interface Science* 446, pp. 185–193. ISSN: 00219797. DOI: 10.1016/j.jcis.2015.01.024.

Messina, Francesca, Tiziana Tosco, and Rajandrea Sethi (2016). "On the failure of upscaling the single-collector efficiency to the transport of colloids in an array of collectors: COLLOIDAL TRANSPORT IN ARRAYS OF SPHERICAL COLLECTORS". In: *Water Resources Research* 52.7, pp. 5492–5505. ISSN: 00431397. DOI: 10.1002/2016WR018592.

Michel, Roger et al. (2002). "A Novel Approach To Produce Biologically Relevant Chemical Patterns at the Nanometer Scale: Selective Molecular Assembly Patterning Combined with Colloidal Lithography". In: *Langmuir* 18.22, pp. 8580–8586. ISSN: 0743-7463, 1520-5827. DOI: 10.1021/la0258244.

Mikolajczyk, Gerd et al. (2018). "Colloid deposition in monolithic porous media. Experimental investigations using X-ray computed microtomography and magnetic resonance velocimetry". In: *Chemical Engineering Science* 175, pp. 257–266. ISSN: 00092509. DOI: 10.1016/j.ces.2017.09.054.

Mustin, Benjamin and Boris Stoeber (2010). "Deposition of particles from polydisperse suspensions in microfluidic systems". In: *Microfluidics and Nanofluidics* 9.4, pp. 905–913. ISSN: 1613-4982, 1613-4990. DOI: 10.1007/s10404-010-0613-4.

Nelson, Kirk E. and Timothy R. Ginn (2005). "Colloid Filtration Theory and the Happel Sphere-in-Cell Model Revisited with Direct Numerical Simulation of Colloids". In: *Langmuir* 21.6, pp. 2173–2184. ISSN: 0743-7463, 1520-5827. DOI: 10.1021/la048404i.

Nimmo, J. R. (2004). "Porosity and pore size distribution". In: *Encyclopedia of Soils in the Environment* 3, p. 295–303.

Nolan, G.T. and P.E. Kavanagh (1994). "The size distribution of interstices in random packings of spheres". In: *Powder Technology* 78.3, pp. 231–238. ISSN: 00325910. DOI: 10.1016/0032-5910(93)02789-D.

Ochiai, Naoyuki, Erika L. Kraft, and John S. Selker (2006). "Methods for colloid transport visualization in pore networks: COLLOID TRANSPORT VISUALIZATION METHODS". In: *Water Resources Research* 42.12. ISSN: 00431397. DOI: 10.1029/2006WR004961.

Overbeek, J. Th. G. and E. J. W. Verway (1947). "Theory of the Stability of Lyophobic Colloids." In: *The Journal of Physical and Colloid Chemistry* 51.3, pp. 631–636. ISSN: 0092-7023, 1541-5740. DOI: 10.1021/j150453a001.

Paykov, Oksana and Harmonie Hawley (2013). "A Protein-Retention Method for Specific Surface Area Determination in Swelling Clays". In: *Geotechnical Testing Journal* 36.4, p. 20120197. ISSN: 01496115. DOI: 10.1520/GTJ20120197.

Phalippou, J. (2002). "Highly porous aerogels of very low permeability". In: *Materials Science* 20.1.

Phenrat, Tanapon, Hye-Jin Kim, et al. (2009). "Particle Size Distribution, Concentration, and Magnetic Attraction Affect Transport of Polymer-Modified Fe0 Nanoparticles in

Sand Columns". In: *Environmental Science & Technology* 43.13, pp. 5079–5085. ISSN: 0013-936X, 1520-5851. DOI: 10.1021/es900171v.

Phenrat, Tanapon, Navid Saleh, et al. (2007). "Aggregation and Sedimentation of Aqueous Nanoscale Zerovalent Iron Dispersions". In: *Environmental Science & Technology* 41.1, pp. 284–290. ISSN: 0013-936X, 1520-5851. DOI: 10.1021/es061349a.

Qu, Deyang (2014). "Fundamental principals of battery design: Porous electrodes". In: REVIEW ON ELECTROCHEMICAL STORAGE MATERIALS AND TECHNOLOGY: Proceedings of the 1st International Freiberg Conference on Electrochemical Storage Materials. Freiberg, Germany, pp. 14–25. DOI: 10.1063/1.4878477.

Ramachandran, Venkatachalam and H. Scott Fogler (1999). "Plugging by hydrodynamic bridging during flow of stable colloidal particles within cylindrical pores". In: *Journal of Fluid Mechanics* 385, pp. 129–156. ISSN: 00221120. DOI: 10.1017/S0022112098004121.

Redner, S. and Somalee Datta (2000). "Clogging Time of a Filter". In: *Physical Review Letters* 84.26, pp. 6018–6021. ISSN: 0031-9007, 1079-7114. DOI: 10.1103/PhysRevLett.84.6018.

Reynolds, W. L. and H. S. Silesky (1960). "Solubilities of Potassium Chloride and Sodium Iodide in Dimethylsulfoxide-Water Mixtures." In: *Journal of Chemical & Engineering Data* 5.3, pp. 250–250. ISSN: 0021-9568, 1520-5134. DOI: 10.1021/je60007a005.

Rice, Philip A. et al. (1970). "Anisotropic Permeability in Porous Media". In: *Industrial and Engineering Chemistry* 62.6, pp. 23–31. ISSN: 0019-7866, 1541-5724. DOI: 10.1021/ie50726a005.

Roussel, N., Thi Lien Huong Nguyen, and P. Coussot (2007). "General Probabilistic Approach to the Filtration Process". In: *Physical Review Letters* 98.11, p. 114502. ISSN: 0031-9007, 1079-7114. DOI: 10.1103/PhysRevLett.98.114502.

Roux, Jean-Noel, Francois Chevoir, and Fabrice Toussaint (2009). "Etats de compacite maximale pour les melanges binaires de grains speriques : etude par simulation numerique". In: *arXiv:0901.3481 [cond-mat, physics:physics]*. arXiv: 0901.3481.

Ruhlman, Michael (2010). *The elements of cooking: translating the chef's craft for every kitchen*. 1st Scribner trade pbk. ed. New York: Scribner. 245 pp. ISBN: 978-1-4391-7252-0.

Ryan, Joseph N and Menachem Elimelech (1996). "Colloid mobilization and transport in groundwater". In: *Colloids and Surfaces A: Physicochemical and Engineering Aspects* 107, pp. 1–56. ISSN: 09277757. DOI: 10.1016/0927-7757(95)03384-X.

Ryan, Joseph N. and Philip M. Gschwend (1994). "Effects of Ionic Strength and Flow Rate on Colloid Release: Relating Kinetics to Intersurface Potential Energy". In: *Journal of Colloid and Interface Science* 164.1, pp. 21–34. ISSN: 00219797. DOI: 10.1006/jcis.1994.1139.

Sakthivadivel, R. (1969). *Clogging of a Granular Porous Medium by Sediment*. Hydraulic Engineering Laboratory, College of Engineering, University of California.

Sakthivadivel, R. (1966). *Theory and Mechanism of Filtration of Non-colloidal Fines Through a Porous Medium*. Technical report (University of California, Berkeley. Hydraulic Engineering Laboratory). University of California, Berkeley.

Sehaqui, Houssine, Qi Zhou, and Lars A. Berglund (2011). "High-porosity aerogels of high specific surface area prepared from nanofibrillated cellulose (NFC)". In: *Composites Science and Technology* 71.13, pp. 1593–1599. ISSN: 02663538. DOI: 10.1016/j.compscitech.2011.07.003.

Shah, S.M., J.P. Crawshaw, and E.S. Boek (2017). "Three-dimensional imaging of porous media using confocal laser scanning microscopy: THREE-DIMENSIONAL IMAGING". In: *Journal of Microscopy* 265.2, pp. 261–271. ISSN: 00222720. DOI: 10.1111/jmi.12496.

Sharp, K. V. and R. J. Adrian (2005). "On flow-blocking particle structures in microtubes". In: *Microfluidics and Nanofluidics* 1.4, pp. 376–380. ISSN: 1613-4982, 1613-4990. DOI: 10.1007/s10404-005-0043-x.

Shehzad, A. et al. (2010). "Porosity and stability of bread dough during proofing determined by video image analysis for different compositions and mixing conditions". In: *Food Research International* 43.8, pp. 1999–2005. ISSN: 09639969. DOI: 10.1016/j.foodres.2010.05.019.

Sparks, Trevor (2012). *Solid-liquid filtration: a user's guide to minimizing cost and environmental impact; maximizing quality and productivity*. 1st ed. OCLC: ocn731925442. [Oxford] ; Waltham, MA: Butterworth-Heinemann. 208 pp. ISBN: 978-0-08-097114-8.

Speight, James G. (2016). *Handbook of hydraulic fracturing*. Hoboken, New Jersey: John Wiley & Sons, Inc. 1 p. ISBN: 978-1-119-22509-6.

Sutherland, William (1904). "A Dynamical Theory of Diffusion for Non-Electrolytes and Molecular Mass of Albumin". In: *The Philosophical Magazine and Journal of Science* 9, pp. 781–785.

Tien, Chi and B. V. Ramarao (1989). *Granular filtration of aerosols and hydrosols*. 2nd ed. Amsterdam ; Boston: Elsevier. 494 pp. ISBN: 978-1-85617-458-9.

Tiraferri, Alberto et al. (2008). "Reduced aggregation and sedimentation of zero-valent iron nanoparticles in the presence of guar gum". In: *Journal of Colloid and Interface Science* 324.1, pp. 71–79. ISSN: 00219797. DOI: 10.1016/j.jcis.2008.04.064.

To, Kiwing, Pik-Yin Lai, and H. K. Pak (2001). "Jamming of Granular Flow in a Two-Dimensional Hopper". In: *Physical Review Letters* 86.1, pp. 71–74. ISSN: 0031-9007, 1079-7114. DOI: 10.1103/PhysRevLett.86.71.

Torquato, S., T. M. Truskett, and P. G. Debenedetti (2000). "Is Random Close Packing of Spheres Well Defined?" In: *Physical Review Letters* 84.10, pp. 2064–2067. ISSN: 0031-9007, 1079-7114. DOI: 10.1103/PhysRevLett.84.2064.

Torquato, Salvatore (2002). *Random heterogeneous materials: microstructure and macroscopic properties*. Interdisciplinary applied mathematics 16. OCLC: 248518949. New York, NY: Springer. 701 pp. ISBN: 978-1-4757-6357-7.

Tosco, Tiziana and Rajandrea Sethi (2009). "MNM1D: A Numerical Code for Colloid Transport in Porous Media: Implementation and Validation". In: *American journal of environmental sciences*. ISSN: 1553-345X. DOI: 10.3844/ajessp.2009.516.524.

— (2010). "Transport of Non-Newtonian Suspensions of Highly Concentrated Micro- And Nanoscale Iron Particles in Porous Media: A Modeling Approach". In: *Environmental Science & Technology* 44.23, pp. 9062–9068. ISSN: 0013-936X, 1520-5851. DOI: 10.1021/es100868n.

Vazquez, Juan Luis (2006). *The Porous Medium Equation*. Oxford University Press. ISBN: 978-0-19-856903-9. DOI: 10.1093/acprof:oso/9780198569039.001.0001.

Vicente, J. de et al. (2000). "Stability of Cobalt Ferrite Colloidal Particles. Effect of pH and Applied Magnetic Fields". In: *Langmuir* 16.21, pp. 7954–7961. ISSN: 0743-7463, 1520-5827. DOI: 10.1021/la0003490.

Vincent, Brian et al. (1986). "Depletion flocculation in dispersions of sterically stabilised particles (soft spheres)". In: *Colloids and Surfaces* 18.2, pp. 261–281. ISSN: 01666622. DOI: 10.1016/0166-6622(86)80317-1.

Wang, Xiaoling et al. (2016). "Probing phenotypic growth in expanding Bacillus subtilis biofilms". In: *Applied Microbiology and Biotechnology* 100.10, pp. 4607–4615. ISSN: 0175-7598, 1432-0614. DOI: 10.1007/s00253-016-7461-4.

Whitaker, Stephen (1969). "ADVANCES IN THEORY OF FLUID MOTION IN POROUS MEDIA". In: *Industrial and Engineering Chemistry* 61.12, pp. 14–28. ISSN: 0019-7866, 1541-5724. DOI: 10.1021/ie50720a004.

— (1986). "Flow in porous media II: The governing equations for immiscible, two-phase flow". In: *Transport in Porous Media* 1.2, pp. 105–125. ISSN: 0169-3913, 1573-1634. DOI: 10.1007/BF00714688.

Wiese, G. R. and T. W. Healy (1970). "Effect of particle size on colloid stability". In: *Transactions of the Faraday Society* 66, p. 490. ISSN: 0014-7672. DOI: 10.1039/tf9706600490.

Wills, B. A., Tim Napier-Munn, and B. A. Wills (2006). *Wills' mineral processing technology: an introduction to the practical aspects of ore treatment and mineral recovery*. In collab. with Julius Kruttschnitt Mineral Research Centre. 7th ed. Amsterdam ; Boston, MA: Elsevier/BH. 444 pp. ISBN: 978-0-7506-4450-1.

Wyss, Hans M. et al. (2006). "Mechanism for clogging of microchannels". In: *Physical Review E* 74.6, p. 061402. ISSN: 1539-3755, 1550-2376. DOI: 10.1103/PhysRevE.74.061402.

Xu, Shangping, Bin Gao, and James E. Saiers (2006). "Straining of colloidal particles in saturated porous media: STRAINING OF COLLOIDS". In: *Water Resources Research* 42.12. ISSN: 00431397. DOI: 10.1029/2006WR004948.

Yao, Kuan-Mu, Mohammad T. Habibian, and Charles R. O'Melia (1971). "Water and waste water filtration. Concepts and applications". In: *Environmental Science & Technology* 5.11, pp. 1105–1112. ISSN: 0013-936X, 1520-5851. DOI: 10.1021/es60058a005.

Yousif, M.H. et al. (1991). "Experimental and Theoretical Investigation of Methane-Gas-Hydrate Dissociation in Porous Media". In: *SPE Reservoir Engineering* 6.1, pp. 69–76. ISSN: 0885-9248. DOI: 10.2118/18320-PA.

Yuan, Dan et al. (2018). "Recent progress of particle migration in viscoelastic fluids". In: *Lab on a Chip* 18.4, pp. 551–567. ISSN: 1473-0197, 1473-0189. DOI: 10.1039/C7LC01076A.

Zarghami, Ahad et al. (2014). "Hydrodynamics in Porous Media: A Finite Volume Lattice Boltzmann Study". In: *Journal of Scientific Computing* 59.1, pp. 80–103. ISSN: 0885-7474, 1573-7691. DOI: 10.1007/s10915-013-9754-4.

Zularisam, A.W., A.F. Ismail, and Razman Salim (2006). "Behaviours of natural organic matter in membrane filtration for surface water treatment, a review". In: *Desalination* 194.1, pp. 211–231. ISSN: 00119164. DOI: 10.1016/j.desal.2005.10.030.

Zuriguel, Iker et al. (2015). "Clogging transition of many-particle systems flowing through bottlenecks". In: *Scientific Reports* 4.1, p. 7324. ISSN: 2045-2322. DOI: 10.1038/srep07324.

Chapter 7

Appendices

7.1 Precisions on the applications mentioned in conclusion

Further visual details on the four complementary projects mentioned in the perspectives. For more information, refer to the project investigators.

Bacterial accumulation in microfluidic channels

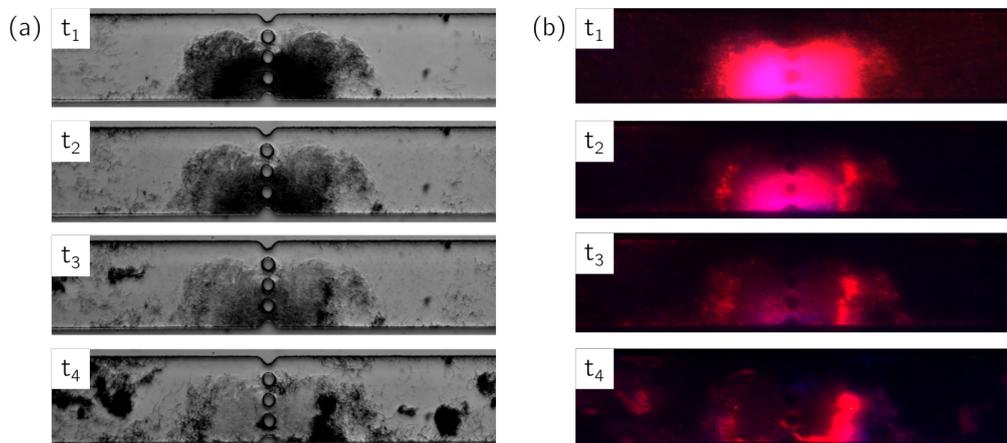

Figure 7.1: (a,b) Bright field and fluorescent images of a biofilm (Bacillus subtilis bacterial 3610 triple labeled; MSgg culture) forming in a microfluidic channel with obstacles, at four different times. Liquid loaded with nutrients flow goes right to left; fluorescence codes the viability of the bacteria forming the film. From a healthy (i.e. fluorescent) biofilm at t_1, viability decreases until t_4 when only upstream bacteria remain alive. Such studies highlight the filtration of nutrients by bacteria, linked to the permeability of the biofilms. Investigators: G. Gerber, X. Wang (Harvard University, SEAS)
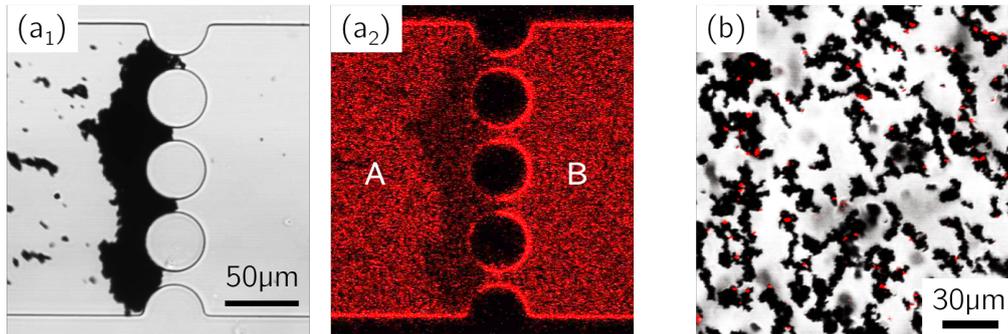
Nanoparticle capture using nZVI particles

Figure 7.2: Study on particle adsorption to nZVI filters. (a_1,a_2) Flow of positively charged nanoparticles through a filter of nZVI particles formed on top of four 10μm constrictions. The two images correspond to the bright field and fluorescent confocal imaging channels at the same time. A and B respectively highlight the upstream and downstream areas: if the filter is efficient at trapping nanoparticles, the concentration (fluorescence) in B is expected to be lower than in A. (b) Settled nZVI clusters (in black) previously mixed with 1μm positively charged colloids (from chapter 6; in red). All colloids are attached to nZVI clusters, which shows their affinity.
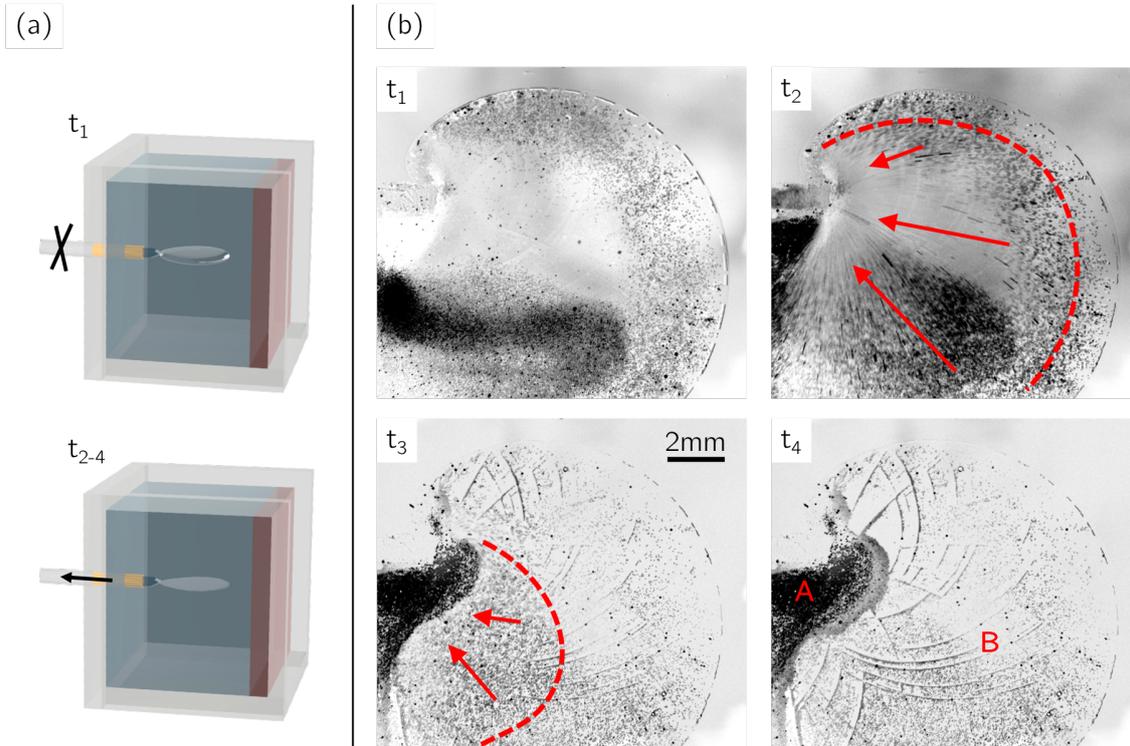
Fracture consolidation using confinement

Figure 7.3: Study on fracture consolidation using confinement. (a) Scheme of the setup: a controlled fracture ($\approx 10mm long$) in cube of brittle hydrogel, formed by injection of water loaded with particles from the left side. (b) Projected view of the particles inside the fracture (black dots), at four times. At t_1, the fracture is open, under pressure, and particles are spreaded in it. The pressure is then released and the fracture collapses: at t_2 and t_3, particles flow back towards the entry point of the fracture (red arrows and areas). At final time t_4, a large number of particles got trapped in a large cake ahead of the confined entry point (see A), and in the roughness (see B). Investigators: G. Gerber, E. Julien, T. Cochard and D.A. Weitz (Harvard University, SEAS).
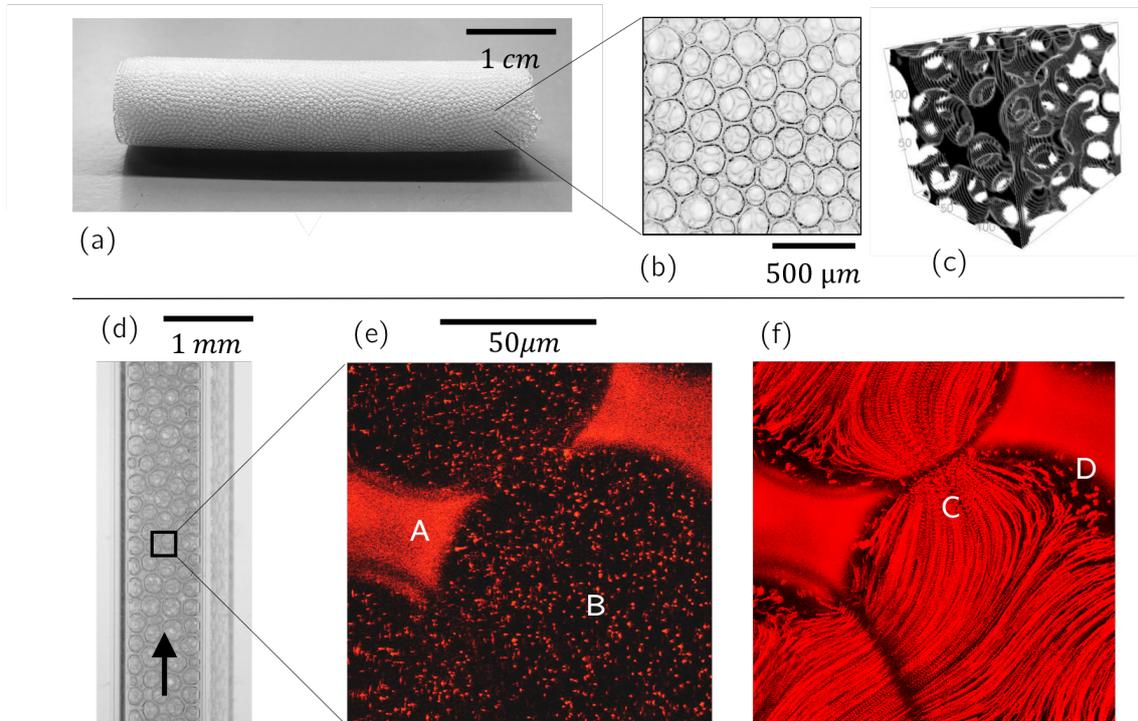
Colloidal transport in inverted RCP matrices

Figure 7.4: (a) Cylindrical centimeter sample of foamed hydrogel. (b) Direct binocular view of bubbles solidified in gel matrix. (c) 3D μ-CT reconstruction of the internal structure of the (open and connected) foam. (d) Material produded in a 1 mm square capillary, for flow experiments. (e) Confocal imaging showing 1 μm colloids flowing in the porosity B. The matrix itself contains a fluorescent dye and appears as A. (f) Particle trajectories in the porosity, highlighting two main regions: fast flow near the inter-bubble connections in C and dead-ends where colloidal diffusion prevails in D. Investigators: G. Gerber, C. Watanabe, O. Pitois (Navier Laboratory).

7.2 Sample making: the pluviation method

The detailed steps are:

i Fix a porous filter at one end of the column. The porosity of the filter must be small enough for the beads not to pass through, while its permeability must be high enough not to limit the flow in the column or over-pressurize it. This non-deformable filter will keep the beads stable in the column.

ii Connect and seal tubing on the same end.

iii Connect to the tubing a syringe filled with working fluid.

iv Saturate the tubing, filter, and ~90% of the column with working fluid. Tap on the system to remove any any bubble trapped in the filter or tubing. The aim of this step is double: create saturated conditions in the column and saturate the filter and therefore give it its final shape (due to swelling for instance).

v On the side, mix the dry beads (at least the volume expected to fill the column) with the working fluid. Let the beads sediment if their density is higher than the fluid.

vi With a syringe capped with a needle, collect the beads/fluid mix. Make sure no air enters the syringe, especially at the end of the needle. The beads sediment in the needle and in the syringe. At the end of the needle, the beads are help by the surface tension of the meniscus of water.

vii Here comes the key step of the method. Gently put in contact the end of the needle and the top free surface of fluid in the column. Since the surface tension breaks, gravity allows the beads to sediment from the syringe to the column, down to the filter. This corresponds to the pluviation step.

viii Let the process go until the desired volume of porous medium is added.

ix Shake with a constant force (mechanically on a vibrator or, by default, manually). Rearrangements will occur inside the pack of beads as they find more stable positions. As the solid fraction increases, the pack height decrease but the system remains completely saturated. A constant average porosity throughout the experiments is achieved by keeping the amplitude and the duration of the vibration constant.

x Insert the entry tubing (previously saturated with the working fluid) until it is in contact with the top layer of beads. Seal this end.

7.3 Making porous media in glass capillaries

The aim is to create a controlled, stable, enclosed and observable porous medium from the glass beads we chose. Two main ways have been used, a first one discovered at

the Weitzlab and used by most people in the Porous Media Team and a second later developed for the purpose of this work.

7.3.0.1 Method 1

The method was developed by S. Parsa Moghaddam and Y. Edery; Harvard Univeristy). It is briefly described here as a reference, but as not been used.

- Fill a $2 - 3mm$ capillary with glass beads (RCP)

- Sinter it to fix the system (beads slightly melt, which allows cohesion between beads at contact points)

- Fix a capillary on a microscopy slice

- Use plastic plugs pieces to form a chamber at each end of the capillary

- Place entry and exit tubing

- Connect the entry to a container of index-matched fluid

- Vacuum until full saturation of the medium (if the pressure is low enough, all air bubbles should disappear)

7.3.0.2 Method 2

This method developed for the present work is quicker and provides satisfying results. It avoids the vacuum step by forming the porous medium directly in saturated conditions. The steps are the following:

- Cut a $20mm$ long section of a $1mm$ width square glass capillary

- Insert a ($\approx 1mm$ long) cork at one end. The cork must be permeable enough not to limit the flow in the sample but impermeable and undeformable enough to retain the beads in place. I usually use a piece of foam with pores of the order of $100\mu m$. It is compacted in the capillary, with a final pore size estimated at $10\mu m$.

- Insert a $15cm$ long, $1mm$ OD, $0.5mm$ ID teflon tubing at the same end, over 2 to $3mm$. This will be the exit tubing. Illustration is provided in Fig.7.5a.

- Use NOA UV glue to fix the capillary at the middle of a standard microscopy slice. Cure under a UV lamp (5min at Weitzlab, 1h at Navier). Make sure the capillary is flat on the slice.

- Use 5min Epoxy glue to seal the gap between the end of the capillary and the inserted teflon tubing. Illustration is provided in Fig.7.5b.
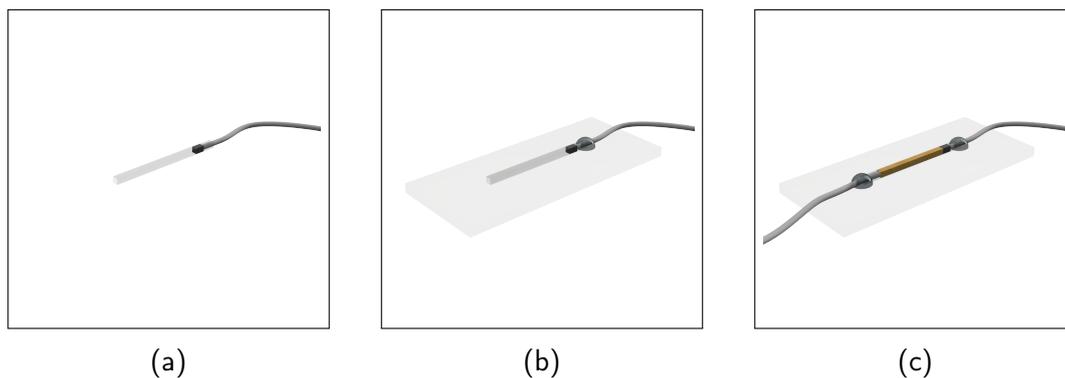
Figure 7.5: Slice preparation steps

- Fix a $1mL$ syringe filled with deionised water at the end of the exit tubing. Saturate the tubing, the cork, and the capillary with dH_2O. Even if the setup is kept horizontal, the fluid should be held in place by the capillary forces.

- Solvate the chosen glass beads in dH_2O and let them sediment. Usually, a few mm^3 of beads is added to $2mL$ of water in a $3mL$ Eppendorf.

- Use a $1mL$ syringe - with a tip large before the beads' diameter but smaller than $1mm$ - to suck the beads. They will quickly sediment in the tip. Push gently on the syringe for the very tip of the tip to be wet.

- Hold the previously saturated setup vertically and insert the tip in the first few millimetres. As soon as the fluids from the syringe and from the capillary merge, beads start to fall. Their pluviation movement towards the bottom (cork) leads to a Random Close Packing [ref from J-N. Roux]. Stop the injection when the beads are $2mm$ from the top.

- Give a dozen of flicks to the setup to densify the pack. The formed porous medium should be roughly $3mm$ from the top, with still fluid above it.

- Using the same syringe as before, saturate a $4cm$ long, $1mm$ OD, $0.5mm$ ID teflon tubing.

- Insert it in the capillary and gently push it in until it is in full contact with the top of the bead pack.

- Use 5min Epoxy glue to seal the gap. Final result is illustrated in Fig.7.5c.

7.3.0.2.1 Warning At several steps of the previous protocol, a perfect saturation is critical. The presence of an air bubble can prevent the beads from falling or lead to defaults in the Random Close Packing. Later on, it can also deform the cork and therefore destabilise the porous medium.
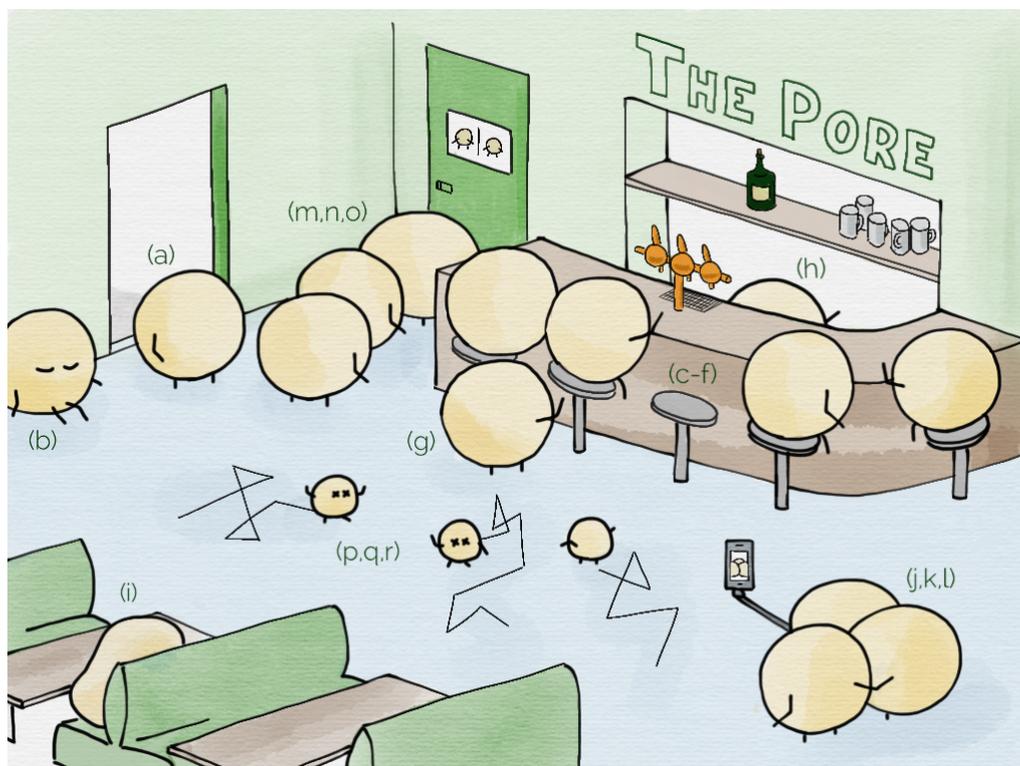
Visual conclusion

Figure 7.6: *My PhD in a bar*.

(a) gently flows through the door of *The Pore* bar and witnesses a strange spectacle.
(b) is laying in a corner, yet not bothering anyone. This spot of low velocity was the best to settle in and not being disturbed.
A bit further is a very appealing surface, to which (c),(d),(e) and (f) are already attached. These guys don't look like they will leave anytime soon, well adsorbed in their seats.
Behind them, (g) is having trouble to find a seat at this nice table. It is wandering around but constantly repelled! This surface only offers a single layer of seats, poor (g).
What is (h) doing? It is moving behind its counter, in a tiny space. It is hard to imagine how it got into this dead-end, it will probably stay there until the end of the night.
(i) seems in an even worse posture! It underestimated its belly, forced itself into this narrow seat and is now geometrically stuck.
Standing out from the crowd, (j),(k) and (l) form a cluster of friends. Always moving together, they want to look attractive to make new people adhere to their band.
(a) suddenly bumps into (m), who is stopped with (n) and (o) in a line. They are forced to accumulate patiently, someone might be clogged behind this door...
But the most impressive are (p),(q) and (r): these tiny devils have abused the liquor and are now walking randomly in the place, diffusing happy vibes.
There is a lot happening here, (a) may as well just turn around and explore the next pore...